



Universidad de Granada

Departamento de Física,
Teórica y del Cosmos

Interstellar Medium in Nearby Elliptical Radio Galaxies

Breezy Ocaña Flaquer
Instituto de Radio Astronomía Milimétrica - IRAM



Tesis Doctoral



Editor: Editorial de la Universidad de Granada
Autor: Breezy Ocaña Flaquer
D.L.: GR 3095-2010
ISBN: 978-84-693-3311-2

Departamento de Física Teórica
y del Cosmos
Universidad de Granada

Instituto de Radio Astronomía Milimétrica - IRAM

Interstellar Medium in Nearby Elliptical Radio Galaxies

Memoria presentada por:

Breezy Ocaña Flaquer

para optar al grado de

Doctora por la Universidad de Granada

Dirigida por:

Stephane Leon Tanne (ALMA/ESO)

Granada, 17 de Febrero de 2010

Como director de la tesis titulada *Interstellar Medium in Nearby Elliptical Radio Galaxies*, presentada por **D. Breezy Ocaña Flaquer**,

Dr. Stephane Leon Tanne, Doctor en Ciencias Físicas.

DECLARA:

Que la presente memoria, titulada *Interstellar Medium in Nearby Elliptical Radio Galaxies* ha sido realizada por **D. Breezy Ocaña Flaquer** bajo su dirección en el Instituto de Radio Astronomía Milimétrica. Esta memoria constituye la tesis que **D. Breezy Ocaña Flaquer** presenta para optar al grado de **Doctora por la Universidad de Granada**.

Granada, a 17 de Febrero de 2010

Fdo:
Stephane Leon Tanne

Breezy Ocaña Flaquer, autora de la tesis *Interstellar Medium in Nearby Elliptical Radio Galaxies*, autoriza a que un ejemplar de la misma quede ubicada en la Biblioteca de la Escuela Superior de Física de Granada.

Fdo.: Breezy Ocaña Flaquer
Granada, a 17 de Febrero de 2010

Esta tesis está dedicada a
todos los que quieren cumplir
un sueño, y a todos los niños
dominicanos, y del mundo,
que lo ven como imposible.

Querer es poder!

También está dedicada a todos
los vivos que forma parte de
mi y a todos los que hoy no
forman parte del mundo tal
como lo entendemos pero que
han estado y han influenciado
en mi vida.

"You must be the change you wish to see in the world."

Mahatma Gandhi

Contents

List of Figures	vii
List of Tables	xiii
Resumen	xix
1 Introduction	1
1.1 Galaxies	1
1.1.1 Elliptical Galaxies	1
1.2 Radio Galaxies	2
1.3 Interstellar Medium in Radio Galaxies	3
1.3.1 Molecular Gas	4
1.3.2 Dust	7
1.3.3 Classification of Radio Galaxies	8
1.4 TANGO	11
1.5 The goals of this work	12
2 TANGO Sample	15
2.1 The Low and Medium redshift TANGO Sample	15
2.1.1 Low z Sample	15
2.1.2 Medium z Sample	17
2.2 Catalog Presentation	18
2.2.1 3CR Catalog	19
2.2.2 New General Catalog -NGC	19
2.2.3 Second Bologna Survey - B2	21
2.2.4 Ohio State University Radio Survey Catalog - OQ	21
2.2.5 Uppsala General Catalog of Galaxies - UGC	21
2.3 Optical Properties	21
3 Instrumentation	23
3.1 Introduction	23
3.2 mm/submm Instrumentation: Institute of Milimetric Radio Astronomy - IRAM.	23
3.2.1 IRAM - 30 meter Telescope	24

3.2.2	Techniques and Instrumentation	24
3.2.3	IRAM -Plateau de Bure	26
3.3	cm Instrumentation: Effelsberg	26
3.4	IR Instrumentation: IRAS and Spitzer	27
3.4.1	IRAS	27
3.4.2	SPITZER	27
3.4.3	IRAC	28
3.4.4	MIPS	29
4	Observations and Data Reduction	31
4.1	Introduction	31
4.2	TANGO LzS observation	31
4.3	Calibration	34
4.4	Data reduction with IRAM 30m Telescope	36
4.4.1	ASTRO	36
4.4.2	CLASS	38
4.4.3	Interferometer: IRAM PdBI	39
4.5	Continuum data	39
4.5.1	SPITZER	40
4.6	Molecular lines observed	42
4.6.1	Carbon monoxide - ^{12}CO	42
4.6.2	Hydrogen cyanide - HCN	43
4.6.3	Formyl cation - HCO^+	43
4.7	Summary and Conclusions	44
5	Molecular Gas	45
5.1	Computation of the molecular gas mass	45
5.2	Results on molecular gas mass	46
5.3	Faranoff and Riley	49
5.4	CO line ratios	51
5.4.1	Beam/source coupling	55
5.5	Molecular gas disk	55
5.6	Continuum Data	57
5.7	Discussion: Origin of the molecular gas	59
5.8	Summary and Conclusions	62
6	Dust	63
6.1	Introduction	63
6.2	Dust properties from IRAS	64
6.2.1	Star Formation	64
6.2.2	Dust Mass and Dust Temperature	64
6.3	Dust properties from SPITZER data	67
6.3.1	IRAC	69
6.3.2	MIPS	69

6.4	Multi Dust Component Fitting	70
6.5	Conclusion	71
7	Neutral Hydrogen - HI	73
7.1	Introduction	73
7.2	TANGO Data	74
7.2.1	Effelsberg Observations	74
7.2.2	Neutral Hydrogen Mass	77
7.3	Discussion and future work	77
8	From Thermal to Synchrotron emission	81
8.1	Introduction	81
8.2	μm Data	81
8.3	mm Data	82
8.4	cm Data	82
8.5	Synchrotron	82
8.5.1	How to calculate the Synchrotron age of the galaxies?	83
8.6	Discussion	85
9	CO vs. FIR Luminosities	87
9.1	L_{CO}	87
9.2	L_{FIR}	87
9.3	Relationship between L_{CO} and L_{FIR}	89
9.4	M_{H_2} vs. L_B	90
9.5	SFE vs L_B	90
10	Comparison with other samples	95
10.1	Introduction	95
10.2	Samples	95
10.3	Molecular gas	96
10.3.1	Molecular gas disk	97
10.4	Dust	98
10.5	CO-FIR Luminosity	98
10.6	Conclusion	102
11	3CR 31	103
11.1	Observation and data reduction	104
11.1.1	Observation	104
11.1.2	Data reduction	104
11.1.3	Continuum	105
11.2	Molecular gas mass	105
11.3	Molecular gas disk	105
11.3.1	Interferometric Data	106
11.4	Dust	107

11.4.1	Multi Dust Components	108
11.5	Luminosity	109
11.5.1	CO Luminosity	109
11.5.2	FIR Luminosity	109
11.5.3	Is there Star Formation in 3CR 31?	109
11.6	How old is the synchrotron emission in 3CR 31?	110
11.6.1	Collecting the Data	110
11.6.2	Using <i>SynAge</i>	114
11.6.3	CASE 2	115
11.6.4	For the future work of this galaxy	117
11.7	Conclusion	119
12	A Control Sample:	
	HCN observations and results	125
12.1	Introduction	125
12.1.1	Control Sample: The AMIGA galaxies	125
12.1.2	Interstellar Medium	125
12.1.3	HCN(1-0) survey in the AMIGA Project	126
12.1.4	The Goals	127
12.2	Observation and Data Reduction	127
12.3	Results	128
12.3.1	HCN-FIR relationship in isolated galaxies	129
12.4	Conclusions	131
13	Summary and Conclusions	135
14	The Future of TANGO	139
15	Conclusiones	141
A	Individual Galaxies	147
A.1	3CR 31	148
A.2	3CR 40	152
A.2.1	HI data	153
A.3	3CR66B	156
A.4	3CR 83.1	160
A.5	3CR 88	163
A.6	3CR 98	167
A.7	3C 129	170
A.8	3CR 236	173
A.9	3C 264	176
A.9.1	HI data	177
A.10	3C 270	180
A.10.1	HI data	183

A.11 3CR 272.1	184
A.12 3C 274	188
A.13 3CR 296	191
A.14 3C 305	194
A.15 3C 321	198
A.16 3C 327	202
A.17 3CR 353	206
A.18 3C 386	209
A.19 3CR 402	212
A.20 3C 403	216
A.21 3CR 433	219
A.22 3C 442	222
A.23 3C 449	225
A.24 3CR 465	228
A.25 NGC 315	231
A.26 NGC 326	235
A.27 NGC 541	238
A.28 NGC 708	241
A.29 NGC 2484	245
A.30 NGC 2892	248
A.30.1 HI data	248
A.31 NGC 3801	252
A.31.1 HI data	253
A.32 NGC 4278	256
A.33 NGC 5127	260
A.34 NGC 5141	263
A.35 NGC 5490	266
A.36 NGC 6251	269
A.37 NGC 7052	273
A.38 B2 0034+25	277
A.39 B2 0116+31	280
A.39.1 HI data	281
A.40 B2 0648+27	285
A.41 B2 0836+29B	289
A.42 B2 0915+32B	292
A.43 B2 0924+30	295
A.44 B2 1101+38	298
A.45 B2 1347+28	301
A.46 B2 1357+28	304
A.47 B2 1447+27	307
A.48 B2 1512+30	310
A.49 B2 1525+29	313
A.50 B2 1553+24	316
A.50.1 HI data	316

A.51 UGC 7115	320
A.52 OQ 208	323
B Abbreviations	327
Bibliography	329
Referencias	

List of Figures

1.1	Hubble Tuning-Fork	2
1.2	Multi Wavelength image form M 87	5
1.3	Blazar, viewing angle.	9
1.4	A general description of an AGN	10
2.1	Low z TANGO galaxies	16
2.2	Histogram of the radio power at 1.4 GHz for the LzS.	17
2.3	Medium z TANGO galaxies	19
3.1	Spitzer's wavelengths with SED.	28
4.1	Galaxies in LzS TANGO visible with ALMA	37
5.1	Distribution of the molecular gas mass in TANGO.	48
5.2	M_{H_2} versus z	50
5.3	Molecular gas mass distribution	51
5.4	Molecular gas mass distribution	52
5.5	Plot of the line ratio of the galaxies.	54
5.6	Correction factor K for the CO(2-1)-to-CO(1-0) line ratio	56
5.7	Histogram of the gas filling time for our sample.	61
5.8	Histogram of the stellar mass loss in M_{\odot}/yr	61
6.1	Histograms of the dust mass and temperature	66
6.2	Histogram of the Gas-to-Dust mass ratio.	67
6.3	3CR83.1 at $70\mu\text{m}$	68
6.4	3CR31 - Fitting of dust components	72
8.1	3CR 31: SED	85
9.1	L_{FIR} vs. L'_{CO}	91
9.2	Molecular gas mass versus blue luminosity	92
9.3	Molecular gas mass versus FIR luminosity	92
9.4	Star formation efficiency compared to the blue luminosity	93
10.1	Histograms of the dust mass and the dust temperature	99

10.2	L_{FIR} vs. L'_{CO} of all the samples used in this study	100
11.1	Image from the HST for 3CR 31 (Martel et al. 1999)	103
11.2	Interferometric map for CO(1-0) from IRAM PdBI.	106
11.3	Position Velocity diagram for the CO(1-0) emission in 3CR 31 . . .	107
11.4	CO(1-0) intensity profile along the major axis for the galaxy 3CR 31.	108
11.5	The orange arrow shows where the location of 3CR 31 is in the plot	110
11.6	Result from <i>SynAge</i> fit	116
11.7	This is the result from <i>SynAge</i> , using only the “new galaxy”. . . .	118
11.8	This is the result from <i>SynAge</i> , using only the “old galaxy”. . . .	119
11.9	3CR 31 contour image from the VLA Telescope	121
11.10	Optical and radio image for 3CR 31	122
11.11	3CR 31 VLA image	123
12.1	L_{HCN} vs L_{IR}	130
12.2	Temperature at the center of the galaxy.	132
12.3	HCN(1-0) maps of CIG 147 and CIG 1004	133
A.1	HST - 3CR 31	148
A.2	3CR 31 CO(1-0)	150
A.3	3CR 31 CO(2-1)	151
A.4	3CR 31: SED	151
A.5	HST - 3CR 40	152
A.6	3CR 40 CO(1-0)	154
A.7	3CR 40 CO(2-1)	154
A.9	HST - 3CR 66B	156
A.10	3CR 66B CO(1-0)	158
A.11	3CR 66B CO(2-1)	158
A.12	3CR 66B: SED	159
A.13	HST - 3CR 83.1	160
A.14	3CR 83.1 CO(1-0)	162
A.15	3CR 83.1 CO(2-1)	162
A.16	HST - 3CR 88	163
A.17	3CR 88 CO(1-0)	165
A.18	3CR 88 CO(2-1)	165
A.19	3CR 88: SED	166
A.20	3CR 98 optical image.	167
A.21	3CR 98 CO(1-0)	168
A.22	3CR 98 CO(2-1)	169
A.23	HST - 3CR 129	170
A.24	3CR 129 CO(1-0)	172
A.25	3CR 129 CO(2-1)	172
A.26	HST - 3CR 236	173
A.27	3CR 236 CO(1-0)	175

A.28 HST - 3CR 264	176
A.29 3CR 264 CO(1-0)	178
A.30 3CR 264 CO(1-0)	178
A.32 HST - 3CR 270	180
A.33 3CR 270 CO(1-0)	182
A.34 3CR 270 CO(2-1)	182
A.36 HST - 3CR 272.1	184
A.37 3CR 272.1 CO(1-0)	186
A.38 3CR 272.1 CO(2-1)	186
A.39 3CR 272.1: SED	187
A.40 HST - 3CR 274	188
A.41 3CR 274 CO(1-0)	190
A.42 3CR 274: SED	190
A.43 HST - 3CR 296	191
A.44 3CR 296 CO(1-0)	193
A.45 3CR 274 CO(2-1)	193
A.46 HST - 3CR 305	194
A.47 3CR 305 CO(1-0)	196
A.48 3CR 305: SED	197
A.49 HST - 3CR 321	198
A.50 3CR 321 CO(1-0)	200
A.51 3CR 321: SED	201
A.52 3CR 327 optical image.	202
A.53 3CR 327 CO(1-0)	204
A.54 3CR 327: SED	205
A.55 HST - 3CR 353	206
A.56 3CR 353 CO(1-0)	208
A.57 3CR 353 CO(2-1)	208
A.58 HST - 3CR 386	209
A.59 3CR 386 CO(1-0)	211
A.60 3CR 386 CO(2-1)	211
A.61 HST - 3CR 402	212
A.62 3CR 402 CO(1-0)	214
A.63 3CR 402 CO(2-1)	214
A.64 3CR 402: SED	215
A.65 HST - 3CR 403	216
A.66 3CR 403 CO(1-0)	218
A.67 HST - 3CR 433	219
A.68 3CR 433 CO(1-0)	221
A.69 HST - 3CR 442	222
A.70 3CR 442 CO(1-0)	224
A.71 3CR 442 CO(2-1)	224
A.72 HST - 3CR 449	225
A.73 3CR 449 CO(1-0)	227

A.74 3CR 449 CO(2-1)	227
A.75 HST - 3CR 465	228
A.76 3CR 465 CO(1-0)	230
A.77 3CR 465 CO(2-1)	230
A.78 NGC 315 optical image.	231
A.79 NGC 315 CO(1-0)	233
A.80 NGC 315 CO(2-1)	233
A.81 NGC 315: SED	234
A.82 NGC 326 optical image.	235
A.83 NGC 326 CO(1-0)	237
A.84 NGC 326 CO(2-1)	237
A.85 NGC 541 optical image.	238
A.86 NGC 541 CO(1-0)	240
A.87 NGC 541 CO(2-1)	240
A.88 NGC 708 optical image.	241
A.89 NGC 708 CO(1-0)	243
A.90 NGC 708 CO(2-1)	243
A.91 NGC 708: SED	244
A.92 NGC 2484 optical image.	245
A.93 NGC 2484 CO(1-0)	247
A.94 NGC 2484 CO(2-1)	247
A.95 NGC 2892 optical image.	248
A.96 NGC 2892 CO(1-0)	250
A.97 NGC 2892 CO(2-1)	250
A.99 NGC 3801 optical image.	252
A.100NGC 3801 CO(1-0)	254
A.101NGC 3801 CO(2-1)	254
A.103NGC 4278 optical image.	256
A.104NGC 4278 CO(1-0)	258
A.105NGC 4278 CO(2-1)	258
A.106NGC 4278: SED	259
A.107NGC 5127 optical image.	260
A.108NGC 5127 CO(1-0)	262
A.109NGC 5127 CO(2-1)	262
A.110NGC 5141 optical image.	263
A.111NGC 5141 CO(1-0)	265
A.112NGC 5141 CO(2-1)	265
A.113NGC 5490 optical image.	266
A.114NGC 5490 CO(1-0)	268
A.115NGC 5490 CO(2-1)	268
A.116NGC 6251 optical image.	269
A.117NGC 6251 CO(1-0)	271
A.118NGC 6251: SED	272
A.119NGC 7052 optical image.	273

A.120NGC 7052 CO(1-0)	275
A.121NGC 7052 CO(2-1)	275
A.122NGC 7052: SED	276
A.123B2 0034+25 optical image	277
A.124B2 0034+25 CO(1-0)	279
A.125B2 0034+25 CO(2-1)	279
A.126B2 0116+31 optical image	280
A.127B2 0116+31 CO(1-0)	282
A.128B2 0116+31 CO(2-1)	282
A.130B2 0116+31: SED	284
A.131B2 0116+31 optical image	285
A.132B2 0648+27 CO(1-0)	287
A.133B2 0648+27 CO(2-1)	287
A.134B2 0648+27: SED	288
A.135B2 0116+31 optical image	289
A.136B2 0836+29B CO(1-0)	291
A.137B2 0915+32B optical image	292
A.138B2 0915+32B CO(1-0)	294
A.139B2 0615+32B CO(2-1)	294
A.140B2 0924+30 optical image	295
A.141B2 0924+30 CO(1-0)	297
A.142B2 0924+30 CO(2-1)	297
A.143B2 0924+30 optical image	298
A.144B2 1101+38 CO(1-0)	300
A.145B2 1101+38 CO(2-1)	300
A.146B2 1347+28 optical image	301
A.147B2 1347+28 CO(1-0)	303
A.148B2 1347+28 CO(2-1)	303
A.149B2 1357+28 optical image	304
A.150B2 1357+28 CO(1-0)	306
A.151B2 1357+28 CO(2-1)	306
A.152B2 1447+27 optical image	307
A.153B2 1447+27 CO(1-0)	309
A.154B2 1447+27 CO(2-1)	309
A.155B2 1512+30 optical image	310
A.156B2 1512+30 CO(1-0)	312
A.157B2 1512+30 CO(2-1)	312
A.158B2 1525+29 optical image	313
A.159B2 1525+29 CO(1-0)	315
A.160B2 1525+29 CO(2-1)	315
A.161B2 1553+24 optical image	316
A.162B2 1553+24 CO(1-0)	318
A.163B2 1553+24 CO(2-1)	318
A.165UGC 7115 optical image	320

A.166UGC 7115 CO(1-0)	322
A.167UGC 7115 CO(2-1)	322
A.168OQ 208 optical image	323
A.169OQ 208 CO(1-0)	325
A.170OQ 208: SED	325

List of Tables

2.1	List of galaxies for LzS depending on their catalog	18
2.2	Medium z TANGO Sample.	20
3.1	IRAS Summary	27
3.2	IRAC Summary	29
3.3	IRAC Apperture Corrections	29
3.4	MIPS Summary	30
4.1	Journal for the observations	34
5.1	Molecular Gas data	47
5.2	Mean and median values of the molecular gas mass	52
5.3	CO(2-1)-to CO(1-0) line ratio of the detected galaxies, not corrected by the different beam dilutions.	54
5.4	Molecular mass gas of the galaxies that present the double horn profile.	57
5.5	IRAM 30m fluxes at 3 mm and 1 mm. <i>X means that there was no data, and "..."</i> refers to undetected flux.	59
6.1	IRAS data for the galaxies that have been detected at 60 μm and at 100 μm	65
6.2	Dust mass and temperature.	66
6.3	SPITZER - IRAC data	69
6.4	SPITZER - MIPS data	70
6.5	Fitted Temperatures and Masses for 3 dust components.	72
7.1	Data from the HI observations with Effelsberg-100m Telescope.	76
7.2	TANGO M_{HI}	78
7.3	Continue measurements at 1.4 GHz	79
9.1	Values of CO(1-0) Luminosities and FIR Luminosities	89
10.1	Comparison samples and their average molecular gas mass	97
10.2	Percentage of the galaxies, within the detected galaxies of each sample of the double horn CO profile feature	98

10.3	FIR-to-CO Luminosities and their ratios.	99
10.4	χ^2 values of each sample for the fitting relation	102
11.1	Flux densities for 3CR 31	105
11.2	Frequencies in boldface are the frequencies finally used.	114
11.3	3CR 31 Synchrotron Ages	117
11.4	3CR 31 New Synchrotron Ages	118
11.5	3CR 31 New Synchrotron Ages	120
12.1	Observed isolated galaxies for HCN(1-0) and CO(2-10)	128
12.2	Expected HCN Luminosities calculated from Gao & Solomon (2004a)	129
A.1	General Data for 3CR 31	149
A.2	Fluxes of 3CR 31	149
A.3	Luminosities for 3CR 31	150
A.4	General Data for 3CR 40	153
A.5	Fluxes of 3CR 40	153
A.6	Luminosities for 3CR 40	153
A.7	General Data for 3CR 31	157
A.8	Fluxes of 3CR 66B	157
A.9	Luminosities for 3CR 66B	157
A.10	General Data for 3CR 83.1	161
A.11	Fluxes of 3CR 83.1	161
A.12	Luminosities for 3CR 83.1	161
A.13	General Data for 3CR 88	164
A.14	Fluxes of 3CR 88	164
A.15	Luminosities for 3CR 88	164
A.16	General Data for 3CR 88	167
A.17	Fluxes of 3CR 88	168
A.18	Luminosities for 3CR 98	168
A.19	General Data for 3CR 129	171
A.20	Fluxes of 3CR 129	171
A.21	Luminosities for 3CR 129	171
A.22	General Data for 3CR 236	174
A.23	Fluxes of 3CR 236	174
A.24	Luminosities for 3CR 236	174
A.25	General Data for 3CR 264	177
A.26	Fluxes of 3CR 264	177
A.27	Luminosities for 3CR 264	177
A.28	General Data for 3CR 270	181
A.29	Fluxes of 3CR 270	181
A.30	Luminosities for 3CR 270	181
A.31	General Data for 3CR 272.1	185
A.32	Fluxes of 3CR 272.1	185

A.33 Luminosities for 3CR 272.1	185
A.34 General Data for 3CR 274	189
A.35 Fluxes of 3CR 274	189
A.36 Luminosities for 3CR 274	189
A.37 General Data for 3CR 296	192
A.38 Fluxes of 3CR 296	192
A.39 Luminosities for 3CR 296	192
A.40 General Data for 3CR 305	195
A.41 Fluxes of 3CR 305	195
A.42 Luminosities for 3CR 305	195
A.43 General Data for 3CR 321	199
A.44 Fluxes of 3CR 321	199
A.45 Luminosities for 3CR 321	199
A.46 General Data for 3CR 327	203
A.47 Fluxes of 3CR 327	203
A.48 Luminosities for 3CR 327	203
A.49 General Data for 3CR 353	207
A.50 Fluxes of 3CR 353	207
A.51 Luminosities for 3CR 353	207
A.52 General Data for 3CR 386	210
A.53 Fluxes of 3CR 386	210
A.54 Luminosities for 3CR 386	210
A.55 General Data for 3CR 402	213
A.56 Fluxes of 3CR 402	213
A.57 Luminosities for 3CR 402	213
A.58 General Data for 3CR 403	217
A.59 Fluxes of 3CR 403	217
A.60 Luminosities for 3CR 403	217
A.61 General Data for 3CR 433	220
A.62 Fluxes of 3CR 433	220
A.63 Luminosities for 3CR 433	220
A.64 General Data for 3CR 442	223
A.65 Fluxes of 3CR 442	223
A.66 Luminosities for 3CR 442	223
A.67 General Data for 3CR 449	226
A.68 Fluxes of 3CR 449	226
A.69 Luminosities for 3CR 449	226
A.70 General Data for 3CR 465	229
A.71 Fluxes of 3CR 465	229
A.72 Luminosities for 3CR 465	229
A.73 General Data for NGC 315	232
A.74 Fluxes of NGC 315	232
A.75 Luminosities for NGC 315	232
A.76 General Data for NGC 326	236

A.77 Fluxes of NGC 326	236
A.78 Luminosities for NGC 326	236
A.79 General Data for NGC 541	239
A.80 Fluxes of NGC 541	239
A.81 Luminosities for NGC 541	239
A.82 General Data for NGC 708	242
A.83 Fluxes of NGC 708	242
A.84 Luminosities for NGC 708	242
A.85 General Data for NGC 2484	246
A.86 Fluxes of NGC 2484	246
A.87 Luminosities for NGC 2484	246
A.88 General Data for NGC 2892	249
A.89 Fluxes of NGC 2892	249
A.90 Luminosities for NGC 2892	249
A.91 General Data for NGC 3801	253
A.92 Fluxes of NGC 3801	253
A.93 Luminosities for NGC 3801	253
A.94 General Data for NGC 4278	257
A.95 Fluxes of NGC 4278	257
A.96 Luminosities for NGC 4278	257
A.97 General Data for NGC 5127	261
A.98 Fluxes of NGC 5127	261
A.99 Luminosities for NGC 5127	261
A.100 General Data for NGC 5141	264
A.101 Fluxes of NGC 5141	264
A.102 Luminosities for NGC 5141	264
A.103 General Data for NGC 5490	267
A.104 Fluxes of NGC 5490	267
A.105 Luminosities for NGC 5490	267
A.106 General Data for NGC 6251	270
A.107 Fluxes of NGC 6251	270
A.108 Luminosities for NGC 6251	270
A.109 General Data for NGC 7052	274
A.110 Fluxes of NGC 7052	274
A.111 Luminosities for NGC 7052	274
A.112 General Data for B2 0034+25	278
A.113 Fluxes of B2 0034+25	278
A.114 Luminosities for B2 0034+25	278
A.115 General Data for B2 0116+31	281
A.116 Fluxes of B2 0116+31	281
A.117 Luminosities for B2 0116+31	281
A.118 General Data for B2 0648+27	286
A.119 Fluxes of B2 0648+27	286
A.120 Luminosities for B2 0648+27	286

A.121	General Data for B2 0836+29B	290
A.122	Fluxes of B2 0836+29B	290
A.123	Luminosities for B2 0836+29B	290
A.124	General Data for B2 0915+32B	293
A.125	Fluxes of B2 0915+32B	293
A.126	Luminosities for B2 0915+32B	293
A.127	General Data for B2 0924+30	296
A.128	Fluxes of B2 0924+30	296
A.129	Luminosities for B2 0924+30	296
A.130	General Data for B2 1101+38	299
A.131	Fluxes of B2 1101+38	299
A.132	Luminosities for B2 1101+38	299
A.133	General Data for B2 1347+28	302
A.134	Fluxes of B2 1347+28	302
A.135	Luminosities for B2 1347+28	302
A.136	General Data for B2 1357+28	305
A.137	Fluxes of B2 1357+28	305
A.138	Luminosities for B2 1357+28	305
A.139	General Data for B2 1447+27	308
A.140	Fluxes of B2 1447+27	308
A.141	Luminosities for B2 1447+27	308
A.142	General Data for B2 1512+30	311
A.143	Fluxes of B2 1512+30	311
A.144	Luminosities for B2 1512+30	311
A.145	General Data for B2 1525+29	314
A.146	Fluxes of B2 1525+29	314
A.147	Luminosities for B2 1525+29	314
A.148	General Data for B2 1553+24	317
A.149	Fluxes of B2 1553+24	317
A.150	Luminosities for B2 1553+24	317
A.151	General Data for UGC 7115	321
A.152	Fluxes of UGC 7115	321
A.153	Luminosities for UGC 7115	321
A.154	General Data for OQ 208	324
A.155	Fluxes of OQ 208	324
A.156	Luminosities for OQ 208	324

Resumen

Esta tesis está basada en un extenso estudio sobre el medio interestelar en una muestra de más de 50 radio galaxias. Se ha hecho un análisis pormenorizado de datos propios y recopilados de la literatura sobre las propiedades del gas molecular en una muestra local de radio galaxias. Se ha mostrado con claridad el extenso rango que cubre la masa de gas molecular en estas galaxias, poniendo en manifiesto los sesgos presentes en los estudios previos. Este análisis se ha centrado también en las propiedades del polvo en estas galaxias, usando datos de varios satélites además de telescopios terrestres.

En este trabajo se comparan las propiedades del medio interestelar de nuestra muestra con las propiedades de otras muestras de galaxias que tienen distinto criterio de selección.

Además, se presentan los resultados preliminares del contenido en HI de la muestra de radio galaxias para analizar los efectos del entorno sobre el origen del gas en estas radio galaxias.

En segundo lugar, se ha realizado un estudio detallado de una radio galaxia en particular, 3CR 31. Se presentan datos interferométricos del gas molecular y se analizan en detalle las propiedades del polvo a partir de datos combinados de Spitzer, IRAS y el radio telescopio IRAM-30m. Usando un programa desarrollado en el Instituto di Radio Astronomia di Bologna (IRA) llamado SynAge, se estudia la edad de la emisión sincrotrón en esta galaxia. Este estudio aporta una visión enfocada de las propiedades estadísticas estudiadas en la muestra completa.

En tercer lugar, se presentan los resultados preliminares de un estudio sobre la emisión del gas molecular denso en galaxias aisladas a través de la molécula HCN. Este estudio proporcionará una muestra de control para analizar los efectos del entorno sobre las propiedades del gas molecular denso en las radio galaxias.

Los resultados de esta tesis doctoral han sentado la base para un proyecto internacional creado con el objetivo de estudiar el medio interestelar en radio

galaxias a múltiples frecuencias. Este proyecto se llama TANGO por sus siglas en inglés: Thorough ANalysis of radio Galaxies Observations ([Ocaña Flaquer et al. 2010](#)).

Chapter 1

Introduction

1.1 Galaxies

Galaxies are usually a massive combination of stars, star remanent and interstellar medium (ISM), mainly formed by gas and dust, tied together by gravitation. The Astronomer Edwin Hubble was the first to categorize galaxies in a comprehensive way. Working with the then recently completed 2.5-m optical telescope on Mount Wilson in California in 1924, he classified the galaxies he saw into 4 basic types - *spirals, barred spirals, ellipticals and irregulars* - only on the basis of appearance. Many modifications and refinements have been incorporated over the years, but the basic **Hubble classification scheme** is still used today ([Chaisson & McMillan 1999](#)).

Hubble originally thought (incorrectly) that the tuning-fork diagram (see figure 1.1) could be interpreted as an evolutionary sequence for galaxies. As a result, he referred to galaxies toward the left of the diagram as being *early types* and those towards the right as *late types*, a terminology that is still widely used today ([Carroll & Ostlie 1996](#)).

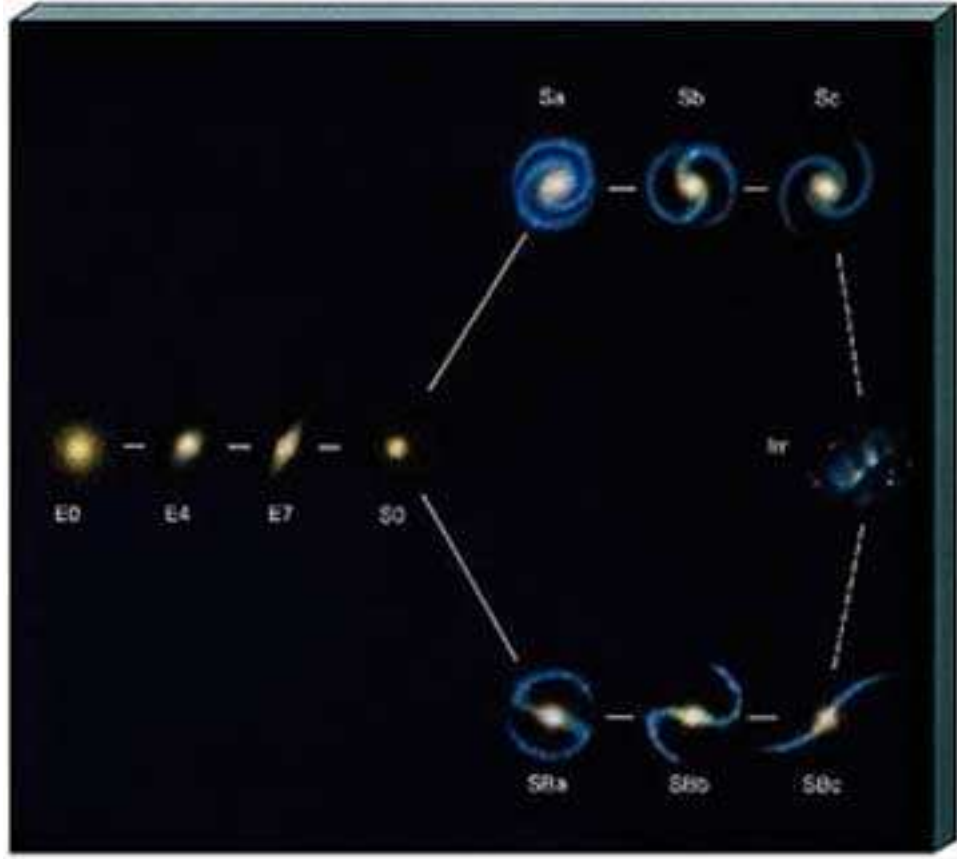
1.1.1 Elliptical Galaxies

All of the galaxies studied in the main sample of this PhD Thesis have an elliptical shape. According to [Carroll & Ostlie \(1996\)](#), Hubble made divisions based on the observed **ellipticity** of the galaxy, defined by:

$$\epsilon \equiv 1 - \beta/\alpha \tag{1.1}$$

where α and β are the apparent major and minor axes of the ellipse, respectively, projected onto the plane of the sky. The Hubble type is quoted as 10ϵ . Elliptical galaxies range from a spherical distribution of stars, E0, to a highly flat distribution, E7, and ellipticities greater than $\epsilon=0.7$ has never been observed.

Figure 1.1: Hubble Tuning-Fork



The surface brightness profile of most elliptical galaxies is defined by **de Vaucouleurs Law**:

$$I(R) = I(0)^{-\kappa R^{0.25}} = I_e^{-7.67[(\frac{R}{R_e})^{0.25} - 1]} \quad (1.2)$$

where R_e is the radius of the isophote containing half the total luminosity, and I_e is the surface brightness at R_e .

1.2 Radio Galaxies

Radio galaxies, as the name implies, are very luminous in the radio wavelengths and have strong radio sources in the range of 10^{41} to $10^{46} \text{ ergs}^{-1}$. This power is due to a synchrotron process, a process in which electromagnetic radiation is generated by acceleration of ultra-relativistic charged particles through magnetic fields. Radio galaxies are normally hosted by giant elliptical galaxies (see section 1.1.1) with visual luminosities of about $2.1 \times 10^{10} h^{-2}$

L_{\odot} (Kellermann & Verschuur (1988), calculated with a Hubble constant of $H = 100 \text{ km s}^{-1} \text{ Mpc}^{-1}$). Although in general relatively deficient in cold gas, elliptical galaxies still contain some dense and cold Interstellar Medium (ISM) detected in CO(1-0) emission (e.g. Wiklind & Rydbeck 1986). Dust is also detected in the far-infrared (FIR) radiation which is assumed to be thermal and to originate from dust heated by young massive stars or by the active galactic nuclei (AGN) (Knapp et al. 1989; Wiklind & Henkel 1995). According to Kennicutt (1998), early-type galaxies show no independent evidence of high star formation rates (SFRs), suggesting that the older stars or AGN are responsible for much of the FIR emission.

Wiklind & Henkel (1995) show that in elliptical galaxies the gas is unrelated to the stellar populations, and favor an external origin of the molecular gas. It is widely believed that the AGN are powered by accretion of ISM onto super massive black holes (SMBHs) (Antonucci 1993). According to de Ruiter et al. (2002), the presence of ISM in the circumnuclear regions of AGN is indeed inevitable and the large-scale dust/gas systems should be related to nuclear activity.

More recent studies by Hardcastle et al. (2007) suggest that it is possible that all the apparently different accretion modes may be a result of a different source for the accreting gas. This hypothesis came from Allen et al. (2006), who showed that some low luminosity radio galaxies in the center of clusters could be powered by Bondi accretion (a spherical accretion) from the hot, X-ray emitting medium and the support argues about the nature of the accretion mode in low-power radio sources made by Best et al. (2006).

For low-luminosity AGN, the stellar component might be sufficient to fuel the active nucleus, but for powerful radio galaxies large scale dynamical processes are required to transfer angular momentum of the interstellar gas across the disk radius (Shlosman et al. 1990; Combes 2002).

Fueling is also dependent on the morphological type of the galaxy, since the radial gas flows are driven by non-axisymmetric instabilities, and the stability of the disk is essentially dependent on the bulge-to-disk ratio (Mihos & Hernquist 1996, 1994). In early type galaxies, for example, once the accreted gas has settled in a symmetric disk, the large-mass black holes (BH) are starving, unless perturbed by an external tide (e.g. Combes 2002).

1.3 Interstellar Medium in Radio Galaxies

The Interstellar Medium (ISM) is the material in the galaxies between stars. This material is mainly composed by gas and dust.

The ISM is playing a key role in the formation and evolution of the AGN in radio galaxies: it is the fuel of the AGN and its dynamics is crucial to model the center of the elliptical galaxy hosting the AGN. Still various competing

physical processes are thought to be responsible for the refilling of the AGN in the radio galaxies: minor/major mergers, cool gas accretion or stellar mass loss. Moreover, it is not yet clear how to feed the very center with gas or, in other words, how to remove angular momentum and kinetic energy to the gas to make it fall towards the center. The origin of the neutral and molecular gas in the host galaxies of the radio galaxies can help to answer these questions. This can be done through the study of large-scale structures of HI around radio galaxies, since it can be used to derive key information about the age, size and type of the merger and about the ISM properties (neutral+molecular gas) involved in the feeding of the eventual star formation and AGN phase. See chapter 7.3 for more information.

To get a closer view of the ISM see Figure 1.2, which is an example of an elliptical radio galaxy M87; in fact, it is one of the galaxies in this sample (3CR 274). This image is a composite of visible (or optical), radio, and X-ray data. From this image, we see that the optical data is shown in yellow, the radio is shown in red and the X-Ray data is shown in blue. M87 lies at a distance of 54 million light-years and is the largest galaxy in the Virgo cluster of galaxies. Bright jets moving at close to the speed of light are seen at all wavelengths coming from the massive black hole at the center of the galaxy. It has also been identified with the strong radio source, Virgo A, and is a powerful source of X-rays as it resides near the center of a hot, X-ray-emitting cloud that extends over much of the Virgo cluster. The extended radio emission consists of plumes of relativistic (extremely hot) gas from the jets rising into the X-ray-emitting cluster medium.

1.3.1 Molecular Gas

The most important ingredient in a galaxy that will give information about the capability of a galaxy to form stars, is the molecular gas mass, H_2 , but this molecular gas mass is very difficult to measure directly, therefore astronomers use CO to trace the H_2 .

The bulk of molecular hydrogen in a galaxy is cold, around 10-20K, and therefore invisible. The first rotational level, accessible only through a quadrupolar transition, is more than 500 K above the fundamental. The presence of H_2 is inferred essentially from the CO tracer. The carbon monoxide is the most abundant molecule after H_2 ; its dipole moment is small (0.1 Debye) and therefore CO is easily excited, the emission of CO(1-0) at 2.6mm (first level at 5.52K) is ubiquitous in the Galaxy (Combes 2000).

As explained by Combes (2000), it is well known now that the conversion ratio might vary considerably from diffuse to dense gas. The CO molecule is excited by H_2 collisions, and should be a good tracer; but its main rotational lines are most of the times optically thick. One can then think of observing its isotopic substitutes like ^{13}CO or $C^{18}O$, but these are poor tracers since they

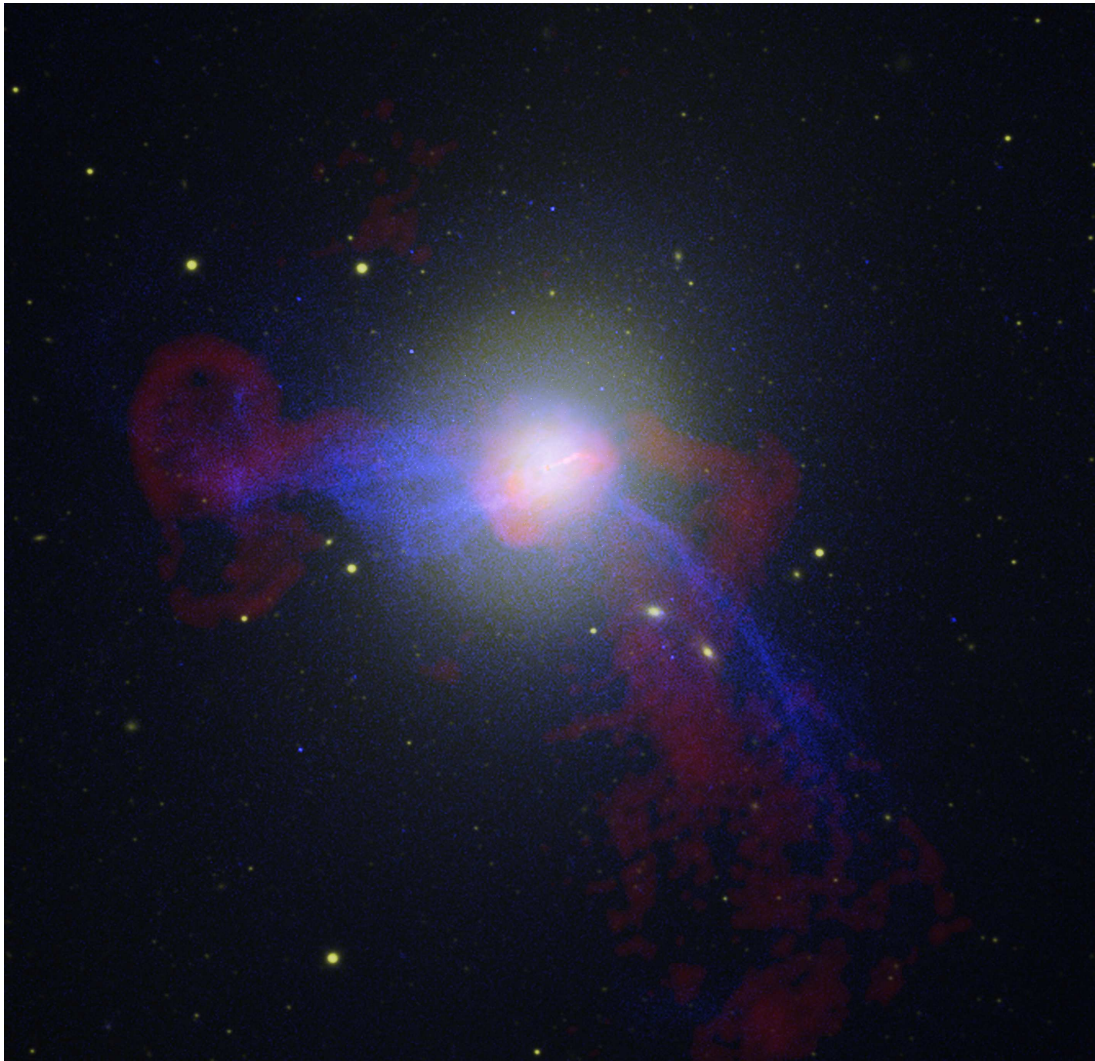


Figure 1.2: M87 Multi-Wavelength image, using VLA for radio wavelength, HST for optical and Chandra for X-ray. Where the optical data is shown in yellow, the radio is shown in red and the X-Ray data is shown in blue

are selectively photo-dissociated, and trace only the dense cores.

Different molecules that are studied in the gas phase give also important information about where is the energy of the galaxy coming from. For example, according to [Sternberg et al. \(1994, 1996\)](#); [Kohno et al. \(1999a, 2001\)](#); [Kohno \(2003, 2005\)](#) HCN-to-CO (J=1-0) intensity ratios appear to be significantly higher and the HCO⁺-to-HCN (J=1-0) intensity ratios significantly lower in AGN than in Star Burst (SB) galaxies.

According to [Combes \(2000\)](#), H₂ can also be observed directly when it is warm. Starbursts and mergers reveal strong 2.2 μm emission, like in NGC 6240 ([Depoy et al. 1986](#)). The source of excitation has long been debated (X-ray heating, UV fluorescence, shocks ...) and it was recently concluded that global shocks were responsible ([van der Werf et al. 1993](#); [Sugai et al. 1997](#)). Pure rotational lines have been observed with ISO. In Arp220, as much as 10% of the ISM could be in the warm phase, i.e. $3 \times 10^9 M_{\odot}$ ([Sturm et al. 1996](#)) while CO observations conclude to a total $M_{H_2} = 3.5 \times 10^{10} M_{\odot}$ ([Scoville et al. 1991](#)). In normal galaxies, the warm H₂ could be less abundant ([Valentijn et al. 1996](#)). At least, the warm CO component does not affect the H₂/CO ratio.

HCN and HCO⁺ molecules are the most abundant H₂ mass tracers after CO, whose much higher dipole moments ($\mu_{10} \sim 2.98; 3.92$ D for HCN, HCO⁺ J = 1-0 vs. $\mu_{10} = 0.11$ D for CO J = 1-0) makes their transitions excellent tracers of dense molecular gas in galaxies. This is due to critical densities of rotational transitions being $n_{crit} \propto \mu^2 \nu_{J+1J}^3$ (for optically thin lines at frequency ν_{J+1J}), allowing the HCO⁺ and HCN lines to trace ~100–500 times denser gas than corresponding (in rotational level) CO transitions ([Papadopoulos 2007](#)).

1.3.1.1 Carbon monoxide - ¹²CO

Carbon monoxide (CO) is a colorless, odorless and tasteless molecule that is highly toxic. Even so, humans naturally produce CO as part of a normal metabolism and it is a nutrient for a bacteria that produces methane. CO is also present in the atmosphere but in small quantities.

In space it is one of the most abundant molecules, together with the molecular hydrogen (H₂). Astronomers discovered CO in space in the year 1970 ([Wilson et al. 1970](#)) beginning a new era in the study of the ISM and SF, revealing to the astronomers the secrets of the mysterious cold universe.

It was found everywhere there was significant amount of excitation. The excitation of this transitions by collision requires sufficiently high densities leading to the idea that the CO clouds had to be composed primarily of hydrogen. It then became clear that the J=1-0 transition of CO was very effectively tracing the cold molecular component of the ISM. In modern astrophysics we use CO as the most effective tracer for molecular gas mass in galaxies. This is the main reason why most of the work of this thesis was concentrated on the CO molecule search in this sample. Details on the observations are in section

4.6.1.

1.3.1.2 Hydrogen cyanide - HCN

It is a colorless and extremely poisonous chemical compound that smells somewhat like almonds, although the smell is not detectable by everyone. It is also found in small quantities in plastic.

Even though CO traces most of the molecular gas mass in galaxies, it does not necessarily trace active star forming regions where the gas density is higher. These regions are better traced by HCN, CS and HCO^+ (see section 1.3.1.3). In space, HCN is a dense molecular gas tracer used to trace star formation. It is found in the center of starbursts, it is tightly correlated with the radio-continuum emission and the total L_{HCN} seems to be very well correlated with the L_{FIR} according to [Solomon et al. \(1992\)](#).

[Gao & Solomon \(2004b\)](#) found that the HCN-CO correlation is extremely tight and linear for normal spiral galaxies (5). Their ratio is tracer of star burst.

1.3.1.3 Formyl cation - HCO^+

This molecule is produced in the gas phase, and it is believed to exist in the gas phase even in the highest densities. The spread in the HCO^+ abundances gives an indication on the effect of local condition on the abundance. This molecule is not commonly found on Earth because it is chemically unstable even under laboratory conditions and it will quickly combine to form other, chemically stable species ([Wilson et al. 2009](#)).

According to [Riquelme \(2010\)](#), HCO^+ is a molecule known to vary considerably in abundance relative to neutral molecules with similar dipole moments and rotational constants, such as HCN, within a galaxy and from galaxy to galaxy ([Nguyen et al. 1992](#); [Seaquist & Frayer 2000](#); [Krips et al. 2008](#)). [Seaquist & Frayer \(2000\)](#) argue that in the environment of circumnuclear galactic or extragalactic gas, the abundance of HCO^+ decreases with increasing cosmic rays ionization rates. However, [Krips et al. \(2008\)](#) observed that the HCO^+ abundance tends to be higher in galaxies with nuclear starbursts than in galaxies with AGNs which would be unexpected if HCO^+ is destroyed by cosmic rays produced by supernova remnants.

1.3.2 Dust

Dust is an important ingredient of the ISM, associated with the molecular gas. In systems with ongoing star formation (SF), the light from both newly formed and older stars can be absorbed by dust, heated by the UV/Optical field coming from (young) stars and/or AGN, and later reprocessed into

the Far Infra-Red (FIR) whose emission, therefore, depends strongly on its temperature giving information about Star Formation (SF) in the galaxies. Between $3\mu\text{m}$ and $30\mu\text{m}$, according to [Genzel & Cesarsky \(2000\)](#), is where the transition from stellar emission to interstellar dust emission in galaxies occurs, these mid-IR wavelengths are covered by IRAS and SPITZER (the IRAC camera). In order to study the dust at different wavelengths we use the fluxes given by the IRAS satellite (see [3.4.1](#)) and by the SPITZER satellite (see [3.4.2](#)).

Since it is well known that early type galaxies contain dust emitting in IR (e.g., [Knapp et al. 1989, 1992](#)), the goal is to understand if the mid-IR emission originated mainly in the photosphere and shells of cool asymptotic giant branch stars or in the interstellar medium, or whether an AGN plays a role. According to [Madden et al. \(1999\)](#) $4.5/6.7\ \mu\text{m}$ and $6.7/15\ \mu\text{m}$ colors of about 60% of their sample galaxies are consistent with the notion of a largely stellar origin for the mid-IR emission, and the rest of their galaxies are dominated by Unidentified Bands (UIB) emission (17%) or an AGN (22%).

1.3.3 Classification of Radio Galaxies

1.3.3.1 Blazars

Many of the brighter blazars were first identified, not as powerful distant galaxies, but as irregular variable stars in our own galaxy. These blazars, like genuine irregular variable stars, changed in brightness on periods of days or years, but with no pattern.

Blazars are very compact quasi-stellar objects (QUASAR) associated with a presumed super massive black hole (SMBH) at the center of a giant elliptical galaxy and are among the most violent phenomena in the universe. Also defined by [Cla \(1997\)](#) as a highly variable active galaxy which, in general, displays no emission lines in its spectrum.

They are AGNs with their jet pointing at the Earth, which could be the reason for their rapid variability, see figure [1.3](#).

1.3.3.2 Quasars

A Quasar is defined by [Lightman & Brawer \(1990\)](#) as an extremely distant and luminous astronomical objects that are much smaller than a galaxy and much more luminous. Quasars may be the central regions of certain very energetic galaxies at an early stage of their evolution. It is believed that the power of a quasar derives from a massive black hole at its center.

Figure 1.3: Viewing angle - 1. at 90 degrees to the jet: Radio galaxy / Seyfert 2 Galaxy; 2, 3. at an angle to the jet: Quasar/Seyfert 1 Galaxy; 4. down the jet: Blazar¹.

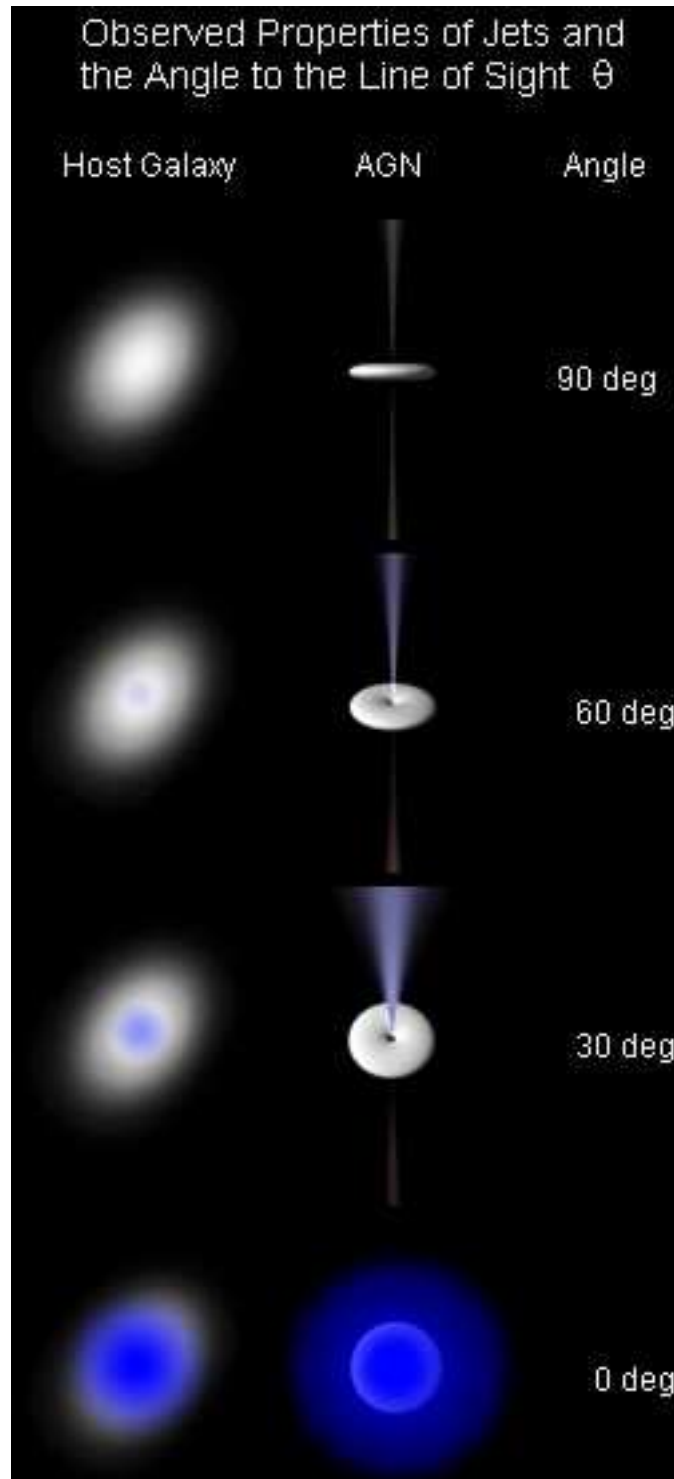
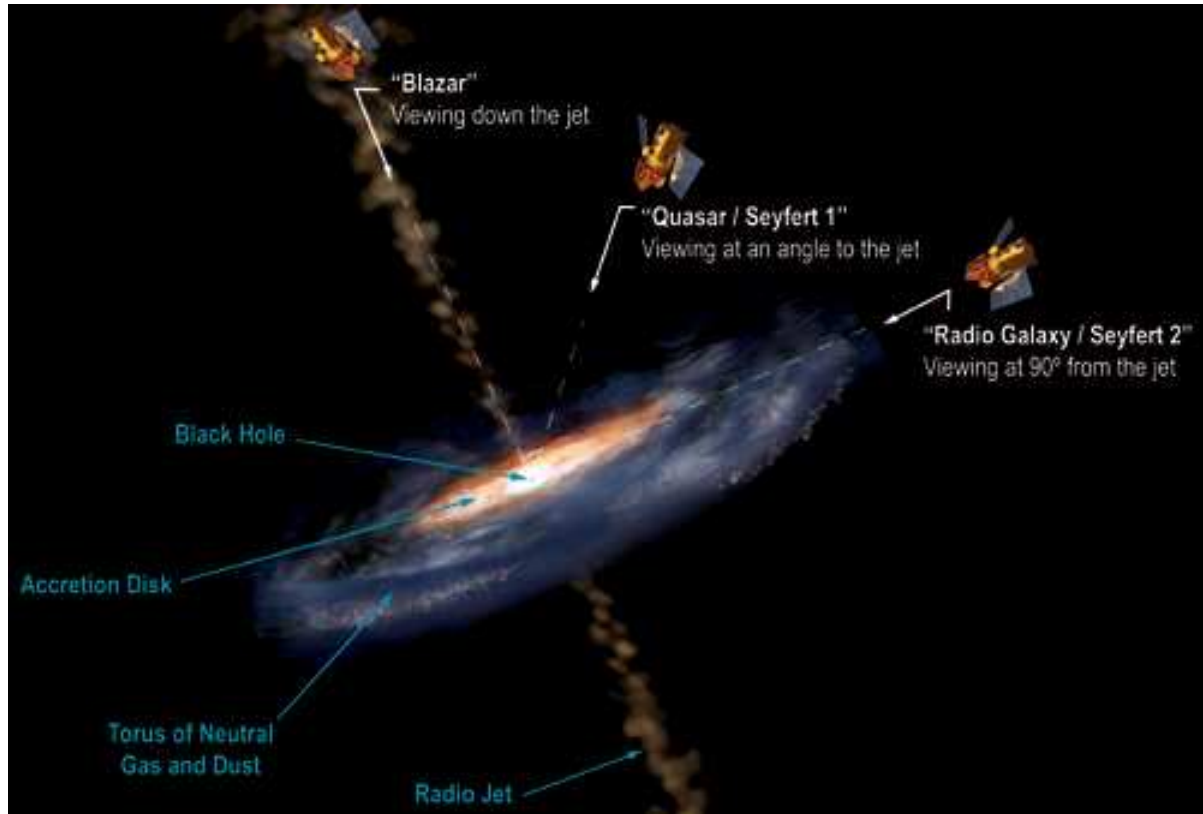


Figure 1.4: A general description of an AGN



1.3.3.3 Compact Symmetric Objects - CSOs

Compact symmetric objects are radio galaxies in which their radio jets are much smaller than normal radio galaxies (about 100 pc - 1Kpc, [García-Burillo et al. 2007](#)). There are two hypothesis for this behavior, one could be the age of the radio galaxy (also called the *youth scenario*, [Phillips & Mutel 1982](#)) and the other one could simply imply that they are smaller or less powerful radio galaxies (also called the *frustration scenario*, [van Breugel et al. 1984](#)).

1.3.3.4 Compact Peaked Spectrum - CPS

Compact Peaked Spectrum (CPS) are powerful and intrinsic small objects (<15 Kpc, corresponding to about 4") associated with distant galaxies and quasars ($z > 0.2$), characterized by a steep radio spectrum turning over at frequencies ranging from a few tens of MHz to a few GHz ([Dallacasa et al. 1997b](#)).

[Dallacasa et al. \(1997b\)](#) argues that various models have been proposed to explain the role played by CPS sources. The current models proposed to ex-

plain the existence of the CPS sources are usually referred to as *frustration* and *youth*. Where the *frustration* model (van Breugel et al. 1984; Baum et al. 1990) is that the radio emitting plasma is strictly confined to the region we observe by an external medium which is dense enough to prevent the expansion of the radio source. This dense environment might have been originated together with the host galaxy or could have been formed after a merger process, when a lot of material is dumped into the nuclear region. Contrary, GPS sources might be small because they are young (Phillips & Mutel 1982; Fanti et al. 1995; Wilkinson et al. 1994; Readhead et al. 1996): they are in an early stage in the life of the radio source, on its way to grow larger.

1.3.3.5 Fanaroff & Riley classification

Radio galaxies are divided mainly in two groups, the Fanaroff and Riley type I (FR-I) and type II (FR-II). As explained by Fanaroff & Riley (1974), the sources were classified using the ratio of the distance between the regions of highest brightness of the radio continuum on opposite sides of the central galaxy or quasar, to the total extent of the source measured from the lowest contour; those sources from which the ratio was less than 0.5 were placed in class I, and those for which the ratio was greater than 0.5 were placed in class II. There is a third classification called FR-C galaxies. These galaxies have a very compact radio continuum emission. Their radio morphologies suggest that they are compact versions of the classical FR-II's, although why they are so small is not yet established: It is hypothesized that these are either young FR-II's or FR-II's trapped in a dense environment (Fanti et al. 1990; O'Dea et al. 1991; Fanti & Fanti 1994).

The FR-class division very nearly correlates with radio power such that the highest-radio-power sources are predominantly FR-II type while those of lower-radio-power are usually FR-I type. According to the FR classification all quasars are FR-IIs, whereas BL Lac sources have been observed with both FR-I and FR-II morphologies (Dallacasa et al. 1997a).

1.4 TANGO

TANGO is not only a sensual dance between two people who move together with the music. Galaxies may dance with each other colliding and activating the gas, bringing lives, re-birth to their Interstellar Medium (ISM) in what we, astronomers, technically may call mergers. So we will define **TANGO** as the acronym for the **Thorough ANalysis of radio-Galaxies Observation**, for which I have been studying the interstellar medium of nearby radio galaxies that are part of this project and the main part of this PhD thesis.

TANGO is a project in which 2 samples of radio galaxies are studied, the

galaxies in the sample are selected based only on their radio continuum fluxes, making this a unique sample, since it is the only one with this criteria of selection. The sample will be described in chapter 2. On appendix A, there is a detailed description of each galaxy of the sample. TANGO covers a redshift of $z \leq 0.8$. For this thesis I will be focusing only on the $z \leq 0.1$, which I will be calling from now on the Low Z TANGO sample - **LzS**. As part of the continuation of this work, we will be studying the medium z TANGO sample - **MzS** ($0.1 \leq z \leq <0.8$).

The purpose of this project is to study the multi-wavelength (optical, radio, Infra Red (IR), x-Ray, ...) fluxes of the galaxies to compare their Spectral Energy Distribution (SED) and to answer the following questions:

- How can we explain the presence of gas in this type of galaxies?
- How does the gas form?
- Do the samples selected on the FIR emission, e.g. [Evans et al. \(2005\)](#), and radio continuum-selected samples (e.g., TANGO) behave in similar ways?
- Is there any environmental influence on the galaxies?
- Is there Star Formation (SF) in the galaxies?
- Is there any influence on the Active Galactic Nuclei (AGN), such as feedback, AGN-ISM?

I believe that engaging **TANGO** in a dance-like exploration, we will be able to understand galaxies and understand their behavior.

1.5 The goals of this work

When this work started, we had observations from the IRAM-30m telescope for many of the galaxies in TANGO. Other galaxies, also from this project, were observed later. The main goal was to collect all this data, including the observation of a galaxy, 3CR 31, from the PdBI.

When we decided to observe these galaxies, our intentions were:

- To observe CO(1-0) on a sample of radio galaxies selected on the basis of their radio continuum fluxes, with the purpose of knowing the amount of molecular gas mass these galaxies have.
- To study these galaxies and understand if they behave differently with a different selection criteria (IF flux density selected galaxies, ULIRGs, galaxies in interactions,...).

- To study the difference in FR-I and FR-II radio galaxies.
- To collect all the dust flux densities from IRAS and SPITZER with the purpose to calculate a dust mass and a dust temperature.
- To calculate the age of the radio galaxies.

Chapter 2

TANGO Sample

2.1 The Low and Medium redshift TANGO Sample

As mentioned in the introduction, the TANGO project sample is divided into two sub-samples. One sub-sample is formed by galaxies with redshifts between 0 and 0.1, as shown in figure 2.1. From now on this sample will be called the Low z Sample - **LzS**. The other sub-sample is formed by medium redshift galaxies, with redshifts between 0.3 and 1, as seen in Fig. 2.3, and which will be called from now on the Medium z Sample - **MzS**.

2.1.1 Low z Sample

In the LzS there are 52 galaxies with a unique criterion of selection, they all must be galaxies with strong radio continuum emission, thus in our LzS all the radio galaxies have a radio power at 1.4 GHz larger than $10^{22.5}$ W.Hz⁻¹ with a median power value of $10^{24.4}$ W.Hz⁻¹, as shown on Fig 2.2. This criterion makes the main difference with previous samples, chosen e.g. by their FIR flux density emission (e.g., Evans et al. 2005). All of the galaxies have been observed with the IRAM 30m telescope (see chapter 4.7) and for all of them we have calculated their molecular gas mass content (see chapter 5), analyzed their dust components (see chapter 6) and we combined all the flux densities emissions to build a SED (see chapter 8). We have studied their CO and FIR luminosities (see chapter 9.5) and compared all the results mentioned above with similar samples (see chapter 10.6). For some of the galaxies we observed HI as well (see chapter 7.3) using Effelsberg centimetric radio telescope.

These galaxies are mainly from the 3CR catalog (2.2.1), NGC (2.2.2) and B2 2.2.3 catalogs, there are as well 2 galaxies from the OQ (2.2.4) and UGC (2.2.5) catalog. See the list of the galaxies on table 2.1 and a detailed description of each galaxy, including their coordinates, can be found on the appendix A. We need to understand the redshift of the galaxies in terms of distance as well,

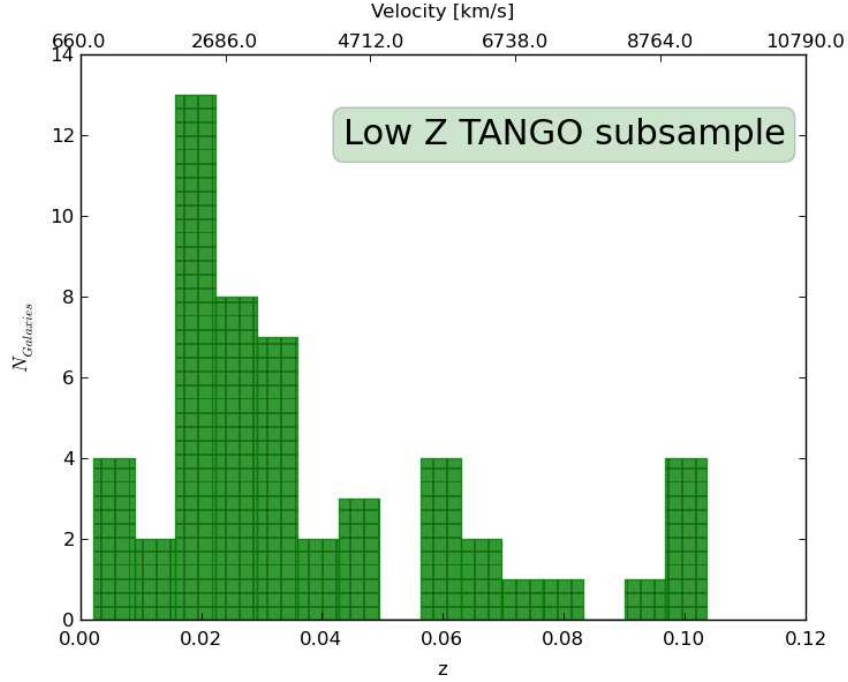


Figure 2.1: Low z TANGO galaxies

which is important at the time of calculating, for example, the molecular gas mass (see equation 5.6). Figure 2.1 is a distribution of the galaxies in the LzS of the TANGO project in terms of redshift (low margins) and in terms of velocity as well (top margin). The relation between z and V_{rad} is :

$$V_{rad} = c * z \quad (2.1)$$

where z is the redshift and c is the speed of light (3×10^5 km/s). Finally:

$$D = \frac{V_{rad}}{H} \quad (2.2)$$

where H is the Hubble constant, from the Hubble law that tells us the distance of a galaxy depending on the velocity with respect to us. The Hubble constant we used for this research is $70 \text{ Mpc}^{-1} \text{ km/s}$. The new value calculated by HST in 2009¹ was $74.2 \pm 3.6 \text{ Mpc}^{-1} \text{ km/s}$, very well in agreement with what we were using.

¹<http://hubblesite.org/newscenter/archive/releases/2009/08/full/>

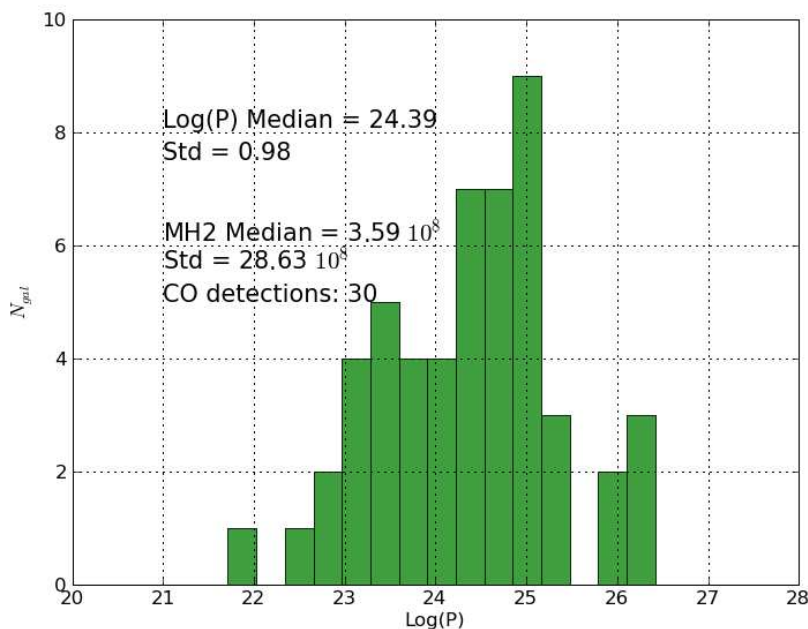


Figure 2.2: Histogram of the radio power at 1.4 GHz for the LzS.

2.1.2 Medium z Sample

Although our research, so far, has concentrated on the LzS, we do have a selection of galaxies we called Medium z Sample (MzS), selected under the same selection criteria as the LzS. We will use the MzS to measure the evolution on the molecular gas content through CO observations. This sub-sample is important since it covers an important range of radio galaxy evolution, with z between 0.3 and 1, after the episodes of intense merging ($z=1-2$). The comparison of the molecular gas content at medium redshifts with their other properties (X-ray, optical, radio continuum, environments, etc) and with the properties of the LzS will allow a better understanding of the origin and evolution of the molecular gas in the elliptical galaxies hosting these radio-AGN, which is a key problem for the evolution of elliptical galaxies.

Figure 2.3 shows the MzS galaxies distribution with respect to redshift (bottom margin) and velocity (top margin).

For the MzS, the galaxies selected are, as mentioned before, strong radio sources (see on table 2.2) all visible with the Atacama Large Millimeter Array (ALMA). Up to now, we have concentrated our studies on the LzS, but we will be working with this MzS, since it is part of a separate work in progress that we plan to complete after the PhD thesis.

Table 2.1: List of galaxies for LzS depending on their catalog

3CR	NGC	B2	OQ	UGC
3CR 31	NGC 315	B2 0034+25	OQ 208	UGC 7115
3CR 40	NGC 326	B2 0116+31		
3CR 66B	NGC 541	B2 0648+27		
3CR 83.1	NGC 708	B2 0836+29B		
3CR 88	NGC 2484	B2 0915+32B		
3CR 98	NGC 2892	B2 0924+30		
3CR 129	NGC 3801	B2 1101+38		
3CR 236	NGC 4278	B2 1347+28		
3CR 264	NGC 5127	B2 1357+28		
3CR 270	NGC 5141	B2 1447+27		
3CR 272.1	NGC 5490	B2 1512+30		
3CR 274	NGC 6251	B2 1525+29		
3CR 296	NGC 7052	B2 1553+24		
3CR 305				
3CR 321				
3CR 327				
3CR 353				
3CR 386				
3CR 402				
3CR 403				
3CR 433				
3CR 442				
3CR 449				
3CR 465				

2.2 Catalog Presentation

The low redshift sample of TANGO is composed of 52 nearby elliptical radio galaxies, where most of them are from the Third Cambridge Catalog of Radio Sources (3CR), NGC, Bologna Catalog of Radio Sources (B2) and finally there are two more galaxies, one from the Uppsala Catalog (UGC) and Ohio State University Radio Survey Catalog (OQ).

When the galaxies are in more than one catalog, as it is the case with many of them, the decision was to use the 3CR catalog as the main catalog. Then, second in order is the NGC, and followed by the B2. The galaxies in the UGC or OQ catalog are in none of the other catalogs.

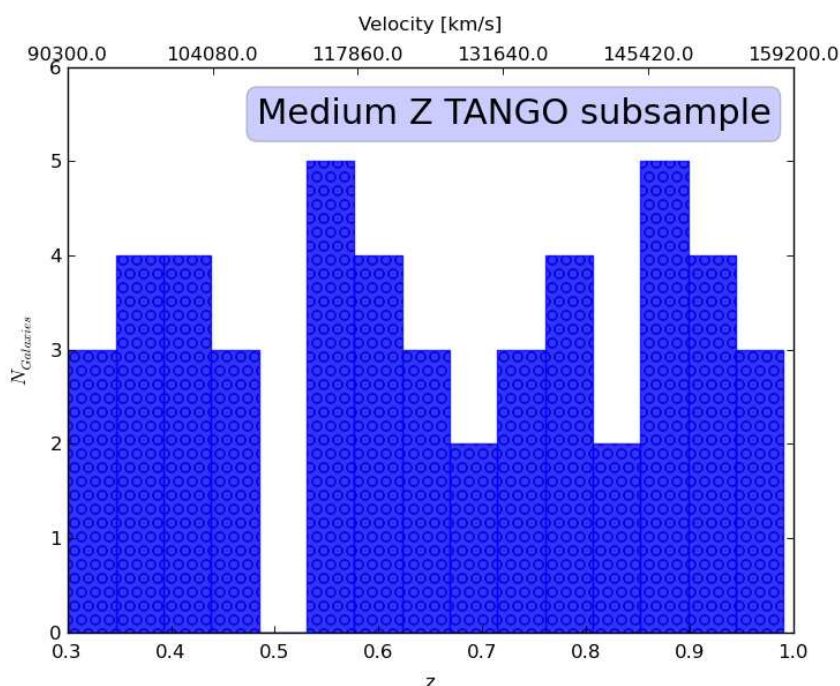


Figure 2.3: Medium z TANGO galaxies

2.2.1 3CR Catalog

The 3C Catalog is the result of observations with the Cambridge four-element interferometer at a frequency of 159 MHz, and contains 471 sources between declinations -22 and +71 degrees, with a flux density larger than 8 Jy.

The Revised version of the 3C (3CR) is based on new observations at a frequency of 178 MHz, and represents a survey of all sources norther than -05 degrees with a flux density brighter than 9 Jy, except in the areas near the ridge of galactic emission. The original numbering system has been preserved ²(Edge et al. 1959).

2.2.2 New General Catalog -NGC

The New General Catalog is a modern, revised, and expanded version of the original NGC Dreyer (1888). In addition to incorporating the many corrections to the NGC found over the years, each object was verified on Palomar Observatory Sky Survey (POSS) prints and on plates for southern objects specifically taken for this purpose (although about 90 southern objects could not be verified, Sulentic & Tifft 1973).

²<http://cdsarc.u-strasbg.fr/viz-bin/Cat?VIII/1A>

Table 2.2: Medium z TANGO Sample.

Z	Position (2000)		Name
	RA	Dec	
0.391	22 11 24	-13 28.2	PKS 2208-13
0.359	10 51 51	-00 51.3	PG 1049-006
0.311	02 24 12	+27 50.2	3CR 67
0.346	16 09 11	+17 56.3	4C 18.47
0.365	08 49 40	+09 49.3	PKS 0846+10
0.301	09 14 02	+05 07.8	4C 5.38
0.357	03 43 30	+04 57.8	3CR 93
0.428	23 12 07.6	+18 45 41	3C 457
0.4580	08 27 25.40	+29 18 44.8	3C 200
0.4115	09 06 31.88	+16 46 13.0	3C 215
0.4350	12 24 54.62	+21 22 47.2	4C 21.35
0.4800	12 42 19.68	-04 46 19.7	3C 275
0.4610	5 10 57.03	+07 51 24.8	3C 313
0.4190	13 09 49.66	-00 12 36.6	4C 00.46
0.5350	10 41 39.01	+02 42 33.0	4C 03.18
0.5362	12 56 11.15	-05 47 20.1	3C 279
0.5550	16 20 21.40	+17 36 29.3	3C 334
0.5500	15 46 09.50	+00 26 24.6	PKS 1543+005
0.5570	12 43 57.63	+16 22 52.7	3C 275.1
0.5800	09 42 15.35	+13 45 49.6	3C 225
0.5920	09 43 12.74	+02 43 27.5	4C 02.29
0.6050	15 40 49.51	+14 47 46.7	4C 14.60
0.6250	13 38 08.07	-06 27 11.2	QSO J1338-0627
0.6162	03 51 28.5	-14 29 09	3C 95
0.6362	16 12 19.02	+22 22 15.6	3C 331
0.6500	13 52 56.36	+11 07 07.7	4C 11.46
0.6800	12 28 11.77	+20 23 19.1	4C 20.29
0.6840	08 40 47.70	+13 12 23.9	3C 207
0.7200	13 57 04.37	+19 19 08.1	4C 19.44
0.7290	11 59 31.80	+29 14 44.3	4C 29.45
0.7590	05 21 09.9	+16 38 22	3C 138
0.7660	12 53 32.70	+15 42 27.3	3C 277.2
0.7750	16 29 37.52	+23 20 13.4	3C 340
0.7920	15 12 25.35	+01 21 08.7	4C 01.42
0.770	07 13 02.4	+11 46 15	3C 175
0.8178	09 44 16.40	+09 46 19.2	3C 226
0.8190	13 57 01.51	+01 04 39.7	4C 01.39
0.8710	14 24 56.93	+20 00 22.7	4C 20.33
0.8800	10 08 00.04	+07 30 16.2	3C 237
0.8710	08 13 36.0	+48 13 03	3C 196
0.8880	10 58 29.62	+01 33 58.2	4C 01.28
0.8920	13 19 38.73	-00 49 40.9	4C -00.50
0.9140	04 23 15.8	-01d20m33s	PKS 0420-01
0.9270	16 24 39.42	+23 45 17.5	3C 336
0.9380	14 55 54.9	-11 08 43	PKS 1453-10
0.9420	20 47 10.3	-02 36 22	3C 422
0.9510	08 23 24.72	+22 23 03.7	4C 22.21
0.9651	03 52 30.5	-07 11 02	3C94
0.9900	21 48 05.4586	+06 57 38.604	4C +06.69

2.2.3 Second Bologna Survey - B2

This catalog lists 9929 radio sources observed at 408 MHz with the Bologna Northern Cross telescope (Colla et al. 1970, 1972, 1973; Fanti et al. 1974).

2.2.4 Ohio State University Radio Survey Catalog - OQ

OQ is a survey at 1415 MHz continuum made by the Ohio State University (OSU) 110×21-cm radio telescope. The survey covers 312 deg² between the declination of 1° N and 11° S and includes four maps and list of 239 sources at or above 0.25 Jy (Scheer & Kraus 1967; Dixon & Kraus 1968; Fitch et al. 1969; Ehman et al. 1970; Kraus & Andrew 1971; Brundage et al. 1971; Rinsland et al. 1974, 1975).

2.2.5 Uppsala General Catalog of Galaxies - UGC

The Uppsala General Catalog of Galaxies (UGC) is an essentially complete catalog of galaxies to a limiting diameter of 1.0' and/or to a limiting apparent magnitude of 14.5 on the blue prints of the Palomar Observatory Sky Survey (POSS). Coverage is limited to the sky north of declination -02.5 degrees. Galaxies smaller than 1.0' in diameter but brighter than 14.5 mag may be included from the Catalog of Galaxies and of Clusters of Galaxies (CGCG, Zwicky et al. 1961, 1963, 1965); all such galaxies in the CGCG are included in the UGC. The galaxies are ordered by 1950 right ascension (Nilson 1973).

2.3 Optical Properties

All the galaxies in the sample have an optical image, in some cases a clear dust lane is noticeable, blocking the light from the galaxy, e.g., 3CR 31, 3CR 449. The case of 3CR 31 is very interesting because in this galaxy we see a dust disk around the center of the galaxy (see figure A.1); and the galaxy 3CR 449 shows a clear dust lane (see figure A.72). This galaxy will be discussed in more detail in section 11.

Martel et al. (1999) present a study of many of the galaxies in this sample observed with Hubble Space Telescope (HST) and, as was well stated by Capetti et al. (2007), these images proved to be a very powerful tool for a better understanding of the properties of FR-I AGNs as it allowed us to isolate, for the first time, their genuine optical nuclear emission from that of the host galaxies. Chiaberge et al. (1999) studied the R band of the HST images of a sample of 33 FR-I galaxies belonging to the 3CR catalog and showed that unresolved optical nuclear sources are detected in the great majority of these galaxies; and their optical and radio nuclear luminosities showed a clear correlation suggestive of a common non-thermal synchrotron origin, most likely from the base of their relativistic jet (For a very detailed study of these

galaxies, see appendix [A](#) where we show the optical images of most of the galaxies).

Chapter 3

Instrumentation

3.1 Introduction

This chapter describes the instruments from which we obtained data used for this work. The most important instrument used was the IRAM-30m telescope (see section 3.2). All the galaxies in this sample have been observed with the IRAM-30m telescope. For one of the galaxies in the sample, 3CR 31, we have obtained data observed with the IRAM-PdBI, which we reduced. The other instrument that we have used for observations was Effelsberg. Finally, for this work we have gotten data from the IRAS and Spitzer archives. There were other instruments from which we also took data, but those instruments are not going to be detailed here. They were mostly used to complete the SED of the galaxies, mainly at low frequencies.

3.2 mm/submm Instrumentation: Institute of Milimetric Radio Astronomy - IRAM.

The Institute of Milimetric Radio Astronomy (IRAM) is an international research institute for radio astronomy. Its overall objective is to explore the universe and to study its origins and evolution.

IRAM was founded in 1979 by the French CNRS (Centre National de la Recherche Scientifique), the German MPG (Max-Planck-Gesellschaft) and the Spanish IGN (Instituto Geográfico Nacional) - initially an associate member, becoming a full member in 1990.

IRAM's headquarters are located in Grenoble. With a staff of more than 120 scientists, engineers, technicians and administrative personnel, IRAM maintains and develops two observatories: the 30-meter telescope located on Pico Veleta near Granada in Spain, and the Plateau de Bure interferometer (an array of six 15-meter antennas) in the French Alps. Both instruments are prime facilities for radio astronomy and the most powerful observatories today operating at millimeter wavelengths.

These radio telescopes play a crucial role in modern astronomy, as they enable the study of cold matter through measuring the emission of molecular gas and dust – key elements in the formation of stars and galaxies and thus for the evolution of the universe. This wavelength range is essential to astronomy, since dust and gas-enshrouded cosmic objects remain optically invisible. Using radio techniques, astronomers can push the frontiers, penetrate the most distant galaxies, analyze Black Holes (BHs) at the edge of the observable universe and trace the cosmological radiation up to its source, the Big Bang. With their unmatched sensitivity, IRAM telescopes are able to detect these radio emissions from within our solar system to the farthest reaches of the universe.

3.2.1 IRAM - 30 meter Telescope

The IRAM-30m telescope¹ is located in Sierra Nevada because of the excellent weather conditions there are for this millimetric and submillimetric observations. One of the biggest issues for millimetric and sub-millimetric wavelength is humidity. Loma de Dilar is one of the driest places at an altitude of 2850 m over sea level, therefore escaping from the atmosphere as much as possible. It was built in only four years (1980 to 1984) and it is one of today's largest and most sensitive radio telescopes for tracing millimeter waves.

The telescope is a classic single dish parabolic antenna, which allows the exploration of extended cosmic objects such as nearby galaxies and interstellar clouds. Due to its large surface, the 30-meter telescope is unrivaled in its sensitivity and is well adapted to detect weak sources. The surface of the parabola is adjusted to a precision of 55 micrometers, corresponding to the width of a human hair.

Today, the 30-meter telescope is one of the most sought-after radio telescopes in the world. Each year, more than 250 astronomers come to Pico Veleta to pursue their scientific projects. In fact, the annual number of submitted proposals is so high that only one third of them can be scheduled. The observatory operates 24 hours a day every day of the year and includes a control room, from which the telescope is operated, along with living quarters for scientists and IRAM staff.

At the forefront of radio astronomy, the 30-meter telescope in the Sierra Nevada also allows astronomers to access parts of the southern skies and therefore to observe the center of our galaxy.

3.2.2 Techniques and Instrumentation

The main part of this PhD Thesis is the analysis of the CO data taken using the 30 meter telescope in order to analyze the molecular gas properties of

¹<http://www.iram-institute.org/EN/30-meter-telescope.php>

Elliptical Radio Galaxies in the TANGO sample.

3.2.2.1 Receivers

The signals that come from space are weak due to great cosmic distance. The main function of the receivers are to amplify the signals and for such purposes it converts the signals to a lower frequency which is then combined inside the mixer-block with a locally produced signal at a frequency similar to that of the original signal. The active element of the mixer, the super conducting junction, sends out the difference between the two incoming signals, the intermediate frequency (IF), which is low enough to be amplified.

The observations at the IRAM-30m telescope were performed using a combination of four of the eight single mixer receivers, that towards the end of this work was changed to a new Eight Mixer Receiver (EMIR). Since four of the single mixer receivers can be used simultaneously we used A100, A230, B100 and B230 to collect the data. This combination of receivers corresponds to 3mm (for the A100 and B100) and 1mm (for the A230 and B230) wavelength; more precisely, 115.27 GHz and 230.54 GHz respectively, redshifted to the velocity of the galaxies.

3.2.2.2 Backends

In the IRAM-30m telescope there are 2 main types of backends: filterbanks and autocorrelators:

A filterbank is an array of band-pass filters (a device that passes frequencies within a certain range and rejects frequencies outside that range) that separates the input signal into multiple components, each one carrying a single frequency sub-band of the original signal. In IRAM-30m telescope there are 2 filterbanks backends, one with a resolution of 1 MHz and the other with a resolution of 4 MHz. The 1 MHz filterbank has a maximum of 4 parts; series, parallel, or mixed mode are possible. The filterbank can be shifted in multiples of 32 MHz from the center frequency of the connected receiver. The 4 MHz filterbank has a maximum of 9 parts.

The autocorrelators available with the IRAM-30m telescope are WILMA (Wideband Line Multiple Autocorrelator) and VESPA (Versatile SPectrometer Array).

Finally there are the Continuum backends, used to measure the continuum for pointing, focus and calibration and with a 1 GHz width for the old receivers, and 8 GHz width for the new receivers.

There is also a backend for the bolometer, ABBA1 and ABBA2, and a backend for polarimetry, XPOL.

Mainly the backend used in my work was the 1MHz filterbanks with 1GHz

bandwidth and configured into two units of $512 \times 1\text{MHz}$ channels and two units of $512 \times 4\text{MHz}$, one for each receiver.

3.2.3 IRAM -Plateau de Bure

The IRAM Interferometer in the Plateau de Bure², is the most advanced facility existing today for millimeter radio astronomy.

Located in the Hautes-Alpes on the wide and isolated Plateau de Bure at an elevation of 2550 meters, the interferometer consists of six antennas, each 15 meters in diameter. Each antenna is equipped with state-of-the-art high-sensitivity receivers. Two rails, extending on a north-south and east-west axis, enable the antennas to be moved up to a maximum separation of 760 meters.

During observations, the six antennas function as a single telescope, a technique called interferometry. With the antennas pointing towards the same cosmic source, the signals received by each of them are subsequently combined. The angular resolution achieved during observation is that of a single telescope, whose diameter corresponds to the maximum distance between the individual antennas. In the case of the IRAM interferometer, this is equivalent (for the longest baselines) to a telescope with a diameter of 760 meters, which can distinguish two one-cent coins placed next to each other at a distance of 5000 meters. Due to the complexity of such an advanced antenna array system, only IRAM operators perform the observations.

To obtain a complete image of a cosmic object, interferometry uses the earth's rotation, which slowly turns the antennas with respect to the source, thus enabling step by step to scan the source's structure. Astronomers are able, after several hours of observation, to reconstruct a high angular resolution image of a cosmic object and study its detailed morphology.

3.3 cm Instrumentation: Effelsberg

For this work observations at the Effelsberg telescope in Bonn, Germany were done. Effelsberg is a 100m radio telescope that observes from 0.8 to 96 GHz in frequency and is located at a longitude of $6^{\circ}53'0.3''$ East and a Latitude of $50^{\circ}31'30''$ North at an altitude of 319m.

Effelsberg antenna has a primary mirror 100m in diameter and a 6.5m secondary mirror. The receivers are mounted at the primary focus and secondary focus on the telescope.

²<http://www.iram-institute.org/EN/plateau-de-bure.php>

Center Wavelength	# Working Detectors	FOV (arcmin)	Bandpass (μm)	Detector Material	Average 10-sigma Sensitivity (Jy)
12	16	$.75 \times 4.5$	8.5 - 15	Si:As	0.7
25	13	$.75 \times 4.6$	19 - 30	Si:Sb	0.65
60	15	1.5×4.7	40 - 80	Ge:Ga	0.85
100	13	3.0×5.0	83 - 120	Ge:Ga	3.0

Table 3.1: Summary of the Instrumentation for IRAS.

3.4 IR Instrumentation: IRAS and Spitzer

3.4.1 IRAS

The cryogenic Infra-Red Astronomical Satellite³ project was born with the main propose of making an unbiased sample of objects centered at 12, 25, 60 and 100 μm . The project was initiated in 1975 as a joint program of the United States, the Netherlands, and the United Kingdom. Launched in January 1983, IRAS ceased operations in November 1983 after having successfully surveyed more than 96% of the sky.

Table 3.1 shows the central wavelengths in μm , how many detectors are working for each wavelength, the Field of View (FOV) in arcminutes, the bandpass in μm , the material used for each detector and the average 10-sigma sensitivity in Jy. For the survey array, the Field of View (FOV) is determined by the rather large detector mask size and is roughly the native "resolution" of the data in that band. The resolution of the IRAS image data is not governed by the resolution of the telescope, which was diffraction limited long wards of 12 μm , but by the size of the detectors. IRAS satellite observes at very useful wavelength range since it allows calculates of dust and mass temperatures as long as it is assumed that the heated dust is mainly radiating by the FIR traced by IRAS fluxes at 60 μm and 100 μm .

3.4.2 SPITZER

The Spitzer Space Telescope is one of NASA's instrument designated for IR observations. The Observatory carries an 85-centimeter cryogenic telescope and three cryogenically cooled science instruments capable of performing imaging and spectroscopy in the 3.6 to 160 μm range. Spitzer was launched on a Delta 7920H from Cape Canaveral into an Earth-trailing heliocentric orbit in August 2003. While the Spitzer cryogenic lifetime requirement is 2.5 years of normal operations, the actual cryogenic lifetime was 5 years, 6 months and 19 days. See <http://ssc.spitzer.caltech.edu/geninfo/> for more details on Spitzer itself. To our work, the most important aspect of SPITZER are the

³<http://irsa.ipac.caltech.edu/IRASdocs/exp.sup/ch1/A.html>

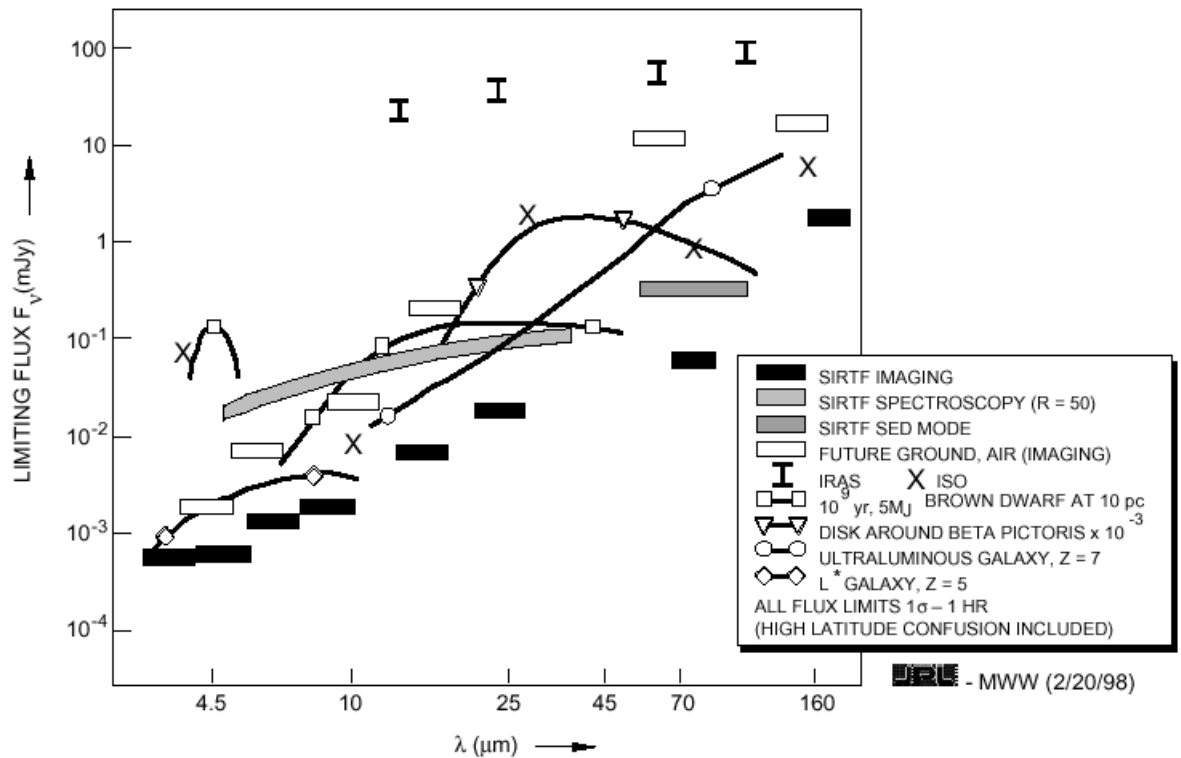


Figure 3.1: This image was taken from <http://ssc.spitzer.caltech.edu/obs/overview.html>. It represents the different parts of the SED in which each part of Spitzer observes.

Multi-band Imaging Photometer for Spitzer (MIPS) and the Infrared Array Camera (IRAC). For an Spitzer Instrumentation Summary, see tables 3.2 and 3.4.

3.4.3 IRAC

IRAC is composed of four channels that provide simultaneous 5.2 arcmin \times 5.2 arcmin images at 3.6, 4.5, 5.8, and 8.0 microns. Two adjacent fields of view are imaged in pairs (3.6 and 5.8 microns; 4.5 and 8.0 microns). All four detector arrays are 256 \times 256 pixels in size, with a pixel size of 1.2 arcsec \times 1.2 arcsec. The two short wavelength channels use InSb detector arrays and the two longer wavelength channels use Si:As detectors. See table 3.2 for a general summary about IRAC and Table 3.3 which shows the Aperture Correction for each frequency depending on the annulus selected when reducing the data.

The IRAC instrument was designed to address the four major scientific objectives defining the Spitzer mission. These are (1) to study the early universe, (2) to search for and study brown dwarfs and superplanets, (3) to study ultraluminous galaxies and active galactic nuclei, and (4) to discover and study protoplanetary and planetary debris disks. The utility of IRAC is in no way limited to these objectives, which are only mentioned to explain the scientific drivers for the instrument design. IRAC is a powerful survey instrument because of its high sensitivity, large field of view, and simultaneous four-color imaging⁴.

Table 3.2: IRAC: InfraRed Array Camera

λ (microns)	Array Type	Resolving Power	Field of View	Pixel Size (arcsec)	Sensitivity [1] (microJy) (5 sigma in 500s, incl. confusion)
3.6	InSb	4.7	5.21' x 5.21'	1.2	1.6 (3.4) [2]
4.5	InSb	4.4	5.18' x 5.18'	1.2	3.1 (4.3)
5.8	Si:As (IBC)	4.0	5.21' x 5.21'	1.2	20.8 (21)
8.0	Si:As (IBC)	2.8	5.21' x 5.21'	1.2	26.9 (27)

3.4.4 MIPS

The Multiband Imaging Photometer for Spitzer provides long-wavelength capability for the mission in imaging bands at 24, 70, and 160 μm and measurements of spectral energy distributions between 52 and 100 μm at a spectral resolution of about 7%. By using true detector arrays in each band, it provides both critical sampling of the Spitzer point-spread function and

⁴<http://ssc.spitzer.caltech.edu/irac/descrip.html>

Table 3.3: IRAC Aperture Corrections

radius on source	background annulus	Aperture correction			
		3.6 μm	4.5 μm	5.8 μm	8.0 μm
infinite	N/A	0.944	0.937	0.772	0.737
10	10-20	1.000	1.000	1.000	1.000
5	10-20	1.049	1.050	1.058	1.068
5	5-10	1.061	1.064	1.067	1.089
3	10-20	1.112	1.113	1.125	1.218
3	3-7	1.124	1.127	1.143	1.234
2	10-20	1.205	1.221	1.363	1.571
2	2-6	1.213	1.234	1.379	1.584

relatively large imaging fields of view, allowing for substantial advances in sensitivity, angular resolution, and efficiency of areal coverage compared with previous space far-infrared capabilities. The 24 μm array has excellent photometric properties, and measurements with rms relative errors of about 1% can be obtained. The two longer-wavelength arrays use detectors with poor photometric stability, but a system of on board stimulators used for relative calibration, combined with a unique data pipeline, produce good photometry with rms relative errors of less than 10% (Rieke et al. 2004). See table 3.4 for a general summary about MIPS.

Table 3.4: MIPS: Multiband Imaging Photometer for Spitzer

λ (microns)	Array Type	Resolving Power	Field of View	Pixel Size (arcsec)	Sensitivity [1] (microJy) (5 sigma in 500s, incl. confusion)
24	Si:As (IBC)	5	5.4' x 5.4'	2.55	110 [5]
70	Ge:Ga	4	5.2' x 2.6' 2.7'x1.4'	9.98 5.20	7.2 mJy [6] 14.4 mJy
160	Ge:Ga (stressed)	5	0.53' x 5.33'	16x18	29 (40) mJy [8]

Chapter 4

Observations and Data Reduction

4.1 Introduction

Since this work is based on a survey of CO(1-0) and CO(2-1) transition lines, most of the galaxies were simultaneously observed at both frequencies, collecting the most important amount of data for the galaxies in TANGO. For 2 of these galaxies we collected also interferometric data, using IRAM-PdBI; these galaxies are 3CR 31.

Besides these wavelengths, we also observed in the centimetric range for astronomy, at about 1.4 GHz, using the Effelsberg 100 meter telescope, in Bonn, Germany.

Additionally we were also interested in studying the dust in the galaxies and with such intentions we collected data from the IR part of the spectrum, using data from satellites such as SPITZER (both cameras, irac and mips) and IRAS. Finally, in order to complement our Spectral Energy distribution (SED), we took advantage of databases such as the Nasa Extragalactic Database (NED)¹ and Astrophysical CATalogs support System (CATS)² where we collected data from many different catalogs. They will be explained in more details in chapter 8.

4.2 TANGO LzS observation

Most of the galaxies observations were first proposed by Jeremy Lim and Stephane Leon in 1999. Since then we have been observing and adding galaxies into this sample we now call TANGO. On Table 4.1 we can see the list of the galaxies, and the date when they were observed.

¹<http://nedwww.ipac.caltech.edu/>

²<http://w0.sao.ru/cats/>

For this work, at the moment, we have a total of 52 nearby galaxies (already described in chapter 2 and defined as LzS). All of the galaxies have been observed at the frequency of CO(1-0) and 43 of them have been simultaneously observed at the frequency of CO(2-1) as well. We have repeated observations for those galaxies where we did not have data for CO(2-1), but the reduction of this data is part of the work we plan to do in the TANGO project.

Even though these galaxies are from the near universe, a correction in terms of velocity or frequency is needed. I chose to correct for the frequencies of the galaxies, as shown in equation 4.1, where f is the redshifted frequency, f_0 is the rest frequency of the molecule that we observe - for CO(1-0) $f_0=115.271$ GHz and for CO(2-1) $f_0=230.537$ GHz - and z is the redshift of the galaxy.

$$f = \frac{f_0}{(1+z)} \quad (4.1)$$

Since we have such a large sample, and for each observing run we had many galaxies, we grouped the galaxies according to their redshifts to avoid tuning the telescope more than necessary, and instead, be more efficient with the telescope time.

With the AB combination of receivers used, 0.5 GHz was the limit of the frequency difference that we could have using the same telescope tuning. With EMIR, we had up to 8 GHz in the frequency width for the E0 band. Since we wanted to combine the data with the E1 band we then can use up to 4 GHz. When using EMIR during the last part of this work, I grouped as many galaxies as possible when their frequency at 1mm was less than 4 GHz apart using an average value between the extreme frequencies of each group.

The filter backends were configured into two units of 512 x 1 MHz channels and two units of 512 x 4 MHz, one for each receiver connected. During the observations, the pointing and focus were monitored by observing planets and standard continuum fluxes every hour with an accuracy of about 3 arc-seconds.

We detected about 58% of the galaxies where 38% were a clear detection, some of them only in CO(1-0), some only in CO(2-1), and some in both CO transitions. A total of 7 galaxies have been detected in both lines, these galaxies are 3CR 31, 3CR 264, NGC 326, NGC 4278, NGC 7052, B2 0116+31 and B2 0648+27. These 7 galaxies have been used to study the CO(2-1)-to-CO(1-0) line ratios that will be discussed in chapter 5 in more detail.

As mentioned in the introduction of this chapter, we have also observed one galaxy with the interferometer IRAM PdBI, the radio galaxy (3CR 31) observed is one of the galaxies studied in more detail in this work, as can be seen later in chapter 11.

Galaxy	Observation Dates
3C31	1999 Dec

	2000 Jan
3C40	1999 Dec
3C66B	2000 Jan
	2003 May
3C83.1	2000 Jan
3C88	1999 Dec
	2000 Jan
3C98	2000 Jan
3C129	2000 Jan
3C236	2004 Mar
3C264	2000 Jan
3C270	2000 Jan
	2002 Jun
3C272.1	2000 Jan
3C274	2000 Jan
3C296	2000 Jan
3C305	2004 Feb
	2004 Mar
3C321	2004 Mar
3C327	2004 Mar
3C353	2000 Jan
3C386	1999 Dec
3C402	1999 Dec
	2000 Jan
	2003 Dec
	2004 Feb
	2004 Mar
3C403	2003 Dec
	2004 Feb
3C433	2003 Dec
	2004 Mar
3C442	2000 Jan
3C449	1999 Dec
	2000 Jan
3C465	2000 Jan
NGC315	2002 Jun
	2006 Oct
	2007 Apr
NGC326	2006 Oct
NGC541	2002 Jun
NGC708	2006 Oct
NGC2484	2006 Dec
	2007 Jan
NGC2892	2003 May

NGC3801	2002 Jun
NGC4278	2007 Jan
	2007 Apr
NGC5127	2002 Jun
NGC5141	2002 Jun
	2006 Nov
	2007 Apr
NGC5490	2002 Jun
NGC6251	2004 Mar
NGC7052	2002 Jun
	2006 Jul
B2 0034 + 25	2006 Jul
	2006 Oct
B2 0116 + 31	2003 Dec
	2006 Jun
	2006 Oct
B2 0648 + 27	2004 Feb
	2004 Mar
	2006 Oct
B2 0836 + 29B	2004 Mar
B2 0915 + 32B	2007 Jan
	2007 Mar
B2 0924 + 30	2007 Apr
B2 1101 + 38	2000 Jan
B2 1347 + 28	2007 Jan
	2007 Apr
B2 1357 + 28	2006 Oct
B2 1447 + 27	2007 Jan
	2007 Apr
B2 1512 + 30	2007 Apr
B2 1525 + 29	2006 Oct
B2 1553 + 24	2006 Oct
UGC7115	2002 Jun
OQ208 s	2004 Mar

Table 4.1: Observation journal for the galaxies in the sample.

4.3 Calibration

Once the data have been observed, it goes automatically to a file called `spectraOdp.30m`, where the IMBFITS "raw" data (data that has not yet been calibrated) is stored, and then it is automatically calibrated by MIRA (Multichannel Imaging and Calibration Software for Receiver Arrays).

The calibration procedure, as explained by [Kramer \(1997\)](#), has to take into account backend and receiver gains and, possibly, drifts, atmospheric transmissions and variations, pointing and focus deviations, losses due to diffraction, spillover, scattering, blockage, etc., although the atmospheric attenuation, in particular, is the main source of spectral calibration uncertainty.

In order to relate backend counts to antenna temperatures, at least two sources of known temperatures and output counts are needed. In a first step of the calibration procedure, the counts on a hot load (the chopper) at approximately room temperature, and the counts on a cold load at approximately the temperature of liquid nitrogen, are measured and averaged over the channels of the specific backend used. For a perfectly linear detector, the output counts C of the copper and cold load signals are proportional to the input temperatures T :

$$\langle C_{chop} \rangle = \langle c_{off} \rangle + (T_{chop} + T_{rec}) * g \quad (4.2)$$

$$\langle C_{cold} \rangle = \langle c_{off} \rangle + (T_{cold} + T_{rec}) * g \quad (4.3)$$

where g is the varying gain factor to be calibrated out. The constant offset $\langle c_{off} \rangle$ possibly arise in some of the backends even when no frontend signal is fed in. The receiver noise temperature is then given by:

$$T_{rec} = \frac{T_{cold} \langle C_{chop} \rangle - T_{chop} \langle C_{cold} \rangle}{\langle C_{cold} \rangle - \langle C_{chop} \rangle} - \langle c_{off} \rangle \frac{T_{chop} - T_{cold}}{\langle C_{cold} \rangle - \langle C_{chop} \rangle} \quad (4.4)$$

$$T_{rec} = \frac{T_{chop} - Y T_{cold}}{Y - 1} \quad (4.5)$$

where $Y = \frac{\langle C_{chop} \rangle - \langle c_{off} \rangle}{\langle C_{cold} \rangle - \langle c_{off} \rangle}$.

This temperature is needed to evaluate the performance of the receiver, including parts of the optics and the backend but without having to consider atmospheric influences. Depending on the pacing of the loads within the signal path, the receiver temperature will vary and will include some optical losses. Receiver temperatures are overestimated when backends $\langle c_{off} \rangle$ are considerably and not taken into account.

During the calibration the counts on the internal cold load and the hot load are measured automatically.

Now, what astronomers like to measure, is the spectral flux density, from a source of specific intensity, I_ν ([Gordon et al. 1992](#)), to do so:

$$S_\nu \equiv \int_{Source} I_\nu d\Omega \quad (4.6)$$

In radio range when $h\nu \ll kT$, the Rayleigh-Jeans³ approximation is used for the specific intensity to obtain:

$$S_\nu = \frac{2k}{\lambda^2} \int_{Source} T(\theta, \phi, \nu) d\Omega \quad (4.7)$$

Where $T(\theta, \phi, \nu)$ is the equivalent temperature of a black-body that radiates I_ν at the frequency ν in the direction (θ, ϕ) . It parametrizes the specific intensity. Since we are working with extragalactic radio lines, what we report is a somewhat different quantity, F , to characterize the flux density received in the line,

$$F \equiv \int_{line} S_\nu d\nu \quad (4.8)$$

$$F = \frac{2k}{\bar{\lambda}^2} \int_{source} \int_{line} T(\theta, \phi, \nu) d\nu d\Omega \quad (4.9)$$

which is a quantity that is the integral of spectral flux density over the width of the line. The parameter $\bar{\lambda}$ is the observed wavelength at the center of the spectral line.

4.4 Data reduction with IRAM 30m Telescope

It was mentioned before that the first set of data that was observed were taken during 1999, and part of this data was already published by [Lim et al. \(2000\)](#). Some of the sources were observed many times during these 10 years, when a galaxy had more than one observation run, all these data were reduced together. We added all the spectra taken for each galaxy, for each line (CO(1-0) or CO(2-1)). The data reduction of the galaxies observed with IRAM was done using the GILDAS software packages, more precisely, CLASS. Although, other GILDAS software was used as well for preparing the observations, such as ASTRO, and the data reduction software, MIRA.

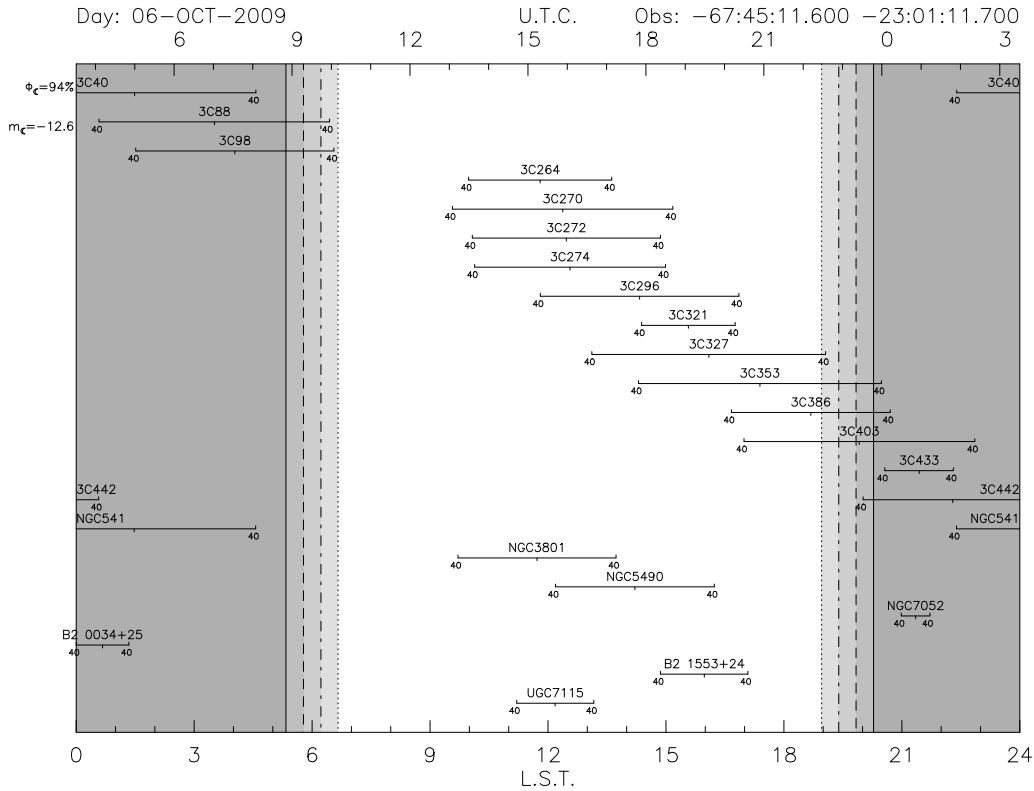
4.4.1 ASTRO

ASTRO⁴ (A Software To pRepare Observations) includes a series of tools to compute ephemeris, typically the position of sources as seen at a given time from a given location. Although they are slightly biased towards (sub)millimeter astronomy, specially in the terminology used for input and output parameters, their commands are generic enough to be used to plan

³Rayleigh-Jeans describe the spectral radiance of electromagnetic radiation at all wavelengths from a black body at a given temperature

⁴<http://iram.fr/IRAMFR/GILDAS/doc/html/astro-html/astro.html>

Figure 4.1: ASTRO plot of the galaxies from the TANGO sample visible using ALMA



observations with any instrument.

A typical example on how to generate a Sky map for the sources is:

Catalog source

Observatory veleta - In this case, there are other telescopes available or you could write the location of the telescope, and the altitude with respect to the sea level.

Time hh:mm (UT time) dd-mm-yy

horizon /source /planet /night_ marks

For example, the galaxies from the TANGO project visible from ALMA are shown in figure 4.1, where we can see the night marks and at what time the galaxies are above 40 degrees in elevation for October 6th, 2009.

4.4.2 CLASS

CLASS stands for Continuum and Line Analysis Single-dish Software and as its name indicates, it is the software used to analyze the continuum data, including pointing and focus as well, and the spectroscopic data observed with the single dish 30m telescope.

Once the data were available to be used by CLASS, this means, after the data were calibrated, we added all the spectra from each galaxy taking into account its respective frequency. Once the data were added together they were smoothed to a resolution between 20 and 50 km/s, depending on the source. Each spectra can be seen on Appendix A.

The next step is to remove a polynomial baseline from the spectra, in order to have the correct peak temperature. For the galaxies in this sample, the baseline was generally a polynomial of degree 0 or 1. The fitting algorithm that CLASS uses is called Chebyshev polynomials, which is a sequence of orthogonal polynomials related to de Moivre's formula:

$$(\cos x + i \sin x)^n = \cos nx + i \sin nx \quad (4.10)$$

where equation 4.10 is important because it connects the complex number with trigonometry. The Chebyshev polynomials are easily defined recursively, like Fibonacci sequence.

In order to remove the baseline, it is necessary to select a window, which in general is the same width as the width of the detection. In the cases where there were no detections, we chose a width of 300 km/s, to be the width of the window. The purpose of this window was to choose a region in which the polynomial will not be fitted and therefore, the baseline will not be affected by the emission inside that window.

Once the spectra comes out from CLASS, it comes in terms of velocity (km/s) and temperature (K - T_A^*). A more universal representation of the temperature is main beam temperature since it is normalized to all the telescopes. In order to convert T_A^* into main beam temperature (T_{MB}), we used the conversion factor given by [Rohlfs & Wilson \(2004\)](#),

$$T_{MB} = T_A^* \frac{F_{eff}}{B_{eff}} \quad (4.11)$$

resulting on a value of 1.27 for 3mm data and 1.75 for 1mm data, and where the B_{eff} is the percentage of all power received which enters the main beam and the F_{eff} which is a model function to the measured antenna temperature and the chopper load temperature ([Kramer 1997](#)).

The data in CLASS comes out in temperature [K] and for scientific purposes we convert the temperature in flux densities [Jy] by multiplying the temperature by a constant value that changes depending on the frequency observed. As [Kramer \(1997\)](#) describes it, and as mentioned in the previous section, the

flux density $S_{\nu, tot}$ is the power radiated per unit area and per unit frequency of a radio source at a given frequency, given by:

$$S_{\nu, tot} = \int_{\Omega_s} B_\nu(T_B) d\Omega = \frac{2k}{\lambda^2} \int_{\Omega_s} J_\nu(T_B) d\Omega \quad (4.12)$$

where Ω_s is the source solid angle and T_B is the Planck brightness temperature of the source. $J_\nu(T_B)$ is the Rayleigh-Jeans brightness temperature at the frequency ν : $J_\nu \equiv T_{RJ} = \frac{h\nu}{k} (\exp(\frac{h\nu}{kT_B}) - 1)^{-1}$, where λ is the wavelength of observations and k is the Boltzman constant⁵. Finally, to convert from temperature to flux, we can assume that for 3mm $S/T_A^* = 6.3$ and for 1mm $S/T_A^* = 8$

4.4.3 Interferometer: IRAM PdBI

We observed emission from CO(1-0) at 113.355013 GHz with the IRAM interferometer at Plateau de Bure in France. This interferometer has 6 antennas where each antenna has a diameter of 15m with dual band SIS heterodyne receivers. The observations were done in configuration B (on 2002). Projected baselines ranged between 60 and 331 m. The source, 3CR 31, was observed at the center, (RA:01h07m24.9s, DEC: +32d24m45s). The accuracy of the flux calibration is about 10% at this frequency. The calibration and data analysis were performed in standard ways, using different GREG⁶ software. For the calibration we used the Continuum and Line Interferometer Calibration (CLIC)⁷ software. And for the image and Deconvolution we used MAPPING⁸.

4.5 Continuum data

The continuous spectrum is defined as the spectrum in which the radiation is distributed over all frequencies, not just a few specific frequency ranges; and where a prime example is the black-body radiation emitted by a hot, dense body⁹.

For this sample, we obtained the continuum data simultaneously with the observations of our lines, at 3mm for CO(1-0) and at 1mm for CO(2-1).

From the 52 galaxies in TANGO, observed at 3mm, 90% were detected in the continuum; from the 49 galaxies observed at 1mm, 65% were detected in the continuum.

The continuum is generally expressed in terms of flux densities, but raw data that came from the 30m telescope is in terms of temperature, in K, rather than

⁵The Boltzman constant is $1.38 \times 10^{-23} \text{ m}^2 \text{ kg s}^{-2} \text{ K}^{-1}$

⁶<http://www.iram.fr/IRAMES/GILDAS>

⁷<http://www.iram.fr/IRAMFR/GILDAS/doc/pdf/clic.pdf>

⁸<http://www.iram.fr/IRAMFR/GILDAS/doc/pdf/map.pdf>

⁹<http://chandra.harvard.edu/resources/glossaryC.html>

the flux densities, that would be in terms of Jy. In order to convert temperatures to flux densities, we used the conversion factor for the point source sensitivity measurement (S/T_A^*) of 6.3 for 3mm and 8 for 1mm. See section 4.4.2 for details on the conversion.

4.5.1 SPITZER

As it has been already discussed on chapter 3, Spitzer is a satellite that covers many of the ranges for the IR emission. In addition to medium resolution 5-38 μm spectroscopy, the Spitzer cameras (IRAC and MIPS) provide 7 broad-band filters which can be used to cover the 3-170 μm range. This turns out to be very useful when calculating the dust temperatures of different components in the galaxies. Spitzer is explained in more detail in section 3.4.2, and the science that we did with the data from Spitzer is in section 10.4. This section concentrates on the data reduction from Spitzer.

4.5.1.1 Spitzer Data Reduction

The data from the Spitzer satellite are released to astronomy community a year after the observations were done. The archive tool to download the data is managed through a software called Leopard¹⁰.

From Leopard software we are most interested in the post-Basic Calibrated Data (BCD), which is the data that already combines all individual BCD frames from a single Astronomical Observation Request (AOR). With post-BCD, no further pipe-line reduction is needed, only checks on data quality and issues of saturation need to be examined. This is an averaged and registered single image suitable for photometric measurements, and with first order removal of seams between the component images and the outcome is in MJy/ster.

when the post-BCD data is downloaded, it comes with different fits:

1. `maic.fits` = the mosaic (MosAIC).
2. `munc.fits` = the errors (UNCertainties) on the fluxes in the mosaic.

¹⁰<http://ssc.spitzer.caltech.edu/documents/leopard/>

3. `mcov.fits` = the coverage (COverage), e.g., how many frames were taken over each part of the sky.
4. `maics.fits` = for IRAC only, mosaic of just the short exposures.
5. `muncs.fits` = for IRAC only, the errors (UNCertainties) on the fluxes in the mosaic of just the short exposures.
6. `mcovs.fits` = for IRAC only, the coverage of just the short; ought to be identical to the long coverage map.
7. `mfilt.fits` = for MIPS-70 only, the mosaic of the filtered data (trying to get rid of instrumental artifacts).
8. `mfunc.fits` = for MIPS-70 only, the errors (UNCertainties) on the fluxes in the filtered mosaic.
9. `mfcov.fits` = for MIPS-70 only, the coverage in the filtered mosaic; ought to be the same as the original (unfiltered) coverage map.

Once we have the fits in which we will work on, with IDL we changed the values that, in the fits, were as Not A Number (NaNs) to 0. We then opened an interactive display tool for astronomical images written in IDL called ATV¹¹, which allows interactive control of the image scaling, color table, color stretch, and zoom, with support for world coordinate systems. It also does point-and-click aperture photometry, simple spectral extractions, and can produce publication-quality postscript output images. We concentrated mainly on modifying the color in logarithmic scales and then did the aperture photometry from where we obtained the counts (equivalent to MJy/Str) from the galaxy that we then had to convert to fluxes(μ Jy). This conversion is done in the following way:

$$1[\mu Jy] = Counts[MJy/Str] \times \frac{1[Str]}{4.25 \times 10^{10}[arcsec^2]} \times (PixelSize)^2[acrsec^2] \times A.C. \times 10^9 \quad (4.13)$$

¹¹<http://www.physics.uci.edu/barth/atv/>

Where AC is the Aperture Correction which is different for every wavelength. For IRAC:

$$1MJy/sr = \frac{1 \times 10^{12} \mu Jy}{4.254517 \times 10^{10} arcsec^2} \times 1.2 arcsec \times 1.2 arcsec = 33.85 \mu Jy \quad (4.14)$$

For MIPS: The default pixel size for MIPS-24 mosaics is $2.45'' \times 2.45''$, so the conversion factor from MJy/sr to μJy is therefore:

$$1MJy/sr = \frac{1 \times 10^{12} \mu Jy}{4.254517 \times 10^{10} arcsec^2} \times 2.45 arcsec \times 2.45 arcsec = 141.09 \mu Jy \quad (4.15)$$

For MIPS-70 the mosaics is $4.0'' \times 4.0''$, so the conversion factor from MJy/sr to μJy is therefore:

$$1MJy/sr = \frac{1 \times 10^{12} \mu Jy}{4.254517 \times 10^{10} arcsec^2} \times 4.0 arcsec \times 4.0 arcsec = 376.067 \mu Jy \quad (4.16)$$

and for MIPS-160 the mosaics is $8.0'' \times 8.0''$, so the conversion factor from MJy/sr to μJy is therefore:

$$1MJy/sr = \frac{1 \times 10^{12} \mu Jy}{4.254517 \times 10^{10} arcsec^2} \times 8.0 arcsec \times 8.0 arcsec = 1504.27 \mu Jy \quad (4.17)$$

The galaxy errors for the flux densities coming from IRAC, are about 10%. The errors for the flux densities coming from MIPS, 24 μm is as well 10% whether MIPS for 70 μm and 160 μm are about 20% ([Engelbracht et al. 2007](#); [Gordon et al. 2007](#); [Stansberry et al. 2007](#)). The results of the observation, and the analysis of the flux densities from Spitzer will be shown in chapter 6.

4.6 Molecular lines observed

4.6.1 Carbon monoxide - ^{12}CO

Carbon monoxide (CO) is a colorless, odorless and tasteless molecule that is highly toxic. Even so, humans naturally produce CO as part of a normal metabolism and it is a nutrient for a bacteria that produces methane. CO is also present in the atmosphere but in small quantities.

CO is one of the most abundant molecules in space, together with the molecular hydrogen (H_2). Astronomers discovered CO in space in the year 1970 ([Wilson et al. 1970](#)) beginning a new era in the study of the ISM and SF revealing to the astronomers the secrets of the mysterious cold universe.

It was found everywhere there was significant amount of excitation. The excitation of these transitions by collision require sufficiently high densities leading to the idea that the CO clouds had to be composed primarily by hydrogen. It then became clear that the J=1-0 transition of CO was very

effectively tracing the cold molecular component of the ISM. In modern astrophysics we use CO as the most effective tracer for molecular gas mass in galaxies.

For this work we are also studying two transitions of CO, $J=1\rightarrow 0$ and $J=2\rightarrow 1$. This will be explained in chapter 5.

The rest frequencies of the CO(1-0) and CO(2-1) emission lines are:

- $J=1\rightarrow 0$ 115.27 GHz
- $J=2\rightarrow 1$ 230.54 GHz

4.6.2 Hydrogen cyanide - HCN

It is a colorless and extremely poisonous chemical compound that smells somewhat like almonds, although the smell is not detectable by everyone. It is also found in small quantities in plastic.

Even though CO traces most of the molecular gas mass in galaxies, it does not necessarily trace active star forming regions where the gas density is higher. These regions are better traced by HCN, CS and HCO^+ (see section 1.3.1.3). In space, HCN is a dense molecular gas tracer used to trace star formation. It is found in the center of starbursts, it is tightly correlated with the radio-continuum emission and the total L_{HCN} seems to be very well correlated with the L_{FIR} according to Solomon et al. (1992).

Gao & Solomon (2004b) find that the HCN-CO correlation is extremely tight and linear for normal spiral galaxies (5). Their ratio is a tracer of star burst.

For this work, I have observed this molecule in only a few radio galaxies, but the majority of the HCN observations were for Isolated Galaxies. A subsample of the AMIGA sample (see Verdes-Montenegro et al. 2005) (see section 12.4). The rest frequencies of the HCN are:

- $J=1\rightarrow 0$ 88.632 GHz
- $J=3\rightarrow 2$ 265.886 GHz

4.6.3 Formyl cation - HCO^+

According to Riquelme (2010), HCO^+ is a molecule known to vary considerably in abundance relative to neutral molecules with similar dipole moments and rotational constants, such as HCN, within a galaxy and from galaxy to galaxy (Nguyen et al. 1992; Seaquist & Frayer 2000; Krips et al. 2008). Seaquist & Frayer (2000) argue that in the environment of circumnuclear galactic or extragalactic gas, the abundance of HCO^+ decreases with increasing cosmic rays ionization rates. However, Krips et al. (2008) observed that the HCO^+ abundance tends to be higher in galaxies with nuclear starbursts than in galaxies with AGNs, which would be unexpected if HCO^+ is destroyed by

cosmic rays produced by supernova remnants.

- $J=1\rightarrow 0$ 89.189 GHz
- $J=3\rightarrow 2$ 267.558 GHz

4.7 Summary and Conclusions

- We have observed 52 Galaxies for CO(1-0).
- From the 52 galaxies observed in CO(1-0), 49 of them were simultaneously observed in CO(2-1).
- 58% of the galaxies were detected in CO(1-0) or CO(2-1), in 7 of them we detected CO(1-0) and CO(2-1).
- 38% of the galaxies in the sample were clearly detected.
- 90% (out of 52) were detected in the continuum at 3mm and 65% (out of 49) were detected in the continuum at 1mm.
- We have reduced a CO(1-0) map obtained with the IRAM interferometer.
- We have reduced data from Spitzer satellite.

Chapter 5

Molecular Gas

5.1 Computation of the molecular gas mass

We follow [Gordon et al. \(1992\)](#) to derive H_2 masses from the $^{12}CO(1-0)$ line observations. Our temperature unit is expressed in T_A^* antenna temperature scale, which is corrected for atmospheric attenuation and rear side-lobes. The radiation temperature T_R of the extragalactic source is then:

$$T_R = \frac{4}{\pi} \left(\frac{\lambda}{D}\right)^2 \frac{K}{\eta_A} \frac{T_A}{\Omega_S} \quad (5.1)$$

where λ is the observed wavelength (2.6 mm), D is the IRAM radio telescope diameter (30 m), K is the correction factor for the coupling of the sources with the beam, η_A is the aperture efficiency (0.55) at 115 GHz, T_A is an antenna temperature which is $F_{eff}T_A^*$ in the IRAM convention, explicitly $T_A = 0.92T_A^*$, and Ω_S is the source size.

Without taking into account cosmological correction, because of the low redshift and using the standard CO-to- H_2 conversion factor, $2.3 \times 10^{20} cm^{-2} (K km s^{-1})^{-1}$ suggested by [Strong et al. \(1988\)](#), the column density of molecular hydrogen can be written as:

$$N(H_2) = 2.3 \times 10^{20} \int_{line} T_R dv (mol.cm^{-2}) \quad (5.2)$$

Where dv is the velocity interval. In Eq. 5.1 $K \equiv \Omega_S/\Omega_\Sigma$ is the factor which corrects the measured antenna temperature for the weighing of the source distribution by the large antenna beam in case of a smaller source. We have defined the source solid angle as:

$$\Omega_S \equiv \int_{source} \phi(\theta, \psi) d\Omega \quad (5.3)$$

where $\phi(\theta, \psi)$ is the normalized source brightness distribution function. The beam-weighted source solid angle is

$$\Omega_\Sigma \equiv \int_{source} \phi(\theta, \psi) f(\theta, \psi) d\Omega \quad (5.4)$$

where $f(\theta, \psi)$ denotes the normalized antenna power pattern (Baars 1973). Experiments have shown that we can approximate f by Gaussian beam. An exponential law of scale length $h = D_B/10$ is taken to model the source distribution function. The factor 10 is used to estimate the scale length of the molecular gas distribution from the optical diameter (B band). We used our own data from the CO(1-0) map of 3CR 31 and the CO(1-0) map of elliptical galaxies presented by Young (2002). In equation 5.5 that optical diameter is represented by θ_s . Using the assumption that the gas surface density is $\mu(r) \propto e^{-r/h}$ and as long as the source is smaller than the beam size, we have the following:

$$K = \frac{\int_0^{\theta_s/2} \sin(\theta) e^{-\frac{10\theta}{\theta_s}} d\theta}{\int_0^{\theta_s/2} \sin(\theta) e^{-\frac{10\theta}{\theta_s} - \ln(2)(\frac{2\theta}{\theta_b})^2} d\theta} \quad (5.5)$$

If I_{CO} is the velocity-integrated temperature for the $^{12}\text{CO}(1-0)$ line in T_{MB} scale and given the IRAM-30m parameters, the total mass of H_2 is then given by

$$M_{H_2} = 5.86 \times 10^4 D^2 K I_{CO} (M_\odot) \quad (5.6)$$

with the distance, D , in Mpc and the I_{CO} in K km/s

5.2 Results on molecular gas mass

In Table 5.1 we show the results of the observations, where $I_{CO(1-0)}$ and $I_{CO(2-1)}$ are the integrated intensities ($\int T_{MB} dv$) for the $^{12}\text{CO}(1-0)$ and $^{12}\text{CO}(2-1)$ line respectively, $\delta I_{CO(1-0)}$ and $\delta I_{CO(2-1)}$ are the standard error on $I_{CO(1-0)}$ and $I_{CO(2-1)}$, $V_{width\ CO(1-0)}$ and $V_{width\ CO(2-1)}$ are the velocity width of CO(1-0) and CO(2-1) respectively; and finally, M_{H_2} is the calculated molecular gas mass for each galaxy in the sample.

As shown in Table 5.1, there are 20 galaxies in this sample, 38 %, that were clearly detected (3CR 31, 3CR 88, 3CR 264, 3CR 274, 3CR 305, 3CR 321, 3CR 535, 3CR 386, 3CR 403, 3CR 442, 3CR 449, NGC 708, NGC 3801, NGC 4278, NGC 5127, NGC 7052, B2 0116+31, B2 0648+27, B2 0836+29B and OQ 208); 10 more were tentatively detected, a total of 30 galaxies equivalent to a 58%, (3CR 66B, 3CR 83.1, 3CR 129, 3CR 272.1, 3CR 327, NGC 315, NGC 326, NGC 541 and B2 0924+30). The rest of the galaxies, the none detected galaxies, were calculated using a velocity width of 300 km/s. For the calculation of the mass they were used as upper limits and with ASURV (Astronomical SURVival Analysis Package) we calculated the statistical values for the molecular gas mass of the sample.

ASURV is a software package (Lavalley et al. 1992) written in FORTRAN that implements the statistical survival analysis techniques presented in Feigelson & Nelson (1985); Isobe et al. (1986); Schmitt (1985). ASURV was written

Table 5.1: Molecular Gas data

Galaxy	Z_{CO}	Distance Mpc	$I_{CO(1-0)}$ [K Km/s]	$\delta I_{CO(1-0)}$ [K Km/s]	$V_{width\ CO(1-0)}$ [km/s]	$I_{CO(2-1)}$ [K Km/s]	$\delta I_{CO(2-1)}$ [K Km/s]	$V_{width\ CO(2-1)}$ [km/s]	M_{H_2} $\times 10^8 M_{sun}$
3CR31 ^{**a}	0.0169	71.06	5.68	0.81	550	14.06	1.13	550	$16.81 \pm 2.38^{**}$
3CR40	<1.11	< 3.25
3CR66B ^{*,b}	0.0157	85.20	0.2081	0.053	250	$0.89 \pm 0.23^*$
3CR83.1 ^{*,c}	0.0251	104.6	0.53	0.002	—	1.13	0.12	200	3.60 ± 0.0013
3CR88 ^{**b}	0.03	126.20	0.23 8	0.05	300	$2.19 \pm 0.44^{**}$
3CR98	<0.73	< 7.27
3CR129 ^{*,c}	0.0208	86.4	0.28	0.024	—	0.59	0.11	200	1.3 ± 0.11
3CR236	<0.75	X	X	X	< 80.70
3CR264 ^{**a}	0.02	90.90	0.70	0.15	200	1.48	0.16	225	$3.37 \pm 0.74^{**}$
3CR270	<1.16	< 0.69
3CR272.1 ^{*,a}	0.0028	12.00	0.36	0.12	200	0.90	0.16	150	$0.03 \pm 0.01^*$
3CR274 ^{**b}	0.0035	14.90	4.02	0.39	200	$0.52 \pm 0.05^{**}$
3CR296	<0.85	< 5.05
3CR305 ^{**b}	0.042	171.70	1.19	0.14	600	X	X	X	$20.52 \pm 2.49^{**}$
3CR321 ^{**b}	0.10	379.97	0.83	0.09	500	X	X	X	$70.58 \pm 7.93^{**}$
3CR327 ^{*,b}	0.1035	401.87	0.28	0.10	200	X	X	X	$26.48 \pm 9.59^*$
3CR353 ^{**b}	0.0327	153.73	0.31	0.05	200	$4.27 \pm 0.68^{**}$
3CR386 ^{**c}	0.017	71.7	0.58	0.02	—	1.23	0.17	175	1.78 ± 0.058
3CR402	<0.95	< 6.59
3CR403 ^{**b}	0.058	134.97	0.44	0.11	500	X	X	X	$4.75 \pm 1.18^{**}$
3CR433	<0.87	X	X	X	< 93.13
3CR442 ^{**c}	0.0263	110.5	0.09	0.02	—	0.20	0.07	300	$0.67 \pm 0.16^{**}$
3CR449 ^{**b}	0.0169	71.40	1.20	0.24	500	3.59 ± 0.73
3CR465	<0.78	< 7.69
NGC315 ^{*,b}	0.0175	73.80	0.26	0.06	150	$0.82 \pm 0.19^*$
NGC326 [*]	0.0474	203.18	0.2320	0.05	100	0.65	0.2	400	$5.61 \pm 1.2^*$
NGC541 ^{*,c}	0.018	75.0	0.72	0.08	400	1.53	0.32	350	2.5 ± 0.27
NGC708 ^{**b}	0.0166	69.86	1.84	0.31	600	$5.25 \pm 0.88^{**}$
NGC2484	<1.00	< 19.77
NGC2892	<1.22	< 6.85
NGC3801 ^{**b}	0.0117	49.50	3.82	1.14	600	$5.49 \pm 1.63^{**}$
NGC4278 ^{**a*}	0.0022	9.40	1.00	0.22	600	3.13	0.31	500	$0.05 \pm 0.01^{**}$
NGC5127 ^{**c}	0.016	67.1	0.28	0.02	—	0.59	0.10	100	0.79 ± 0.053
NGC5141	<1.55	< 5.04
NGC5490	<1.92	< 5.41
NGC6251	<1.03	X	X	X	< 6.78
NGC7052 ^{**a}	0.016	66.36	0.76	0.16	700	0.58	0.16	180	$1.96 \pm 0.41^{**}$
B2 0034 + 25	<0.96	< 10.41
B2 0116 + 31 ^{**b}	0.06	242.10	1.77	0.49	700	4.29	0.69	1000	$60.63 \pm 16.92^{**}$
B2 0648 + 27 ^{**a}	0.04	169.83	0.72	0.07	300	1.44	0.34	350	$12.25 \pm 1.18^{**}$
B2 0836 + 29B ^{**b}	0.065	261.70	1.20	0.30	500	X	X	X	$48.18 \pm 11.95^{**}$
B2 0915 + 32B	<1.83	< 70.52
B2 0924 + 30 ^{*,b}	0.025	104.25	0.32	0.11	200	$2.01 \pm 0.68^*$
B2 1101 + 38	<1.35	< 13.09
B2 1347 + 28 ^{*,b}	0.072	297.9	0.35	0.08	—	0.75	0.25	500	17.04^*
B2 1357 + 28	<1.13	< 48.09
B2 1447 + 27	<0.79	< 7.96
B2 1512 + 30	<1.19	< 110.54
B2 1525 + 29	<1.52	< 69.55
B2 1553 + 24	<1.52	< 29.68
UGC 7115	<1.53	< 7.66
OQ 208 ^{**b}	0.0766	304.90	2.51	0.33	400	X	X	X	$136.51 \pm 17.94^{**}$

The * means that this galaxy is a tentative detection, the ** means this galaxy is detected. The letter *a* is for (1-0)&(2-1) detected galaxies, *b* is for the CO(1-0) only detected galaxy and *c* is for the galaxies detected in CO(2-1) only; note that in this cases the velocity with is represented as — since the CO(1-0) value was calculated using the average of the ratio and therefore the width of the line is unknown. The case of NGC 4278, that has an *a** is because this galaxy has been detected in (2-1) and tentatively detected in (1-0). In M_{H_2} the * have the same meaning, only that in this case refers strictly to CO(1-0) since the integrated velocity for 3 mm was the one used to calculate the molecular mass.

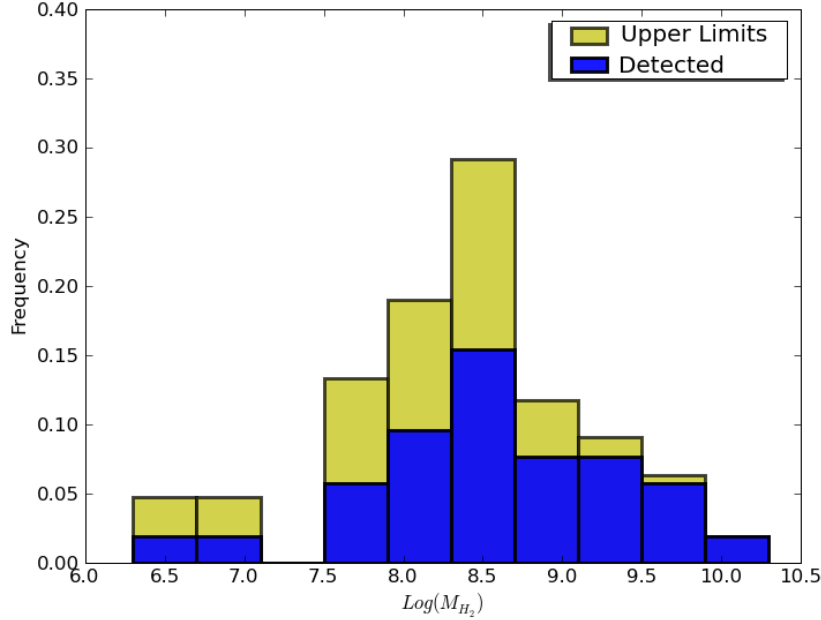


Figure 5.1: Distribution of the molecular gas mass in TANGO. Note that the yellow is only for the upper limits, and the blue for the detected galaxies.

between 1987 and 1992 and can be obtained at <http://astrostatistics.psu.edu/statcodes/asurv>.

In this project, ASURV was used to do some statistical calculations since in this sample of galaxies, not all of them were detected and those were called upper limits. These upper limits gave us important information about the amount of CO in the galaxies, it tells us the maximum amount we can possible expect from those upper limit galaxies. Using ASURV we calculated the molecular gas mass of TANGO, which, on average is $2.3 \times 10^8 M_{\odot}$ and its median value is $2.2 \times 10^8 M_{\odot}$; which is a different result compared to when we do no consider the upper limits. The mean value for the molecular gas mass, using only detected galaxies, is $3.7 \times 10^8 M_{\odot}$ with a median value of $3.4 \times 10^8 M_{\odot}$.

Figure 5.1 is the molecular gas distribution, normalized to one for the whole sample including the detections and the upper-limits for CO(1-0) observations. On the same Figure we show, in blue, the histogram of only the galaxies detected, the median value of the molecular gas mass of these 30 detected galaxies is $3.4 \times 10^8 M_{\odot}$.

To normalize the sample, we divided the distribution per bin of the histogram by the total number of galaxies in the sample, and to normalize the sub-sample that has the detected galaxies only, we divided the distribution

per bin by the total number of galaxies in the complete sample, with the purpose of comparing both samples. The range of the molecular gas mass (in Log) for the sub-group of the detected galaxies is between 6.3 and 10.2. The number of galaxies with a molecular gas mass lower than 6.3 (in Log) is obviously unknown.

The molecular gas mass in the sample ranges over 4 orders of magnitude, from $3 \times 10^6 M_{\odot}$ for 3C272.1 to $1.4 \times 10^{10} M_{\odot}$ for OQ 208. Most of the galaxies have a molecular gas mass between 8.3 ($2 \times 10^8 M_{\odot}$) and 8.7 ($5 \times 10^8 M_{\odot}$), this is true for the complete sample including the upper limit calculation as for the sub-sample that includes only the detected galaxies.

5.3 Faranoff and Riley

We have explain in the introduction the difference between the FR type galaxies. There is an important bias with respect to the classification, in general FR-II galaxies are brighter in molecular gas and FR-I galaxies and are usually farther away, higher redshift (z). Figure 5.2 is the molecular gas mass vs. the z . It is clear that for higher z the galaxies tend to have higher molecular gas mass, following the sensitivity of the telescope. The sensitivity limit was computed, assuming a typical value of 300 km/s for the velocity width and 1 mK for the rms noise temperature. It is clear that there is a larger number of FR-II galaxies, compared to FR-I and FR-c galaxies, at higher z , implying a larger threshold of the upper limit for the FR-II type galaxies. This also agrees with the idea that FR-II galaxies are stronger AGN and more luminous, and this is also why they are seen at a higher distance. A factor 3 in the median mass can be expected, and we conclude that the difference between the radio galaxy types for the molecular gas mass could be only due to the Malmquist bias.

In the present sample, 69.2% are FR-I type galaxies; 19.2% are FR-II type galaxies and 11.5% are FR-c type galaxies.

We have previously said that the molecular gas mass average of our sample is $2.2 \times 10^8 M_{\odot}$ and that the FR-II type galaxies have the largest molecular gas mass compared to the FR-I type galaxies and the FR-c type galaxies, as shown in Table 5.2, using the detected galaxies and the upper limits with the survival analysis statistics. The mean molecular gas mass is lower for the FR-I type galaxies than for the FR-II type galaxies with $1.7 \times 10^8 M_{\odot}$ and $8.1 \times 10^8 M_{\odot}$ respectively. This difference is clearly visible in Figures 5.3 (to see the distribution separately for each type) and 5.4 (where the distributions are all in one plot) where the molecular gas mass distribution is shown according to the types of radio galaxies: FR-I, FR-II and FR-c. We can draw the following conclusions regarding the different types of radio galaxies and their molecular gas masses:

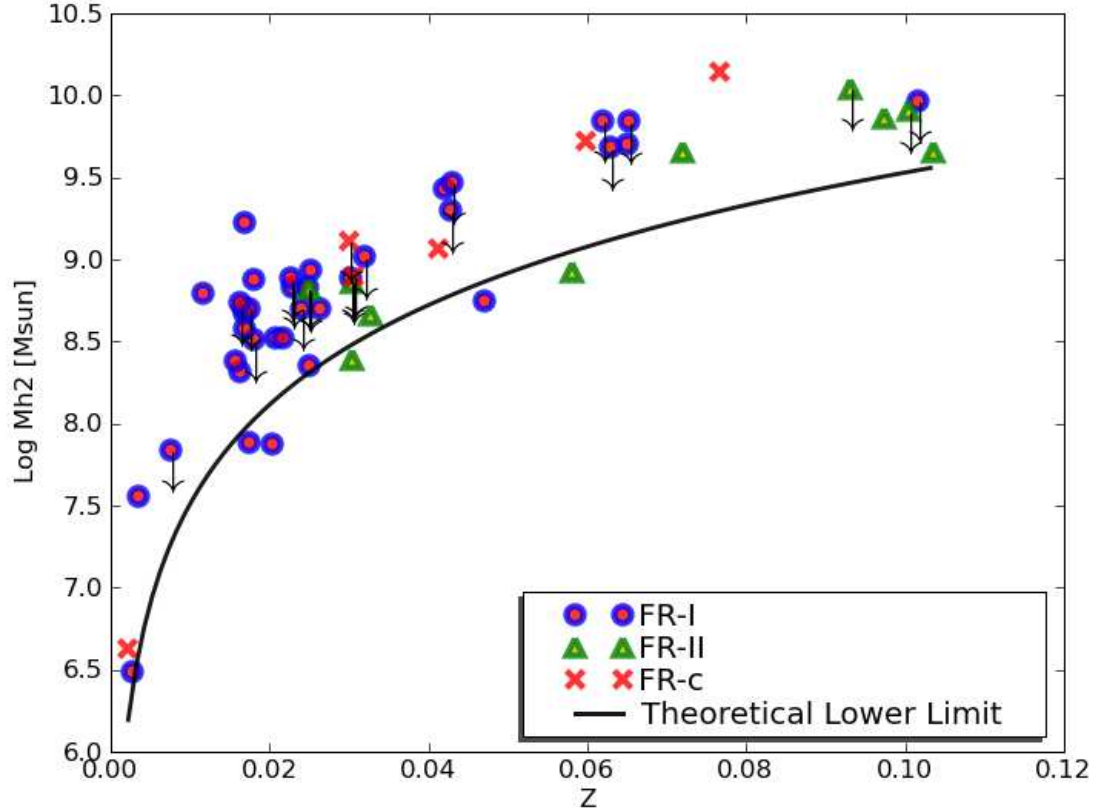


Figure 5.2: M_{H_2} versus z and a lower limit of the theoretical value for the mass with respect to the distance and to the IRAM-30m telescope observations.

1. For the FR-I types, which are the less powerful AGN, the elliptical host galaxy does not need much molecular gas mass to host the radio AGN. Molecular gas masses can be as low as $10^6 M_\odot$, which is a few Giant Molecular Clouds (GMC).
2. For the median value of the molecular gas mass, FR-II type galaxies ($8.1 \times 10^8 M_\odot$) are clearly more massive than the FR-I ($1.98 \times 10^8 M_\odot$) and FR-c ($2.0 \times 10^7 M_\odot$) type galaxies. Note that there are only a few FR-c galaxies and therefore the statistical values for them are not very reliable.

Evans et al. (2005) found only an 8% detection rate of CO emission in their FR-II galaxies, a very low value compared to the $\sim 35\%$ detection rate of the FR-I detected in their sample. We also found a higher detection rate in FR-I

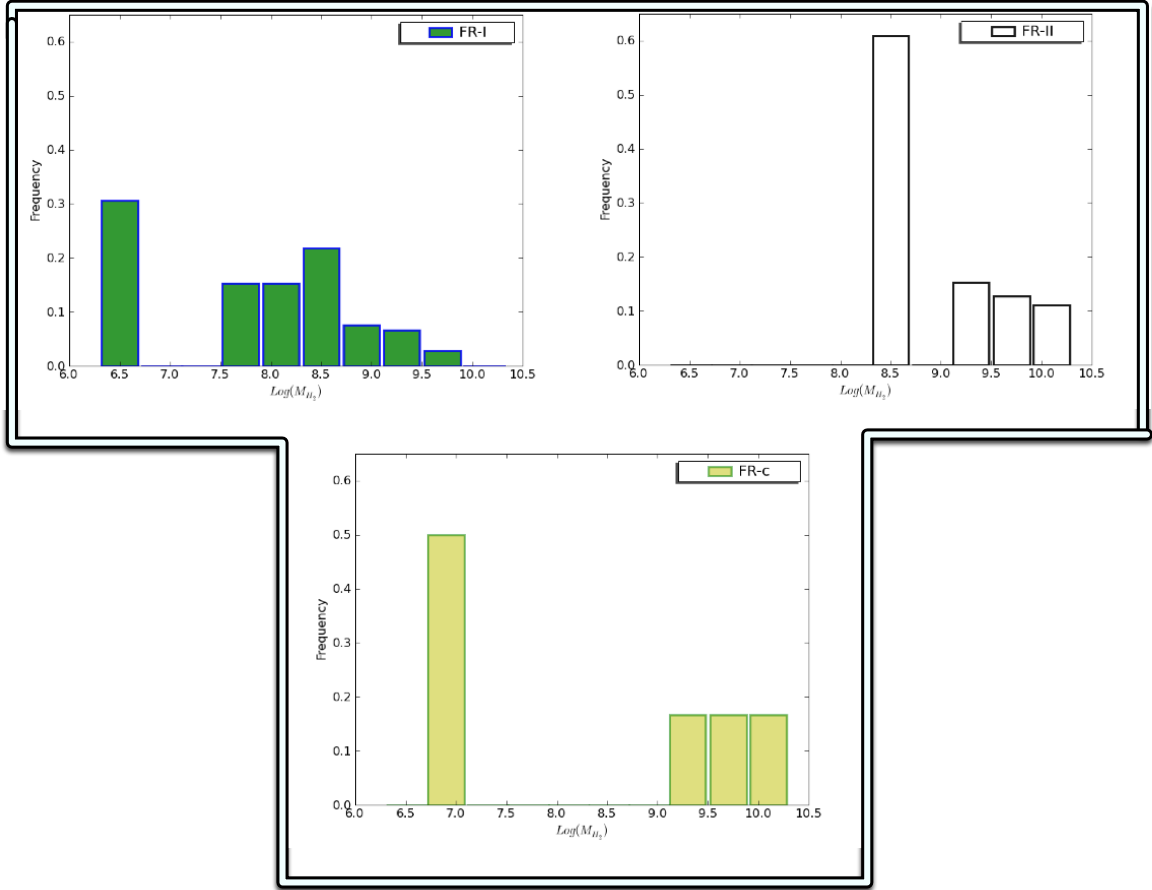


Figure 5.3: Molecular gas mass distribution in the radio galaxies depending on their Fanaroff-Riley classification.

galaxies compared to the FR-II galaxies. In our sample, the detection rate is 38.5% for FR-I, 11.5% for FR-II and 7.7% for FR-c galaxies. Note that the FR-II being more powerful AGN, they are rarer and are found at larger distances. This can also explain both their lower detection rate, and their higher median molecular content.

5.4 CO line ratios

The line ratio between the CO(2-1) and the CO(1-0) transitions is computed by comparing the integrated intensity ratio of the lines $I_{\text{CO}(2 \rightarrow 1)} / I_{\text{CO}(1 \rightarrow 0)}$ where the intensity was measured on one point at the center of each galaxy. Because

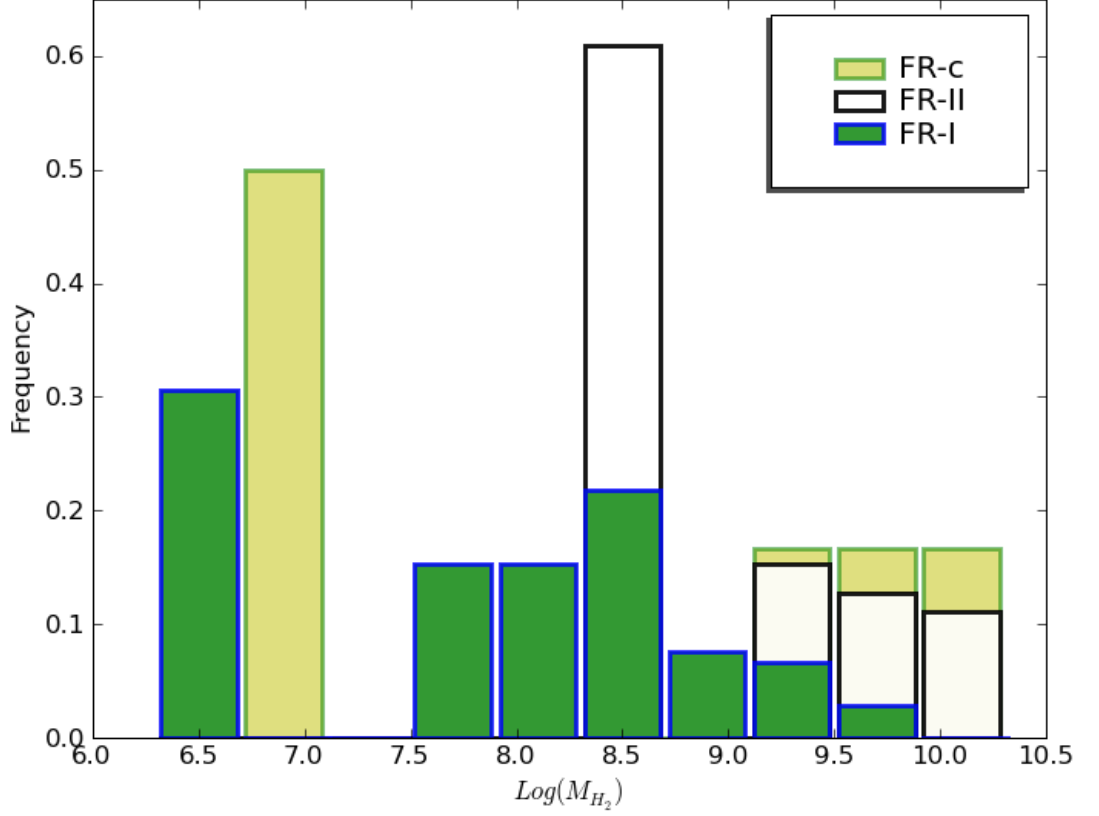


Figure 5.4: Molecular gas mass distribution in the radio galaxies depending on their Fanaroff-Riley classification.

Galaxy Name	Detected plus upper limits		Detected only	
	Mean	Median	Mean	Median
FR-I	1.7×10^8	1.86×10^8	2.3×10^8	2.01×10^8
FR-II	8.1×10^8	4.45×10^8	1.1×10^9	4.6×10^8
FR-c	2.1×10^8	2.03×10^7	8.5×10^8	1.2×10^9
Total	2.3×10^8	2.2×10^8	3.7×10^8	3.4×10^8

Table 5.2: Mean and median values of the molecular gas mass of all sub-samples separately in logarithmic values in units of M_{\odot}

of the different beam sizes at CO(1-0) and CO(2-1), the intensities should be compared only after having carried out small maps in CO(2-1) to sample the CO(1-0) beam. However, in most of our galaxies, the CO emission is expected to be almost a point source, at both frequencies. Except for NGC 4278, the distance of our detected galaxies is around or above 100 Mpc, where the CO(1-0) beam is 10 kpc, and in elliptical galaxies, the gaseous disks are expected to be, according to [Young et al. \(2008\)](#), concentrated in the nuclear disks at Kpc scales. Therefore, equal I_{CO} intensities in both lines will result in ratios of ~ 4 , the point source dilution ratio of the two beams (to have a more detailed derivation of beam couplings, see § 5.4.1).

As previously noticed by [Lim et al. \(2000\)](#), the 2 galaxies studied in their paper have a stronger observed intensity in CO(2-1) than in CO(1-0). This sample has a line ratio well over unity. Seven of our galaxies have been detected in both frequencies and 6 more have been detected only in CO(2-1). From the galaxies detected in both frequencies, only NGC 7052 has an integrated intensity stronger in the CO(1-0) line than in the CO(2-1) line. The maximum line ratio was found to be 3.1 (for NGC 4278) and the average value is 2.3 ± 0.1 . When correcting by the factor 4 of the beam dilution ratio, the average value is ~ 0.6 . This corresponds to an average over a moderate density disk, where most of the CO emission is optically thick, but sub-thermally excited. The maximum ratio obtained precisely for the most nearby galaxy NGC 4278 is 0.8, comparable to the typical value obtained for the central parts of spiral galaxies by [Braine & Combes \(1992\)](#).

Figure 5.5 is a plot of the integrated intensity $I_{CO(2\rightarrow 1)}$ vs. $I_{CO(1\rightarrow 0)}$ with a line fit indicating a clear correlation. The dotted line in the plot is for the intensities with the same value for both lines. Table 5.3 lists the line ratios for each galaxy and to see the spectra of those galaxies detected in both frequencies see the Appendix, Figures in A, where the spectra of all galaxies in the sample are plotted. Note that the galaxy B2 0116+31 presents in its CO(1-0) line profile a strong absorption line, as well as the double line profile that can still be clearly seen. This absorption is the signature of molecular gas mass on the line of sight towards the AGN covering a very small area. Most of the radio galaxies observed have a radio continuum in millimeter strong enough to be detected in absorption, but only in one galaxy the CO(1-0) transition is absorbed towards the radio continuum. The double horn profile of B2 0116+31 is visible as well in the CO(2-1) transition line, where the absorption is much weaker, as well as the continuum at this frequency. The absorption line in this galaxy should cause an underestimation of the CO(1-0) integrated intensity and therefore an overestimate of the line ratio.

For those galaxies detected in CO(2-1) emission line, and not detected in CO(1-0) we derived a value for the integrated velocity $I_{CO(1-0)}$ using the ratio of 2.3 calculated with the galaxies detected in both lines. Again, for a closer view to the spectra of those galaxies please see the online material, Figures in Appendix A. The values of the derived molecular gas masses are already

Galaxy Name	Ratio
3CR 31	2.5 ± 0.2
3CR 264	2.1 ± 0.2
3CR 272.1	2.5 ± 0.4
NGC 326	2.8 ± 0.3
NGC 4278	3.1 ± 0.4
NGC 7052	0.8 ± 0.1
B2 0116+31	2.4 ± 0.3
B2 0648+27	2.0 ± 0.3

Table 5.3: CO(2-1)-to CO(1-0) line ratio of the detected galaxies, not corrected by the different beam dilutions.

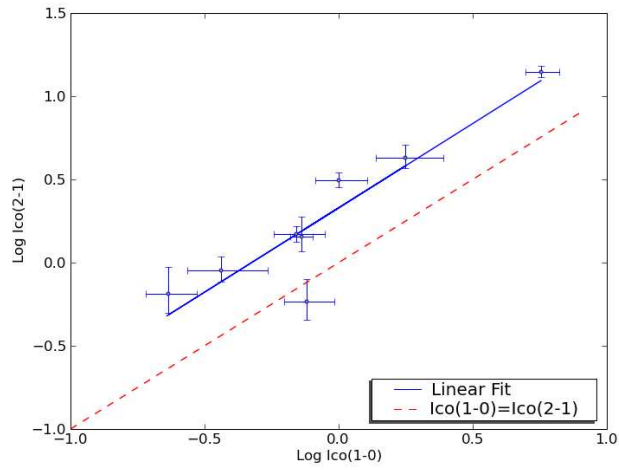


Figure 5.5: Plot of the line ratio of the galaxies. The point that is outside of the linear fit is of the galaxy NGC 7052

included in Table 5.1.

5.4.1 Beam/source coupling

To correct the observed emission line brightness temperatures for beam dilution we know that (Thi et al. 2004):

$$T'_{MB} = \frac{T_{MB}(\Omega_{source} + \Omega_{beam})}{\Omega_{source}} \quad (5.7)$$

where T'_{MB} is the real main beam temperature and T_{MB} is the observed main beam temperature. By assuming an axisymmetric source and beam distribution we can represent their distribution by an angular θ parameter leading to a correction factor for the CO(2-1)-to-CO(1-0) line ratio of:

$$K = \frac{\theta_{b-230}^2 + \theta_s^2}{\theta_{b-115}^2 + \theta_s^2} \quad (5.8)$$

(see de Rijcke et al. 2006, for more details) where θ_{b-230} is the beam size at 230 GHz and θ_{b-115} is the beam size at 115 GHz; θ_s is the angular size of the source. We recall that for a Gaussian beam $\Omega_{beam} = \int_{beam} P_\omega \omega d\omega = \frac{1}{4\ln 2} \pi \theta_b^2 \simeq 1.133 \theta_b^2$, although the 1.133 cancels out in Equation 5.8. The correction factor K for the CO(2-1)-to-CO(1-0) line ratio is shown on Fig. 5.6 as a function of the angular source size θ , it varies between 0.25 for a point source up to 1. for a completely extended source.

Besides for the galaxy 3CR 31, we did not apply the beam dilution correction because we do not have the molecular size of the galaxies and therefore we do not know which correction we should apply.

5.5 Molecular gas disk

The double horn CO line profiles observed in 8 of the galaxies (3CR 31, 3CR 264, 3CR 403, 3CR 449, NGC 3801, NGC 7052, B2 0116+31 and OQ 209) are characteristic of an inclined molecular gas rotating disk, these 8 galaxies are equivalent to 29% of the detected galaxies in our sample. In the Appendix, §A, you can find the spectra of those galaxies that present a double horn profile. In the case of 3CR 31 and 3CR 264 the double horn profile is clearly visible in both transitions, CO(1-0) and CO(2-1), and for 3CR 403 and OQ 208 we see only this feature in the CO(1-0) transition since there is no data for the CO(2-1) transition.

Five of the galaxies that present the double horn profile are FR-I types. Only one galaxy, 3CR 403, is an FR-II type, and two galaxies, OQ 208 and B2

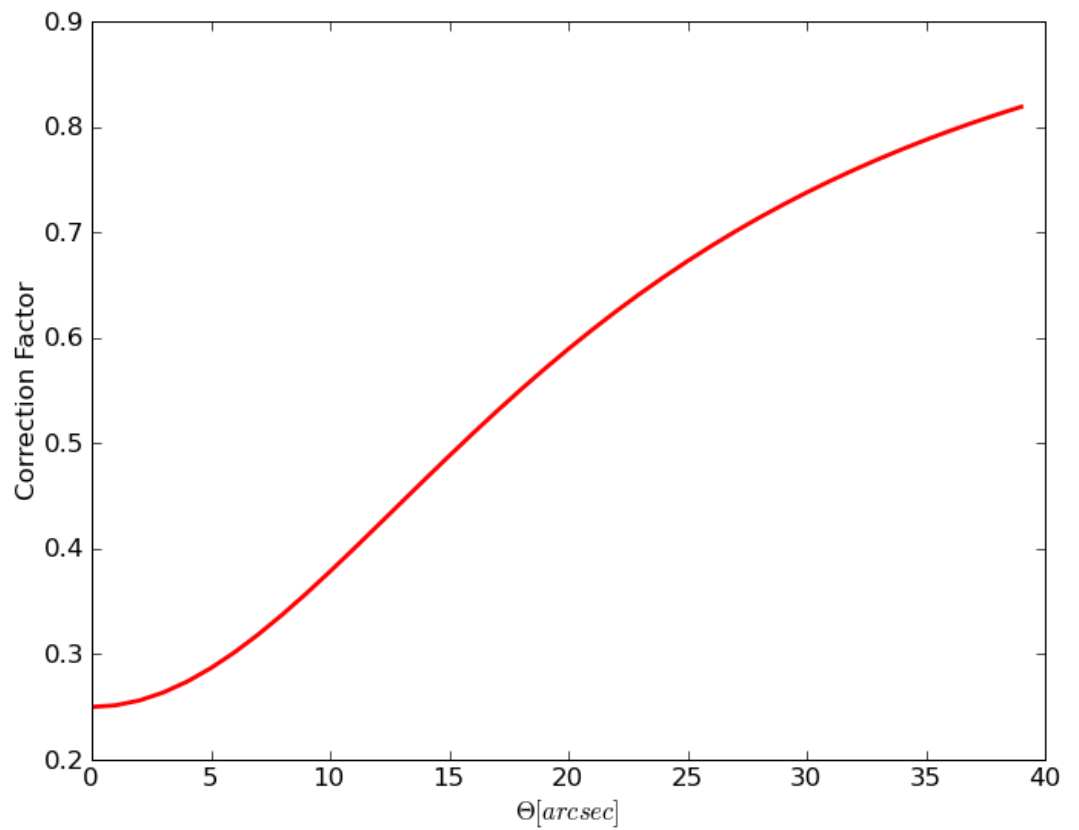


Figure 5.6: Correction factor K for the CO(2-1)-to-CO(1-0) line ratio as a function of the size θ of the source detected in CO(1-0), to take into account the beam dilution. The possible sources go from a point like source to a source with a size of $22''$

Galaxy	M_{H_2} $\times 10^8 M_\odot$
3CR 31	16.81 ± 2.38
3CR 264	3.37 ± 0.74
3CR 403	4.75 ± 1.18
3CR 449	3.59 ± 0.73
NGC 3801	5.49 ± 1.63
NGC 7052	1.96 ± 0.41
B2 0116+31	60.63 ± 16.92
OQ 208	136.51 ± 17.94
Average Value:	29.14 ± 5.24

Table 5.4: Molecular mass gas of the galaxies that present the double horn profile.

0116+31, are FR-c type.

We also note that 4 of our 8 galaxies have been detected in both transitions (3CR 31, 3CR 264, NGC 7052 and B2 0116+31) and in all 4 cases the CO(2-1) line is stronger than the CO(1-0) line (more details about the line ratios of these galaxies in § 5.4).

The galaxies that present the double horn profile feature are also within the largest H_2 masses. The average value for this sub-sample is $29.1 \times 10^8 M_\odot$, an order of magnitude higher value than the average value of the complete sample for the detected galaxies only ($2.2 \times 10^8 M_\odot$), see the molecular gas mass of each galaxy in Table 5.4.

We note that in some cases the absorption of the CO transitions could mimic a double horn profile. It appears from the peak temperature in the double horn profiles that in all cases, except for the CO(2-1) emission in 3CR 31, the double horn profile could be perturbed by an absorption line.

5.6 Continuum Data

While searching for CO(1-0) and CO(2-1) molecular lines, we used the baseline level of their spectra to calculate the continuum flux densities at 3mm and 1mm. The continuum level and the detections were given in antenna temperature, T_a^* , and then converted to main beam temperature, T_{MB} . The conversion factor used was the one given by Rohlfs & Wilson (2004), where we divided the forward efficiency (which is a model function to the measure antenna temperature and the copper load temperature) by the beam efficiency (which is the percentage of all power received that enters the main beam), F_{eff}/B_{eff} . Applying this for each frequency in the case of the IRAM-30m telescope, the relationship is 1.27 at 3mm and 1.75 at 1mm.

To convert the data from temperature (K) to flux (Jy), the point source sensitivity measurement (S/T_A^*) is 6.3 for 3mm and 8 for 1mm wavelength. The results for these conversions are listed in Table 5.5. For more details on the conversion, see section 4.3. From the observations, in summary, 90% out of the 52 galaxies were detected in the continuum at 3mm and 65% out of the 43 galaxies were detected in the continuum at 1mm.

Galaxy	S_{3mm} (mJy)	δS_{3mm} (mJy)	S_{1mm} (mJy)	δS_{1mm} (mJy)
3C31	79.07	1.13	74.39	2.78
3C40	96.91	0.9	20.11	1.8
3C66B	110.12	0.43	73.08	1.39
3C83.1	33.45	0.69
3C88	121.84	0.43	87.05	1.3
3C98	18.09	0.52	6.18	1.54
3C129	28.53	0.65	0.91	1.27
3C236	225.06	0.57	X	X
3C264	174.64	0.5	87.35	1.13
3C270	326.34	0.82	204.71	1.57
3C272.1	138.29	1.2	73.86	6.79
3C274	2347.13	1.83	1312.31	2.78
3C296	99.23	0.6	54.55	1.22
3C305	21.23	4.28	X	X
3C321	67.33	0.52	X	X
3C327	105.81	0.69	X	X
3C353	3.46	1.35
3C386	50.21	0.88	105.01	2.26
3C402	332.57	39.27
3C403	20.35	0.48	X	X
3C433	91.29	0.76	X	X
3C442	9.62	0.43	75.51	9.99
3C449	25.82	0.5	15.83	1.65
3C465	86.06	0.56	27.32	1.31
NGC315	353.56	0.67	62.12	1.39
NGC326	63.47	0.63
NGC541	4.73	2.02	27.23	2.60
NGC708	8.11	0.98	148.94	3.83
NGC2484	110.63	0.69	11.92	1.65
NGC2892	190.05	0.87	272.39	2.23
NGC3801	1181.72	210
NGC4278	215.9	1.08	194.34	1.28
NGC5127	25.62	1.13
NGC5141	63.50	1.01
NGC5490	27.72	1.44	88.61	5.46

NGC6251	367.88	0.71	X	X
NGC7052	85.51	12.13	18.77	1.49
B2 0034 + 25	72.97	0.68	190.81	1.82
B2 0116 + 31	164.53	1.22
B2 0648 + 27	152.99	0.37	172.99	2.09
B2 0836 + 29B	X	X
B2 0915 + 32B	11.39	1.29	24.41	2.17
B2 0924 + 30	9.44	1.13
B2 1101 + 38	359.89	0.97	0.165	0.002
B2 1347 + 28	8.96	0.51
B2 1357 + 28
B2 1447 + 27	13.94	0.53	52.41	0.81
B2 1512 + 30
B2 1525 + 29	14.48	1.07	0.13	0.003
B2 1553 + 24	35.28	1
UGC7115	30.57	1.03
OQ208	40.43	16.67	X	X

Table 5.5: IRAM 30m fluxes at 3 mm and 1 mm. *X* means that there was no data, and "..." refers to undetected flux.

5.7 Discussion: Origin of the molecular gas

As will be shown on chapter 10.6, the molecular gas content of the host elliptical galaxies of the powerful radio-AGN is low compared to spiral galaxies. The origin of that gas can either be internal (stellar mass loss, cooling gas from a galaxy halo of hot gas) or external (minor/major merger, accretion-fed from cosmological filaments, cooling flows), when the radio galaxy is at the center of a cluster. [Salomé et al. \(2008\)](#) provided an exhaustive discussion about the molecular gas in cooling flows which can be accreted by an elliptical galaxy. We estimated the stellar mass loss η by using the B magnitude of the elliptical host ([Athey et al. 2002](#)), namely:

$$\eta = 0.0078(M_{\odot}/10^9 L_{\odot,B})M_{\odot}/yr. \quad (5.9)$$

Fig. 5.8 shows the distribution of the stellar mass loss in our sample of radio galaxies detected in CO or with an upper limit of molecular gas mass lower than $5 \times 10^9 M_{\odot}$ in order to constrain the stellar mass loss contribution. The median value of the stellar mass loss is $0.37 M_{\odot} \cdot \text{yr}^{-1}$. This value implies a median time of 1 Gyr to refurbish the galaxy of molecular gas provided by the stellar mass loss without taking into account the consumption rate of the AGN (e.g. [David et al. 2006](#)). As shown on Fig. 5.7, a substantial fraction of radio galaxies have a filling time $M(H_2)/\eta$ of molecular gas provided by the stellar mass loss larger than 1 Gyr (36%) reaching time-scales close to the age

of the Universe. It allows, together with the accretion rate of the radio-AGN (see e.g. [Lagos et al. 2009](#)), to discard the stellar mass loss as a mechanism sufficient to provide the molecular gas in these elliptical galaxies.

In other words, we would expect the gas lost by the stars to be hot and to enrich the hot halo gas through stellar wind, in spheroidal galaxies; spherical geometry dilutes the gas, such that the density is never high enough to cool. The cooling time begins $>10\text{Gyr}$, so most of this gas remains hot and will not be seen in H_2/CO . This is not the case in spiral galaxies where the gravity and density are stronger so that the gas can cool back to the HI-H_2 phase.

If the molecular gas in the radio galaxies was provided by the stellar mass loss we would expect, at a first order, the molecular gas mass to correlate with the blue luminosity, a proxy of the galaxy stellar mass. That hypothesis is discarded by the data on [Fig. 9.2](#)

The external hypothesis for the origin of the molecular gas is more likely to explain a large part of the molecular gas present in the elliptical galaxies hosting the radio-AGN. [Lim et al. \(2000\)](#) favored the minor merger scenario for the origin of the molecular gas in 3CR 31 because of the smooth isophotes which do not show any signs of recent perturbations caused by a major merger. However, 3CR 31 is the brightest galaxy in a cluster showing a cooling flow ([Crawford et al. 1999](#)).

The inspection of the optical images shows that several radio galaxies are in dense environment where the minor/major mergers should be frequent enough to deposit molecular gas in the elliptical galaxies. The accretion of gas from cosmological filaments has been studied recently by numerical simulations ([Dekel et al. 2009](#)) and should be an additional source of molecular gas in these galaxies.

In the case of 3CR 31 there are suggestions, by [Martel et al. \(1999\)](#) that the galaxy is interacting. [Baldi & Capetti \(2008\)](#) suggest that 3C 264 has no young stellar population. [Emonts et al. \(2006\)](#) propose that B2 0648+27 formed from a major merger event that happened $\lesssim 1.5\text{Gyr}$ ago. [García-Burillo et al. \(2007\)](#) state that the distortions in B2 0116+31 may reflect that the disk is still settling after a merger or an event of gas accretion; or maybe the jet and the cone-line features might be interacting with the disk producing the reported distortion. [Giroletti et al. \(2005b\)](#) states for NGC 4278 that its central BH is active and able to produce jets, however, the lifetime of its components of $<100\text{yr}$ at the present epoch, combined with the lack of large-scale emission, suggests that the jets are disrupted before they reach kilo-parsec scales. In conclusion, the origin of the gas in these galaxies can be multiple, in majority external, and a composite scenario can be invoked in each galaxy.

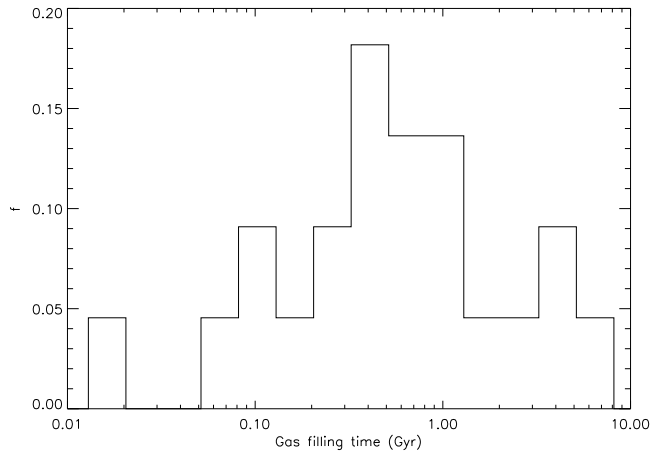


Figure 5.7: Histogram of the gas filling time for our sample.

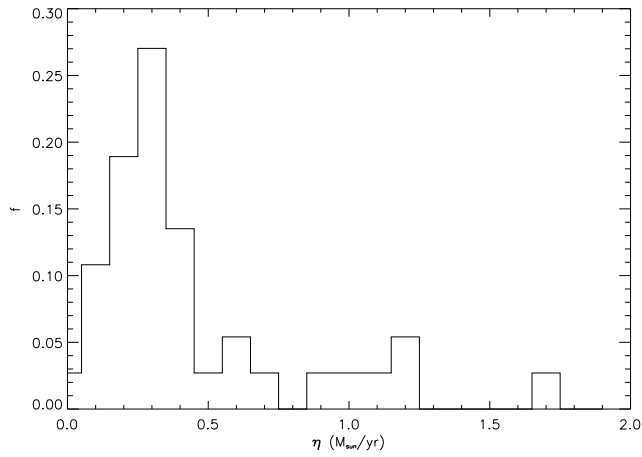


Figure 5.8: Histogram of the stellar mass loss in M_{\odot}/yr for our sample of radio galaxies.

5.8 Summary and Conclusions

- The detection rate is 38% firm (20/52) with 58% total (30/52), including tentative detections
- Indications of molecular gas disk (double-horn profile) is found in 15% of the galaxies (27% of the detected galaxies).
- The CO(2-1)-to-CO(1-0) line ratio is 2.3 without taking into account beam dilution effect, and likely to be ~ 0.6 with corrections, suggesting optically thick and sub-thermal CO emission.
- The median value for the stellar mass loss in this sample is about $0.37 M_{\odot}/\text{yr}$.
- The origin of the gas for the galaxies in TANGO can be multiple, in majority external, and a composite scenario can be invoked in each galaxy.

Chapter 6

Dust

6.1 Introduction

Dust is an important ingredient of the ISM, associated with the molecular gas. Although dust mass is typically 1% of the mass of the gas, it is very important since it acts as a catalyst for the formation of molecular gas. Dust grains have different sizes and as a result they are heated to different temperatures by the underlying stellar population. As a result, the processed emission by dust peaks in different infrared wavelengths. In systems with ongoing star formation (SF), the light from both newly formed and older stars can be absorbed by dust, heated by the UV/Optical field coming from (young) stars and/or AGN, and later reprocessed into the Far Infra Red (FIR) whose emission, therefore, depends strongly on its temperature giving information about dust enshrouded SF in the galaxies. Between $3\mu\text{m}$ and $30\mu\text{m}$, according to [Genzel & Cesarsky \(2000\)](#), is where the transition from stellar emission to interstellar dust emission in galaxies occurs, these mid-IR wavelengths are covered by IRAS and SPITZER (in particular the Infrared Array Camera (IRAC) camera). In order to study the properties of dust we sampled the infrared emission as widely as possible using data from both the IRAS (see [3.4.1](#)) and Spitzer (see [3.4.2](#)) satellites.

Since it is well known that early type galaxies contain dust emitting in IR (e.g., [Knapp et al. 1989, 1992](#)), the goal is to understand if the mid-IR emission originated mainly in the photosphere and shells of cool asymptotic giant branch stars or in the interstellar medium, or whether an AGN plays a role. According to [Madden et al. \(1999\)](#) $4.5/6.7\ \mu\text{m}$ and $6.7/15\ \mu\text{m}$ colors of about 60% of their sample of E and SO galaxies are consistent with the notion of a largely stellar origin for the mid-IR emission, and the rest of their galaxies are dominated by Unidentified Bands (UIB) emission (17%) or an AGN (22%). The main purpose of collecting all these data, was to add flux densities to our Spectral Energy Diagram (SED) which will be used to fit different dust components to get the mass and the temperature of the dust components.

6.2 Dust properties from IRAS

We analyzed the dust emission at $60\mu\text{m}$ and $100\mu\text{m}$ in our sample. The fluxes at these frequencies gave an estimation of the temperature and the mass of the warm dust component.

We will use the flux densities at $12\mu\text{m}$ and $25\mu\text{m}$ as well as the flux densities from Spitzer to build the Spectral Energy Diagrams (SED), more details will be given in chapter 8.

6.2.1 Star Formation

We know that in systems with ongoing star formation (SF), the light from both newly formed and older stars can be absorbed by dust and reprocessed into the FIR. And, as stated by Bell (2003), since young stars in HII regions heat up dust at relatively high temperatures (with a low $100\mu\text{m}$ -to- $60\mu\text{m}$ ratio of about ~ 1) we could use the fluxes already collected from IRAS (see Table 6.1) to have an idea of where is this IR emission coming from in our galaxies. This ratio leads to a wide range in $f_{100\mu\text{m}}/f_{60\mu\text{m}}$ on galaxy-wide scales, from ~ 10 for early type spiral galaxies to $\lesssim 1$ for the most intensely star forming galaxies suggesting that earlier types are influenced by old stellar population.

Our sample has a median value of $f_{100\mu\text{m}}/f_{60\mu\text{m}} = 1.9$ with its smaller value being 0.55 for 3C 327, which could be interpreted as a galaxy with high temperature heated up by young stars in HII regions or by an AGN. And its highest value is 4.5 for 3CR 88, which is, still, a small value compared with ~ 10 for quiescent early type spirals suggested by Bell (2003).

6.2.2 Dust Mass and Dust Temperature

We first calculated the dust mass and temperature assuming that the dust emission is completely characterized by the IRAS observations at 60 and 100 microns. To analyze the dust components we used the $60\mu\text{m}$ and $100\mu\text{m}$ from the IRAS satellite (see Table 6.1), because the fluxes at this frequencies give an estimation of the temperature and mass of the warm components.

The dust temperature, T_d , is calculated by adopting a modified black body emissivity law:

$$S_\nu \propto \kappa_\nu \beta_\nu(T_d) \quad (6.1)$$

where κ_ν is the dust emissivity and $\beta_\nu(T_d)$ is the Planck function at the dust temperature T_d . Then we calculate the dust mass as follows:

$$M_{dust} = 4.78 f_{100} D_L^2 (e^{(143.88/T_d)} - 1) M_\odot \quad (6.2)$$

where f_{100} is the flux at $100\mu\text{m}$ in Jy, D_L is the luminosity distance in Mpc and T_d the dust temperature in K. We should not forget that estimating masses

Galaxy Name	$f_{60} \mu\text{m}$ mJy	$f_{100} \mu\text{m}$ mJy
3CR 31	435 ± 65.3	1675 ± 251
3CR 88	180 ± 27	816 ± 122
3CR 272.1	556 ± 83.4	1024 ± 154
3CR 274	546 ± 81.9	559 ± 83.9
3CR 305	298 ± 44.7	450 ± 67.5
3CR 321	1067 ± 160	961 ± 144
3CR 327	670 ± 101	371 ± 55.7
3CR 402	257 ± 38.6	1052 ± 158
NGC 315	368 ± 55.2	460 ± 69
NGC 708	200 ± 34	660 ± 157
NGC 4278	580 ± 53	1860 ± 60
NGC 6251	188 ± 28.2	600 ± 90
NGC 7052	524 ± 78.6	1150 ± 173
B2 0116+31	150 ± 22.5	524 ± 78.6
B2 0648+27	2633 ± 395	1529 ± 229
B2 0836+29B	472 ± 70.8	595 ± 89.2
B2 1101+38	181 ± 22	361 ± 68
OQ 208	753 ± 113	1029 ± 154

Table 6.1: IRAS data for the galaxies that have been detected at 60 μm and at 100 μm .

is very tricky since it depends to high power in temperature. A cold dust component (which is hard to trace) could dominate the total dust mass in a system. We should not forget either that galaxies with no carbon (low metallicity) is an issue on estimating the dust masses (Franco & Cox 1986).

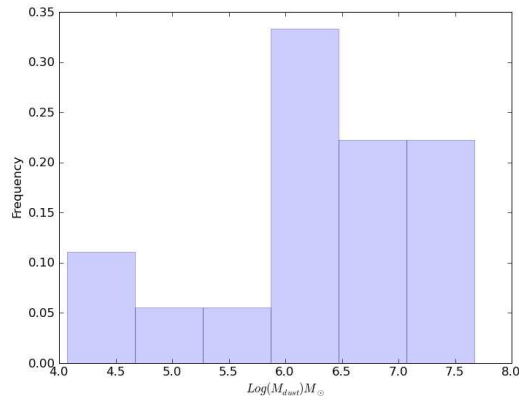
The median value of the dust temperature for this sample, using the galaxies detected by IRAS is 35.8K and the median value of the dust mass of the sample, is $2.5 \times 10^6 M_{\odot}$. The list of the dust masses and temperatures are shown in Table 6.2.

We then calculated the M_{H_2}/M_{dust} gas-to-dust mass ratio for this sample, using the galaxies detected with both IRAS and IRAM-30m, an upper limit ratio of about 260. On Figure 6.2 the distribution of the gas-to-dust mass ratio is shown, where the galaxies range between 20 and 4450 in the gas-to-dust mass ratio. If we use as well the galaxies in the sample that were considered upper limits for the molecular gas mass, we obtained an upper limit gas-to-dust mass ratio of 254 on average.

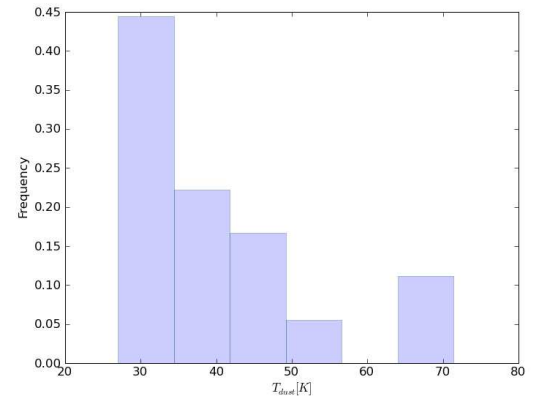
Figure 6.1a is the histogram of the dust mass of this sample. Note that most of

Table 6.2: Dust mass and temperature.

Galaxy Name	$\text{Log}(M_{dust})$ (M_{\odot})	T_{dust} (K)
3CR 31	6.8	28.3
3CR 88	7.1	27.0
3CR 272.1	4.6	36.4
3CR 274 (M87)	4.1	47.4
3CR 305	6.4	39.5
3CR 321	7.1	50.8
3CR 327	6.4	71.3
3CR 402	7.0	27.8
NGC 315	5.5	42.9
NGC 708	6.3	29.7
NGC 4278	5	20
NGC 6251	6.9	30
NGC 7052	6.2	34.1
B2 0116+31	7.4	29.2
B2 0648+27	6.2	68.5
B2 0836+29B	6.8	42.8
B2 1101+38	6.2	35.3
OQ 208	7.2	41.2



a)



b)

Figure 6.1: Histograms of the dust mass and temperature characteristic of the sample. Figure a) is the dust mass in Logarithmic values and Figure b) is the dust temperature.

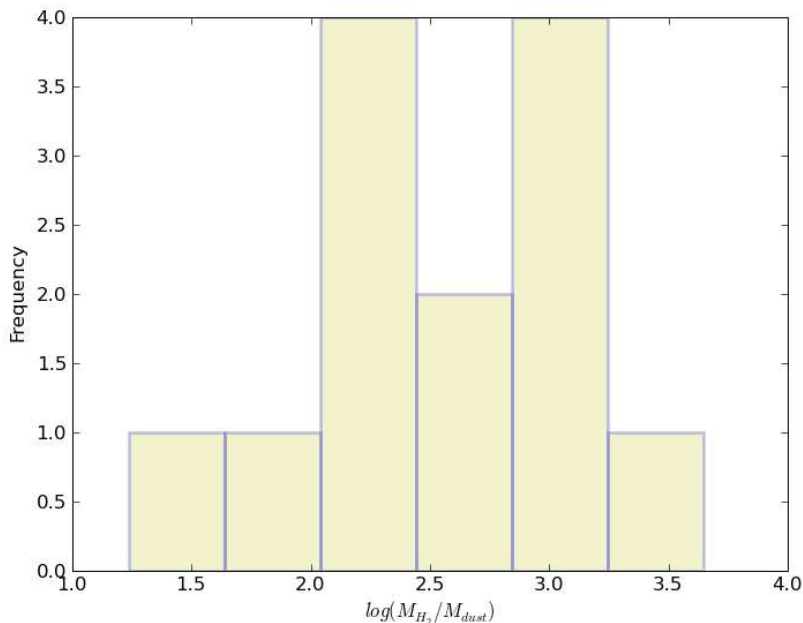


Figure 6.2: Histogram of the Gas-to-Dust mass ratio.

the galaxies lie in the range of $7.4\text{--}30 \times 10^5 M_{\odot}$. The dust temperature is mostly between 27.0 and 34.4 K, with the majority of the galaxies in this range, (see Figure 6.1b) although there are 2 galaxies with an estimated dust temperature of 64 and 71.4 K respectively. These 2 galaxies with a hotter dust component than the others are 3CR 327 and B2 0648+29B. These temperatures are derived assuming that the heated dust is mainly radiating by the FIR traced by the IRAS fluxes at 60 and $100 \mu m$. Nevertheless we cannot discard a contribution of warmer and colder dust components traced by other wavelength different than than the ones measured than IRAS (see chapter 8).

6.3 Dust properties from SPITZER data

In this section we will present the galaxies in TANGO with respect to Spitzer observations.

A total of 40% (21/52) of the galaxies in TANGO have shown detections with Spitzer, either with IRAC or MIPS. There are some data in the archive, in which the main object was not centered in the beam. In fact, in some cases, the galaxy was actually at edge of the beam, implying that some of the flux emission could be lost. An example of this situation is the galaxy 3CR 88.1,

Figure 6.3: MIPS image of the radio galaxy 3CR 31 at $70\ \mu\text{m}$

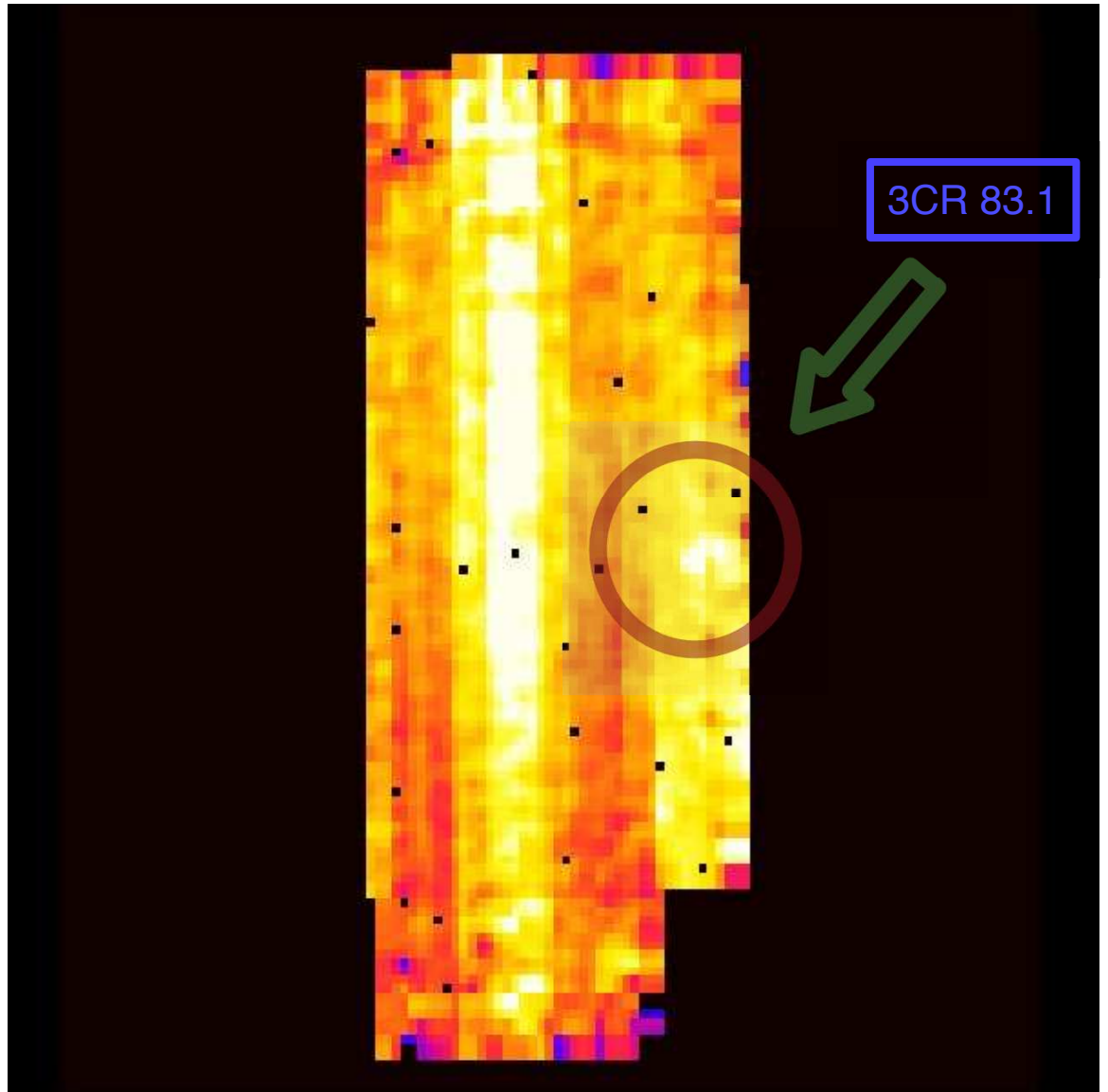


Fig. 6.3, where we can see that the galaxy is on the edge of the SPITZER image and therefore we are not sure to obtain all the emission. Cases like this one were not taken into account for this work.

6.3.1 IRAC

From IRAC (see § 4.7 for the description of the data reduction) we had a total of 20 galaxies with data for the near-IR (NIR) band observed at $3.6 \mu\text{m}$, $4.5 \mu\text{m}$, $5.8 \mu\text{m}$ and $8.0 \mu\text{m}$.

If we look at table 6.3 we see that 3CR 272.1 is the galaxy with the strongest emission at $3\mu\text{m}$, and 3CR 88 together with 3CR 321 are the weakest.

Table 6.3: Data from Spitzer-IRAC for the TANGO Galaxies.

Source	Flux mJy			
	$3.6 \mu\text{m}$	$4.5 \mu\text{m}$	$5.8 \mu\text{m}$	$8.0 \mu\text{m}$
3CR 31	35.00 ± 0.35	30.62 ± 0.31	18.82 ± 1.88	12.93 ± 0.13
3CR 66B	26.31 ± 2.60	15.67 ± 1.57	5.11 ± 0.51	3.17 ± 0.32
3CR 83.1	49.62 ± 4.96	30.39 ± 3.04	21.94 ± 2.20	9.98 ± 1.00
3CR 88	3.04 ± 0.30	2.11 ± 0.21	1.91 ± 0.19	2.53 ± 0.25
3CR 98	11 ± 1.10	7.32 ± 0.73	7.19 ± 0.72	10.94 ± 1.09
3CR 236	14.89 ± 1.49	12.42 ± 1.24	14.46 ± 1.45	19.77 ± 1.98
3CR 264	26.48 ± 2.65	16.58 ± 1.66	14.40 ± 1.44	11.25 ± 1.13
3CR 270	110.57 ± 1.11	63.14 ± 6.31	49.26 ± 4.93	25.29 ± 2.53
3CR 272.1	225.09 ± 22.51	127.44 ± 12.7	95.99 ± 9.60	42.51 ± 4.25
3CR 296	40.99 ± 4.10	16.68 ± 1.67	12.12 ± 1.21	5.91 ± 0.59
3CR 305	14.78 ± 1.48	10.41 ± 1.04	8.35 ± 0.83	13.37 ± 1.34
3CR 321	3.93 ± 0.39	6.64 ± 0.66	11.69 ± 1.17	23.05 ± 2.31
3CR 386	22.95 ± 2.30	13.78 ± 1.38	9.92 ± 0.99	6.59 ± 0.66
3CR 442	10.70 ± 1.07	6.36 ± 0.63	3.47 ± 0.35	2.47 ± 0.25
3CR 449	24.71 ± 2.47	14.49 ± 1.45	12.10 ± 1.21	9.48 ± 0.95
3CR 465	26.80 ± 2.68	15.94 ± 1.60	7.65 ± 0.77	5.44 ± 0.54
NGC 315	60.71 ± 6.07	35.77 ± 3.58	30.14 ± 3.01	26.19 ± 2.62
NGC 4278	155.30 ± 15.53	90.12 ± 9.01	70.43 ± 7.04	54.36 ± 5.44
NGC 6251	38.13 ± 3.81	24.90 ± 2.49	20.89 ± 2.09	19.80 ± 1.98
UGC 7115	33.15 ± 3.32	19.17 ± 1.92	14.07 ± 1.41	9.96 ± 1.00

6.3.2 MIPS

For 18 of our 52 galaxies we have data from Spitzer-MIPS. 17 of them were detected at $24 \mu\text{m}$ (33%), 12 at $70 \mu\text{m}$ (23%) and only 10 of them were detected at $160 \mu\text{m}$ (19%). See table 6.4 for the fluxes and errors.

Note that the strongest galaxy at $24 \mu\text{m}$ is 3CR 321, one of the weakest galaxies at $3\mu\text{m}$.

Table 6.4: Data from Spitzer-MIPS for the TANGO Galaxies.

Source	Flux mJy		
	24 μm	70 μm	160 μm
3CR 31	20.63 \pm 2.06	427.82 \pm 85.56	4650.79 \pm 930.16
3CR 66B	7.33 \pm 0.73	—	—
3CR 83.1	4.01 \pm 0.40	—	—
3CR 236	17.58 \pm 1.76	—	—
3CR 264	15.92 \pm 1.59	140 \pm 28	—
3CR 270	37.01 \pm 3.7	229.98 \pm 46.00	260.25 \pm 52.05
3CR 272.1	25.53 \pm 2.56	782.04 \pm 156.41	642.08 \pm 128.416
3CR 274	62.76 \pm 6.28	546 \pm 109.2	463.29 \pm 92.66
3CR 296	6.83 \pm 0.68	39.62 \pm 7.92	—
3CR 305	44.55 \pm 4.46	1045.81 \pm 209.16	576.33 \pm 115.27
3CR 321	277.05 \pm 27.71	—	642.37 \pm 128.47
3CR 327	247.95 \pm 24.80	566.04 \pm 113.208	270.22 \pm 54.04
3CR 386	—	44.95 \pm 8.99	—
3CR 449	7.62 \pm 0.76	196.39 \pm 39.28	399.25 \pm 75.85
3CR 645	9.6 \pm 0.96	—	—
NGC 315	92.07 \pm 9.21	—	513.25 \pm 102.65
NGC 4278	20.93 \pm 2.09	735.25 \pm 4.19	194.34 \pm 38.87
NGC 6251	40.15 \pm 4.02	188.00 \pm 37.6	—

6.4 Multi Dust Component Fitting

As already mentioned in the Introduction, the main purpose of collecting these data, was to add flux densities to our SED which we used to fit different dust components to get the mass and the temperature of the cold, warm and hot dust components.

For such purpose we wrote a computer program that fits the modified black body emissivity as indicated previously on equation 6.1, where it looks for 6 parameters; 3 dust temperatures (T_1 , T_2 and T_3) and their 3 respective dust masses (M_1 , M_2 and M_3) fitting the data by minimizing the χ^2 . When the computation is excessively time consuming, the program fits the 2 lowest temperatures and masses between 5 and 200 K in step of 200. It finds the minimum value of χ^2 and fits this value again with a third component finding a new minimum with a new χ^2 . The program then returns the values for 3 temperatures and 3 masses which are finally plotted along the rest of the fluxes. For the fit we used the same weight for the data without taking into account the errors. It is done in such a way to minimize the large differences in precision between the different sets of data which would give an "artificial" larger importance to one of the observed band.

In some cases we deliberately ignored some of the data. It will be indicated hereafter in which cases the data were flagged. We have observed with the IRAM 30m to collect data for mm wavelength, and when calculating the dust parameters we used the redshift frequencies for the continuum.

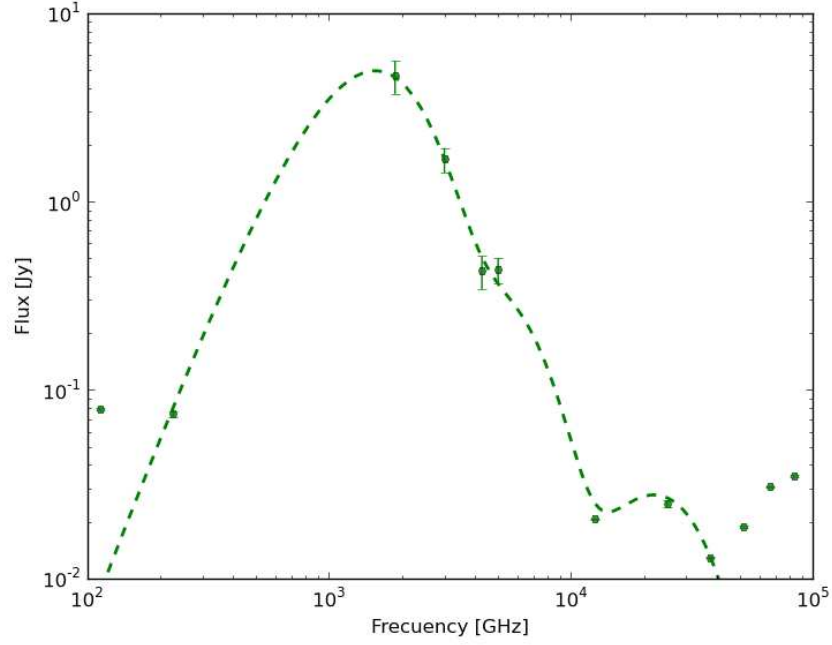
On Fig 6.4 we show the result for 3CR 31, represented in logarithmic values for the flux densities in Jy and the Frequencies in GHz. We used a total of 12 data points in order to fit the dust components in this galaxy. We discarded the 3mm points since we found that the synchrotron emission is dominating (see section 11.6). We removed the synchrotron emission of 54 mJy to the 1mm data to get only the thermal contribution. As can also be seen on the plot, we discarded all the Spitzer fluxes below $14 \mu\text{m}$ since it seems that the spectra is not typical of dust emission. In fact, [Armus et al. \(2007\)](#) noted the presence of absorption from amorphous silicates centered at 9.7 and $18 \mu\text{m}$ which dominates the spectra in nearly all of their galaxies, and that will not allow the modified black body component to fit properly at those frequencies. According to [Cleary et al. \(2007\)](#), the thermal contribution in radio galaxies is $>80\%$, in quasars the thermal contribution is in the range of 10% - 100% . According to their analysis all the quasars in their sample were estimated to have a nonthermal contribution $>20\%$.

We will calculate the different dust components masses and temperatures for the rest of the galaxies in the sample in a future work, since we have already collected all the data that will allow us to do such calculations. In the mean time, we have calculated the dust components for the galaxy for which we have collected the maximum amount of data possible. This galaxy is 3CR 31, and from fitting 3 dust components from the higher frequency part of the spectrum, as seen on figure 6.4, for the masses and temperatures, we can tell that the dust components have temperatures between 19.7K , 71.7K and 495.05K and the dust masses have components of $3.16 \times 10^7 M_{\odot}$, $3.98 \times 10^5 M_{\odot}$ and $1.31 M_{\odot}$ (see table 6.5).

6.5 Conclusion

- We have IRAS data for 35% of the galaxies in TANGO.
- We have calculated a $f_{100 \mu\text{m}}$ -to- $f_{60 \mu\text{m}}$ ratio of 1.9, which according to [Bell \(2003\)](#) which could be interpreted as a galaxy with high temperature heated up by young stars in HII regions or by an AGN.
- Taking into account the flux densities only from IRAS, We have an average dust temperature of 35.8K and a dust mass of $2.5 \times 10^5 M_{\odot}$.
- The M_{H_2}/M_{dus} gas-to-dust mass ratio is about 260.
- We have Spitzer's flux emissions of 40% of the galaxies in TANGO.

Figure 6.4: Fitting of the SED in 3C 31 using 3 dust components (temperature, mass)



	T K	M $\times 10^5 M_{\odot}$
1.	19.5	316.228
2.	71.7	3.98107
3.	495.05	0.000131826

Table 6.5: Fitted Temperatures and Masses for 3 dust components.

- We calculated 3 dust component for the mass and temperature of 3CR 31. $T_1=19.7\text{K}$ and $M_1=3.16 \times 10^7 M_{\odot}$; $T_2=71.7\text{K}$ and $M_2=3.98 \times 10^5 M_{\odot}$; $T_3=495.05\text{K}$ and $M_3=1.31 M_{\odot}$.

Chapter 7

Neutral Hydrogen - HI

7.1 Introduction

Neutral Hydrogen (HI) is a tracer of the dynamical evolution of elliptical galaxies. It falls very well into the radio frequencies (1.4 GHz or 21 cm in wavelengths) and it is a galaxy interaction tracer giving information about the dynamics and evolution of a system of galaxies. This is due to the fact that HI extent is normally larger than any other component of the ISM and that the collisional property of the HI makes it very sensitive to gravitational perturbations. According to [Emonts et al. \(2007\)](#), there has been various propositions on the origin of HI in elliptical radio galaxies:

1. The HI would be accreted from a reservoir of cold gas around the host galaxy.
2. Radio sources can self regulate the balance between cooling and heating of hot gas surrounding these systems.
3. HI would be provided during mergers between spiral galaxies or cooling through dry mergers.

HI is extended within the galaxy and it is dynamically cold, which makes it very sensitive to dynamical perturbations. [Morganti et al. \(2006\)](#) argues that galaxies with relatively young stellar population are found among those with a low HI mass fraction and the galaxies with high HI mass fraction tend to have an old stellar component. On the other hand, even when the large reservoir is found, the gas is spread over a large area, and it is, therefore, very diluted. It is not able to reach, at least on large scales, a column density high enough for star formation to occur. This means that many systems acquire gas but only some of this gas manages to form stars and becomes consumed while in the other systems this is not the case. Hence, [Morganti et al. \(2006\)](#) found no correlation between the presence/morphology of the HI and stellar population.

The neutral hydrogen content in elliptical galaxies is found to be low compared to its content in spiral galaxies of similar optical magnitude. So far, most of the surveys have been done in FIR-selected elliptical galaxies leading to a bias towards dust rich galaxies. [Huchtmeier \(1994\)](#) and [Huchtmeier et al. \(1995\)](#) found indications that the gravitational interactions and mergers may be an important source of interstellar material for elliptical galaxies. In the case of their sample, the galaxies were selected both with and without previous IRAS data and the vast majority of the elliptical galaxies observed are found to be relatively HI-poor.

On the other hand, more recent studies argue that, at least on a volume limited sample of $z \sim 0$ elliptical galaxies have $\geq 25\%$ of their galaxies containing HI at the level of $M_{\text{HI}} > 10^8 M_{\odot}$, and that M_{HI} is of the order of a few percent of the total stellar mass ([Serra & Oosterloo 2010](#)).

As explained in chapter 1.3, the ISM is playing a key role in the formation and evolution of the AGN in radio galaxies and HI gas gives information about the distribution of the ISM in the host galaxies. HI can be traced in large scales (in emission), as well as in the central region of the galaxy (in absorption against the radio continuum), where it may serve as fuel for the AGN ([Emonts et al. 2007](#)) and star formation.

While [Serra & Oosterloo \(2010\)](#) found that optically disturbed ellipticals are systematically younger than relaxed objects, which was interpreted as an evidence of their continuing, gas-rich assembly, not all ellipticals with HI are young (e.g., NGC 4278 in [Morganti et al. 2006](#)). Clearly, the dynamics of the accretion plays a very important role in determining the effect of gas on structure and (distribution of) stellar population of the accreting galaxy. Understanding where the young stars and cold gas are, and what their kinematics is, is as important as estimating their mass.

Even though in early-type galaxies the HI masses are known to be proportionally lower than in spirals, some early-type galaxies have a M_{HI} similar to spirals suggesting that the HI gas in this kind of galaxies may have an external origin ([van Driel & van Woerden 1991](#)).

7.2 TANGO Data

7.2.1 Effelsberg Observations

In section 3.3 we already gave a brief description of the 100m Telescope located in Bonn, Germany and from where we obtained data for the 21cm line. From the total of 52 galaxies in the LzS for the galaxies in TANGO, we observed 20 of them, detecting only 2 galaxies, 3CR 264 and 3CR 270, and possibly detecting two more, NGC 7052 and 3CR 83.1.

The TANGO galaxies observed with Effelsberg were 3CR 66B, 3CR 40, 3CR 83.1, 3CR 264, 3CR 270, 3CR 274, 3CR 305, 3CR 386, 3CR 402, 3CR 433, 3CR

442, 3CR 465, NGC 708, NGC 2892, NGC 3801, NGC 5490, NGC 6251, NGC 7052, B2 0116+31 and B2 1553+24. For the completed galaxies, the spectra can be seen in appendix [A](#), and the observations details are in table [7.1](#).

Galaxy Name	Frequency GHz	Conversion Factor	Time min.	D_{Vel} km/s	Vel. Width km/s	Area K km/s	Area Jy km/s
NGC 7052	1.378	1.31	146.1	68.02	553.48	2.40 ± 0.006	1.2 ± 0.004
3CR 305	1.375	1.31	94.83	10.32	300	9.01 ± 0.6	4.5 ± 0.3
B2 0116+31	1.316	1.60	37.57	17.78	300	2.58 ± 0.82	1.3 ± 0.4
B2 1553+24	1.339	1.36	23.48	17.47	300	18.84 ± 0.11	9.4 ± 0.06
3CR 264	1.369	1.26	58.98	34.18	277.4	1.26 ± 0.012	0.8 ± 0.005
3CR 270	1.389	1.31	112.4	16.85	300	32.1 ± 0.16	16.0 ± 0.08
3CR 274	1.395	1.31	30.47	16.78	300	81.67 ± 1.34	40.83 ± 0.87
3CR 386	1.376	1.31	56.25	17.01	300	10.6 ± 0.077	5.3 ± 0.04
3CR 40	1.374	1.31	56.31	17.03	300	8.69 ± 0.09	4.34 ± 0.05
3CR 402	1.365	1.31	56.31	17.15	300	1.62 ± 0.027	0.81 ± 0.013
3CR 433	1.339	1.36	37.46	17.47	300	8.52 ± 0.49	4.26 ± 0.24
3CR 442	1.363	1.31	37.46	34.34	300	2.1 ± 0.07	1.03 ± 0.03
3CR 465	1.357	1.31	56.31	17.24	300	28.5 ± 0.11	14.2 ± 0.06
3CR 66B	1.371	1.31	56.25	34.13	300	19.65 ± 0.1	9.8 ± 0.05
3CR 83.1	1.364	1.31	37.46	34.30	300	22.28 ± 0.09	11.14 ± 0.04
NGC 2892	1.368	1.31	93.88	17.11	300	0.18 ± 0.02	0.09 ± 0.01
NGC 3801	1.383	1.31	225	8.468	300	0.34 ± 0.02	0.17 ± 0.01
NGC 5490	1.377	1.31	56.31	17	300	2.42 ± 0.02	1.2 ± 0.01
NGC 6251	1.365	1.29	37.52	37.29	304	5.37 ± 0.03	2.68 ± 0.01
NGC 708	1.376	1.31	159.5	17.02	300	0.34 ± 0.02	0.17 ± 0.01

Table 7.1: Data from the HI observations with Effelsberg-100m Telescope.

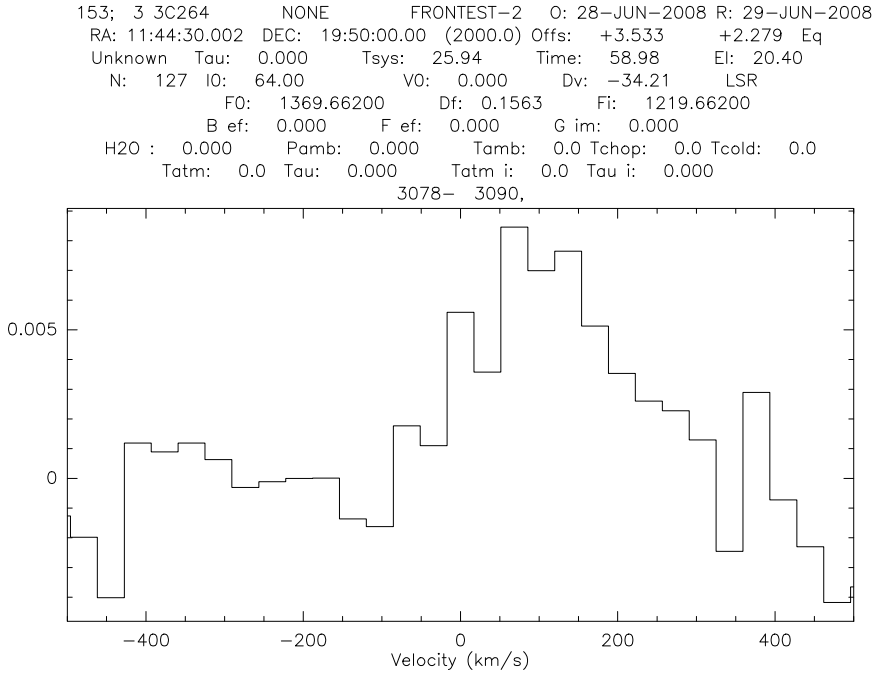


Figure 7.1: HI emission for 3CR 264

7.2.2 Neutral Hydrogen Mass

We computed the HI mass as following,

$$M_{HI} = 2.36 \times 10^5 D_{[Mpc]}^2 I_{21cm} [Jykm/s] \quad (7.1)$$

where D is the distance in Mpc, and I_{21cm} is the integrated intensity of the line at 21 cm, which is equivalent in frequency at 1.4 GHz.

The only two galaxy for which we had a clear detection, as mentioned in the previous section, are 3CR 264 and 3CR 270, (see Figure 7.2.1 and 7.2.1 for their spectra) for which we calculated an HI mass of $15.5 \pm 0.01 \times 10^8 M_{\odot}$ and $34 \pm 0.17 \times 10^8 M_{\odot}$ respectively.

7.3 Discussion and future work

An interesting result from [Emonts \(2006\)](#) is that, in contrast with several compact radio sources, the extended FR-I sources in their sample do not contain large-scale HI. [Heckman et al. \(1986\)](#) and [Baum et al. \(1992\)](#) argue that merger features are much more common around FR-II galaxies than around the less powerful lobe dominated FR-I sources and radio-quiet ellipticals, proposing that different types of radio galaxies might have a different formation history.

49: 3 3CR270 NONE FRONTTEST-2 O: 07-JUN-2008 R: 12-JUL-2008
 RA: 12:19:23.200 DEC: 05:49:31.00 (2000.0) Offs: -2.002 -0.578 Eq
 Unknown Tau: 0.000 Tsys: 32.23 Time: 112.5 El: 43.50
 N: 127 I0: 64.01 V0: 0.000 Dv: -33.72 LSR
 F0: 1389.54200 Df: 0.1563 Fi: 1239.54200

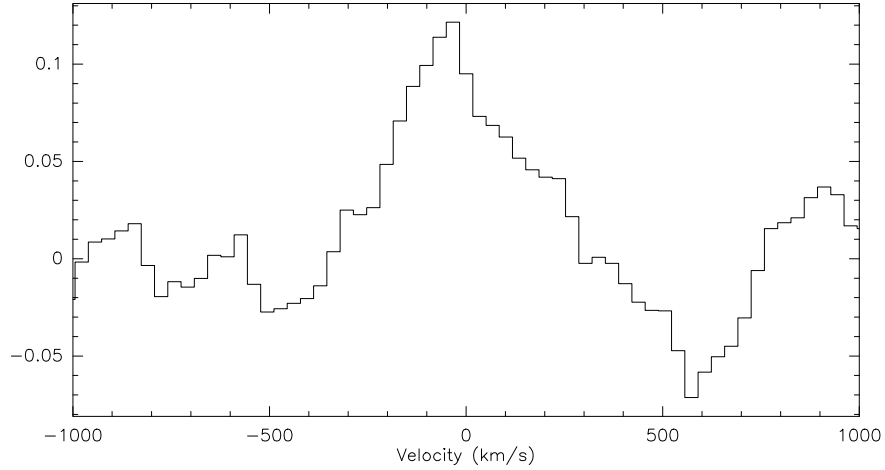


Figure 7.2: HI emission for 3CR 270

Table 7.2: M_{HI} emission collected for our galaxies.

Galaxy	M_{HI} emission $\times 10^8 M_{\odot}$	Reference
3CR 31	<0.71	Emonts (2006)
3CR 264	15.6	This Work
3CR 270	34	This work
3CR 449	<1.3	Emonts (2006)
NGC 315	0.68	Morganti et al. (2009)
NGC 4278	6.9	Morganti et al. (2006)
NGC 5127	<0.84	Emonts (2006)
NGC 5141	0.69	Emonts et al. (2007)
NGC 7052	0.30	Emonts (2006)
B2 0034+25	<3.4	Emonts (2006)
B2 0648+27	85	Emonts et al. (2006)
B2 0924+30	<2.8	Emonts (2006)
B2 1447+27	<3.9	Emonts (2006)

Table 7.3: Continuum Measurements at 1.4 GHz from [Emonts \(2006\)](#)

Galaxy	Peak Flux mJy/beam	Core Flux mJy/neam	Total Flux mJy
3CR 31	263.7	205.5	5083
3CR 449	170.3	68.4	3279
NGC 5127	26.2	24.6	957
NGC 7052	87.9	87.9	303
B2 0034+25	15.5	15.5	91
B2 0648+27	155.2	155.2	155
B2 0924+30	4.8	-	121
B2 1447+27	69.0	69.0	69

In contrast to the powerful FR-II sources, [Heckman et al. \(1986\)](#) propose that the less powerful FR-I sources might be powered by processes involving the stored rotation energy of the black-hole or the accretion of the intra-cluster or circum-galactic medium.

Among all the sources observed, we only observed one FR-II source, 3CR 402, but this source was not detected and the only two clearly detected sources, 3CR 264 and 3CR 270, were FR-I radio galaxies.

Computing the continuum flux at 1.4 GHz gives valuable information at the time of analyzing the synchrotron emission. We will see in chapter 8 that in order to calculate the synchrotron age of a galaxy we need the lowest frequencies in the spectral energy diagram (SED), and the frequencies lower than about 200 GHz are a fingerprint of the synchrotron behavior. The fluxes at millimeter/submm wavelengths are dominated by the dust emission and/or the synchrotron, therefore the fluxes densities at centimetric wavelengths are critical to this point. We found on the literature measurements of continuum emission at 1.4 GHz, they are listed on table 7.3. We plan to build SED for all the galaxies in the sample, to calculate the dust components (see chapter 6) and to calculate their synchrotron ages (see chapter 8).

Chapter 8

From Thermal to Synchrotron emission

8.1 Introduction

In this chapter we describe all the data we collected to build our spectral energy distribution (SED). We first describe the wavelength ranges for which we have data collected to meet our purposes. Then we describe the synchrotron emission and the way to calculate the synchrotron age of a source.

8.2 μm Data

The shorter wavelengths, or higher frequencies, from our analysis are in the range of the dust measurements, where most of the data in our work have been measured with Spitzer. From [Soifer et al. \(2008\)](#) and references therein, we know that regardless of the resolution, galaxy images at 3.6 and 4.5 μm reveal to first order of low excitation view of the photospheric light. The longer-wavelength images are dominated by interstellar dust emission. Aromatic features contribute or dominate at 5.8 and 8 μm , stochastically heated very small grains are most important at 24 μm , and large grains dominate at 70 and 160 μm ([Desert et al. 1990](#); [Dale et al. 2001](#)). Photometry at 3.6 and 4.5 μm is valuable in a number of applications, from extending the mass-metallicity relation to lower masses ([Lee et al. 2006](#)) to improving the stellar synthesis models of evolving galaxies ([Maraston et al. 2006](#)). The bands at 5.8 and 8 μm contain emission from both stars and dust, and normal practice is to remove the stellar contribution estimated from 3.6 and 4.5 μm to obtain "dust-only" maps. ([Helou et al. 2004](#); [Pahre et al. 2004](#); [Smith et al. 2007](#)).

We collected the μm data from Spitzer; how we reduced the data is explained in section [4.5.1](#) and the flux densities for our measurements are listed in section [6.3](#).

8.3 mm Data

The millimetric continuum data collected for these galaxies and used in the SED, were obtained from our observations at the IRAM-30m telescope where their measurements were taken at 3mm and 1 mm wavelengths. The observations are explained in section 4.2 and the data reduction is explained in section 4.4.

Since both the synchrotron and the thermal emission can extend to the mm range, the flux at these wavelengths is a contribution of both processes. For our particular case of 3CR 31, and for reasons explained in chapter 6 and chapter 11, we believe that the flux density at mm wavelength is more related to synchrotron emission rather than to dust emission.

8.4 cm Data

We have also observed at centimetric wavelengths (21 cm, equivalent to 1.4 GHz), which is the frequency at which HI radiates. The continuum measurements of this range in the spectrum is also crucial because it connects the mm emissions with the lower frequencies. That is of extreme importance if we want to calculate the synchrotron age of the galaxies.

8.5 Synchrotron

In 1947, for the first time in history, Floyd Haber observed radiation emitted by electrons as they moved circularly in the magnetic field of a chamber of an accelerator. This occurred during the adjustment of a cyclic accelerator. The radiation was observed as a bright luminous patch on the background of the chamber of the synchrotron. It was clearly visible in the daylight. In this way, "electronic light" was experimentally seen for the first time as radiation emitted by relativistic electrons having a larger centripetal acceleration. This radiation was called Synchrotron radiation since it was observed for the first time in a synchrotron ([Bordovostsyn 1999](#)).

The Synchrotron emission is detected at low frequencies, large wavelengths, generally lower frequencies than the ones observed with the IRAM 30m telescope, although in some cases the flux emitted by the galaxies and received by the IRAM 30m telescope at frequencies of about 115 GHz or 230 GHz, (see chapter 4.7 for details on the IRAM 30m telescope frequencies observations) might still be due to the synchrotron emission. In order to differentiate from where this flux is coming, we need to understand the dust emission analysis as well, and see if, according to the fit (Black Body fit for the dust, chapter 6, and the Injection model for the Synchrotron, chapter 11.6) the data are better explained by dust and/or synchrotron emission.

8.5.1 How to calculate the Synchrotron age of the galaxies?

The main tool used for modeling a synchrotron aged spectrum was a software developed by [Murgia et al. \(1999\)](#). With the help of this software, called *SynAge*, spectral fits to the spectra have been made with the continuous injection model (CIm - which do not consider expansion effects), which allowed to determined a non-aged spectral index α_{inj} and the break frequency (ν_{break}), that together with the normalization are the free parameters characterizing the model.

To calculate the age of the galaxies from TANGO, we used data from CATS¹ (Database - Astrophysical CATalogs support System) and from the Nasa Extragalactic database (NED)².

Assuming a constant magnetic field and no expansion after the switch-off, the total source age can be calculated from the break frequency, ν_{break} ([Parma et al. 2007](#)):

$$t_s = 1590 \frac{B^{0.5}}{(B^2 + B_{IC}^2)[(1+z)\nu_b]^{0.5}} \quad (8.1)$$

Where the synchrotron age t_s is in Myr, B is the magnetic field in μG , the break frequency, ν_{break} in GHz, while the inverse Compton equivalent field is $B_{IC} = 3.25(1+z)^2 \mu\text{G}$.

We know from [Govoni & Feretti \(2004\)](#) that the equipartition magnetic field is:

$$B_{eq} = \left(\frac{24\pi}{7} U_{min}\right)^{1/2} \times 10^6 \quad (8.2)$$

Where the minimum energy is:

$$U_{min} = \xi(\alpha, \nu_1, \nu_2)(1+k)^{4/7} (\nu_0 \text{ MHz})^{4\alpha/7} (1+z)^{(12+4\alpha)/7} \left(I_0 \left[\frac{\text{mJy}}{\text{arcsec}^2}\right]\right)^{4/7} (d_{[Kpc]})^{-4/7} \quad (8.3)$$

where z is the source redshift, I_0 is the source brightness at the frequency ν_0 , d is the source depth, and the constant $\xi(\alpha, \nu_1, \nu_2)$ is tabulated in Table 1 of [Govoni & Feretti \(2004\)](#) for the frequency ranges: 10 MHz–10 GHz and 10 MHz – 100 GHz. I_0 can be measured directly by the contour levels of a radio image (see chapter 11 for more details.):

$$I_0 = \frac{Flux}{\theta_x \theta_y} \quad (8.4)$$

In order to arrive at this point, there are many assumptions we needed to make. We followed the review of [Miley \(1980\)](#) to understand them. He argues that for a region in a synchrotron radio source delineated by an ellipse of angular diameter θ_x and θ_y in orthogonal directions, we can write the minimum energy density as:

$$u_{me} = (7/3)(B_{me}^2/8\pi) = 0.0928B_{me}^2 \text{ erg/cm}^3 \quad (8.5)$$

¹<http://w0.sao.ru/cats/>

²<http://nedwww.ipac.caltech.edu>

where the corresponding minimum energy magnetic field is

$$B_{me} = 5.69 \times 10^{-5} \left[\frac{1+k}{\eta} (1+z)^{3-\alpha} \frac{1}{\theta_x \theta_y s \sin^{3/2} \phi} \times \frac{F_0}{v_0^\alpha} \frac{v_2^{\alpha+1/2} - v_1^{\alpha+1/2}}{\alpha + 1/2} \right]^{2/7} \text{ Gauss} \quad (8.6)$$

Here k is the ratio of energy in the heavy particles to that in the electrons, η is the filling factor of the emitting regions, z is the redshift, θ_x and θ_y (arcsec) correspond either to the source/component sizes or to the equivalent beam widths, s (kiloparsec) is the path length through the source in the line of sight, ϕ is the angle between the uniform magnetic field and the line of sight, F_0 (Jy or Jy per beam) is the flux density or brightness of the region at frequency ν_0 (GHz), ν_1 and ν_2 (GHz) are the upper and lower cut off frequencies presumed for the radio spectrum, and α is the spectral index [$F(\nu) \propto \nu^\alpha$, $\nu_1 < \nu < \nu_2$].

Apart from the assumption that the radiation is synchrotron emission and that the radio and optical emission are redshifted by the same amount, there are several more mundane uncertainties inherent in these formulas.

First, k is unknown and could have a value between 1 and 2000 (Pacholczyk 1970). Indirect argument has usually led to canonical values of $k+1$ or $k=100$ (eg Moffet 1975). $k=1$ is clearly more consistent with the use of the minimum energy condition. Note that a difference of 100 in the assumed k results in an order-of-magnitude difference in the minimum energy densities derived. Second, to obtain s , the path though the source along the line of sight, one must make some assumptions about the symmetry and distance of the source. Frequently cylindrical symmetry is assumed, with s equal to the width of the source in the plane of the sky. Third, the formulas depend on the form on the source spectrum, but this dependence is weak. For extended sources $\alpha \leq -0.6$ and ν_1 dominates over ν_2 . Usually $\nu_1=0.01$ GHz is assume. Forth, the ϕ term is unknown in individual cases. It arises because the emission measure depends on the perpendicular component of the magnetic field and the visible radiation is beamed from electrons moving towards us. Fifth, and perhaps most concerning, is the strong dependence on the filling factor. It is possible that on a scale much less than an arcsec or a Kpc the radiation is clumpy or filamentary. This would result in much greater local energy densities and less total energy.

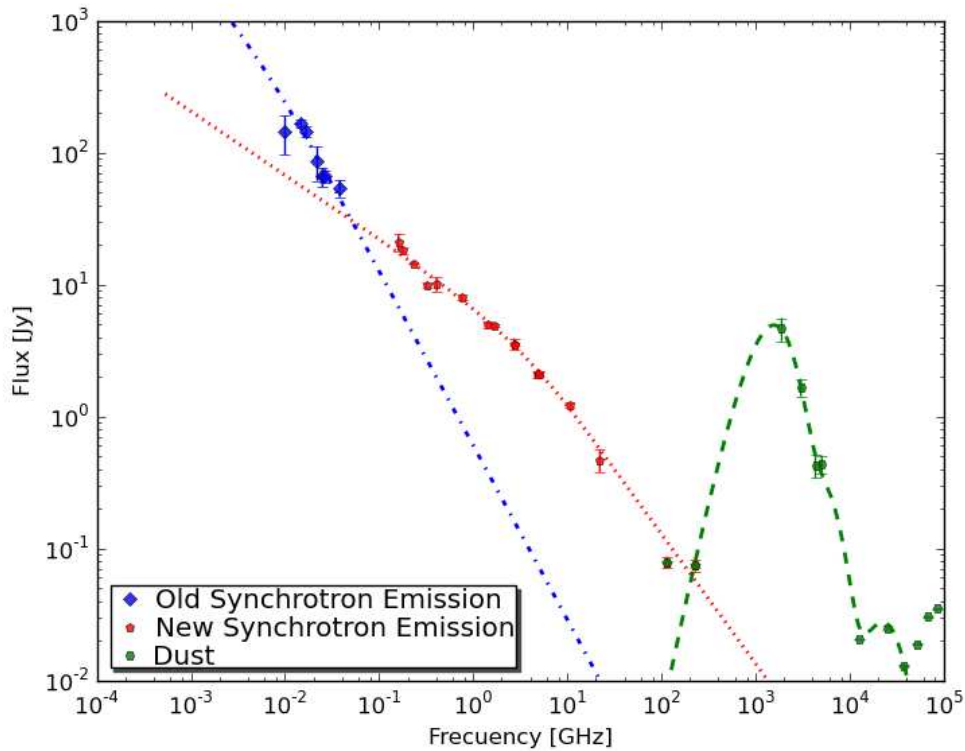
Taking $k=1$, $\eta=1$, $\sin \phi=1$, $\nu_1=0.01$ GHz, $\nu_2=100$ GHz, $\alpha=-0.8$ we obtain approximate expressions for the minimum energy condition,

$$B_{me} \simeq 1.4 \times 10^{-4} (1+z)^{1.1} \nu_0^{0.22} \left[\frac{F_0}{\theta_x \theta_y s} \right]^{2/7} \text{ Gauss} \quad (8.7)$$

$$u_{me} \simeq 1.9 \times 10^{-9} (1+z)^{2.2} \nu_0^{0.44} \left[\frac{F_0}{\theta_x \theta_y s} \right]^{4/7} \text{ erg/cm}^3 \quad (8.8)$$

In order to calculate the age of the galaxy we also need to take into account the magnetic field of the cosmic microwave background, which, according to

Figure 8.1: The Spectral Energy diagram for 3CR31



Murgia et al. (1999) is:

$$B_{CMB} = 3.25(1+z)^2 \mu\text{G} \quad (8.9)$$

8.6 Discussion

After collecting all the data, we were able to plot them all together as can be seen in figure 8.1. Please go to chapter 11 for more detailed explanations on this topic. Assuming CASE 2 from section 11.6.3, the blue diamonds are from the old synchrotron, the red pentagons are from the new synchrotron and the green hexagons are the millimetric/dust part of the spectrum.

Chapter 9

CO vs. FIR Luminosities

9.1 L_{CO}

We calculated the CO(1-0) line luminosity, L'_{CO} , which is expressed as velocity-integrated source brightness temperature, $T_b \Delta V$, multiplied by source area $\Omega_s D_A^2$, and which for our sample resulted in a mean value of $4.2 \times 10^7 \text{ K kms}^{-1} \text{ pc}^2$. This value was calculated using ASURV for the upper limits. The CO(1-0) luminosity mean value is $6.4 \times 10^7 \text{ K kms}^{-1} \text{ pc}^2$ calculated only with the detected values of the CO(1-0) emission lines. The formula used for the calculation is taken from [Solomon et al. \(1997\)](#):

$$L'_{CO} = 23.5 \times \Omega_{s*b}^2 D_L^2 I_{CO} (1+z)^{-3} \quad (9.1)$$

Where Ω_{s*b} is the solid angle of the CO(1-0) emission for the source convolved with the telescope beam, D_L the distance in Mpc, I_{CO} is the integrated velocity in K km/s (in T_{MB}) and z the redshift of the galaxy. If the source is smaller than the beam, which is the case for all the galaxies in this sample, we can assume that $\Omega_{s*b} \approx \Omega_b$ which is given in arcsec². The constant value of 23.5 is the conversion factor from arcsec² Mpc² Kkm/s to $\text{K kms}^{-1} \text{ pc}^2$ which is how the luminosity is represented.

9.2 L_{FIR}

L_{FIR} is the far-IR luminosity using the fluxes at 60 μm , associated with warm component, and 100 μm . associated with cooler components. It was computed using the following relation from [Sanders & Mirabel \(1996\)](#):

$$L_{FIR} = \left[1 + \frac{f_{100}}{2.58 f_{60}} \right] L_{60} \quad (9.2)$$

Where f_{60} and f_{100} are the fluxes at 60 and 100 μm respectively and are in units of Jy; L_{60} is the luminosity at 60 μm in L_\odot and it is represented as:

$$\text{Log}(L_{60}) = 6.014 + 2\text{Log}(D) + \text{Log}(f_{60}) \quad (9.3)$$

Where D is the distance of the galaxy in Mpc.

The results can be seen in Table 9.1 for which the median of the $L_{FIR} = 6.9 \times 10^9 L_{\odot}$. This value was calculated using ASURV to take into account the upper limits.

Galaxy	$Log(L'_{CO})$ $K km s^{-1} pc^2$	$Log(L_{FIR})$ L_{\odot}
3CR 31	8.51	9.77
3CR 40	<7.86	<9.30
3CR 66B	7.23	<9.32
3CR 83.1	7.78	<9.50
3CR 88	7.62	9.94
3CR 98	<8.12	<9.54
3CR 129	7.38	...
3CR 264	7.81	<9.46
3CR 270	<7.13	< 8.51
3CR 272.1	5.77	8.23
3CR 274	7.01	8.25
3CR 296	<7.99	< 9.53
3CR 305	8.60	10.21
3CR 321	9.12	11.43
3CR 236	<9.10	< 10.28
3CR 327	8.69	11.24
3CR 353	7.80	...
3CR 386	7.52	< 8.75
3CR 402	<8.07	9.90
3CR 403	8.43	<10.62
3CR 433	<9.17	< 11.20
3CR 442	7.08	...
3CR 449	7.84	<9.34
3CR 465	<8.14	< 9.66
NGC 315	7.20	9.51
NGC 326	7.98	< 9.88
NGC 541	7.64	<8.79
NGC 708	8.01	9.38
NGC 2484	< 8.54	...
NGC 2892	<8.10	...
NGC 3801	8.03	<9.60
NGC 4278	6.00	8.08
NGC 5127	7.14	< 8.45
NGC 5141	< 7.97	<8.72
NGC 5490	< 8.00	<8.74
NGC 6251	< 8.09	9.69
NGC 7052	7.58	9.65

B2 0034+25	<8.27	...
B2 0116+31	9.06	10.39
B2 0648+27	8.37	11.03
B2 0836+29B	8.96	10.76
B2 0915+32B	<9.10	< 9.93
B2 0924+30	7.59	...
B2 1101+38	< 8.37	9.75
B2 1347+28	8.50	...
B3 1357+28	< 8.90	...
B3 1447+27	< 8.16	...
B3 1512+30	< 9.23	...
B3 1525+29	< 9.06	...
B3 1553+24	< 8.72	...
UGC 7115	< 8.19	...
OQ 208	9.41	11.12

Table 9.1: Values of CO(1-0) Luminosities and FIR Luminosities

9.3 Relationship between L_{CO} and L_{FIR}

The ratio of L_{FIR}/L'_{CO} is normally related in spiral galaxies to the star formation efficiency (SFE). This assumes that most of the FIR emission is coming from dust heated by young stars. In the case of powerful AGN, there is always the possibility of an added FIR contribution from dust heated by the AGN in a dusty torus. However, this contribution is rarely dominant (see eg. [Genzel & Cesarsky 2000](#)). Figure 9.1 is a plot of the galaxies in our sample that represents the L_{FIR} vs L'_{CO} relation. The detected galaxies in both FIR luminosities and CO luminosities are plotted with their error bars; the galaxies with upper limits are represented with arrows (eg, down arrows are for when the CO luminosities are upper limits and FIR luminosities are detections, right arrows are for when the CO luminosities are detected and FIR luminosities are upper limits; finally, the diagonal arrows are for the CO and FIR luminosities are both upper limits). In some cases, we had upper and lower limits for the FIR Luminosities. This situation was true when we had upper limits for $f_{100\mu m}$ and detection for the $f_{60\mu m}$, and it was represented on Figure 9.1 with a line marked with circles at the lower and upper limits.

It is evident that the CO luminosities increase linearly with increasing L_{FIR} with a relation such as $\log(L'_{CO}) = 0.8\log(L_{FIR}) + 0.1$ with a χ^2 of 0.024. Finally the relationship itself has a median value for the L_{FIR}/L'_{CO} ratio of about $52 L_{\odot} (K km s^{-1} pc^2)^{-1}$.

We note that the detection rate for both FIR and CO together is independent of the type of radio galaxy. Out of the 15 radio galaxies detected for both FIR and CO, 8 (22%) are FR-I (3CR 31, 3CR 272.1, 3CR 274, 3CR 305, NGC 315,

NGC 708, NGC 7052 and B2 0836+29B), 3 (30%) are FR-II (3CR 88, 3CR 321 and 3CR 327) and 4 (66%) are FR-c (NGC 4278, B2 0116+31, B2 0648+27 and OQ 208).

We note as well that from the 15 galaxies detected for both FIR and CO, only 4 have a double horn profile feature (3CR 31, NGC 7052, B2 0116+31 and OQ 208).

As mentioned, L_{FIR}/L'_{CO} is interpreted as a measure of SFE. Then, the Star formation Rate (SFR) per unit gas mass, according to [Gao & Solomon \(2004b\)](#), is represented as:

$$\dot{M}_{SFR} \approx 2 \times 10^{-10} (L_{FIR}/L_{\odot}) M_{\odot} yr^{-1} \quad (9.4)$$

From this estimation we compute a mean SFR for this sample of about $3.7 \pm 1.5 M_{\odot}/yr$, assuming that all the FIR emission comes from the dust heated by the young formed stars. This is likely an overestimation since it does not take into account the AGN heating of the dust.

Going back to Figure 9.1, we can see that there are two linear fits, one has already been mentioned at the beginning of this section, the other relation, represented with a red dotted line, is the linear fit of our sample with a combination of samples (this samples will be explained on chapter ??) to compare our galaxies with similar galaxies selected with a different criteria.

We noted that the galaxy 3CR 88 has the lowest gas-to-dust mass ratio, 17, a very low value compared to NGC 4278 with a ratio of 600.

9.4 M_{H_2} vs. L_B

If we look at the relation between the optical luminosity (L_B) and the molecular gas mass of the galaxies (M_{H_2}), as shown in Fig. 9.2, we find that there is no correlation, which is interpreted as that the molecular gas mass is independent of the size of the galaxies. The FIR Luminosity (section 9.2), and the molecular gas mass (chapter 5), normalized by the optical luminosity has also no correlation, as can be confirmed on Fig. 9.3.

9.5 SFE vs L_B

We also compared the SFE (L'_{CO}/L_{FIR}) vs. L_B (Blue Luminosity), as shown in figure 9.4 where we found no correlation at all. In the figures the triangles are for the FR-I type galaxies, the squares are for the FR-II and the circles for the FR-c. The sample all together do not show correlations as well as all the sub-samples separately.

As we can see on Figure 9.4, there is no correlation between the SFR of the galaxies in TANGO with the L_B . This relation has been generally used as an

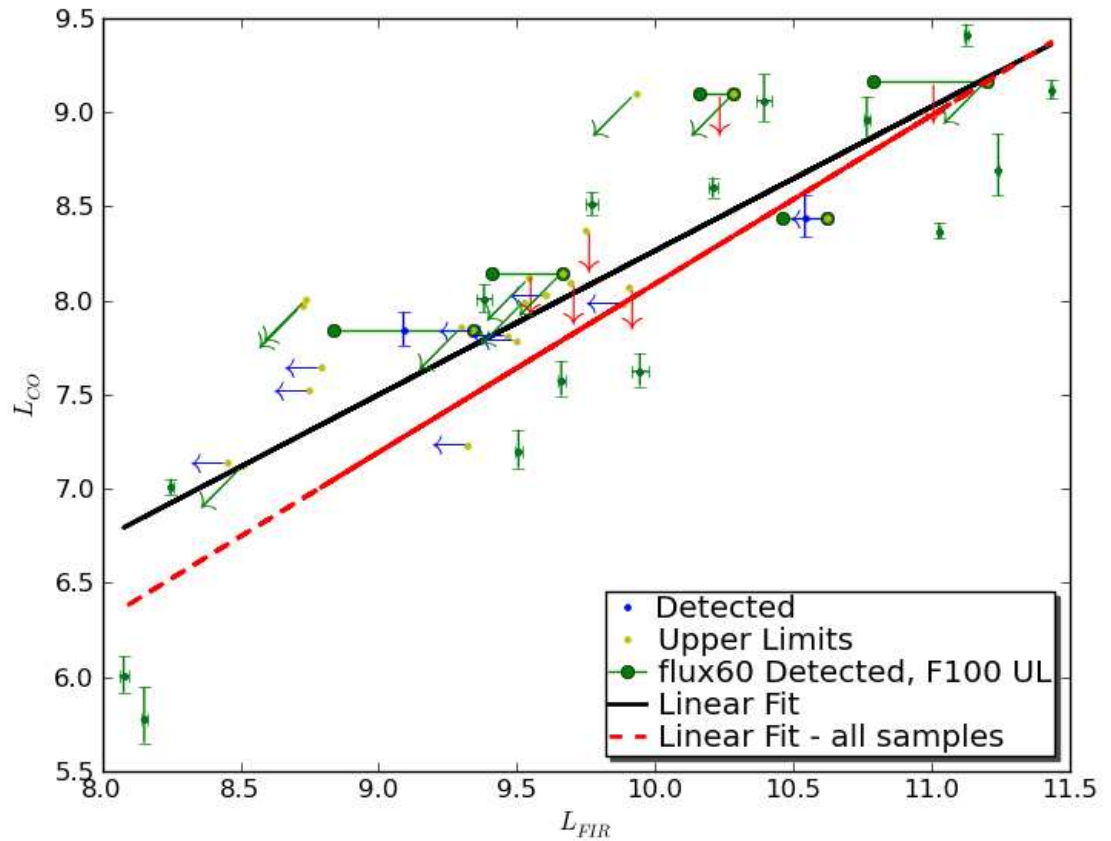


Figure 9.1: L_{FIR} vs. L'_{CO} of the galaxies in this sample. The upper limits are shown, where the L_{CO} upper limits are represented by a down arrow, the L_{FIR} upper limits are represented by a left arrow and the $L_{CO}-L_{FIR}$ upper limits are represented by southwest arrow. It is also possible to appreciate the galaxies in which the flux at $100 \mu\text{m}$ was and upper limit and the flux at $60 \mu\text{m}$ was detected, and in the plot we see the lower and upper limits with a grin line with the extreme, and either the error bar or the arrow indicating the upper limit in CO.

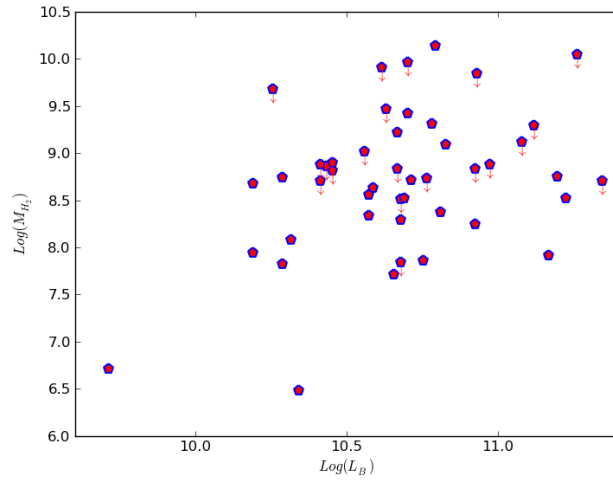


Figure 9.2: Molecular gas mass versus blue luminosity with the upper limits for the molecular gas mass indicated.

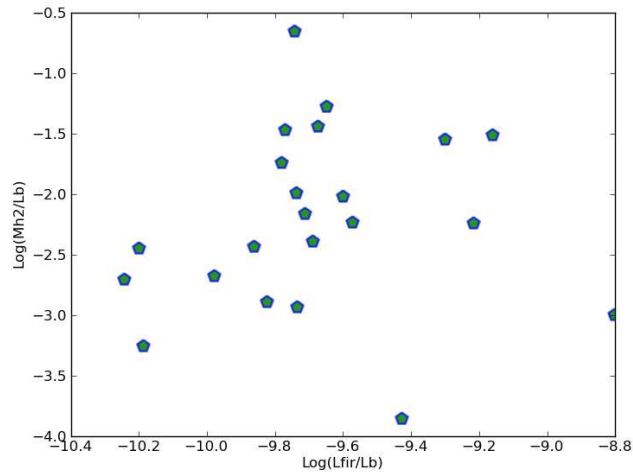


Figure 9.3: Molecular gas mass versus FIR luminosity, both normalized by the blue Luminosity, using only detected values.

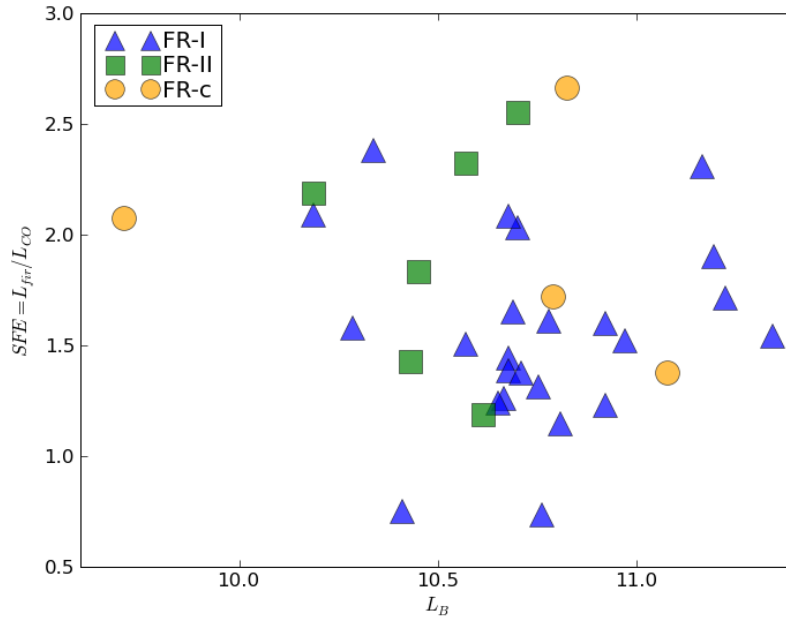


Figure 9.4: Star formation efficiency compared to the blue luminosity of this sample of galaxies.

indicator for current or recent star formation activity; although, according to [Sage & Solomon \(1989\)](#) the blue luminosity is not an accurate star formation indicator. In fact, they argue that the blue light is not an accurate indicator for recent star formation activity because of extinction or blocking by molecular clouds and the wide range of spectral type contributing to the blue luminosity. In conclusion, we should not use this plot against the argument that the galaxies in TANGO might have at least low level of star formation activity.

Chapter 10

Comparison with other samples

10.1 Introduction

We are comparing the properties of our sample with the ones of other samples in order to better understand the behavior of the galaxies in the TANGO project. As we know, different galaxies behave in different ways and this might be due to the history of their evolution (did they go through a minor/major merger?). The interesting situation is that not only do we need different types of galaxies to see how different they might be from one another, also galaxies of the same type might be having a different life. One possible scenario is that this happens because they are in different moments of their life (evolution), or because their destiny has changed (influenced by their environment).

In order to understand this, and to answer questions like:

- Do the galaxies in a sample, selected because of their FIR emission, behave differently than the galaxies in a sample selected only because of their radio continuum?
- Is there any environmental influence on the galaxies?

We compared the galaxies in TANGO with other samples. In section 10.2 we have a detailed description of the comparison samples used in this work; in section 10.3 and 10.4 we compared the molecular gas and dust properties of the samples. In section 10.5 we compared the CO and FIR luminosities of our sample with the comparison samples, and finally, in section 10.6 we make our conclusions on whether TANGO is or not similar to other samples and what does this mean.

10.2 Samples

- [Evans et al. \(2005\)](#) observed a sample of elliptical radio galaxies, like our own, but selected with the IRAS fluxes densities at $60 \mu\text{m}$, $f_{60 \mu\text{m}}$, or $100 \mu\text{m}$, $f_{100 \mu\text{m}}$, greater than 0.3 Jy , since they assumed that this level is a good indicator of a dusty, gas-rich, interstellar medium.
- [Wiklind et al. \(1995\)](#) observed a sample of elliptical galaxies selected on the basis of their morphological type. They argued that there is a major difficulty in defining a sample of elliptical galaxies due to uncertain morphological classification. According to them, the best criterion for defining an elliptical galaxy appears to be de Vaucouleurs $r^{1/4}$ luminosity profile, and based on this, they selected genuine ellipticals, or galaxies that had a consistent classification as *E* in several catalogs. A $100 \mu\text{m}$ flux $\gtrsim 1 \text{ Jy}$ and $\delta > 0^\circ$ were an additional criterion.
- [Mazzarella et al. \(1993\)](#) studied an infrared limited sample with $60 \mu\text{m}$ flux greater than 0.3 Jy . The objects were chosen to fully cover the sky, and to be relatively near ($z < 0.1$), with no other selection criteria.
- [Bertram et al. \(2007\)](#) studied a sample of galaxies hosting low-luminosity quasi-stellar objects (QSOs) where they argued that an abundant supply of gas is necessary to fuel both, an active galactic nucleus and any circumnuclear starburst activity. The only criterion of selection was their small cosmological distance: only objects with a redshift $z < 0.060$ were chosen.
- [Solomon et al. \(1997\)](#) studied a sample of 37 infrared-luminous galaxies in the redshift range $z=0.02-0.27$. Eleven of these galaxies have a $60 \mu\text{m}$ flux $S_{60} > 5.0 \text{ Jy}$, and are part of the near bright galaxy sample ([Sanders et al. 1988, 1991](#)). Twenty galaxies were chosen from a redshift survey ([Strauss et al. 1992](#)) of all IRAS sources with $60 \mu\text{m}$ fluxes $S_{60} > 1.9 \text{ Jy}$. And a few lower luminosity sources were also included in the sample.

10.3 Molecular gas

Comparing our sample with the other samples mentioned above, we noticed that [Wiklind et al. \(1995\)](#) and our sample have an average of the molecular gas mass of a few $10^8 M_\odot$ (using only detected galaxies, not the survival analysis median value) and that both samples are being hosted by elliptical galaxies; [Mazzarella et al. \(1993\)](#), [Evans et al. \(2005\)](#) and [Bertram et al. \(2007\)](#) samples all have a median value of the molecular gas mass about $10^9 M_\odot$, their samples are FIR selected galaxies or galaxies in interaction, therefore with an expected higher molecular gas mass than in the sample hosted by normal elliptical galaxies. They concluded that the majority of luminous, low-redshift QSOs have gas-rich host galaxies. We noticed that from all galaxies in our sample, the QSO, OQ 208, is the galaxy with the highest molecular gas mass

Criteria of selection	Sample Name	Molecular gas mass
Elliptical galaxies	Ocaña Flaquer et al. (2010)	3.7×10^8
	Wiklind et al. (1995)	6.8×10^8
FIR galaxies and QSO's	Evans et al. (2005)	3.7×10^9
	Mazzarella et al. (1993)	1.1×10^9
	Bertram et al. (2007)	3.0×10^9
ULIRGS	Solomon et al. (1997)	1×10^{10}

Table 10.1: Comparison samples and their average molecular gas mass

($1.4 \times 10^{10} M_{\odot}$). Finally, the sample of Solomon et al. (1997) has the highest average of molecular gas mass of $10^{10} M_{\odot}$, with a sample of ULIRGs, where intense star formation is happening. Table 10.1 gives a summary of the average molecular gas masses compared with other samples, and the characteristics of the samples.

Note that when we compared our sample with the others, we used the median value for the molecular gas mass that was calculated using only the detected galaxies for consistency with the other studies where the upper limits were not used for their calculations.

If we compare now with a subsample of galaxies from TANGO itself, that have been detected in both, IRAS (for $60 \mu m$ and $100 \mu m$) and CO(1-0); we have a total of 15 galaxies with a median value of $1.22 \times 10^9 M_{\odot}$. This is an order of magnitude higher than with the median value of the molecular gas mass of the complete sample. It is in complete agreement with the statement that galaxies with higher FIR fluxes have more molecular gas mass than the galaxies dimmer in the FIR emission.

10.3.1 Molecular gas disk

The double-horn CO profile was previously noticed by other authors. We compared the fraction of double horn CO profile in our sample with the fraction in other samples. For instance, Evans et al. (2005) noted a double horn CO emission line profile in many of the spectra. Out of nine detected galaxies, 5 present the double horn profile feature. They studied two cases for which they had interferometric data, finding that in one case this was caused by a CO absorption feature at the systemic velocity of the galaxy (Evans et al. 1999) and in the other case, 3CR 31, the molecular gas is distributed in a molecular gas disk (Okuda et al. 2005). Wiklind et al. (1995) had one case of double horn profile out of 4 galaxies detected. Bertram et al. (2007) found 11 double horn profile feature within their 26 detected galaxies and Mazzarella et al. (1993) has 2 out of 4 galaxies detected with the double horn profile. In Table 10.2 we give the percentage of molecular gas disk traced by the

Sample	Molecular gas disk (%)	Dispersion (%)
Ocaña Flaquer et al. (2010)	27.6%	9.4%
Wiklind et al. (1995)	25%	25%
Mazzarella et al. (1993)	50%	35%
Evans et al. (2005)	55.6%	25%
Bertram et al. (2007)	42.3%	13%

Table 10.2: Percentage of the galaxies, within the detected galaxies of each sample of the double horn CO profile feature

double horn profile for each sample. Like for the molecular gas properties, the closest sample to our radio galaxy sample is the one of [Wiklind et al. \(1995\)](#) composed by genuine elliptical galaxies. Thus it seems that the presence or not of a radio source is independent of the molecular gas properties, at the kpc scale, of the host elliptical galaxy. The FIR-selected samples have higher percentage of molecular gas disk than the sample selected only on the basis of the radio continuum properties. The dispersion value of the percentage of the molecular gas disks in each sample was computed using a Poissonian statistics.

We need to add that we do not discard the possibility of the double horn profile in these galaxies might be due only to the projection effect (i.e. inclination of the galaxy onto the sky plane).

10.4 Dust

We have also compared the dust properties in our sample of radio galaxies, hosted by massive elliptical galaxies, with the sample of elliptical galaxies of [Wiklind et al. \(1995\)](#) (see Fig. 6.1 and 10.1). The dust component in our sample is slightly hotter than in the comparison sample of [Wiklind et al. \(1995\)](#) with a median value of 34 K. The median value of the gas-to-dust mass ratio for [Wiklind et al. \(1995\)](#) is 700, much higher than the median value of the ratio in our sample, which is near 260. [Evans et al. \(2005\)](#) found a gas-to-dust mass ratio even higher with a median value of 860. The sample of low luminosity QSOs (from [Bertram et al. 2007](#)) has a lower ratio of 452, and [Mazzarella et al. \(1993\)](#) with their sample of radio galaxies detected by IRAS has a higher gas-to-dust mass ratio of 506.

10.5 CO-FIR Luminosity

The sample of [Solomon et al. \(1997\)](#), composed of ULIRGs, is the sample with the highest L_{FIR}/L'_{CO} of $146 L_{\odot}(Kkm/spc^2)^{-1}$ meaning, according to [Solomon & Sage \(1988\)](#), that this group of galaxies is strongly interacting/merging

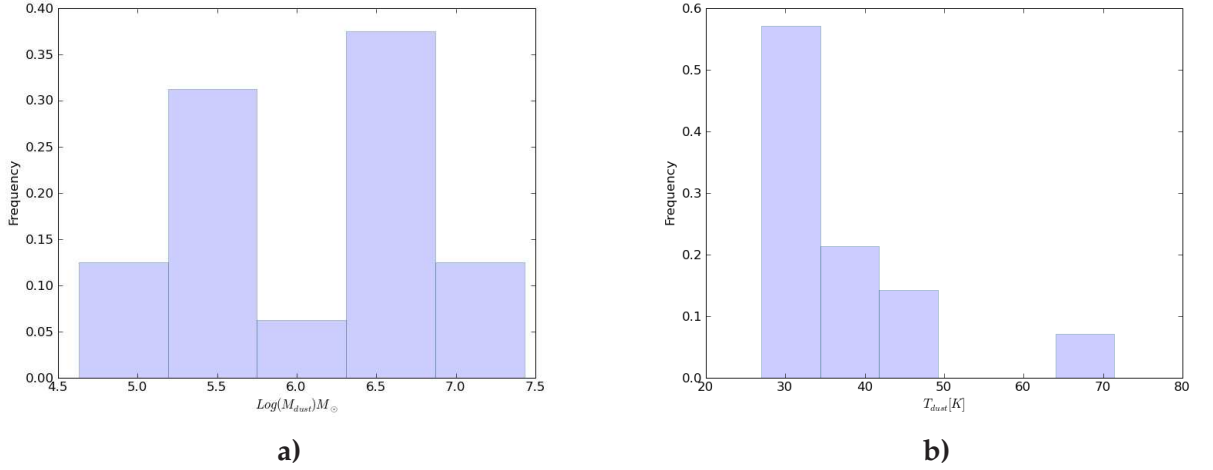


Figure 10.1: Histograms of the dust mass and the dust temperature of the sample of Wiklind et al. (1995). Fig. a) is the distribution of the logarithmic mass and Fig. b) is the distribution of the temperature.

Table 10.3: FIR-to-CO Luminosities and their ratios.

Sample name	L_{FIR} L_{\odot}	L'_{CO} Kkm/spc^2	$L_{\text{FIR}}/L'_{\text{CO}}$ ratio. $L_{\odot}(\text{Kkm}/\text{spc}^2)^{-1}$
Ocaña Flaquer et al. (2010)	8.9×10^9	4.2×10^7	52.0
Wiklind et al. (1995)	6.5×10^9	1.6×10^8	39.4
Mazzarella et al. (1993)	1.94×10^{11}	1.1×10^9	82.2
Evans et al. (2005)	3.6×10^{10}	1.2×10^9	35.4
Bertram et al. (2007)	4.2×10^{10}	9.2×10^8	49.1
Solomon et al. (1997)	1.2×10^{12}	7.9×10^9	146.8

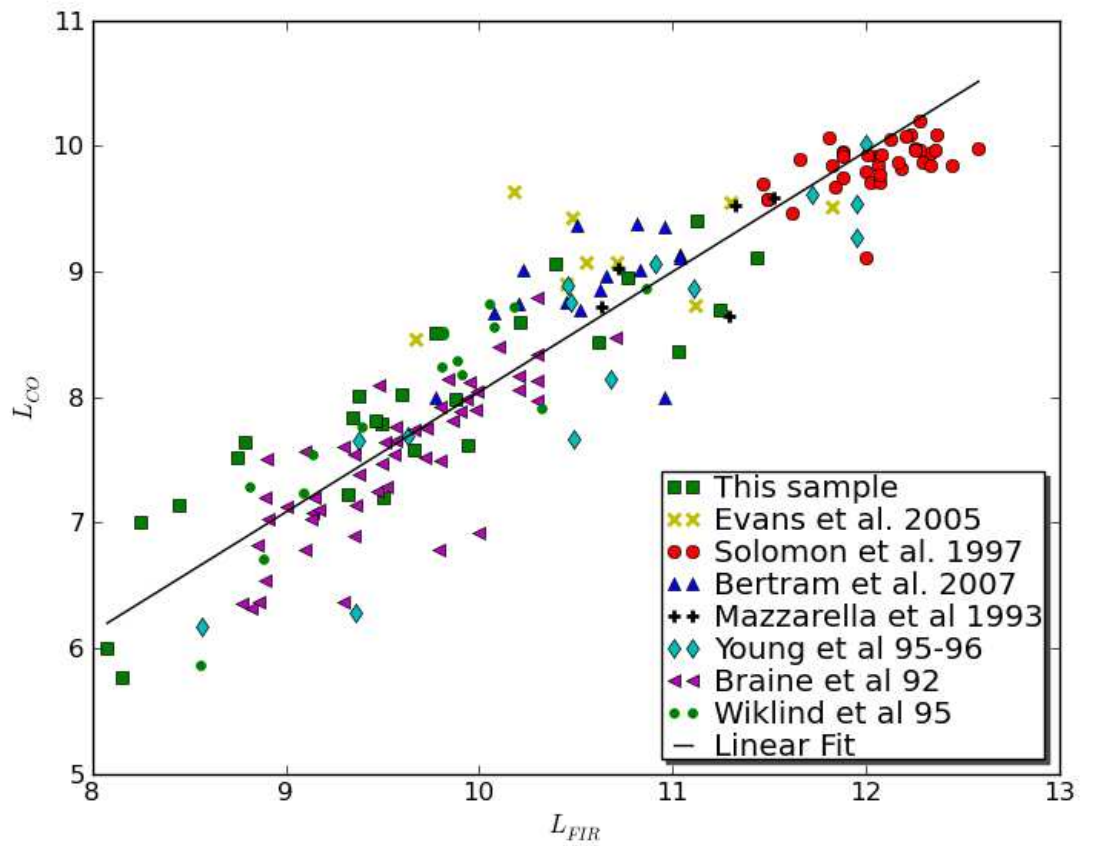


Figure 10.2: L_{FIR} vs. L'_{CO} of all the samples used in this study. Looking at table 10.4 we can see the χ^2 for each sample. As can be appreciated in the plot, the Solomon sample, of ULIRGs, is the one that better fits; this information agrees in both the graph and in the table.

galaxies with a strong SF, although this is mainly for spiral galaxies and we cannot use this study to classify the rest of the galaxies listed here. Our sample has a ratio of 52, which is quite different from the ratio of 39 in the elliptical galaxies observed by Wiklind et al. (1995). Evans et al. (2005) and Wiklind et al. (1995) seem to have similar ratios, since Evans et al. (2005) has a ratio of 35. Then Bertram et al. (2007) have a ratio of 49, and finally Mazzarella et al. (1993) has a very high ratio of 82.

On Table 10.3 we give the median values of the CO(1-0) and FIR luminosity for the comparison samples together with the median value of the star formation efficiency ($SFE=L_{FIR}/L'_{CO}$). As already known (see e.g. Gao & Solomon 2004b), the ULIRG sample of Solomon et al. (1997) has the largest SFE indicator with a value of 147. With a median value of L_{FIR} of 1.94×10^{11} , the sample of radio galaxies of Mazzarella et al. (1993) exhibits a high SFR tracing probably the star formation in merger galaxies. Similarly to the ULIRGs, they show a quite large SFE indicator (82). The sample of low luminosity QSO host galaxies from Bertram et al. (2007), as well as the galaxies in this sample (which are the galaxies from Ocaña Flaquer et al. (2010)), were chosen without any bias towards the FIR emission and their SFE appear to be similar with a value of 49 and 52 respectively. Finally, the sample of elliptical galaxies (Wiklind & Henkel 1995) and of FIR-selected radio galaxies (Evans et al. 2005) share a low value for the SFE indicator of 39 and 35.

The CO versus FIR luminosity is used in spiral galaxies to relate a tracer of the molecular gas, the CO emission, with a tracer of the star formation, the FIR emission. We compared the L_{FIR} vs. L'_{CO} relationship in our sample with the one in other samples.

A linear regression was fitted to the whole set of data (see Fig. 10.2) and to the individual samples. The linear regression is then $\log(L_{CO})=m.\log(L_{FIR})+b$; where $m=0.9$ and $b=-0.9$ with a mean square error of 0.43. Considering the samples all together we obtain a $\chi^2=0.022$.

Since our data are well fitted by the CO-FIR relationship compared to the other samples, we can argue that the radio galaxies hosted by the elliptical galaxies should exhibit at least a low level of star formation.

Besides the samples mentioned before, in Figure 10.2, we also include 3 more samples: Young et al. (1995) and Young et al. (1996), a sample of spiral galaxies observed as part of the FCRAO Extragalactic CO survey. We included also the sample of Braine & Combes (1992), composed of spiral galaxies. These samples were used to add well-defined samples for the CO-FIR relationship since the star formation is completely dominating that relationship in spiral galaxies.

Table 10.4: χ^2 values of each sample for the fitting relation

Sample name	$\chi^2_{linear\ fit}$
Ocaña Flaquer et al. (2010)	0.033
Evans et al. (2005)	0.038
Solomon et al. (1997)	0.006
Bertram et al. (2007)	0.031
Mazzarella et al. (1993)	0.015
Young et al. (1995) Young et al. (1996)	0.033
Braine & Combes (1992)	0.020
Wiklind et al. (1995)	0.029

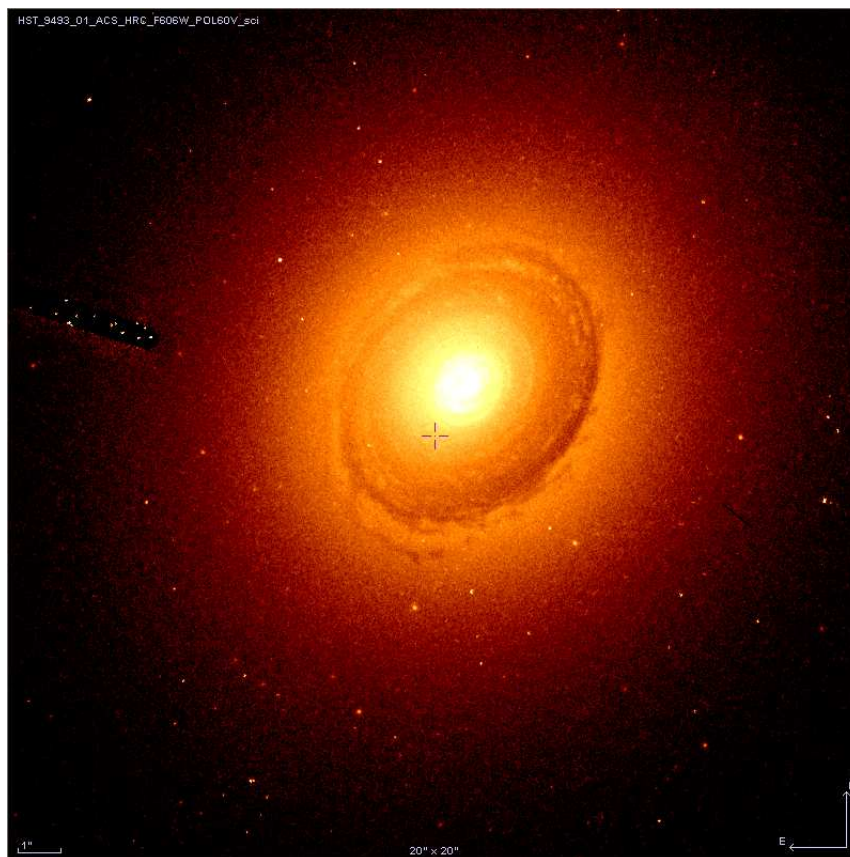
10.6 Conclusion

- We find that sample of galaxies chosen for their FIR emission, or because they are quasars or galaxies in interactions, are in general an order of magnitude higher, in the order of $10^9 M_{\odot}$, than elliptical galaxies, in the order of $10^8 M_{\odot}$.
- We find low molecular gas content compared to the other selected samples, with a median value of $2.2 \times 10^8 M_{\odot}$.
- We confirmed that FR-II type galaxies are characterized by lower CO detection rates than FR-I and FR-c radio sources as claimed by [Evans et al. \(2005\)](#), and that the FR-II have a higher molecular gas mass, as supposed by malmquist bias.
- The L_{FIR} vs. L'_{CO} relation is similar to what is found in the other samples suggesting that some star formation could be taking place in these elliptical radio galaxies.

Chapter 11

3CR 31

Figure 11.1: Image from the HST for 3CR 31 ([Martel et al. 1999](#))



Since this galaxy has been observed in more detail than the rest of the galaxies in this sample, for this PhD thesis, I dedicated a complete chapter exclusively to the analysis of this particular galaxy. It should serve as a

reference of how to proceed with the rest of the galaxies for a complete analysis, which is part of the future work for the TANGO project.

3CR 31 is hosted by an elliptical D galaxy in Zwicky cluster 0107.7+3212. It is a radio galaxy of type FR-I with $z=0.0169$, which means, recapping equations 2.1 and 2.2:

$$V_{rad} = c * z = 3 \times 10^5 [km/s] * 0.0169 = 4993 km/s \quad (11.1)$$

$$D = \frac{V_{rad}}{H_0} = \frac{4993 [km/s]}{70 \frac{km}{s.Mpc}} = 71 Mpc \quad (11.2)$$

11.1 Observation and data reduction

11.1.1 Observation

3CR 31 was observed with the IRAM 30m Telescope during December 1999 and January 2000 using A100 and B100 receivers at 113.265 GHz and A230 and B230 receivers at 226.661 GHz. Note that the frequencies are redshifted (from the original frequencies) because we adapt the central frequency of the receivers for the molecule we are interested in with the purpose of centering the line at a velocity of 0 km/s using equation 4.1.

We are interested in observing CO(1-0) and CO(2-1) for this galaxy. We know that the rest frequencies for these molecules are 115.27 GHz and 230.54 GHz respectively.

For CO(1-0):

$$f = \frac{f_0}{(1+z)} = \frac{115.27}{1+0.0169} = 113.35 \quad (11.3)$$

For CO(2-1):

$$f = \frac{f_0}{(1+z)} = \frac{230.54}{1+0.0169} = 226.71 \quad (11.4)$$

Note that the new frequencies at which we should have observed to have the galaxy centered at 0 in the spectra is not exactly the value at which we observed the source, this is because, in order to save time tuning the telescope for each galaxy, we grouped some galaxies with close values in z and observed many of them with the same receiver configurations. Operating by groups of galaxies allows us to optimize the observing time.

11.1.2 Data reduction

After the galaxy was observed, and we looked at all the spectra one by one to confirm their quality, we added them all together. Once we had only one

spectra with all the integrations, we selected a window as thick as the width of the line, in this case 550 km/s for CO(1-0) and 550 km/s for CO(2-1), and removed the baseline (see section 4.4.2) resulting on the spectra shown in figure A.2 and A.3.

This spectra is given in Velocity (in km/s) for the x axis and Temperature (in K for T_A^*) for the y axis. We converted the T_A^* in T_{MB} as shown in equation 4.11. The values in table 5.1 are already converted to T_{MB} .

11.1.3 Continuum

From these spectra (the frequencies at 3mm and 1mm), and as explained in section 5.6, we calculated the continuum flux densities for this galaxy. The temperature was converted into flux density multiplying by a factor of 6.3 for the flux densities at 3mm and by a factor of 8 for the flux densities at 1mm. See table 11.1 where the data are already in flux density.

Table 11.1: Flux densities for 3CR 31

3CR 31	$S_{3mm} = 79.07 \pm 1.13$ mJy	$S_{1mm} = 74.39 \pm 2.78$ mJy
--------	--------------------------------	--------------------------------

11.2 Molecular gas mass

From chapter 5, I used the equation 5.6 to calculate the molecular gas mass of this galaxy and Table 5.1 for the data of 3CR 31.

$$M_{H_2} = 5.86 \times 10^4 D^2 K I_{CO} = 5.86 \times 10^4 (71^2 [Mpc^2] \times 1 \times 5.68 [K km/s]) = 16.81 \times 10^8 M_{\odot} \quad (11.5)$$

For the error, since the only variable in this equation is the integrated velocity, we did calculate it as:

$$\delta M_{H_2} = 5.86 \times 10^4 D^2 K \delta I_{CO} = 5.86 \times 10^4 (71^2 [Mpc^2] \times 1 \times 0.81 [K km/s]) = 2.38 \times 10^8 M_{\odot} \quad (11.6)$$

We have seen that the average value for this sample of galaxies is about $2.2 \times 10^8 M_{\odot}$, therefore this galaxy has more molecular gas mass than the average for the sample.

11.3 Molecular gas disk

From the spectra in A.2 and A.3, we see a double horn profile typical of molecular gas disk. This galaxy is one of the 7 that presents this feature and one of the 2 that clearly shows it on both frequencies, being stronger for the

CO(2-1) emission line than for the CO(1-0) emission line.

11.3.1 Interferometric Data

For this galaxy we have interferometric data observed using the IRAM PdBI interferometer. We see from the integrated CO intensity in figure 11.2 the presence of a molecular gas disk of 8" size. Applying the correction factor for the beam dilution, shown in figure 5.6 in section 5.4.1, to the CO(2-1)-to-CO(1-0) line ratio of 2.47 found with the IRAM-30m observations, the actual line ratio would go down to 0.8, assuming that CO emission is 8" as shown in figure 11.4, which, according to Braine & Combes (1992) it would imply an optically thick gas with an excitation temperature of about 7K.

Figure 11.3 shows the position-velocity (PV) diagram for the CO(1-0) emis-

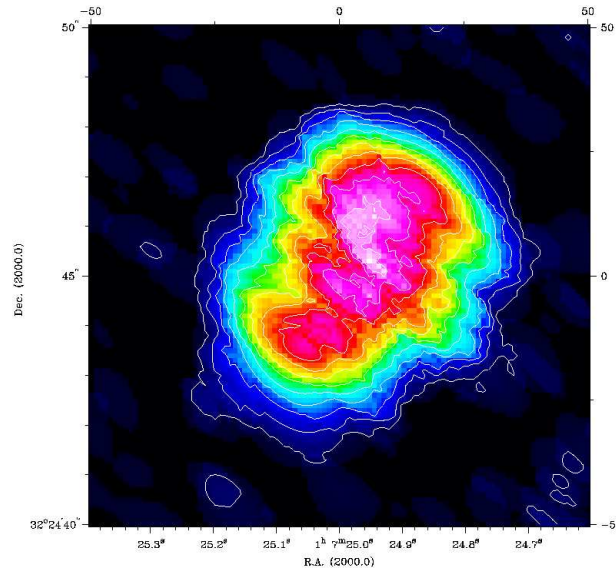


Figure 11.2: Interferometric map for CO(1-0) from IRAM PdBI.

sion in 3CR 31. From this figure we can see that at 1" the maximum velocity is $v_{max}=190$ km/s. Applying the correction for the inclination ($i=39^\circ$), the maximum rotation velocity at a radius of 1" is $v_{rot}=v_{max}/\sin(i)=317$ km/s. Thus the dynamical mass inside a radius of 1" is estimated using $M_{dyn}=\frac{R_* V_{rot}^2}{G}=1.02 \times 10^{10} M_\odot$. We estimate the total molecular gas mass inside a radius of 1" to be $1.04 \times 10^8 M_\odot$ using the mean surface gas density, therefore the molecular gas represents about 1% of the dynamical mass in the very center of 3CR 31. The dynamics and stability implications for the molecular gas in the center of 3CR 31 are discussed in Okuda et al. (2005).

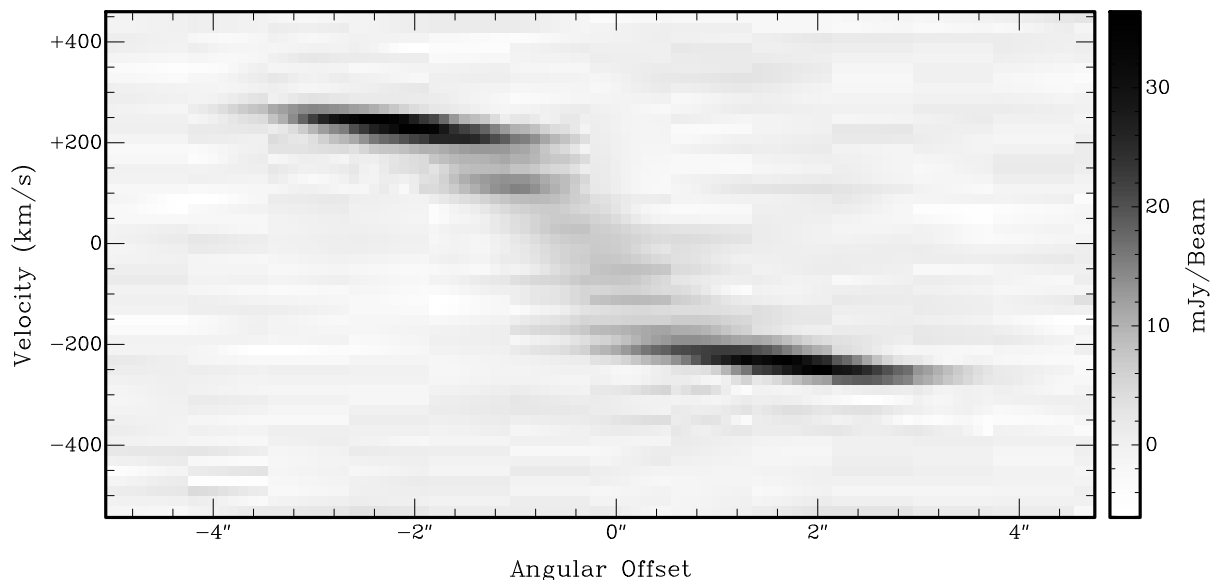


Figure 11.3: Position Velocity diagram for the CO(1-0) emission in 3CR 31

11.4 Dust

The IRAS data for this galaxy are: $f_{60\mu\text{m}}=435\pm 65.3$ mJy and $f_{100\mu\text{m}}=1675\pm 251$ mJy.

Going back to chapter 6, and using the modified black body emissivity law, we calculated a dust temperature of 28.3K, colder than the 36K found as a median value for this sample. Using this dust temperature, and equation 6.2, we found a dust mass of:

$$M_{\text{dust}} = 4.78 * f_{100} * D_L^2 * (e^{\frac{143.88}{T_{\text{dust}}}} - 1) = 4.78 * 1675 \text{ mJy} * 71^2 [\text{Mpc}^2] * (e^{\frac{143.88}{28.3\text{K}}} - 1) = 6.3 \times 10^6 M_{\odot} \quad (11.7)$$

Recall from chapter 6 that the average value for the sample for the dust mass is $2.5 \times 10^6 M_{\odot}$. For 3CR 31 alone, the dust mass is $6.3 \times 10^6 M_{\odot}$, this galaxy has a dust mass typical of the galaxies in TANGO.

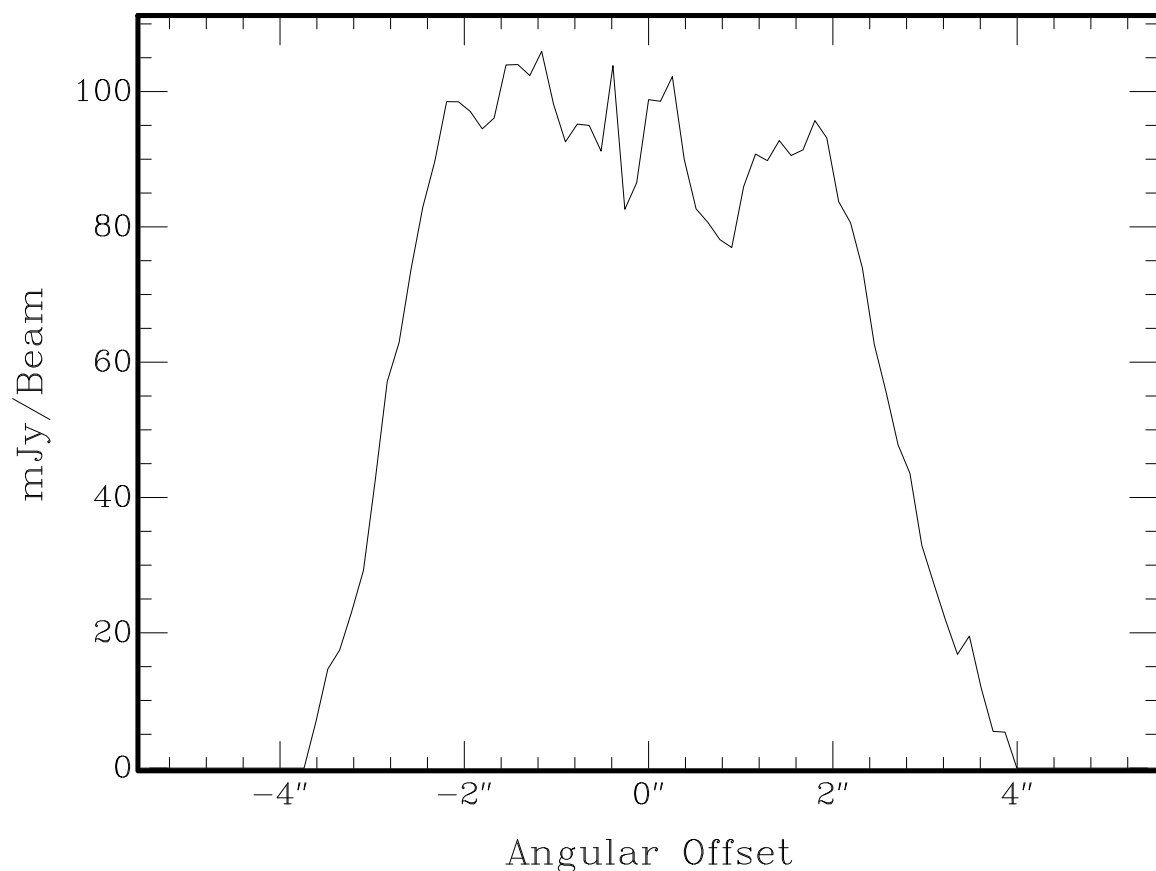


Figure 11.4: CO(1-0) intensity profile along the major axis for the galaxy 3CR 31.

11.4.1 Multi Dust Components

When we fitted 3 dust components to the SED of 3CR 31, see chapter 6, we found the following temperature of 16.6K, 47.1K and 237.7K with respective masses of $5.3 \times 10^7 M_{\odot}$, $3.3 \times 10^4 M_{\odot}$ and $1 M_{\odot}$. Comparing with IRAS estimation, we find 8.4 times more mass of dust mainly from the cold component at 16.6 K. We noted that the warm temperature is larger than the IRAS temperature, which means that cold and warm components contribute to the IRAS flux density.

An important factor is the ratio of the molecular gas mass-to-dust mass (M_{H_2}/M_{dust}). For this sample this ratio is equivalent to 30, a much lower value than 250 (value calculated only with IRAS dust) from studies in other galaxies, typically spiral galaxies, using miliometric and submillimetric data, we know that this ratio is around 150. This low ratio could be due to different reasons:

- the molecular gas is underestimated, which is typical of lower metallicity galaxies.
- A more likely explanation is that the cold component is slightly hotter with a smaller dust mass. This is due to the sparsity of the data in the submillimetric far-IR range and it could be tested by further observations in this range (ALMA).

11.5 Luminosity

11.5.1 CO Luminosity

In chapter 9.5 we calculated the CO luminosity for all the galaxies in the sample, which turned out to be 4.2×10^7 K km/s pc². The CO Luminosity formula is, as stated in equation 9.1,:

$$L_{CO} = 23.5 \Omega_{s*b}^2 D_L^2 I_{CO} (1+z)^{-3} = 23.5 * (22)^2 * (71)^2 * 5.86 * (1+0.0169)^{-3} = 3.2 \times 10^8 \frac{K km/s}{pc^2} \quad (11.8)$$

As expected from the amount of molecular gas, this galaxy is more luminous than the average galaxy in TANGO.

11.5.2 FIR Luminosity

As for the FIR Luminosity, we have already mentioned how it is calculated (see equation 9.2). For the calculations we used the warm component (at 60 μ m) and the cooler component (at 100 μ m). For the calculation of the FIR luminosity we need to know beforehand the luminosity at the warmer component, from eq. 9.3:

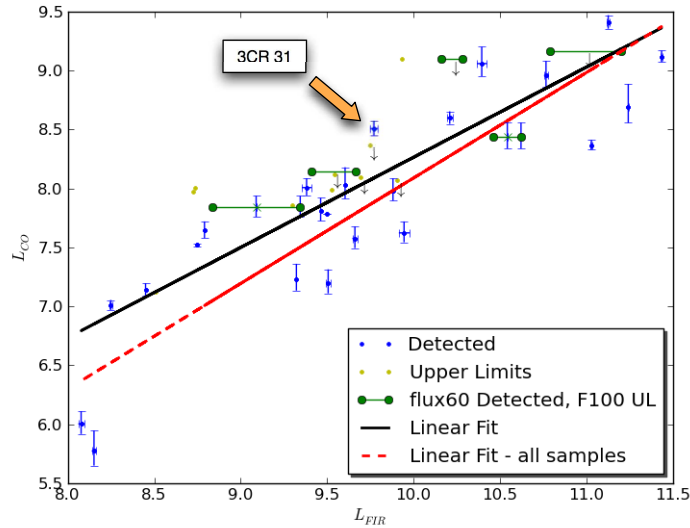
$$\text{Log}(L_{60}) = 6.014 + 2\text{Log}(D) + \text{Log}(f_{60}) = 6.014 + 2\text{Log}(71) + \text{Log}(435) = 9.4 L_{\odot} \quad (11.9)$$

$$L_{FIR} = \left[1 + \frac{f_{100}}{2.58 f_{60}} \right] L_{60} = 12.4 * \left[1 + \frac{1675}{2.58 * 435} \right] = 6.26 \times 10^9 L_{\odot} \quad (11.10)$$

11.5.3 Is there Star Formation in 3CR 31?

In chapter 9.5 we have studied the luminosity properties of the galaxies from TANGO as a sample, and in chapter 10.6 we have compared the characteristics with similar samples. We concluded that the galaxies in TANGO follow a linear correlation typically used in spiral galaxies as a measurement of star formation efficiency (SFE), which would imply that there is Star Formation in the galaxies from our sample. Looking at figure 11.5 we can see the same plot as in figure 9.1 with an orange arrow that highlights where 3CR 31 is in comparison with the rest of the galaxies. We can see that 3CR 31 is more

Figure 11.5: The orange arrow shows where the location of 3CR 31 is in the plot



luminous in its CO emission than in its FIR emission compared to what would be expected from the linear fit, both for this sample alone, and for the linear fit of all the galaxies together (recall figure 10.2).

The Star Formation Rate (SFR) was also calculated for the sample in equation 9.4, resulting in a value of $3.7 \pm 1.5 M_{\odot}/\text{yr}$. For 3CR 31, the SFR is about $1.18 M_{\odot}/\text{yr}$, lower than the value for the rest of galaxies, implying that there is less star formation per year in this particular radio galaxy compared to the sample as a whole.

We also mentioned in chapter 6.2 that according to Bell (2003), we could calculate what is heating the dust, since young stars in HII regions heat up dust at relatively high temperatures (with low $100\mu\text{m}$ -to- $60\mu\text{m}$ ratio of about 1). 3CR 31 in particular has a ratio of 3.85, closer to the values proposed as star forming galaxies.

11.6 How old is the synchrotron emission in 3CR 31?

11.6.1 Collecting the Data

From section 11.6 we learned that we need to collect all the frequencies we can from the source, as long as they are lower than 200 GHz, in order to have a better estimation of the break frequency that will be used to calculate the

age of the galaxy. To begin, we collected all the data from the "star" galaxy using Nasa Extragalactic Database (NED) ¹, Astrophysical CATalogs support System (CATS) ² and our own data observed with the 30m telescope (Ocaña Flaquer et al. 2010).

After the data had been collected, we went through the flux densities one by one to analyze their origin. The frequencies with their flux densities are listed in table 11.2.

As can be seen from table 11.2, there are 4 measurements from the work of Laing & Peacock (1980), in which they have compiled a set of flux densities over the range 10-14900 MHz, adjusted to the scale of Baars et al. (1977), who fit empirical formulas to the absolute measurement. The fit is good for frequencies above 38 MHz but the spectra with lower frequencies show severe downward curvature. They use, therefore, the Baars et al. (1977) scale fitted for $\nu \geq 38$ MHz and independent absolute measurements for $\nu < 38$ MHz. For 3CR 31, Laing & Peacock (1980) state that the spectral curvature at low frequencies (10, 22 and 26 MHz) is too large to allow adjustment of these flux-density scales by extrapolation from higher frequencies. The lowest frequency we have is 10 MHz; we then have to be aware of the fact that the calibration is not very well adjusted. At 22 MHz we have a flux density very similar to the one proposed by Roger et al. (1986), where they used the calibrated Grakovo UTR-2 scale (Braude et al. 1978), but for consistency with calibration scales we will not use their flux densities since the result proposed by Laing & Peacock (1980) is sufficient. In the case of 178 MHz we have again about the same values proposed by Laing & Peacock (1980) and Kühr et al. (1981). I will use the average of both values since their values are about the same, and both use the Baars et al. (1977) scale for the calibration, in contrast to the other flux density values suggested for this frequency, proposed by Haynes et al. (1975). For these cases I will not use the flux densities, since the information is not clear, I will only use the data for which we have a more reliable information.

The catalog of Verkhodanov et al. (2000), contains sources observed using the Ukrainian T-shaped Telescope. The frequencies observed were 14.7, 16.7 and 25 MHz and the flux densities from them were used for the age calculation. Kühr et al. (1981), which is a complete sub-sample of Kühr et al. (1979), have all the flux densities on the scale of Baars et al. (1977). The flux densities from this catalog are flux densities we consider to be reliable and we will use them to find the break frequencies and to calculate the synchrotron age.

Also Zhang et al. (1997) used the Baars et al. (1977) flux densities scale for calibration for the 232 MHz.

Douglas et al. (1996) used the Texas Interferometer, and the basis for the Texas Survey flux densities is a slightly modified version of the flux density scale de-

¹<http://nedwww.ipac.caltech.edu/>

²<http://w0.sao.ru/cats/index.html>

veloped by [Wills \(1973\)](#). This scale was recreated from basic flux density data, reduced, and modified to reflect an assumed frequency-independent secular decrease of the flux density of CAS A ([Rees 1990](#)) of 0.8% per year, rather than 1.3% per year originally used by [Wills \(1973\)](#). The resulting scale is about 2% below the [Wills \(1973\)](#) scaled at 365 MHz. For comparison purposes, a reduction was also done using a CAS A ([Rees 1990](#)) spectrum adopted by [Baars et al. \(1977\)](#) with very similar results. These flux densities were not used with *SynAge* (see chapter 8) because the flux densities are much lower compared to the rest of the flux densities at similar frequencies, and therefore it is assumed that the galaxy was probably observed at the center, which means that we are missing emission from the galaxy.

Also, even though the NVSS flux densities ([Condon et al. 1998](#)) are ultimately based on the [Baars et al. \(1977\)](#) scale, these flux densities are much lower than flux densities from the same frequencies of other references; one reason for this lower flux density is most likely due to the "missing flux" problem from VLA.

[Polatidis et al. \(1995\)](#) collected the data from [Kühr et al. \(1979\)](#), therefore, for this analysis we will not take these flux densities into account.

The data from [Gregory & Condon \(1991\)](#) are an older version of the data presented by [Gregory et al. \(1996\)](#), where they used the unresolved steep-spectrum from [Kühr et al. \(1981\)](#) to tie the Green Bank (GB) 4.85GHz flux density to the [Baars et al. \(1977\)](#) scale. The data that will be used are the data presented by [Gregory et al. \(1996\)](#) instead of the data from [Gregory & Condon \(1991\)](#). Note that in some cases there are two flux densities at the same frequency (e.g., 4850 MHz), in this case, both coming from the same article of reference and the flux densities are within the errors. In cases like this, an average of the flux densities was used.

Frequency MHz	Flux Density Jy	Notes
10	144 ± 48	Laing & Peacock (1980)
14.7	167 ± 13	Verkhodanov et al. (2000)
16.7	146 ± 14	Verkhodanov et al. (2000)
22	86 ± 13	Roger et al. (1986)
22	86.3 ± 25	Laing & Peacock (1980)
25	66 ± 11	Verkhodanov et al. (2000)
26	66 ± 7	Kühr et al. (1981)
38	58.8 ± 5.3	Kühr et al. (1981)
38	54 ± 8	Kühr et al. (1981)
74	6.1 ± 0.67	Condon et al. (1998)
80	20 ± 2	Haynes et al. (1975)
80	21 ± 3	Kühr et al. (1981)
86	34 ± 1.6	Laing & Peacock (1980)

111.5	22.4 ± 3.6	Niell (1971)
159	10.5 ± 0.5	Edge et al. (1959)
160	21 ± 3.1	Kühr et al. (1981)
178	15.5 ± 3	Haynes et al. (1975)
178	16.7 ± 2.5	Haynes et al. (1975)
178	18.5 ± 1.5	Laing & Peacock (1980)
178	17.97 ± 0.9	Kühr et al. (1981)
178	18.2 ± 1.2	Laing & Peacock (1980); Kühr et al. (1981)
232	14.43 ± 0.05	Zhang et al. (1997)
318	10.2 ± 0.43	Dixon (1970)
318	10.92 ± 0.44	Kühr et al. (1981)
318	11.87 ± 0.59	Kühr et al. (1981)
318	10.0 ± 0.51	An average of all the 318 MHz
325	13.456 ± 0.0054	Rengelink et al. (1997)
365	1.58 ± 0.092	Douglas et al. (1996)
370	1.58 ± 0.092	Douglas et al. (1996)
408	13 ± 2.34	Kühr et al. (1981)
408	8.26 ± 0.68	Kühr et al. (1981)
408	9.05 ± 0.68	Kühr et al. (1981)
408	10.1 ± 1.23	An average of all the 408 measurements.
606	6.18 ± 0.37	Niell (1971)
617	9.1 ± 2.3	Haynes et al. (1975)
750	8.1 ± 0.4	Kühr et al. (1981)
750	8.63 ± 0.16	Niell (1971)
1400	0.9155 ± 0.0282	Condon et al. (1998)
1400	0.0153 ± 0.0005	Condon et al. (1998)
1400	1.1082 ± 0.0337	Condon et al. (1998)
1400	1.11 ± 0.0337	White & Becker (1992)
1400	5 ± 0.3	Kühr et al. (1981)
1400	4.6 ± 0.2	Haynes et al. (1975)
1400	4.99 ± 0.14	Kühr et al. (1981)
1400	5.22 ± 0.22	Haynes et al. (1975)
1400	4.99 ± 0.26	Kühr et al. (1981)
1417	4.59 ± 0.7	Haynes et al. (1975)
1670	4.89 ± 0.13	Kühr et al. (1981)
2290	4 ± 0.2	Polatidis et al. (1995); Thakkar et al. (1995); Xu et al. (1995)
2695	3.53 ± 0.05	Condon et al. (1998)
2700	3.57 ± 0.35	Kühr et al. (1981)
4850	2.1 ± 0.12	Gregory et al. (1996)
4860	1.12 ± 0.144	Gregory & Condon (1991)
5000	0.423 ± 0.017	Kleinmann et al. (1986)

5000	2.1 ± 0.03	Moshir & et al. (1990)
5000	2.09 ± 0.1	Kühr et al. (1981)
5010	2.09 ± 0.1	Kühr et al. (1981)
6630	$2.1 \pm .12$	Haynes et al. (1975)
10630	1.21 ± 0.18	Haynes et al. (1975)
10630	1.21 ± 0.18	Haynes et al. (1975)
10695	1.23 ± 0.05	Kühr et al. (1981)
10700	1.09 ± 0.1	Kellermann & Pauliny-Toth (1973)
22000	0.47 ± 0.09	Kühr et al. (1981)
113265	0.0791 ± 0.0079	Ocaña Flaquer et al. (2010)
226661	0.0748 ± 0.0075	Ocaña Flaquer et al. (2010)

Table 11.2: Frequencies in boldface are the frequencies finally used.

11.6.2 Using *SynAge*

SynAge is a computer program created by Murgia et al. (1999), to model a synchrotron aged spectrum (see chapter 8). After checking all the data in the plot, we noticed that according to the best fit given by *SynAge*, at lower frequencies, the flux densities have higher values compared to what would be expected from the rest of the flux densities, at a frequency of about 80 MHz and lower. Assuming that those flux densities are correct, (we should remember that, according to Laing & Peacock 1980, the flux densities at those lower frequencies might be overestimated), this could be an implication that the galaxy has an older component (this concept is known as "double-double morphology" Schoenmakers et al. 2000). This would mean that at some point in the past this galaxy stopped (or interrupted) its activity and for reasons that are still unknown, this galaxy started having an active nucleus again. If we believe that the flux densities are simply overestimated, which means that we do not consider this *rebirth* as a possibility, we will call this scenario CASE 1 (see section 11.6.2.1). If, on the other hand, we believe that, even though the flux densities might be overestimated, we could have a second generation galaxy, we will refer to this scenario as CASE 2 (see section 11.6.3). To calculate the synchrotron age of the galaxy we need not only all the flux densities lower than 226.661 GHz that we can collect, but also the dimensions of the galaxy in order to calculate the equipartition magnetic field (see chapter 8). From Govoni & Feretti (2004) we take the equipartition parameters needed to calculate the equipartition magnetic field. In this case we are assuming 0.5 for the α (spectral index), and in this case, the equipartition parameter is $\xi(\alpha, 10 \text{ MHz}, 10 \text{ GHz}) = 2.13 \times 10^{-12}$.

For the K (recall from chapter 11.6, k is the ratio of energy in the heavy particles to that in the electrons) we assume a value of 1 (see Miley 1980, and chapter 8), and we find an extent of the source of 10.34 Kpc.

11.6.2.1 CASE 1

For CASE 1, we applied all the values, as shown in table 11.2 where some were flagged for different reasons, and that are thoroughly explained in section 11.6. Note that in the case of 3CR 31 we used the NVSS and the VLA image and calculated the area. We can see from figure 11.9 that the width of the galaxy is about 22 arcsec and the length 1080 arcsec. From this information we can assume an area of 23760 arcsec². Since we assume the galaxy as an ellipse, we can also assume that the depth of the galaxy is about the same as the minor axis, 22 arcsec, which is the same as 7.58 Kpc.

We then calculated the synchrotron age for 3CR 31, from Parma et al. (2007):

$$t_{syn} = 1590 \frac{B^{0.5}}{(B^2 + B_{CMB}^2)[(1+z)v_{BR}]^{0.5}} \quad (11.11)$$

Where B and B_{CMB}, which are explained in section 11.6, are the equipartition magnetic field and cosmic background magnetic field respectively. We also find in this equation the v_{break} , which according to *SynAge* and, as can be seen in Figure 11.6.2.1, for this combination of data is equal to 9060 MHz. We chose frequencies lower than the v_{break} , on a flat range on the fit proposed by *SynAge* to calculate the age of the synchrotron at those frequencies. In table 11.6.2.1 we can find these frequencies in MHz and their flux densities in mJy, their intensity in mJy/arcsec², their minimum energy in erg/cm³, their equipartition magnetic field in μ G and finally the synchrotron age corresponding to these frequencies in Myr. We can conclude that 3CR 31, assuming CASE 1, has a synchrotron age of about 26 Myr.

11.6.3 CASE 2

If we, instead, consider CASE 2 as our real scenario, then we should consider two different components, and give them separately to *SynAge*. One of the components is for the *old galaxy* and the other one is for the *new galaxy* 8.

We proceed for CASE 2, just in the same way we did for CASE 1. First we need the size of the *new* source. If we look at figure 11.10, we note that the Blue color represents the optical image from the POSS2 and the Red color is the radio image from the VLA at a 21cm wavelength (1.4 GHz). The red color of this figure shows different intensities that are clearly visible from the image, we used this difference to divide the source in the 2 groups, *old* and *new*. The *new* jet would be the most intense part (more intense red color) and the *old* jet would be the weaker part (less intense red color), it is larger and still visible. Looking at figure 11.11, we see that figure 11.11b and figure 11.11a are the same as figure 11.10 and figure 11.9, with the difference that on the second figure we have drawn circles, in the case of the blue circle, it contains the *new* part of the galaxy and the red circle contains the whole the galaxy.

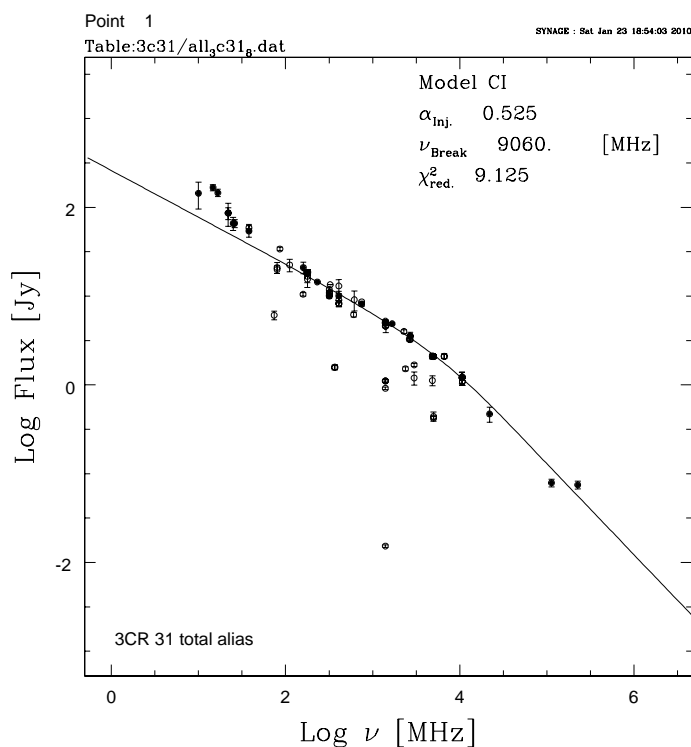


Figure 11.6: This is the result from *SynAge* where we cleaned the list of flux densities flagging all of the flux densities that for one reason or another we thought should not be part of the fit.

We note that the *new galaxy* has a major axis of 540 arcsec and a minor axis of 22 arcsec and where, since we are assuming the galaxy is an ellipse, and the depth of the galaxy is assumed to be the same as the minor axis, 22 arcsec, which is equivalent to 6.89 Kpc for a galaxy at 71.06 Mpc. For the old galaxy, the size parameters are the same as CASE 1.

When fitting the data into *SynAge*, to find the new ν_{break} , we need to remember that we are considering this CASE 2 as if there were 2 galaxies. Therefore, fitting the old components separately than the new component, and finding different break frequencies for each case.

11.6.3.1 The New Component

The new value for the ν_{break} is 4789 MHz, as can be seen in figures 11.6.3.1 and where the synchrotron age, for the new part only, is about 27 Myrs as can be interpreted from Table 11.6.3.1

Frequency MHz	Flux Density mJy	Intensity mJy/arcsec ²	U_{min} erg/cm ³	B_{eq} μ G	Synchrotron Age Myr
100	22840	0.96	3.74×10^{-12}	6.35	25.55
200	15700	0.66	3.69×10^{-12}	6.30	25.77
300	12560	0.53	3.64×10^{-12}	6.27	25.93
400	10700	0.45	3.61×10^{-12}	6.24	26.06
500	9435	0.40	3.58×10^{-12}	6.21	26.17
600	8503	0.36	3.56×10^{-12}	6.18	26.27
700	7780	0.33	3.53×10^{-12}	6.17	26.36
800	7198	0.30	3.51×10^{-12}	6.14	26.45
900	6716	0.28	3.49×10^{-12}	6.13	26.53
1000	6309	0.26	3.47×10^{-12}	6.11	26.61

Table 11.3: Synchrotron Ages in 3CR 31.

11.6.3.2 The Old Component

The new value for the ν_{break} is 10.92 MHz, as can be seen in figures 11.6.3.2. The flux density for the *old* component can be influenced by the flux density of the new component, for this reason, in table 11.6.3.2 we show the flux density that the *new* component would have at this frequency, according to *SynAge*, the flux density the *old* component has, according to *SynAge* as well, then the difference of both flux densities, which would be the actual flux density with no contamination from the *new* component. We calculated a synchrotron age, for the *old* component only, of about 1165 Myrs.

11.6.4 For the future work of this galaxy

This galaxy shows a very interesting high frequency SED. In fact, from Fig. 11.6.3.1 we can see that from the fit suggested by *SynAge*, and after flagging all the data that was not considered valid, we expected to have lower flux densities at these lowest frequencies, instead we have higher flux densities that could be interpreted as if the galaxy was revealing to us the existence of a previous generation. This would mean that 3CR 31 is a galaxy that is going through a re-birth, or a "double-double morphology" (as suggested by Schoenmakers et al. 2000). In this case, what we see from the fit are the data of the second generation.

In order to have stronger conclusions about whether this galaxy is a second generation galaxy, or we have overestimated the flux densities, we should observe at lower frequencies. For this purpose we are waiting for the LOW Frequency ARray (LOFAR)³ to observe at radio frequencies below 250 MHz.

³<http://www.lofar.org/>

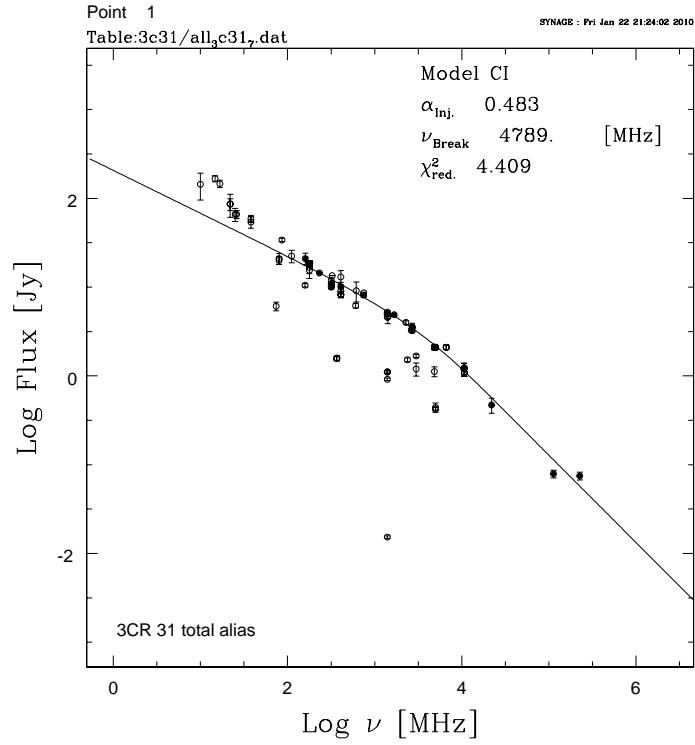


Figure 11.7: This is the result from *SynAge*, using only the “new galaxy”.

Frequency MHz	Flux Density mJy	Intensity mJy/arcsec ²	U_{min} erg/cm ³	B_{eq} μG	Synchrotron Age Myr
100	22070	2.04	6.09×10^{-12}	8.10	26.66
200	15570	1.44	6.08×10^{-12}	8.10	26.68
300	12630	1.17	6.06×10^{-12}	8.08	26.74
400	10850	1.00	6.03×10^{-12}	8.06	26.82
500	9623	0.89	6.00×10^{-12}	8.04	26.90
600	8708	0.81	5.97×10^{-12}	8.02	26.98
700	7991	0.74	5.94×10^{-12}	8.00	27.06
800	7409	0.69	5.91×10^{-12}	7.98	27.14
900	6926	0.64	5.88×10^{-12}	7.96	27.22
1000	6510	0.60	5.85×10^{-12}	7.94	27.30

Table 11.4: Synchrotron Ages for the “New Galaxy” in 3CR 31.

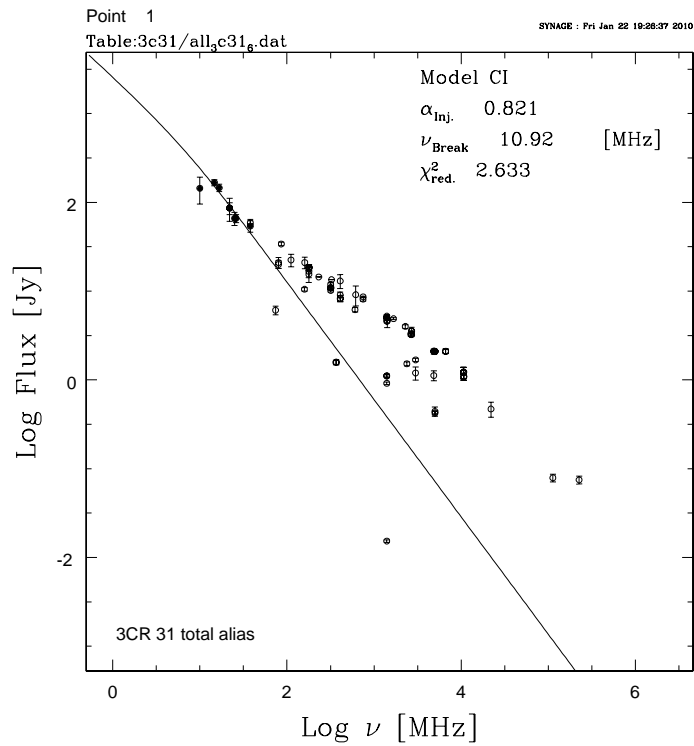


Figure 11.8: This is the result from *SynAge*, using only the “old galaxy”.

11.7 Conclusion

- With the CO(1-0) map obtained from IRAM-PdBI, we confirmed the presence of a molecular gas disk around this galaxy.

Table 11.5: Synchrotron Ages for the "New Galaxy" in 3CR 31.

Frequency MHz	Flux Density ¹ mJy	Flux Density ² mJy	Flux Density ³ mJy	Intensity mJy/arcsec ²	U_{min} $\times 10^{-14}$ erg/cm ³	B_{eq} μG	Synchrotron Age Myr
10	67.88	240.70	172.82	0.007	11.92	1.13	1276.80
14.7	56.36	151.80	95.44	0.004	9.47	1.01	1231.43
16.7	52.99	129.7	76.71	0.003	8.67	0.97	1213.03
22	46.37	91.68	45.31	0.002	6.95	0.86	1165.24
25	43.58	77.85	34.27	0.001	6.14	0.81	1138.12
26	42.76	74.02	31.26	0.001	5.89	0.80	1128.95
38	35.54	45.18	9.64	0.0004	3.35	0.6	1003.54

The flux density¹ is the flux density proposed by *SynAge* for the *new* component. The flux density² is the flux density proposed by *SynAge* for the *old* component. The flux density³ is the difference of both flux densities, and the one used to calculate the age.

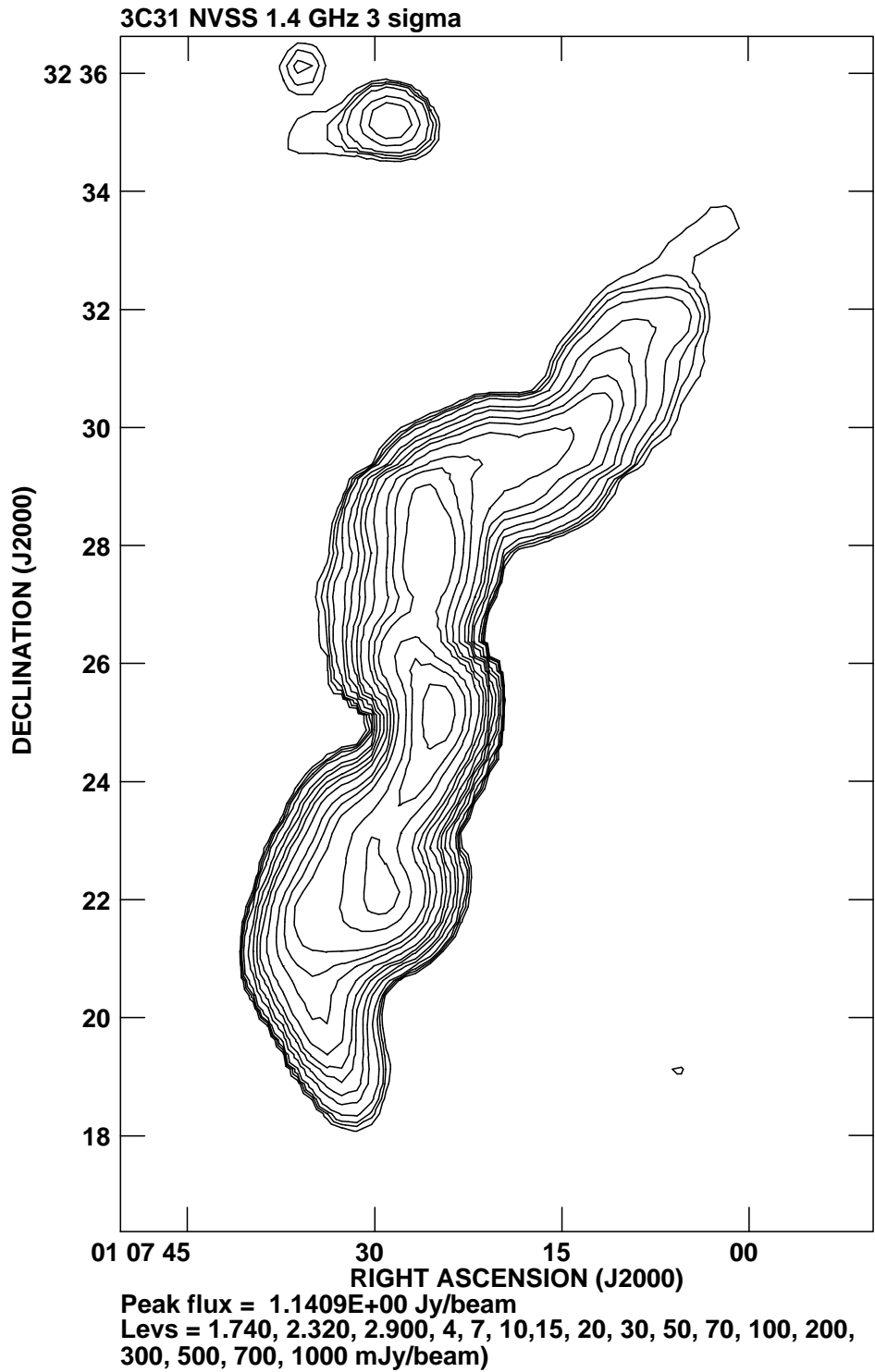


Figure 11.9: Image of the contour of 3CR 31 from the continuum at 1.4 GHz from the VLA Telescope.

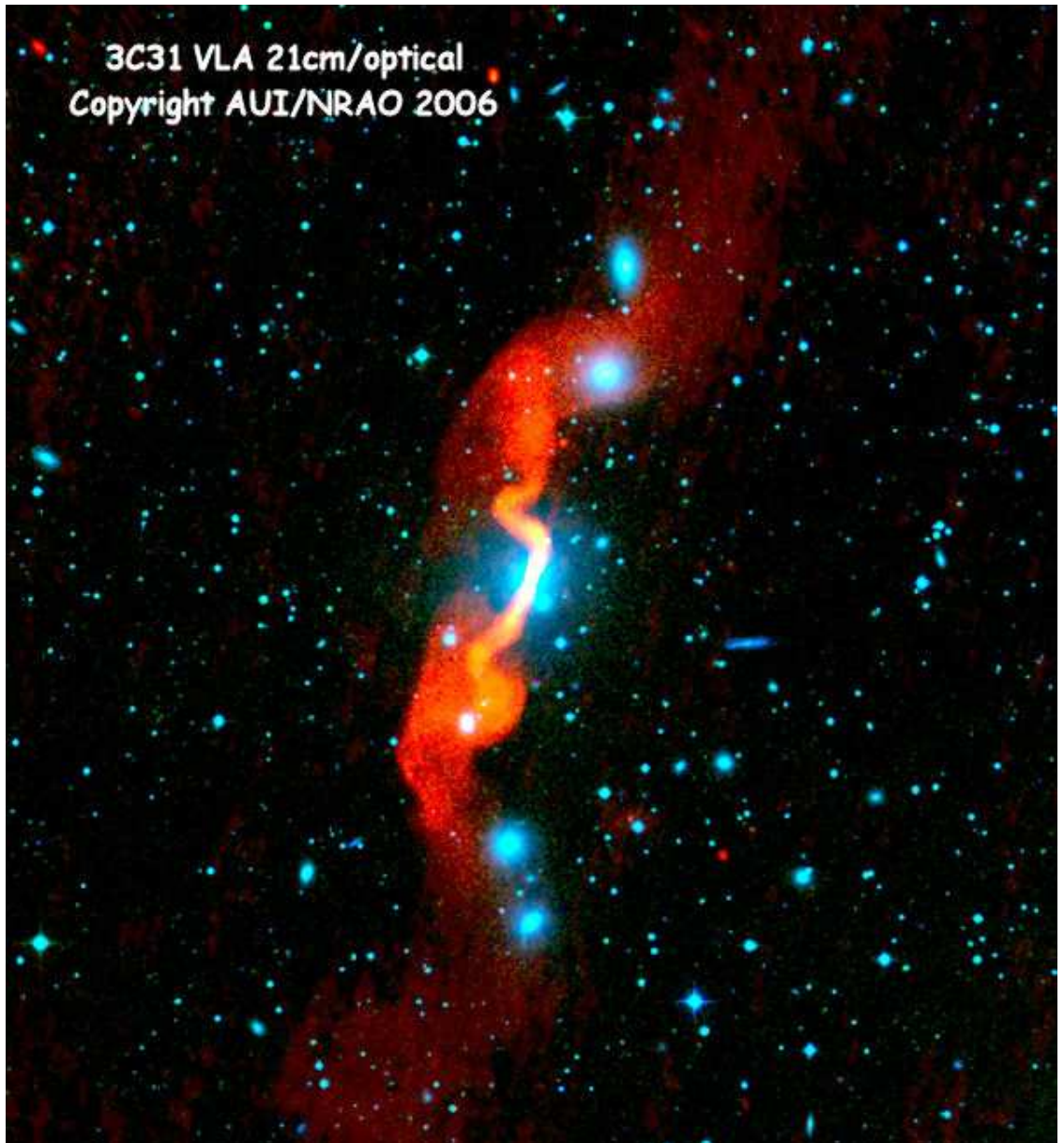
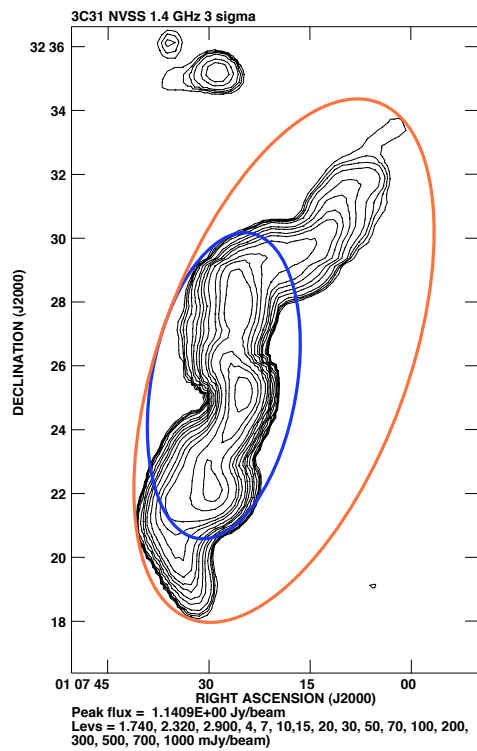
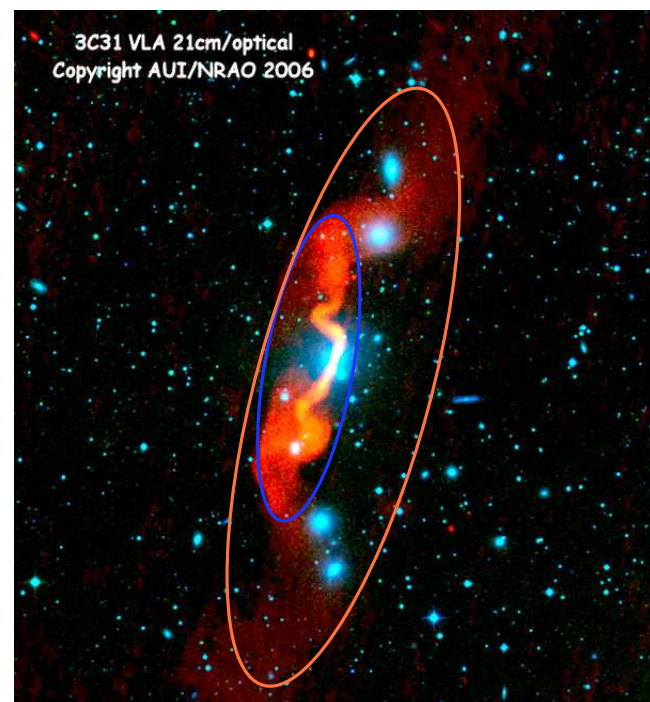


Figure 11.10: Blue: optical image from the POSS2 (blue); Red: radio image from the VLA at 21cm wavelength (1.4 GHz).



(a) VLA contour



(b) VLA map

Figure 11.11: 3CR 31 VLA image where the blue circle marks the edge of what we call "new galaxy" (in the case we consider CASE 2 as our real scenario) and the orange circle contains the whole galaxy.

Chapter 12

A Control Sample: HCN observations and results

12.1 Introduction

12.1.1 Control Sample: The AMIGA galaxies

We will study the environment of the galaxies in the TANGO project. In order to have a control sample for the effects of the environment, we choose to use a sample of isolated galaxies where we have information about their CO emission lines and where we observed HCN since it is a dense gas tracer (see sections [1.3.1.1](#) and [1.3.1.2](#) for description about these molecules).

The isolated sample used was from the AMIGA project (Analysis of the Interstellar Medium of Isolated Galaxies) which is a compilation of a multi-wavelength database of isolated galaxies that includes optical (B and H_α), infrared (FIR and NIR) and radio (continuum plus HI and CO lines) properties ([Verdes-Montenegro et al. 2005](#); [Sulentic et al. 2006](#); [Lisenfeld et al. 2007](#); [Verley et al. 2007b,a](#); [Leon et al. 2008](#); [Sabater et al. 2008](#)).

The most important learning we can acquire from this comparison, once we have a better analysis of the environment of the galaxies in TANGO, is how different galaxies can behave due to environmental effects, and this analysis will give us a better understanding on where the gas is coming from in our galaxies.

12.1.2 Interstellar Medium

The molecular interstellar medium (ISM) in galaxies has been extensively studied through the CO transitions at millimeter wavelengths. These transitions are good tracers of the molecular gas mass and represent the general distribution of molecular hydrogen ([Young & Scoville 1982](#); [Young & Devreux 1991](#)).

High-density tracers, like HCN, add relevant information concerning the

densest gas ($>10^4 \text{ cm}^{-3}$).

Observational evidence accumulated in recent years (Nguyen et al. 1992; Reynaud & Downes 1997; Kohno et al. 1999a,b) suggests a close relationship between dense molecular gas and massive star formation (SF) in the center of galaxies. Indeed, in the center of starbursts, HCN is tightly correlated with the radio-continuum emission and the total L_{HCN} seems to be very well correlated with the L_{FIR} according to Solomon et al. (1992). Gao & Solomon (2004a,b) presented the results of a sensitive HCN(1-0) survey of IR-luminous galaxies where they concluded that the L_{IR} and L_{HCN} correlate linearly indicating a tight relationship between the SF and the dense molecular gas, and that they also found a strong correlation between the L_{CO} and the L_{HCN} . The relation was confirmed at lower luminosity by Wu et al. (2005) in the Giant Molecular Clouds of our galaxy.

However, such important study is missing a genuine control sample for studying the behavior of the HCN emission in galaxies without interactions and with low L_{FIR} . For such purpose, the AMIGA project was created (see Verdes-Montenegro et al. 2005; Leon & Verdes-Montenegro 2003; Sulentic et al. 2006). Moreover, a recent study (Graciá-Carpio et al. 2006) has casted doubts on the use of HCN as an unbiased quantitative tracer of the dense molecular gas content in LIRGs and ULIRGs, mainly because of the X-rays coming from an embedded AGN which may play a dominant role in the chemistry of the molecules.

12.1.3 HCN(1-0) survey in the AMIGA Project

Although it is widely accepted that galaxy interactions can stimulate secular evolution effects in galaxies (e.g. enhance star formation, morphology, morphological peculiarities including transitions to earlier type, active nuclei)(e.g. Sulentic 1976; Hernquist 1989; Xu & Sulentic 1991) there are still many open questions. Interaction induced SF enhancements are observed at optical, FIR and radio wavelengths (e.g. Xu & Sulentic 1991; Verdes-Montenegro et al. 1998), but studies which aimed at quantifying the level of interaction induced SF, have produced contradictory results: e.g. some study of interacting pairs find a clear SF enhancement (Bushouse 1987), while others find only a marginal increase (Bergvall et al. 2003). Much of this uncertainty reflects the lack of well defined baseline for assessing the frequency and amplitude of this external influences. The goal of the AMIGA project is to provide such a baseline by quantifying the properties of a well defined sample of isolated galaxies where the effects of *nurture* are minimized.

This sample has several advantages, including isolation (they are selected on the basis of a well defined isolated criterion, Verley et al. 2007a), large sampling of morphologies (Sulentic et al. 2006), depth (allowing to sample a large part of the optical and FIR luminosity functions, Verdes-Montenegro et al. 2005; Lisenfeld et al. 2007), completeness and multi-wavelength infor-

mation: radio (0.3, 1.4 and 4.8 GHz), CO(1-0), FIR, Optical (B), NIR and H_α . The full sample of ~ 1000 galaxies shows only modest FIR luminosities, with only $< 2\%$ of the sample with $\log(L_{FIR}/L_\odot)$ above 10.5. The mean $\log(L_{FIR})$ of the sample is 0.26 dex below the corresponding value for the CfA sample, a sample of nearby galaxy similar to this one, but selected without considering environment. A lower value was also found for the mean L_{FIR}/L_B of this sample. Supporting the idea that the FIR emission is a parameter driven by interaction and that this sample of isolated galaxies shows a value close to the lower possible. This is a key point in the study of the L_{FIR} - L_{HCN} correlation and makes this sample particularly suitable in order to study intrinsic drivers of such correlation, separately from environmental effects. A study of AGN population in the CIG sample indicate a very low frequency of Seyfert galaxies with nearly no radio-AGNs (Sabater et al. 2008).

12.1.4 The Goals

- To test whether the relation between FIR and HCN(1-0) luminosity found by Gao & Solomon (2004a) for FIR luminous ($L_{FIR} \geq 10^{10}L_\odot$) galaxies, is still valid for a sample with: a) a high level of isolation, b) mild SF (reflected in a low FIR luminosity, Lisenfeld et al. 2007; Leon et al. 2007) and c) a very low level of nuclear activity (Sabater et al. 2008) necessary to rule out the effects of X-ray emission (Graciá-Carpio et al. 2006). A deviation of that relation at low FIR luminosities will indicate whether the SF efficiency and/or the HCN, as a tracer of the dense gas, is at the same level at all kinds of galaxies from mild SF to starburst.
- To study the luminosity distribution of the HCN(1-0) emission line in the sample of isolated galaxies without interactions. By comparing with the high- L_{FIR} sample, we will be able to estimate the efficiency $\epsilon_{denseGas} = M_{HCN}(H_2)/M_{CO}(H_2)$

12.2 Observation and Data Reduction

We observed HCN(1-0) in 19 well known isolated galaxies where 9 galaxies were clearly detected (see Table 12.1 for the list of the observed galaxies). The aim of these observations was to confirm the relationship between the (dense) molecular gas and star formation (SF) activity through the correlation found by Gao & Solomon (2004a,b) between the FIR and HCN luminosity.

We used A100, A230, B100 and B230 receivers with the telescope tuned at 88.6316024 GHz (for HCN(1-0)) and 230.537990 GHz (for CO(2-1)) with the frequencies redshifted according to the galaxies velocity. We did Wobbler switch with a phase of 0.5s

We then reduced the data with standard procedures, as explained on chapter

Galaxy	RA	Dec	V(LSR)
CIG 80	01h59m19.6s	+19d00m27s	2458
CIG 105	02h27m16.9s	+33d34m45s	553
CIG 143	04h18m58.2s	+05d26m03s	3870
CIG 147	04h23m27.1s	+75d17m44s	2461
CIG 435	10h43m31.1s	+24d55m20s	586
CIG 442	10h46m36.8s	+63d13m27s	1014
CIG 448	10h25m35.7s	+22d56m03s	1283
CIG 461	11h05m48.6s	-00d02m09s	805
CIG 469	11h11m31.0s	+55d40m27s	695
CIG 477	11h22m54.6s	+16d35m25s	1473
CIG 543	12h39m59.4s	+61d36m33s	143
CIG 559	12h56m43.7s	+21d40m58s	408
CIG 610	14h03m12.6s	+54d20m57s	241
CIG 638	14h37m41.1s	+02d17m27s	1753
CIG 643	14h42m57.6s	+21d25m14s	12528
CIG 837	17h49m26.5s	+70d08m40s	60
CIG 850	18h19m46.4s	+74d34m06s	1489
CIG 947	22h07m52.4s	+31d21m34s	952
CIG 1004	23h04m56.6s	+12d19m22s	2376

Table 12.1: Observed isolated galaxies for HCN(1-0) and CO(2-10)

4.7, and those galaxies clearly detected at the center were proposed for mapping to study the area around the center of the galaxy, to see if the HCN(1-0) emission was extended. We observed the galaxies up to a radius of 1/4 of their major axis, with a sampling of a beam size (26'' for 88 GHz). Finally, we mapped 4 galaxies, CIG 80, CIG 147, CIG 850 and CIG 1004 where three of them had detection around the center and 1 (CIG 1004) was not detected around the center. The maps are shown on figure 12.1, and the HCN luminosities are listed on table 12.2.

12.3 Results

Using the detected galaxies, we calculated the HCN luminosity we expected from Gao & Solomon (2004a), where they argue that their sample of galaxies have a relation such as:

$$\log(L_{IR}) = 0.97\log(L_{HCN}) + 3.1 \quad (12.1)$$

Table 12.2 is a summary of the detected galaxies, their IR Luminosity and the expected HCN luminosity calculated using equation 12.1. The next column is

CIG	L_{IR} $10^{10} L_{\odot}$	Expected L_{HCN} 10^7 K km/s pc^2	L_{HCN} - center 10^7 K km/s pc^2	L_{HCN} - Total 10^7 K km/s pc^2
80	3.95	5.36	1.06	3.75
147	4.30	5.85	4.5	7.17
448	1.14	1.48	0.32	0.32
461	2.32	3.09	0.16	0.16
469	1.11	1.44	0.11	0.11
477	1.28	1.67	0.84	0.84
610	0.09	0.11	0.021	0.021
850	2.03	2.7	0.65	1.33
1004	6.22	8.55	3.86	3.86

Table 12.2: Expected HCN Luminosities calculated from [Gao & Solomon \(2004a\)](#)

the HCN luminosity calculated from the integrated intensity (I_{HCN} [K km/s]) for HCN (1-0) observed at the center of the galaxy. Finally, as can be seen on table 12.2, the observed HCN luminosity is less than the luminosity expected from the relation of [Gao & Solomon \(2004a\)](#). After mapping 4 of the galaxies, where 3 had detection around the center, we obtain a higher value for the HCN luminosity getting closer to the expected value from [Gao & Solomon \(2004a\)](#) relation. The Galaxy CIG 147, in fact, after mapping showed a stronger value for the HCN luminosity than the one expected from the relation. The rest of the galaxies simply became closer to the expected value without reaching the HCN luminosity proposed.

12.3.1 HCN-FIR relationship in isolated galaxies

If the L_{HCN} is a dense gas tracer and the L_{FIR} a high-mass SF indicator, then the star formation rate (SFR)/mass of dense gas would be the same for normal spirals and IR-luminous interacting galaxies ([Solomon et al. 1997](#)).

From the 9 galaxies detected at the center, we found a lower L_{HCN} than expected from the relation with the L_{FIR} (Fig. 12.1). We interpreted this result as that we are only observing at the center of the galaxies, and we are missing some of the HCN(1-0) emission spread around the center. Indeed, the $L_{HCN(1-0)}$ is much lower than the predicted for the largest galaxies. According to [Gao \(1996, 1997\)](#) and [Gao & Solomon \(2004a\)](#) a substantial fraction of the HCN emission originates from their inner disks outside the central 1 Kpc, even though the dense molecular gas is strongly concentrated in the central regions.

Therefore, we mapped some of the galaxies to observe whether the HCN emission is concentrated only at the center or spread around the galaxy. Fig-

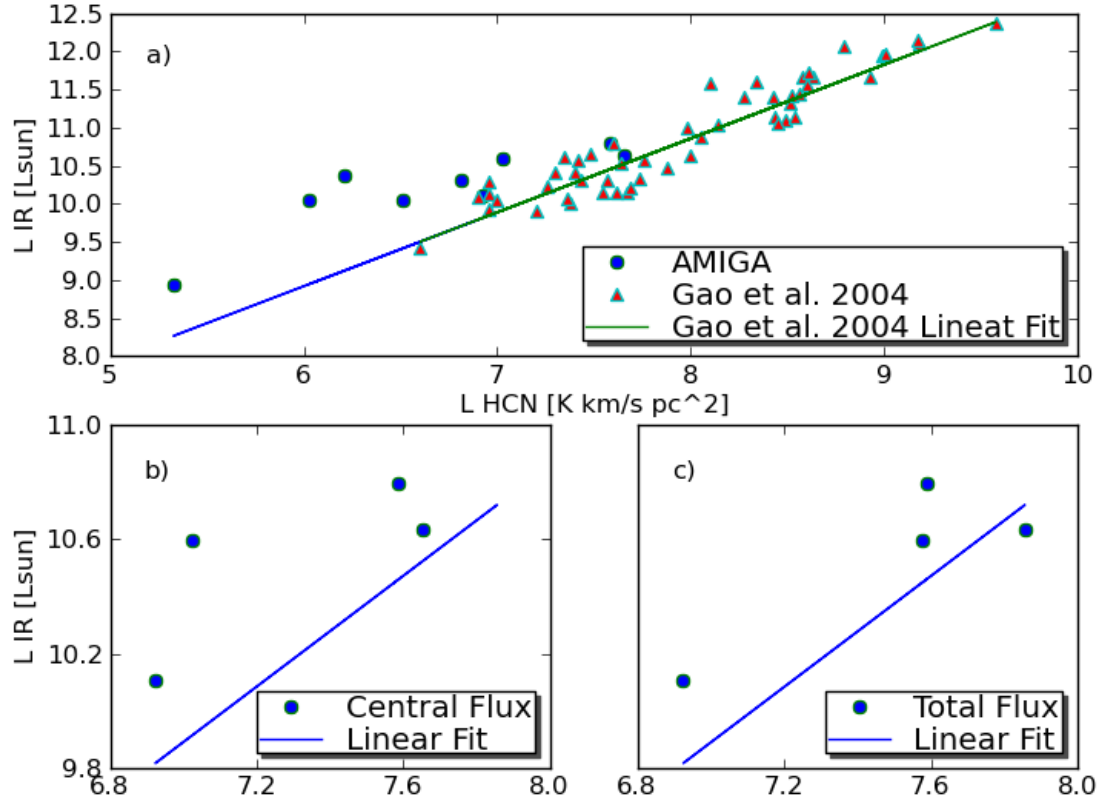


Figure 12.1: L_{HCN} vs L_{IR} . a) All the galaxies in the sample compared with Gao & Solomon (2004a), b) central flux of the mapped galaxies and c) sum of the central flux plus the flux around the center.

Figure 12.2, shows the plot of the spectra for the temperature at the center of 8 of the 9 clearly detected galaxies. We noted that the galaxy CIG 610 is clearly detected although it was not proposed for mapping. The reason for not mapping this galaxy yet is that it is the closest galaxy to us ($z=0.0008$), and the largest galaxy in size in the sample (major axis: 28', Minor axis: 26.9'), observing this galaxy could be part of a future work.

The galaxies were mapped with the purpose of observing the extended HCN(1-0) emission. We observed the galaxies up to a radius of 1/4 of the major axis, with a sampling of a beam size (26"). The two galaxies that we finished mapping are CIG 147 and CIG 1004, both of them with a total of 8 points around the central part of the galaxy. The maps are shown in figure 12.3.

From the maps we were able to tell that most of the dense gas seems to be concentrated at the center of each galaxy, only that we are not reaching the total amount expected according to [Gao & Solomon \(2004a\)](#) relation (Fig. 12.3), some emission seems to be spread outside the center. Fig. 12.1b) represents the total flux for the galaxies after mapping them and where we can see that the HCN flux density gets closer to what we expected from [Gao & Solomon \(2004a\)](#) relation on those galaxies with detections outside the central part, see also table 12.2 where we show the expected I_{HCN} , the I_{HCN} observed and the total I_{HCN} in the cases when mapping was completed.

We compared the HCN flux density that we expected, calculated from the [Gao & Solomon \(2004a\)](#) relation, with the actual HCN from the IRAM-30m telescope for both, the flux density at the center and the total flux density. From the $HCN_{\text{expected}}/HCN_{\text{real}}$ we know that we expected 2 times the amount of HCN flux density that we actually observed at the center of the galaxies. If we compare only the galaxies where we detected HCN around the center as well, the ratio at the center of these galaxies is 1.26 and the ratio of the total HCN of the same galaxies is 0.52; therefore, supporting the idea that the HCN gas is not only at the center. HCN/CO ratio in our sample is 0.048, which according to [Gao & Solomon \(2004b\)](#) is a value for normal galaxies with low a dense gas fraction.

12.4 Conclusions

- Relation HCN-FIR from [Gao & Solomon \(2004a\)](#) extends as well to isolated galaxies with lower FIR luminosities.
- The HCN is mainly concentrated in the center but, with some emission outside the center.
- HCN/CO for this sample is low, indicating that the galaxies are normal with a low level of activity.

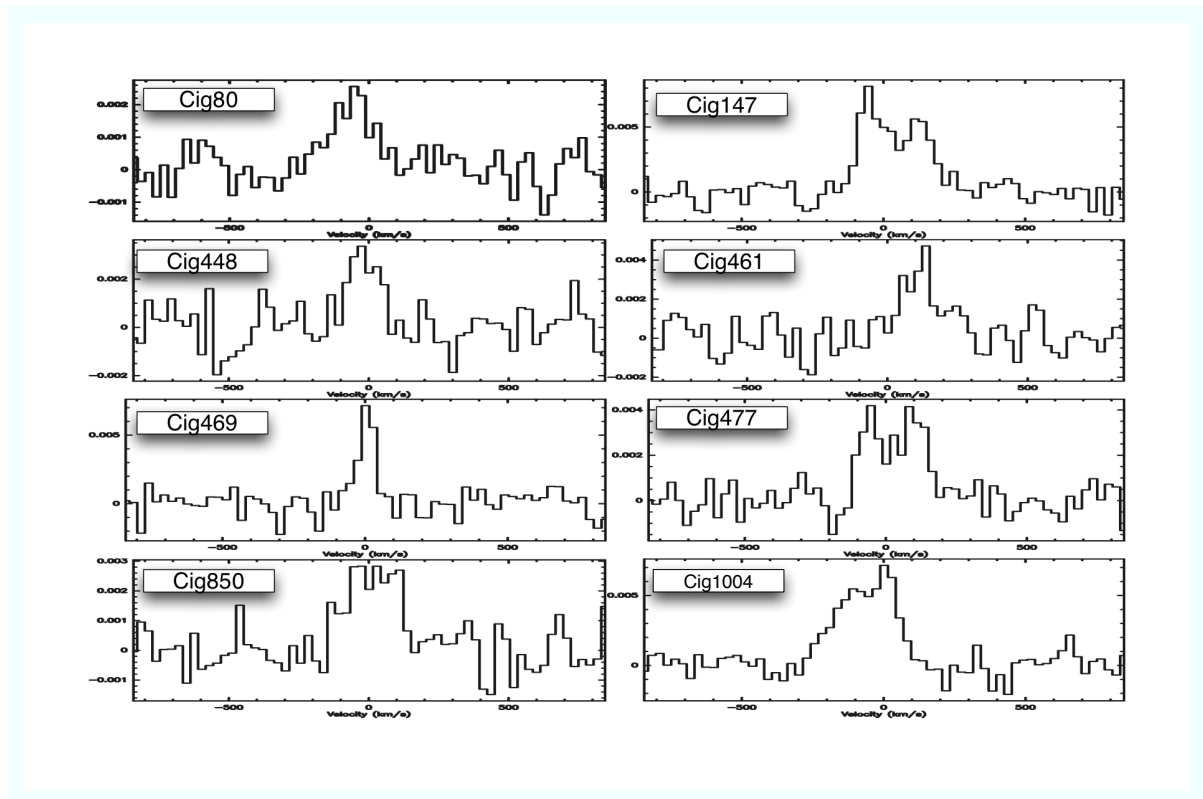
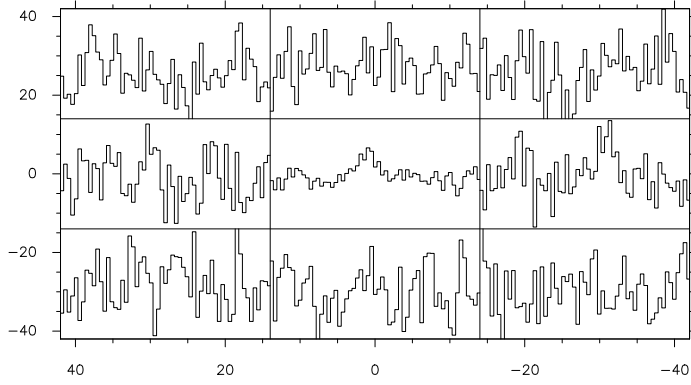
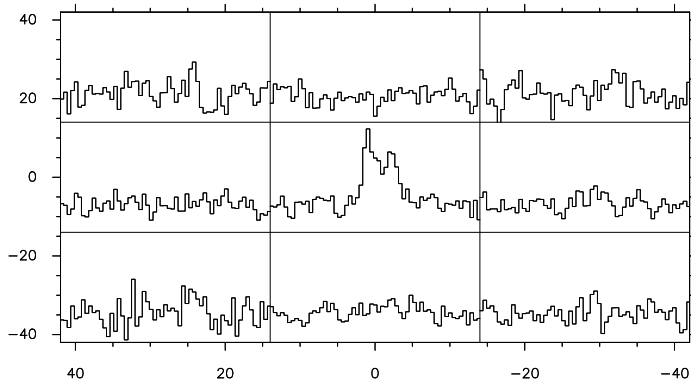


Figure 12.2: Temperature at the center of the galaxy.

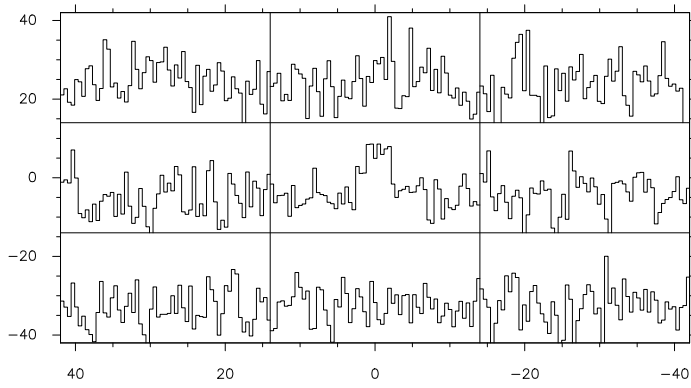
CIG 80



CIG 147



CIG 850



CIG 1004

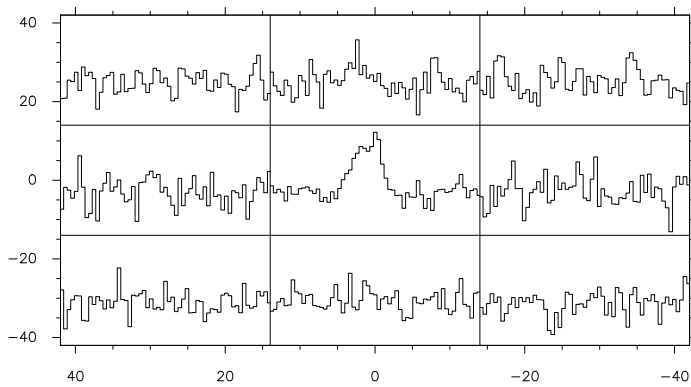


Figure 12.3: HCN(1-0) maps of CIG 147 and CIG 1004

Chapter 13

Summary and Conclusions

During these 4 years of PhD work, I have concentrated on a sample of galaxies that are part of the Thorough ANalysis of radio Galaxies Observations (TANGO) project. As described in chapter 2, TANGO is divided into two sub-samples, one of nearby galaxies, which is the Low z Sample (LzS) and the second sub-sample is of galaxies at medium redshifts, the Medium z Sample (MzS). This work has been based on the LzS of the TANGO project.

We have also compared the properties of our sample with different samples of elliptical galaxies, QSOs and ULIRGs with the purpose to better understand the behavior of the galaxies in the TANGO project. Those samples used as comparison sample were:

- [Wiklind et al. \(1995\)](#), a sample of elliptical galaxies, selected on the basis of their morphological type.
- [Evans et al. \(2005\)](#), a sample of elliptical radio galaxies selected according to their IR flux emission.
- [Mazzarella et al. \(1993\)](#), a sample of elliptical radio galaxies selected according to their IR flux emission.
- [Bertram et al. \(2007\)](#) a sample of galaxy hosting Low-Luminous QSOs.
- [Solomon et al. \(1997\)](#) a sample of ULIRGs.

We presented a survey of CO(1-0) and CO(2-1) lines for the 52 radio galaxies that belong to this sub-sample in the local universe, selected only on the basis of their radio continuum emission ([Ocaña Flaquer et al. 2010](#)) and we concluded that:

1. We clearly detected 38% (20/52) of the galaxies in the LzS, with 58% (38/52) total, including upper limits. The detection was for CO(1-0) and/or CO(2-1), and it was simultaneously detected in 11.5% of the galaxies.

2. Indication of molecular gas disk (double-horn) is found in 15% of the galaxies in LzS TANGO (27% of the detected galaxies) with confirmation on 3CR 31 with PdBI CO(1-0) map. We noted as well that our sample has less galaxies that show this pattern compared to the other samples where we noted that Wiklind et al. (1995) have 25%, the closest value to our sample. For the galaxies selected for their FIR emission or because they are QSOs, the percentage was higher, Evans et al. (2005) have 55 % of their galaxies with double-horn, Mazzarella et al. (1993) have 50% and Bertram et al. (2007) have 42.3%.
3. The CO(2-1)-to-CO(1-0) line ratio is 2.3 without taking into account the beam dilution effect, and likely to be ~ 0.6 with corrections, suggesting optically thick and sub-thermal CO emission.
4. From the 52 galaxies observed for CO(1-0), 90% were detected in the continuum; 43, out of the 52 galaxies, were simultaneously observed at CO(2-1) with a 65% detection rate for the continuum and this frequency.
5. We calculated the molecular gas mass for our sample using the data collected from the IRAM-30m telescope in Granada, Spain. The median value of the molecular gas mass for the LzS TANGO sample is $2.2 \times 10^8 M_{\odot}$. We found that when the sample of galaxies was chosen for their FIR emission, or because they are quasars or galaxies in interaction, the samples are in general an order of magnitude higher, in the order of $10^9 M_{\odot}$, compared to a sample of elliptical galaxies, which is in the order of $10^8 M_{\odot}$.
6. We confirmed that FR-II type galaxies are characterized by lower CO detection rates than FR-I and FR-c radio sources as claimed by Evans et al. (2005), and that the FR-II have a higher molecular gas mass, probably because of a malmquist bias.
7. Since one of the goals of this work was to build a Spectral Energy diagram (SED), we collected all the information about the FIR emission of our galaxies and we found that 35% of our galaxies were detected by IRAS at 60 and 100 μm .
8. We have calculated a $f_{100 \mu\text{m}}$ -to- $f_{60 \mu\text{m}}$ ratio of 1.9, which according to Bell (2003) could be interpreted as a galaxy with high temperature heated up by young stars in HII regions or by an AGN.
9. Taking into account the flux densities only from IRAS, We have an average dust temperature of 35.8K and a dust mass of $2.5 \times 10^5 M_{\odot}$.
10. The $M_{\text{H}_2}/M_{\text{dust}}$ gas-to-dust mass ratio, for the M_{dust} calculated with the IRAS fluxes, was about 260.

11. We collected Spitzer's flux density emissions with the same purpose of adding data to our SED and to calculate the mass and temperature for the different dust components. We found that 40% of the galaxies in TANGO were detected with Spitzer.
12. We succeeded in calculating 3 dust components for the mass and temperature of 3CR 31 showing a mass and temperature for the different components of: $T_1=19.7\text{K}$ and $M_1=3.16\times 10^7 M_\odot$; $T_2=71.7\text{K}$ and $M_2=3.98\times 10^5 M_\odot$; $T_3=495.05\text{K}$ and $M_3=1.31 M_\odot$.
13. Neutral Hydrogen is one of the most important molecules we could use for the analysis of our galaxies because it is a tracer of dynamical evolution. It also falls in the 1.4GHz part of the spectrum, which means that the continuum emission is one of the key values needed to study the synchrotron emission at lower frequencies. We observed with Effelsberg-100m telescope 20 of our galaxies, detecting only two, 3CR 264 and 3CR 270. In the literature, we found data for 11 more of the galaxies in our sample, where they were either detected (5 galaxies), or upper limits (6 galaxies).
14. Using the data we collected from the observations at IRAM-30m telescope, and using the astronomical statistical software (ASURV), we calculated a mean L_{CO} of the LzS in TANGO of $4.2 \times 10^7 K km/s pc^2$.
15. Using the data we collected from IRAS, and using ASURV, we calculated a median L_{FIR} of the LzS in TANGO of $6.9 \times 10^9 L_\odot$.
16. Once we calculated the L_{FIR} and L'_{CO} for the galaxies in our sample, we compared them with other samples and noted that the L_{FIR} vs. L'_{CO} relation is similar to what is found in the other samples. This suggests that some star formation could be taking place in these elliptical radio galaxies.
17. We calculated the Star Formation Rate (SFR) per unit gas mass in our galaxies and we found that it is $3.7 \pm 1.5 M_\odot/yr$, assuming that all the FIR emission comes from the dust heated by the young formed stars. Although we do keep in mind that this value is probably an overestimation since it does not take into account the AGN heating of the dust.
18. We calculated the stellar mass loss of the galaxies in TANGO for the galaxies detected in CO and the galaxies with upper limits larger than $5\times 10^9 M_\odot$. The median value stellar mass loss of the galaxies in TANGO is about $0.37 M_\odot/yr$, implying a median time of 1Gyr to refurbish the galaxy of molecular gas provided by the stellar mass loss without taking into account the consumption rate of the AGN and SF.

19. The gas in these galaxies can be due to multiple origins: stellar mass loss, accretion (cooling flow, hot X-ray halo), major/minor mergers or cosmological filament-fed. We cannot discard that the origin of the molecular gas could be a combination of some of the processes mentioned previously.
20. One of the conclusions already mentioned was the double horn profile feature in the spectra of 27% of the detected galaxies, which could be due to the presence of a molecular gas disk. With the CO(1-0) map obtained from IRAM-PdBI, for 3CR 31, we confirmed the presence of a molecular gas disk around this galaxy.
21. We calculated the synchrotron age for 3CR 31 assuming 2 different scenarios. For the first one, we assumed that all the flux density emission of this galaxy comes from its AGN and in this case the synchrotron age of 3CR 31 is about 26 Myr. For the second scenario, we considered the possibility that an old AGN existed, that probably stopped and a new AGN originated. This scenario has already been proposed as a "double-double morphology". For this case we calculated an old synchrotron age of about 11650 Myr and a new component of about 27 Myr.

We used a Control Sample to observe HCN in isolated galaxies from the AMIGA project with the purpose of comparing them with our sample of galaxies in the TANGO project. We observed HCN(1-0) in 15 galaxies with the IRAM-30m telescope and we concluded that:

- Relation HCN-FIR from [Gao & Solomon \(2004a\)](#) extends also in isolated galaxies with lower FIR luminosities.
- The HCN is mainly concentrated in the center, but with some emission outside the center.
- HCN/CO for this sample is low, 0.0048, which according to [Gao & Solomon \(2004b\)](#) is a value for normal galaxies with a low dense gas fraction.

Chapter 14

The Future of TANGO

As it has been mentioned already in the introduction, the project TANGO (Thorough ANalysis of radio Galaxies Observations, PIs: S. Leon & B. Ocaña Flaquer) is an international collaboration born from my PhD Thesis (in IRAM Granada, Spain), supervised by S. Leon (in ALMA/ESO), with the purpose of understanding the role of the Interstellar Medium (ISM) in elliptical radio galaxies. We have built two samples of radio galaxies, at low redshift ($z=0.0-0.1$, $n=52$ galaxies) and at medium redshift ($z=0.3-1.0$, $n=49$). The galaxies are selected only on the basis of their radio continuum flux densities. The main driver of this project is to study the origin of the molecular gas in the radio galaxies (stellar mass loss, X-ray cooling flow, minor/major mergers, cosmological filaments,...), its distribution and dynamics related with the properties of the radio galaxies and the interplay between the molecular gas and the Active Galactic Nuclei (AGN) via the radio jet, X-ray/Optical field, etc. We also want to correlate ISM properties as a function of age of the radio sources which can be determined from the Spectral Energy Distribution (SED). This study will enlighten us on the factor driving the evolution of the radio galaxies and conditioning their characteristics (type, duty cycle, star formation, etc.).

In chapter 2 we have described the properties of the two samples of the TANGO project. This PhD thesis is a detailed study of the ISM for the Low z Sample (LzS), concentrated on the molecular gas and dust properties.

The future work for the LzS TANGO will be:

- To study the star formation in the elliptical host galaxies using different instruments such as GALEX (for UV emissions), optical instruments such as Calar Alto, VLT etc (for H_α).
- To study the environment of the radio galaxies using optical images (SLOAN) in order to correlate the environment with the ISM properties.

- To study the SED of all the galaxies (as was already done with 3CR 31) by fitting various dust components for the thermal part of the SED using the data presented in this work.
- To study the synchrotron emission (in order to calculate the synchrotron age) the same way that we have already done with 3CR 31.
- To investigate the interaction between the radio jet and the ISM using high spatial resolution (ALMA, PdBI, CARMA).
- To study in detail the difference between the FR-I and FR-II galaxies in this sample.
- To prepare observations with ALMA in order to have better frequency coverage, special resolution, sensitivity in spectroscopy and continuum to sample the SED. For the preparation we plan to observe our galaxies with currently available radio telescopes.

With the MzS TANGO:

- To measure the effects of evolution in the molecular gas content by observing CO transitions.
- To observe the CO transitions we plan to use different radio telescopes such as VLA, IRAM-PdBI, ATCA, CARMA, SMA, IRAM-30m, APEX.
- To prepare the ALMA observations for CO, HCN, HCO⁺ because these rotational lines and their ratios will be able to probe obscure central energy sources of active galaxies in terms of chemical abundances (as explained by [Yamada et al. 2009](#), and references therein).
- To compare the molecular gas content with other properties such as X-Ray, optical, radio continuum, environment, etc.
- To compare the properties of the FIR versus the molecular gas.
- To compare all the properties from the study of the MzS with the LzS. The comparison will reveal the effects of the evolution.

This work, as mentioned at the beginning, is an international collaboration. We note that the studies stated in this chapter will be done with international collaborators.

Chapter 15

Conclusiones

Durante estos 4 años de doctorado he concentrado mi trabajo en una muestra de galaxias que forman parte del proyecto TANGO (*Thorough ANalysis of radio Galaxies Observations*; en castellano *Análisis detallado de observaciones de radio-galaxias*) que se centra en el estudio del medio interestelar de estas radio galaxias. Como se describió en el capítulo 2, TANGO está dividido en dos sub-muestras, la primera formada por galaxias cercanas a bajo redshift¹ (LzS: Low-z Sample), y la segunda que comprende las galaxias a medio redshift (MzS: Medium-z Sample). El presente trabajo se basa en el conjunto LzS del proyecto TANGO.

También hemos comparado las propiedades de nuestra muestra con diferentes muestras de galaxias elípticas, quásares (QSOs) y galaxias ultra-luminosas en el infrarrojo (ULIRGs) con el propósito de entender mejor el comportamiento de las galaxias del proyecto TANGO. En particular, las muestras utilizadas en la comparación fueron:

- [Wiklind et al. \(1995\)](#), una muestra de galaxias elípticas seleccionadas con base en su tipo de morfología.
- [Evans et al. \(2005\)](#), una muestra de radio galaxias elípticas seleccionadas con base en su emisión en el infrarrojo (IR).
- [Mazzarella et al. \(1993\)](#), una muestra de radio galaxias elípticas seleccionadas con base en su emisión en el IR.
- [Bertram et al. \(2007\)](#), una muestra de galaxias anfitrionas de QSOs poco luminosos.
- [Solomon et al. \(1997\)](#), una muestra de ULIRGs.

¹corrimiento al rojo.

Presentamos un sondeo de líneas de CO(1-0) y CO(2-1) de las 52 radio galaxias pertenecientes a nuestra sub-muestra en el Universo local, seleccionadas solamente con base en su emisión continua en el radio ([Ocaña Flaquer et al. 2010](#)) y concluimos que:

1. Detectamos líneas de CO(1-0) y/o CO(2-1) en un total de 58% (38/52) de las galaxias de tipo LzS (incluyendo sus límites superiores), donde el 38% (38/52) están claramente detectadas. En 11.5% de las galaxias se detectaron ambas líneas simultáneamente.
2. La presencia de disco de gas molecular se encontró en 15% de las galaxias tipo LzS de TANGO (27% de las galaxias detectadas) confirmadas en 3CR 31 con un mapa de CO(1-0) hecho con el interferómetro PdBI del IRAM. Resaltamos que nuestra muestra contiene menos galaxias que presentan estas características con respecto a otras muestras analizadas; en particular en la muestra de [Wiklind et al. \(1995\)](#) estas características se detectaron en el 25% de las galaxias, el porcentaje más cercano a nuestra muestra. Para las galaxias seleccionadas por su emisión en el IR lejano o porque sean QSOs, su porcentaje era mayor; [Evans et al. \(2005\)](#) tenía un 55%, [Mazzarella et al. \(1993\)](#) tenía un 50% y [Bertram et al. \(2007\)](#) tenía un 42.3%.
3. La tasa de las líneas de CO(2-1)-a-CO(1-0) es de 2.3 sin tomar en cuenta el efecto de la dilución del haz, y podría ser de ~ 0.6 con las correcciones, implicando una emisión de CO sub-termal y ópticamente grueso.
4. De las 52 galaxias observadas para la línea de CO(1-0), el 90 % fueron detectadas en el continuo; de las 43 galaxias observadas para la línea CO(2-1), 65 % fueron detectadas en el continuo a estas frecuencias.
5. Calculamos la masa del gas molecular de nuestra muestra utilizando los datos observados con el radio telescopio IRAM-30m localizado en Granada, España. El valor medio del gas molecular para la muestra de LzS en TANGO es de $2.2 \times 10^8 M_{\odot}$. Encontramos que cuando la muestra de galaxia fue elejida por su emisión en el IR lejano, o por ser QSOs o galaxias en interacción, su gas molecular es de un orden de magnitud mayor, en el orden de $10^9 M_{\odot}$, comparado con una muestra de galaxias elípticas que está en el orden de $10^8 M_{\odot}$.
6. Confirmamos que las radio galaxias de tipo FR-II se caracterizan por tener una tasa de detección menor para la molécula de CO comparado con las radio galaxias de tipo FR-I o de tipo FR-c como había propuesto [Evans et al. \(2005\)](#), y que las FR-II tienen mayor cantidad de gas molecular, probablemente por el sesgo de malmquist.

7. Como una de las metas de este proyecto era hacer un distribución de energía espectral (SED), recopilamos toda la información sobre la emisión del IR lejano de nuestra muestra y encontramos que un 35% de las galaxias están detectadas a las frecuencias de IRAS de $60\mu\text{m}$ y $100\mu\text{m}$.
8. Hemos calculado una tasa de $f_{100\mu\text{m}}-a-f_{60\mu\text{m}}$ de 1.9, lo cual, según Bell (2003) puede ser interpretado como una galaxia de alta temperatura calentado, o bien por estrellas jóvenes en regiones HII o bien por su núcleo galáctico activo (AGN).
9. Tomando en cuenta sólo la densidad de flujo proveniente de IRAS, tenemos un promedio de la temperatura del polvo de 35.8K y un promedio de masa de polvo de $2.5 \times 10^5 M_{\odot}$.
10. La tasa de masa de gas-a-masa de polvo (M_{H_2}/M_{dust}) utilizando la masa de polvo proveniente de las mediciones de IRAS solamente, es alrededor de 260.
11. Recaudamos emisiones de densidades de flujo de Spitzer con el propósito de añadir datos al SED y de calcular la masa y la temperatura de polvo de diferentes componentes. Encontramos que el 40% de las galaxias en TANGO están detectadas con Spitzer.
12. Hemos tenido éxito calculando tres componentes para la masa y la temperatura del polvo para la galaxia 3CR 31 mostrando una masa y una temperatura de $T_1=19.7\text{K}$ y $M_1=3.16 \times 10^7 M_{\odot}$; $T_2=71.7\text{K}$ y $M_1=3.98 \times 10^5 M_{\odot}$; $T_1=495.05\text{K}$ y $M_1=1.31 M_{\odot}$.
13. El hidrógeno neutro (HI) es una de las moléculas más importantes que se pueden utilizar en el análisis de nuestras galaxias, porque es un trazador de evolución dinámica. También se encuentra a una frecuencia de 1.4 GHz en el espectro, lo cual implica que su emisión en continuo es una de las claves que se necesitan para estudiar la emisión sincrotrón a frecuencias bajas. Hemos observado con el telescopio Effelsberg-100m 20 de nuestras galaxias detectando solamente 2 de ellas, 3CR 264 y 3CR 270. En la literatura hemos encontrado datos para 11 más de nuestras galaxias donde 5 de ellas fueron detectadas y 6 más se encontraron como límites superiores.
14. Utilizando los datos recopilados de observaciones hechas con el telescopio IRAM-30m, y utilizando un software para el análisis de supervivencia estadística (ASURV) hemos calculado la media de L'_{CO} para LzS en TANGO de $4.2 \times 10^7 K km/s pc^2$.
15. Utilizando los datos recopilados de IRAS, y utilizando ASURV, hemos calculado una mediana para L_{FIR} para LzS en TANGO de $6.9 \times 10^9 L_{\odot}$.

16. Una vez calculados L'_{CO} y L_{FIR} para las galaxias en nuestra muestra, los hemos comparados con los de otras muestras donde notamos que la relación L'_{CO} vs. L_{FIR} es similar a la relación de otras muestras. Esto sugiere que podría haber formación estelar (SF) en nuestra muestra.
17. Hemos calculado una tasa de SF en unidades de masa de gas molecular en nuestra muestra y encontramos que es $3.7 \pm 1.5 M_{\odot}/yr$, asumiendo que toda la emisión del IR lejano viene del polvo calentado por las estrellas jóvenes. Aún así, tenemos presente que este valor es una sobre estimación porque no toma en cuenta el calentamiento del polvo por el AGN.
18. Calculamos una pérdida de masa estelar para las galaxias de TANGO detectadas para la molécula de CO y las galaxias con límites superiores mayores que $5 \times 10^9 M_{\odot}$. La media del valor de la pérdida de masa estelar es de $0.37 M_{\odot}/yr$, lo que implica una media del tiempo de 1 Gyr para llenar de nuevo de gas molecular proveniente de la pérdida de masa estelar sin tomar en cuenta la tasa de consumición del AGN y de SF.
19. El origen del gas en estas galaxias puede ser por: pérdida de masa estelar, acreción (flujos de enfriamiento, aureola de rayos X calientes) fusiones mayores/o menores o alimentación por filamentos cosmológicos. No debemos olvidar que el origen del gas molecular puede ser una combinación de éstos procesos.
20. Se ha mencionado ya que el 27% de nuestras galaxias han mostrado un perfil en el espectro que podría ser debido a un disco de gas molecular. Con un mapa de CO(1-0) hecho en el interferómetro IRAM-PdBI para la galaxia 3CR 31, hemos confirmado que es efectivamente debido a la presencia de un disco de gas, que el espectro muestra dicha forma.
21. Hemos calculado la edad del sincrotrón para 3CR 31 asumiendo 2 distintas posibilidades. En la primera hemos asumido que toda la emisión de densidad de flujo de esta galaxia viene de su AGN y en este caso la edad del sincrotrón es de 26 Myr. En la segunda posibilidad se plantea que existió un AGN que probablemente dejó de ser activo y por razones desconocidas aún, se ha reactivado. Esta posibilidad ha sido propuesta con el nombre de "doble-doble morfología". Para este caso se ha calculado una edad para el sincrotrón de 11650 Myr para el sincrotrón emitido por el viejo AGN, y una edad de 27 Myr para el nuevo.

Hemos utilizado una muestra de control para observar AGN en galaxias aisladas del proyecto AMIGA, con el propósito de compararlas con nuestras galaxias en el proyecto de TANGO. Hemos observado HCN(1-0) en 15

galaxias aisladas con el radiotelescopio del IRAM-30m y hemos concluido que:

1. La relación de [Gao & Solomon \(2004a\)](#) de HCN-FIR se extiende también en galaxias aisladas con baja luminosidad en el IR lejano.
2. El HCN está mayormente concentrado en el centro aunque también emite fuera del centro.
3. La tasa de HCN/CO para esta muestra es bajo, 0.0048, lo cual, según [Gao & Solomon \(2004a\)](#) es un valor para galaxias normales con una fracción baja de gas denso.

Appendix A

Individual Galaxies

A.1 3CR 31

Other Names: NGC 0383, B2 0104+32

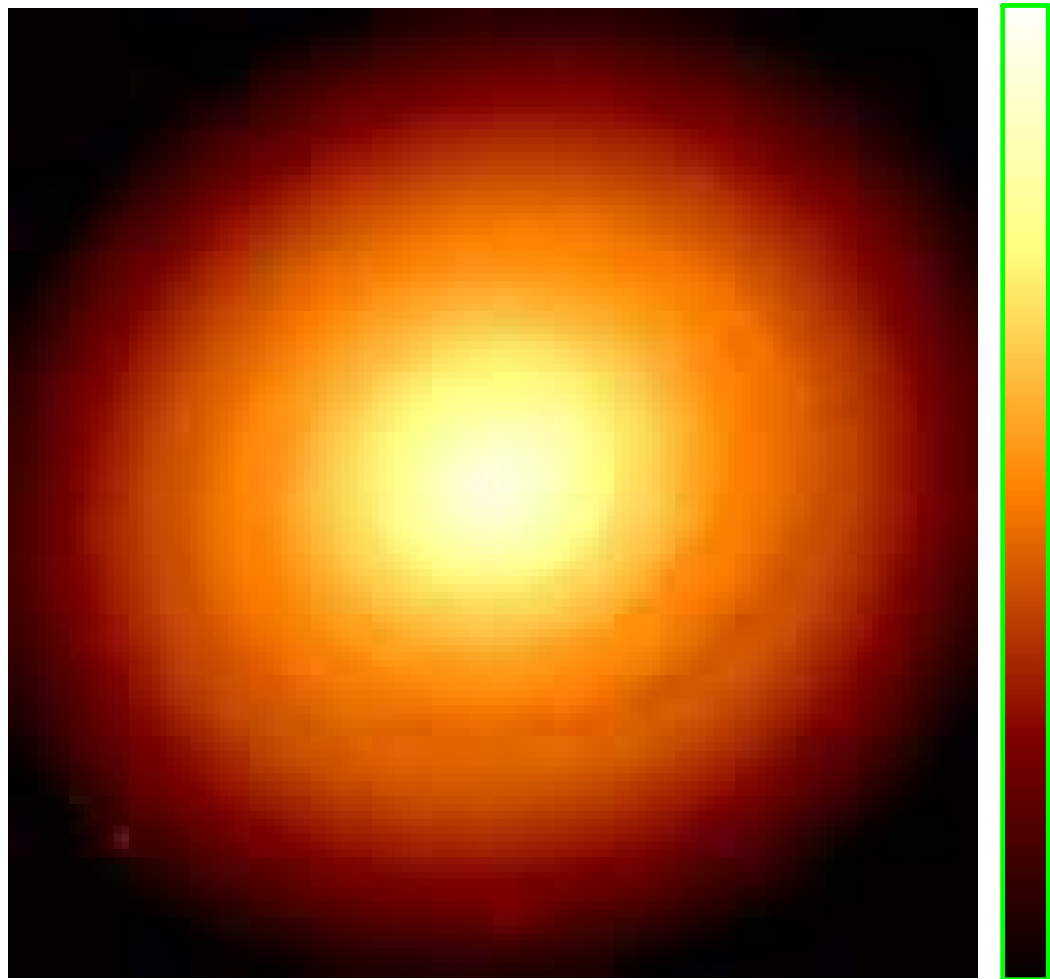


Figure A.1: 3CR 31 HST image.

This galaxy have been studied in many specific ways. We have observed this galaxy with the IRAM 30m telescope, clearly detecting CO(1-0) and CO(2-1) where the spectra showed a *double-horn* profile typical of the presence of a molecular gas disk. We have also used observations from IRAM PdBI which resulted in a confirmation of the molecular gas disk around the center of this galaxy.

This galaxy is the only galaxy so far where we have studied the dust components taking into account the flux density emission at the lower frequencies to calculate the age (see explanation on chapters 8 and 11). We calculated, on chapter 6, different dust components for temperature and mass using the SED. For more information on this galaxy, see chapter 11 where we have done a complete analysis.

Table A.1: General Data for 3CR 31

RA:	01h07m24.9s
Dec:	+32d24m45s
FR:	I
z_{CO} :	0.0169
Distance [Mpc]:	71.06
Line Width [km/s]:	550
$I_{CO(1-0)}$ [K km/s]:	5.68 ± 0.81
$I_{CO(2-1)}$ [K km/s]:	14.06 ± 1.13
M_{H_2} [M_{\odot}]:	$16.81 \pm 2.38 \times 10^8$
M_{Dust} [M_{\odot}]:	6.76×10^6
T_{Dust} [K]:	28.33
Line Ratio:	2.5 ± 0.2

Table A.2: Fluxes of 3CR 31

Wavelength	flux measurement mJy
S_{3mm}	79.07 ± 1.13
S_{1mm}	74.39 ± 2.78
$f_{12\mu m}$	<30
$f_{25\mu m}$	<45
$f_{60\mu m}$	435 ± 65.3
$f_{100\mu m}$	1675 ± 251

Table A.3: Luminosities for 3CR 31

Parameter	Luminosity
L_{CO} [K km/s pc ²]	3.24×10^8
L_{FIR} [L_{\odot}]	5.89×10^9
L_{178MHz} [W Hz ⁻¹ sr ⁻¹]	9.08×10^{23} (Evans et al. 2006)

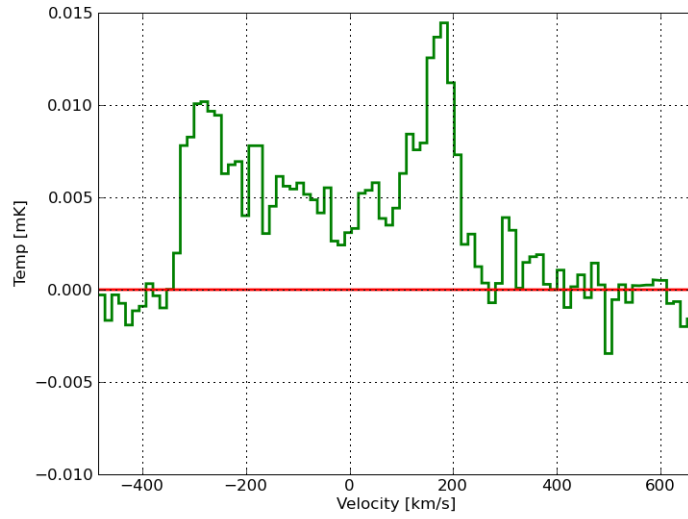


Figure A.2: 3CR 31 CO(1-0)

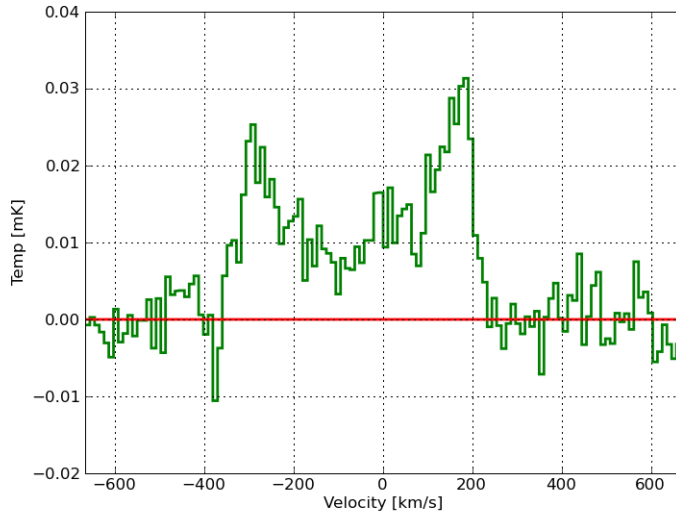
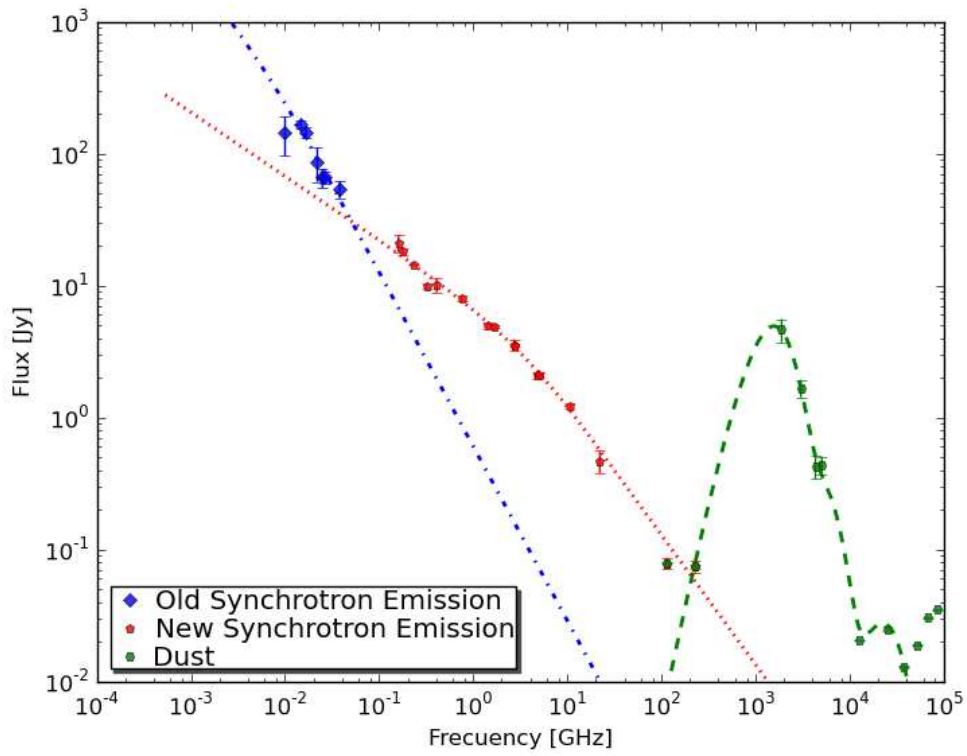


Figure A.3: 3CR 31 CO(2-1)

Figure A.4: The Spectral Energy diagram for 3CR31



A.2 3CR 40

Other Names: ARP 308, NGC 547

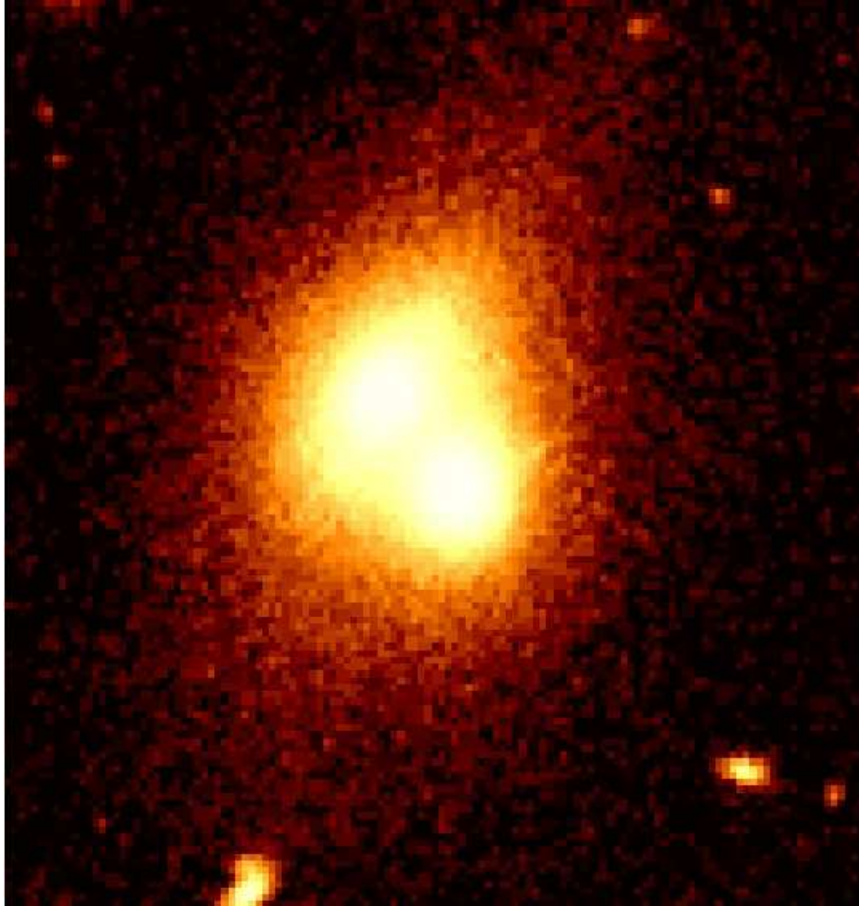


Figure A.5: 3CR 40 HST image.

We observed this galaxy for CO(1-0) and CO(2-1) but it was not detected. A dusty disk on 100 pc scales is seen in both $H_{\alpha}+[N II]$ and [O III] images, marked by the absence of emission along a circumnuclear rim that is more prominent in the [O III] image than it is in $H_{\alpha}+[N II]$. Low- and high-excitation line emission is seen tracing the edges of the disk on the southern side, while [O III] emission on the northern side of the disk appears less extensively distributed. The band marking the disk is not continuous, rather in both images it is interrupted by low-surface brightness line emission apparently connecting the southern and northern sides of the disk in the same general location. Note that the apparent major axis of the disk appears roughly orthogonally oriented with respect to the FR II radio jet axis ([Tremblay et al.](#)

2009).

Table A.4: General Data for 3CR 40

R.A.:	01h25m59.8s
Dec:	-01d20m34s
FR:	I
z_{CO} :	0.018
D [Mpc]:	70.37
Line Width [km/s]:	Not Detected.
$I_{CO(1-0)}$ [K km/s]:	<1.11
$I_{CO(2-1)}$ [K km/s]:	-
$M_{H_2} M_{\odot}$:	$< 3.25 \times 10^8$

Table A.5: Fluxes of 3CR 40

Wavelength	flux measurement mJy
S_{3mm}	96.91 ± 0.9
S_{1mm}	20.11 ± 1.80
$f_{12\mu m}$	< 115
$f_{25\mu m}$	< 160
$f_{60\mu m}$	< 165
$f_{100\mu m}$	< 405

Table A.6: Luminosities for 3CR 40

Parameter	Luminosity - L_{\odot}
L_{CO} [K km/s pc^2]	$< 7.24 \times 10^7$
L_{FIR} [L_{\odot}]	$< 2 \times 10^9$

A.2.1 HI data

3CR 40 was observed with Effelsberg-100m Telescope during the summer of 2008. We integrated for 56.31 minutes. With an $I_{HI}=4.34\pm 0.05$ Jy km/s. Figure A.8 is the spectra observed. This galaxy could be tentative detected in emission and may be a tentative detection in absorption.

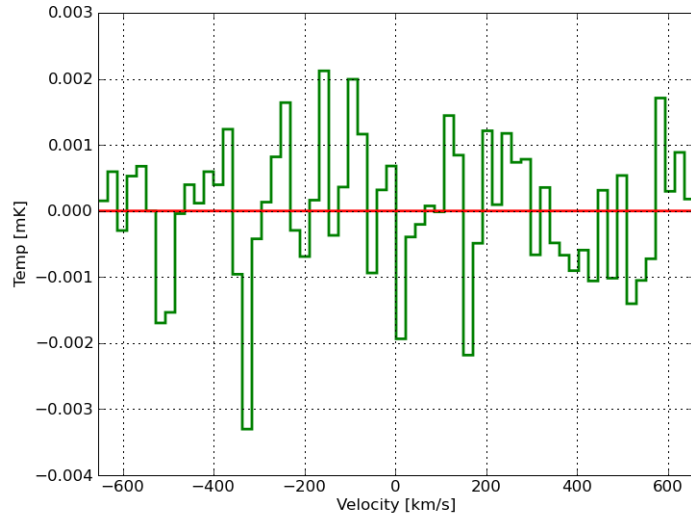


Figure A.6: 3CR 40 CO(1-0)

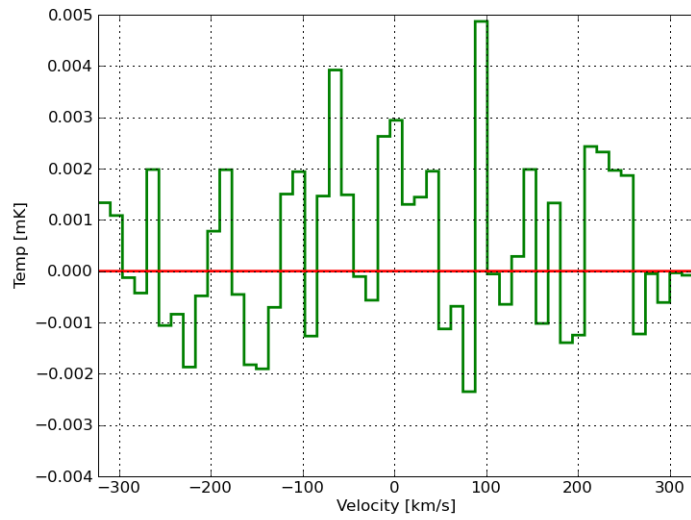


Figure A.7: 3CR 40 CO(2-1)

57; 3 3C40 NONE FRONTTEST-2 O: 28-JUN-2008 R: 29-JUN-2008
RA: 01:25:59.800 DEC: -01:20:34.00 (2000.0) Offs: -2.676 -1.078 Eq
Unknown Tau: 0.000 Tsys: 27.62 Time: 56.31 El: 29.15
N: 255 I0: 128.0 V0: 0.000 Dv: -17.04 LSR
FO: 1374.80000 Df: 7.8144E-02 Fi: 1224.80000
B ef: 0.000 F ef: 0.000 G im: 0.000
H2O : 0.000 Pamb: 0.000 Tamb: 0.0 Tchop: 0.0 Tcold: 0.0
Tatm: 0.0 Tau: 0.000 Tatm i: 0.0 Tau i: 0.000
2926- 2937,

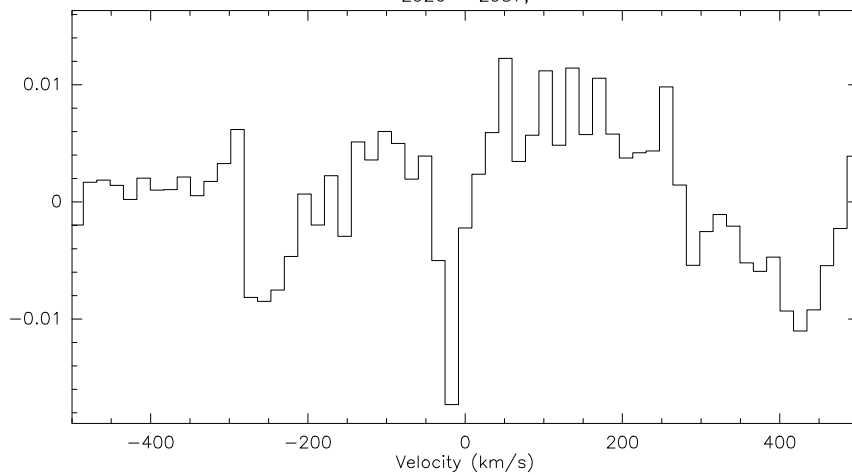


Figure A.8: HI emission for 3CR 40

A.3 3CR66B

Other Names: UGC 01841

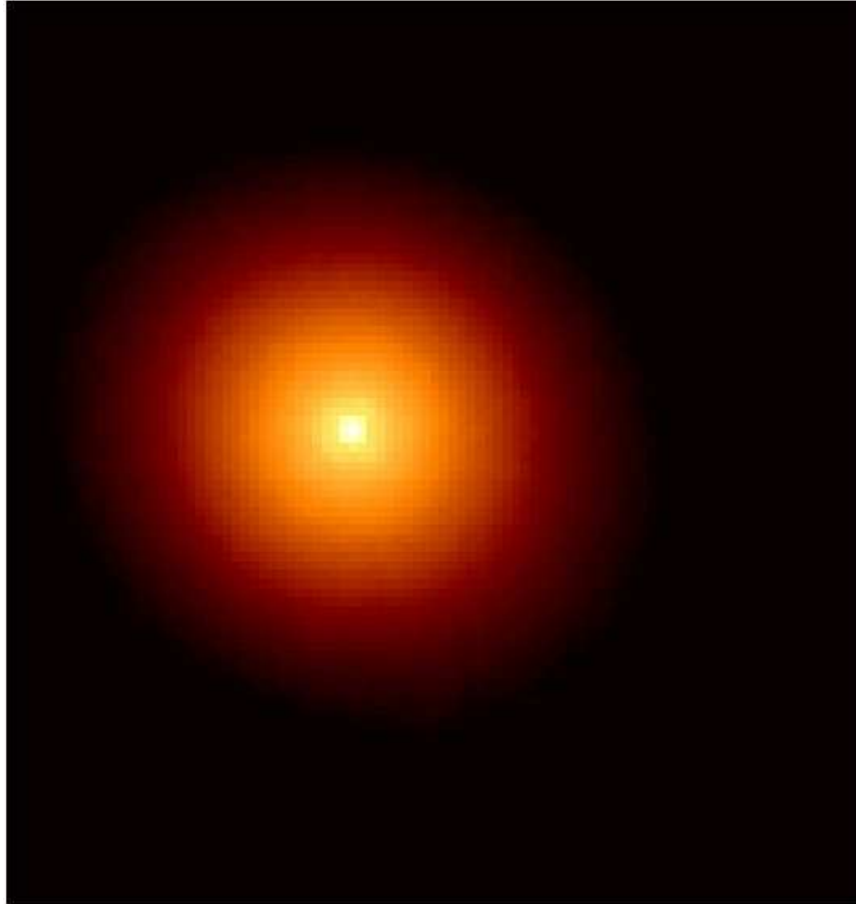


Figure A.9: 3CR 66B HST image.

The well known bright radio jet of this galaxy was first discovered by [Northover \(1973\)](#) and the optical jet was first detected by [Butcher et al. \(1980\)](#). [Meng & Zhou \(2006\)](#) were able to performed a detail study of the jet using the HST/WFPC2 images comparing them with the radio images and finding an excellent correspondence. We can see in the optical image of the figure the presence of a disk, and this is in agreement with the spectra of the galaxy, which has a detection but a very faint one. The central galaxy disk width is about 10'' in the optical image, and the velocity width for CO(1-0) is about 250 km/s.

Table A.7: General Data for 3CR 31

RA:	02h23m11.4s
Dec:	+42d59m31s
FR:	I
z_{CO} :	0.0157
Distance [Mpc]:	85.20
Line Width:	250
$I_{CO(1-0)}$ [K km/s]:	0.21 ± 0.053
$I_{CO(2-1)}$ [K km/s]:	...
$M_{H_2} M_{\odot}$:	$0.89 \pm 0.23 \times 10^8$

Table A.8: Fluxes of 3CR 66B

Wavelength	flux measurement mJy
S_{3mm}	110.12 ± 0.43
S_{1mm}	73.08 ± 1.39
$f_{12\mu m}$	<100
$f_{25\mu m}$	<85
$f_{60\mu m}$	<130
$f_{100\mu m}$	<350

Table A.9: Luminosities for 3CR 66B

Parameter	Luminosity
L_{CO} [K km/s pc^2]	1.70×10^7
L_{FIR} [L_{\odot}]	$<2.09 \times 10^9$
L_{178MHz} [W Hz ⁻¹ sr ⁻¹]	2.21×10^{24} (Evans et al. 2006)

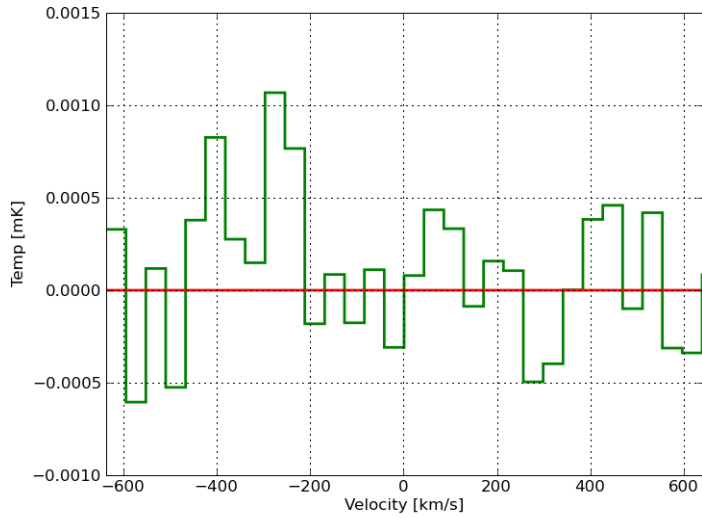


Figure A.10: 3CR 66B CO(1-0)

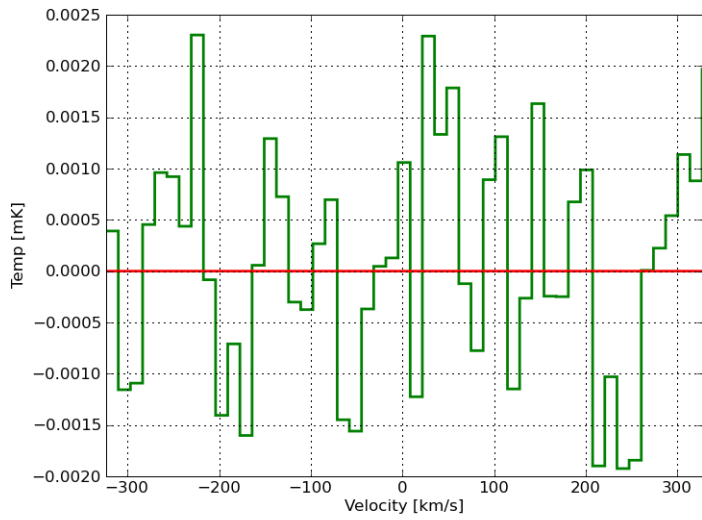
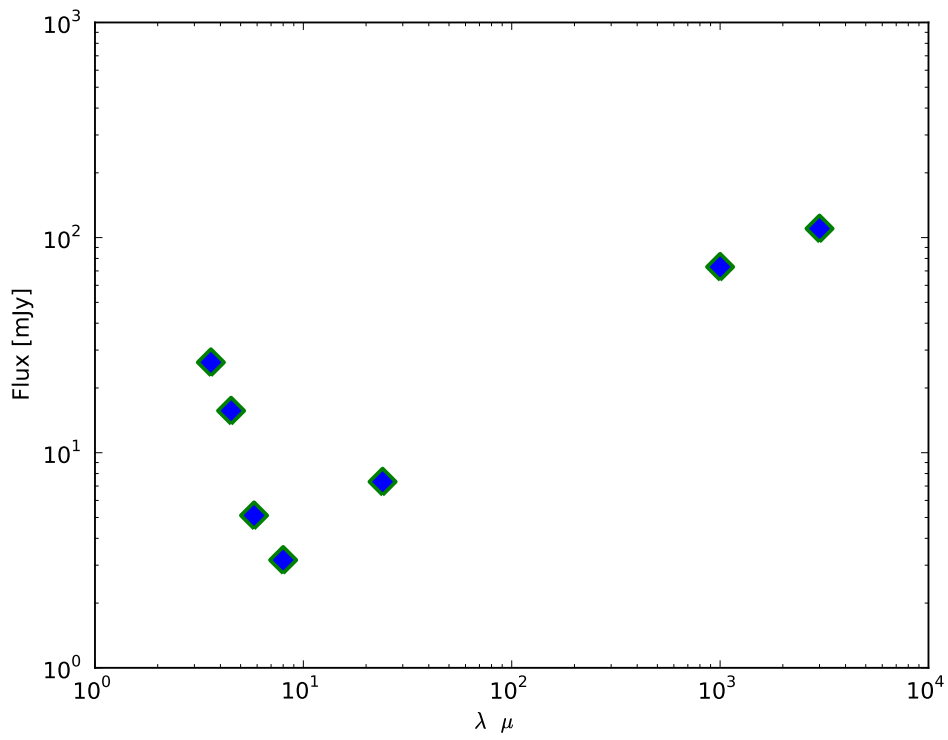


Figure A.11: 3CR 66B CO(2-1)

Figure A.12: The Spectral Energy diagram for 3CR 66B



A.4 3CR 83.1

Other Names: NGC 1265, UGC 02651

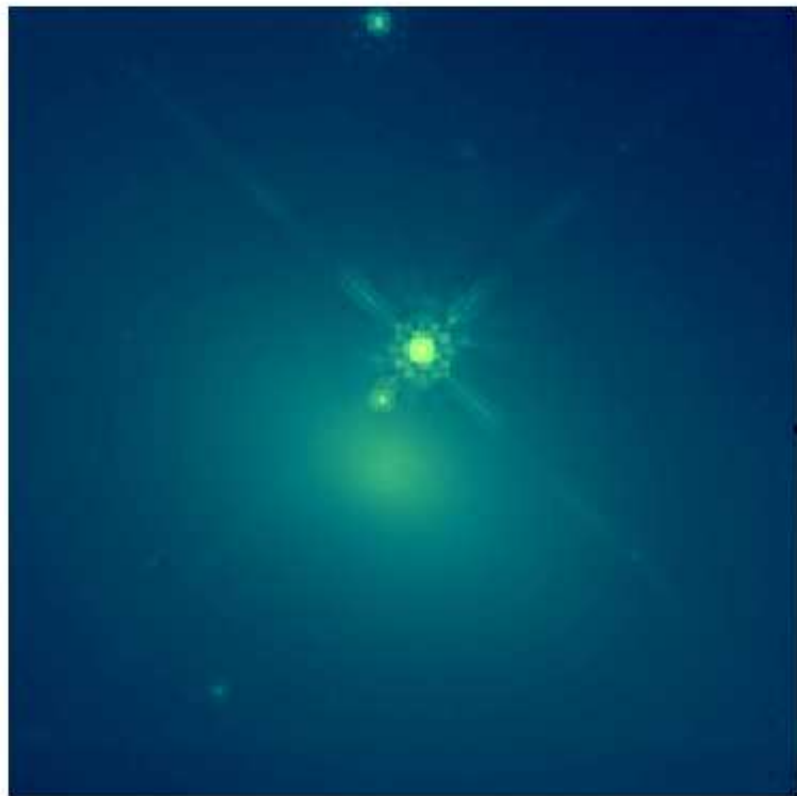


Figure A.13: 3CR 83.1 HST image.

It is one of the seven cases where the molecular gas has been clearly detected in the CO(2-1) transition and not in the CO(1-0) transition. We calculated the CO(1-0) intensity using the 2.3 average line ratio of the galaxies

detected in both lines. If we look at the optical image we can see a dust lane of about $2.24''$, according to [Martel et al. \(1999\)](#) this dust lane is oriented in $\sim 171^\circ$, nearly orthogonal to the radio jet.

This galaxy was observed in X-Ray with the Einstein Observatory by [Fabbiano et al. \(1984\)](#) but it was not detected.

Table A.10: General Data for 3CR 83.1

RA:	03h18m15.8s
Dec:	+41d51m28s
FR:	I
z_{CO} :	0.0251
Distance [Mpc]:	104.6
Line Width:	-
$I_{CO(1-0)}$ [K km/s]:	0.53 ± 0.002
$I_{CO(2-1)}$ [K km/s]:	1.13 ± 0.12
$M_{H_2} M_\odot$:	$3.60 \pm 0.0013 \times 10^8$

Table A.11: Fluxes of 3CR 83.1

Wavelength	flux measurement mJy
S_{3mm}	33.45 ± 0.69
S_{1mm}	...
$f_{12\mu m}$	<50
$f_{25\mu m}$	<35
$f_{60\mu m}$	<105
$f_{100\mu m}$	<395

Table A.12: Luminosities for 3CR 83.1

Parameter	Luminosity - L_\odot
L_{CO} [K km/s pc^2]	6.02×10^7
L_{FIR} [L_\odot]	$<3.16 \times 10^9$
L_{178MHz} [W Hz $^{-1}$ sr $^{-1}$]	3.39×10^{24} (Evans et al. 2006)

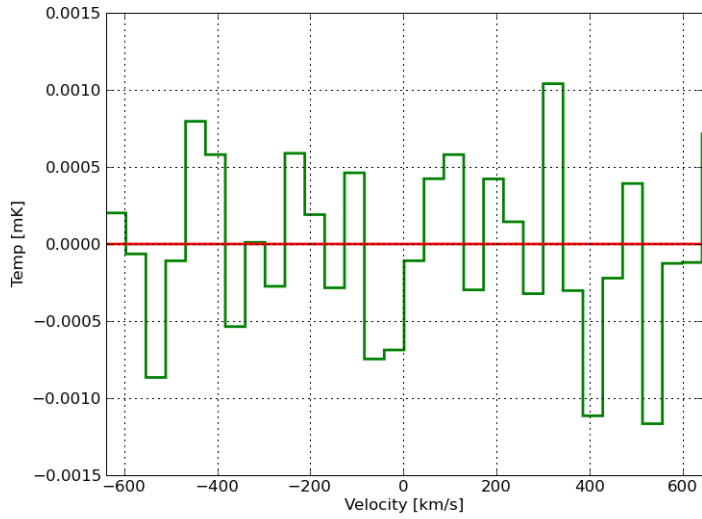


Figure A.14: 3CR 83.1 CO(1-0)

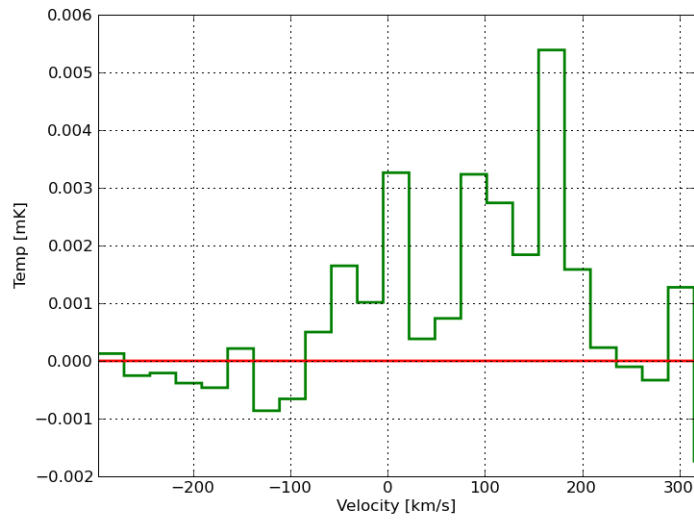


Figure A.15: 3CR 83.1 CO(2-1)

A.5 3CR 88

Other Name: UGC 02748

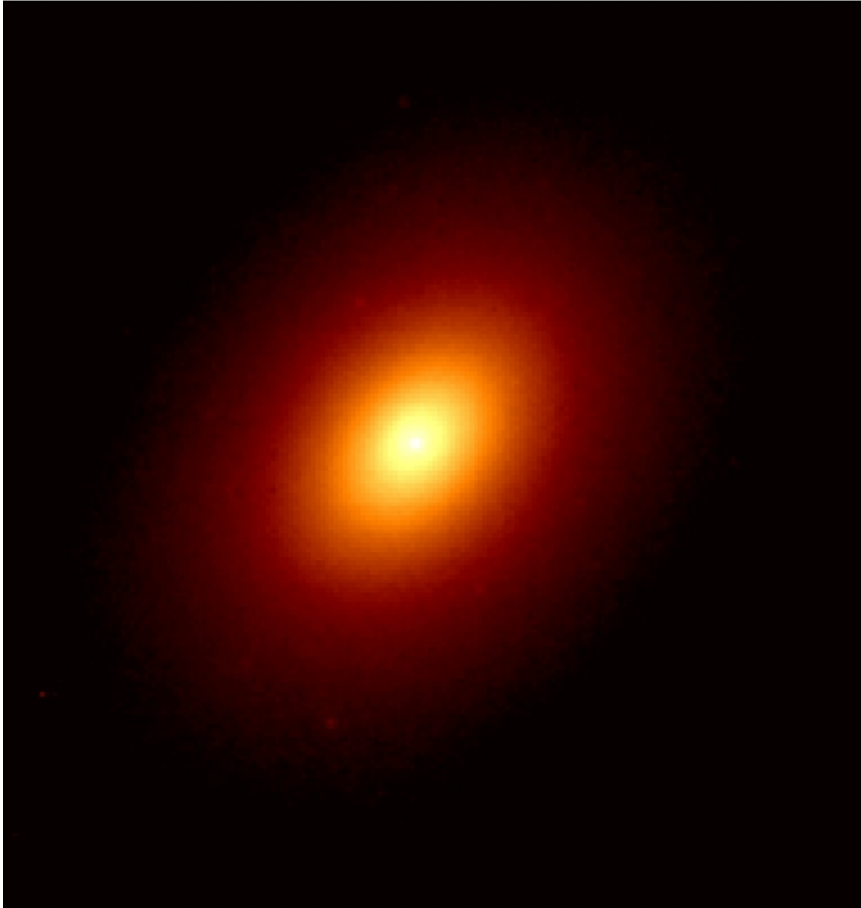


Figure A.16: 3CR 88 HST image.

This galaxy is clearly detected in the CO(1-0) transition. In the optical image there is no sign of disturbance. It has a f_{100} -to- f_{60} ratio of 4.5, the highest in the sample, and the lowest M_{H_2}/M_{gas} gas-to-dust mass ratio with a ratio of 17.

Table A.13: General Data for 3CR 88

RA:	03h27m54.2s
Dec:	+02d33m42s
FR:	II
z_{CO} :	0.03
Distance [Mpc]:	126.20
Line Width [km/s]:	300
$I_{CO(1-0)}$ [K km/s]:	0.238 ± 0.05
$I_{CO(2-1)}$ [K km/s] :	-
$M_{H_2} M_{\odot}$:	$2.19 \pm 0.44 \times 10^8$
$M_{Dust} M_{\odot}$:	1.38×10^7
T_{Dust} [K]:	27.02

Table A.14: Fluxes of 3CR 88

Wavelength	flux measurement mJy
S_{3mm}	121.84 ± 0.43
S_{1mm}	87.05 ± 1.3
$f_{12\mu m}$	<95
$f_{25\mu m}$	<115
$f_{60\mu m}$	180 ± 27
$f_{100\mu m}$	816 ± 122

Table A.15: Luminosities for 3CR 88

Parameter	Luminosity
L_{CO} [K km/s pc^2]	4.17×10^7
L_{FIR} [L_{\odot}]	9.71×10^9

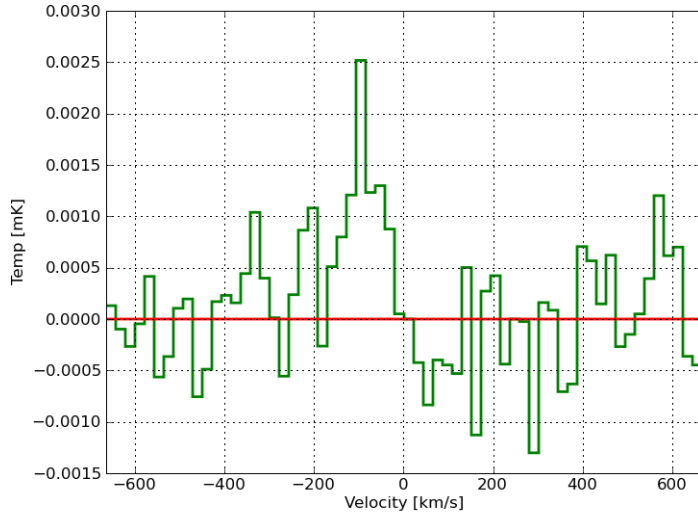


Figure A.17: 3CR 88 CO(1-0)

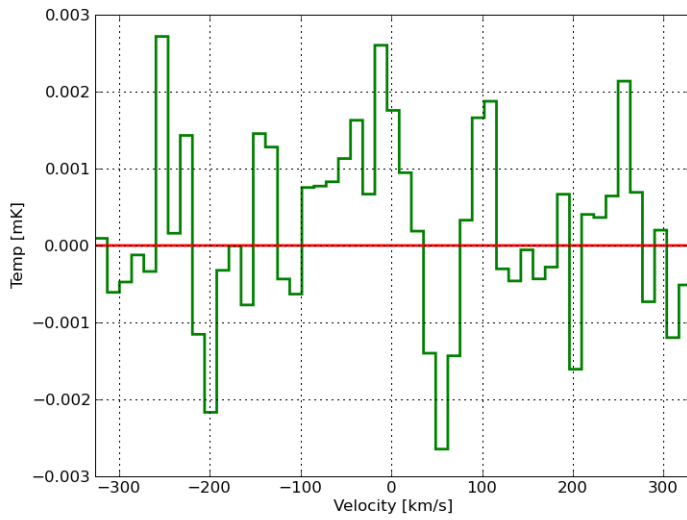
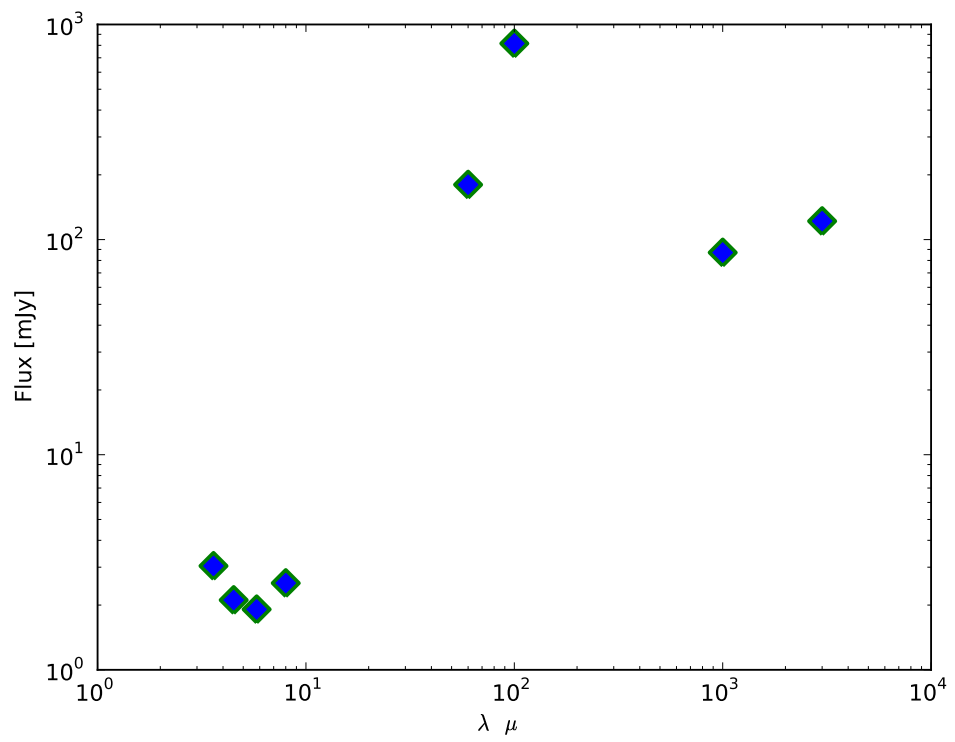


Figure A.18: 3CR 88 CO(2-1)

Figure A.19: The Spectral Energy diagram for 3CR 88



A.6 3CR 98

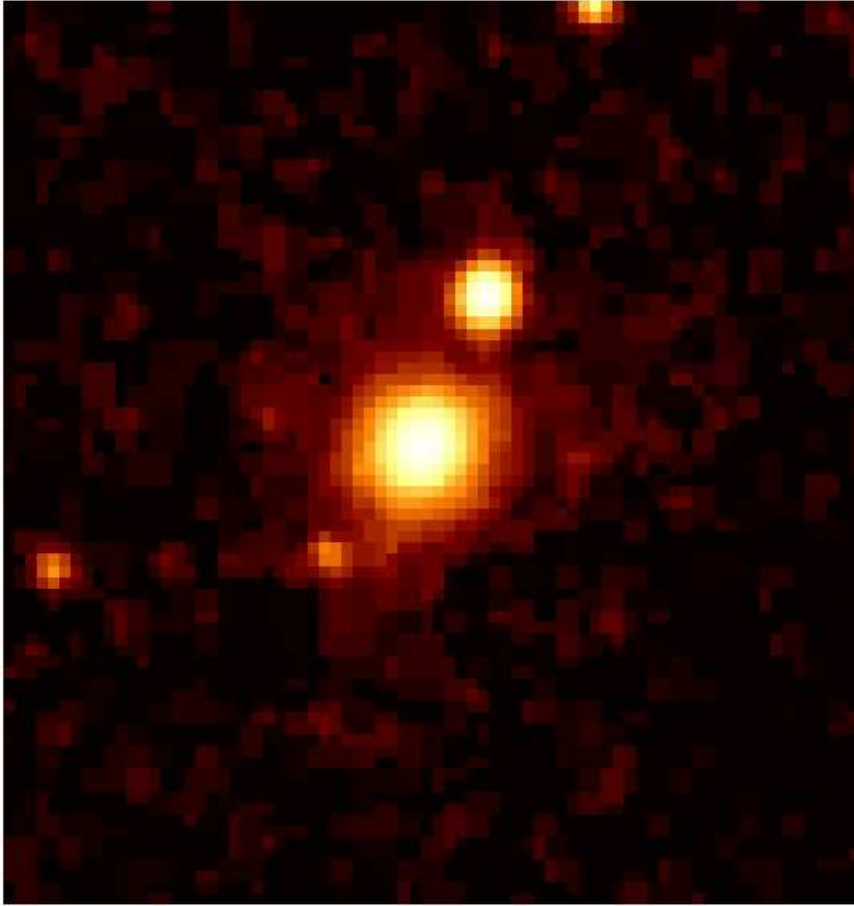


Figure A.20: 3CR 98 optical image.

Table A.16: General Data for 3CR 88

RA:	03h58m54.4s
Dec:	+10d26m03s
FR:	II
z_{CO} :	0.03
Distance [Mpc]:	126.20
Line Width [km/s]:	-
$I_{CO(1-0)}$ [K km/s]:	<0.73
$I_{CO(2-1)}$ [K km/s]:	-
M_{H_2} [M_{\odot}]:	< 7.27×10^8

Table A.17: Fluxes of 3CR 88

Wavelength	flux measurement mJy
S_{3mm}	18.09 ± 0.52
S_{1mm}	6.18 ± 1.54
$f_{12\mu m}$	<20
$f_{25\mu m}$	85 ± 12.8
$f_{60\mu m}$	<80
$f_{100\mu m}$	<300

Table A.18: Luminosities for 3CR 98

Parameter	Luminosity
L_{CO} [K km/s pc^2]	$<1.32 \times 10^8$
L_{FIR} [L_{\odot}]	$<3.47 \times 10^9$
L_{178MHz} [W Hz $^{-1}$ sr $^{-1}$]	8.75×10^{24} (Evans et al. 2006)

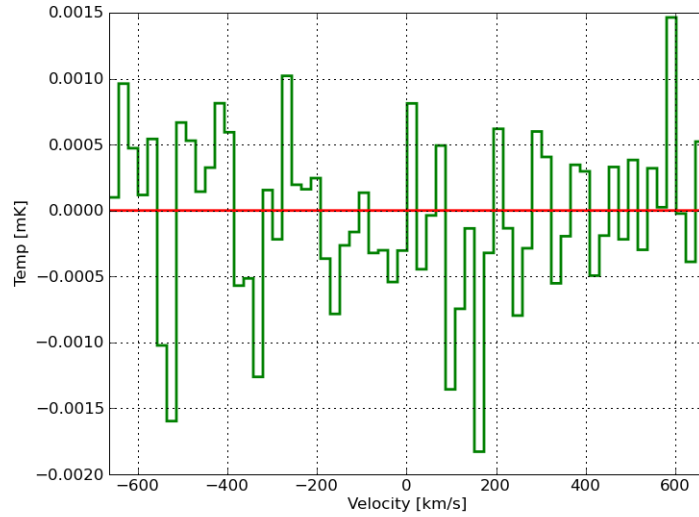


Figure A.21: 3CR 98 CO(1-0)

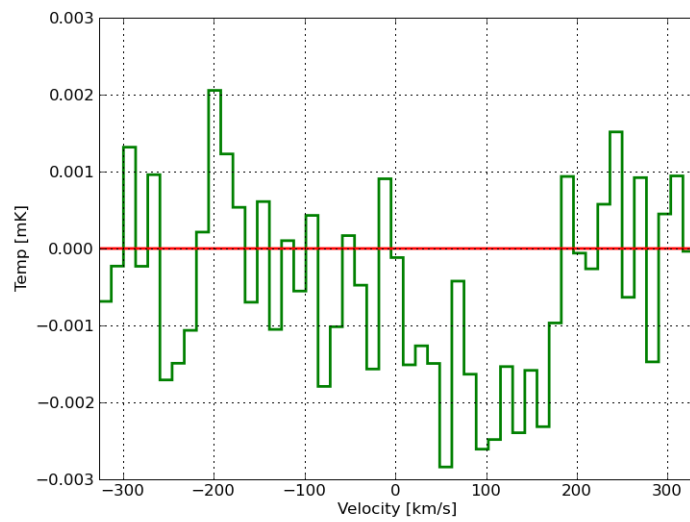


Figure A.22: 3CR 98 CO(2-1)

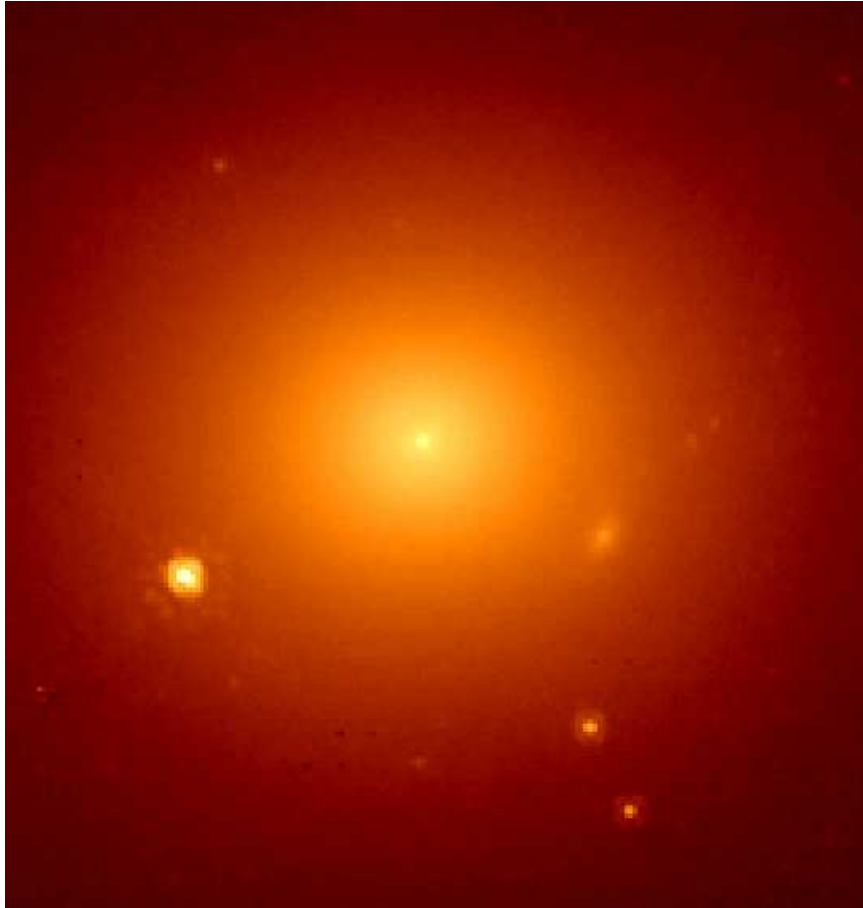
A.7 3C 129

Figure A.23: 3CR 129 HST image.

It is another example of CO(2-1) detection with no detection in the CO(1-0) transition line. The maximum velocity width of this galaxy is 200 km/s. There is no hint on interaction in the Hubble image of this galaxy. We calculated the CO(1-0) intensity using the 2.3 average line ratio of the galaxies detected in both lines.

Compact H_{α} + [N II] emission with very low surface brightness is observed to be co-spatial with the nucleus. Conversely, the nucleus is not detected in the [O III] image, where instead only very faint extended emission that appears to be associated with the nucleus extends $1''$ to the north and south (Tremblay et al. 2009).

Table A.19: General Data for 3CR 129

RA:	04h49m09.1s
Dec:	+45d00m39s
FR:	I
z_{CO} :	0.0208
Distance [Mpc]:	86.4
Line Width:	-
$I_{CO(1-0)}$ [K km/s] :	0.28 ± 0.024
$I_{CO(2-1)}$ [K km/s] :	0.59 ± 0.11
$M_{H_2} M_{\odot}$:	$1.3 \pm 0.11 \times 10^8$

Table A.20: Fluxes of 3CR 129

Wavelength	flux measurement mJy
S_{3mm}	28.53 ± 0.65
S_{1mm}	0.91 ± 1.27
$f_{12\mu m}$...
$f_{25\mu m}$...
$f_{60\mu m}$...
$f_{100\mu m}$...

Table A.21: Luminosities for 3CR 129

Parameter	Luminosity -
L_{CO} [K km/s pc^2]	2.40×10^7
L_{FIR}	...

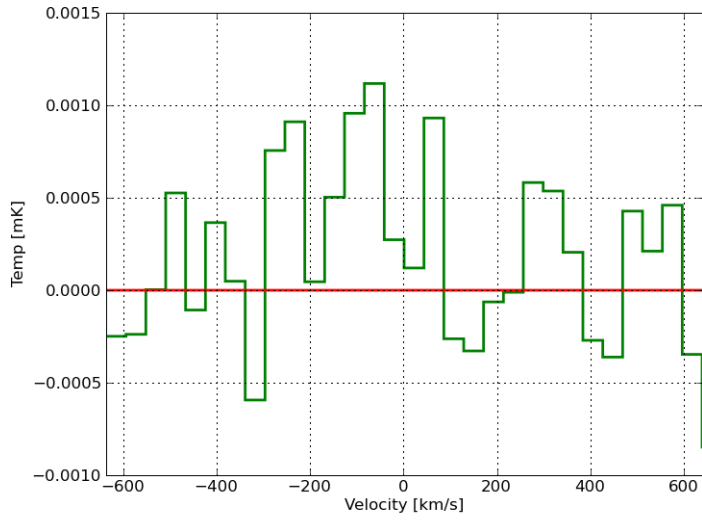


Figure A.24: 3CR 129 CO(1-0)

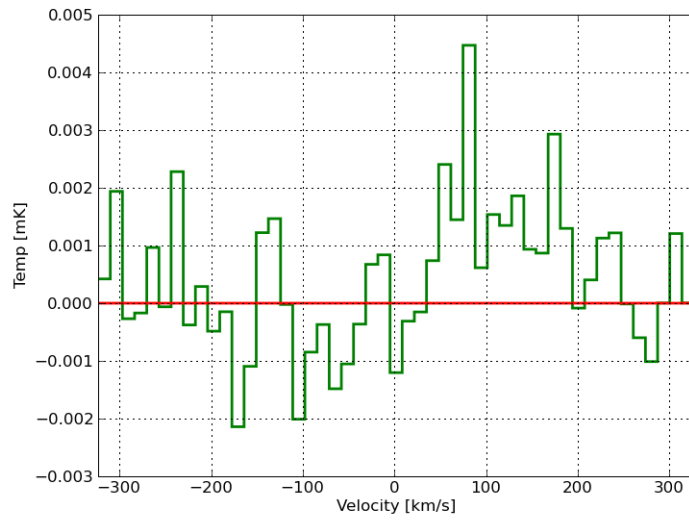


Figure A.25: 3CR 129 CO(2-1)

A.8 3CR 236

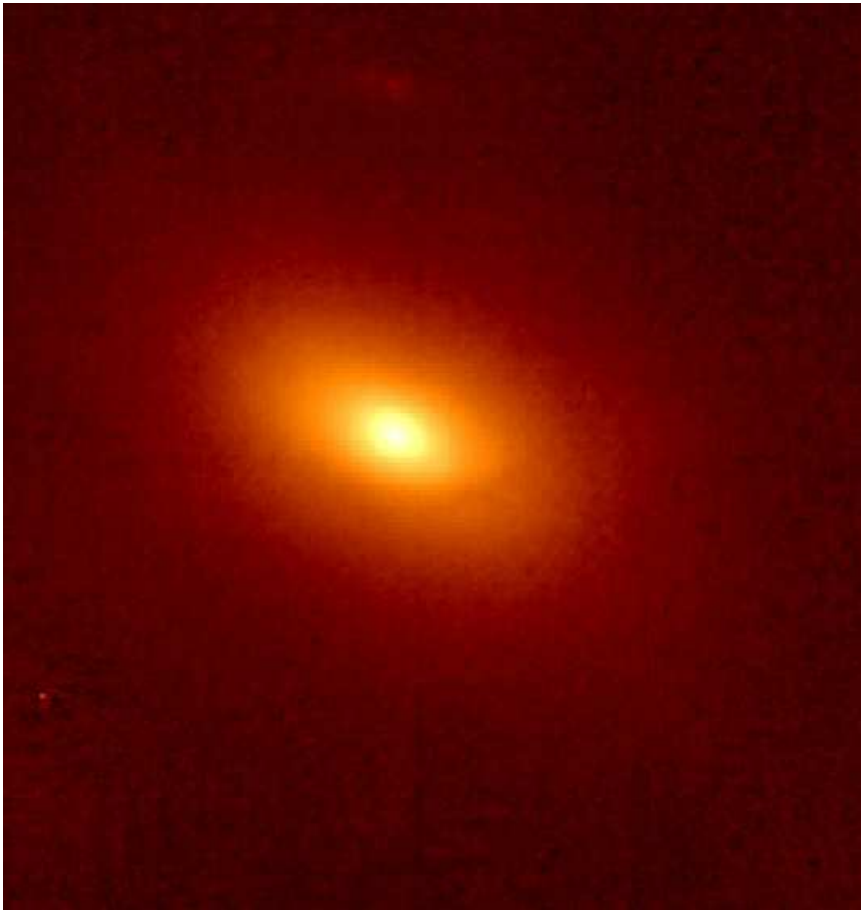


Figure A.26: 3CR 236 HST image.

We did not detect this galaxy for CO(1-0), and we do not have data for CO(2-1).

Table A.22: General Data for 3CR 236

RA:	10h06m01.7s
Dec:	+34d54m10s
FR:	II
z_{CO} :	0.1
Distance [Mpc]:	412
Line Width:	-
$I_{\text{CO}(1-0)}$ [K km/s]:	<0.75
$I_{\text{CO}(2-1)}$ [K km/s]:	XXX
$M_{\text{H}_2} M_{\odot}$:	$<80.70 \times 10^8$

Table A.23: Fluxes of 3CR 236

Wavelength	flux measurement mJy
$S_{3\text{mm}}$	225.06 ± 0.57
$S_{1\text{mm}}$	Not Observed
$f_{12\mu\text{m}}$	<20
$f_{25\mu\text{m}}$	<20
$f_{60\mu\text{m}}$	72 ± 10
$f_{100\mu\text{m}}$	<60

Table A.24: Luminosities for 3CR 236

Parameter	Luminosity
L_{CO} [K km/s pc^2]	1.26×10^9
L_{FIR} [L_{\odot}]	$<1.9 \times 10^{10}$

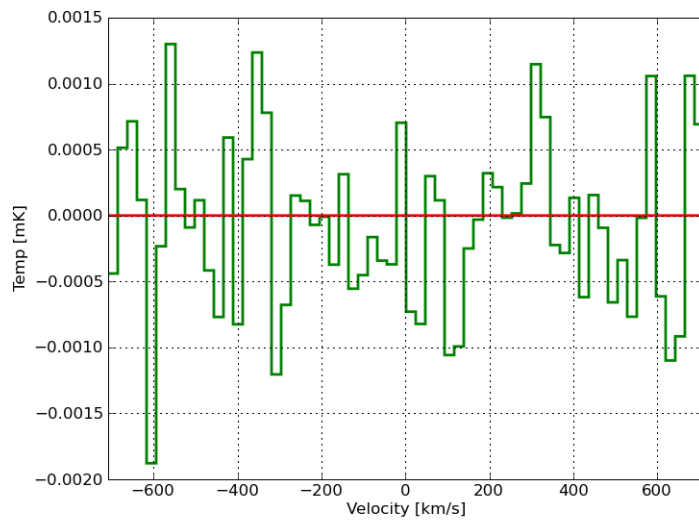


Figure A.27: 3CR 236 CO(1-0)

A.9 3C 264

Other Names: NGC 3862, UGC 06723

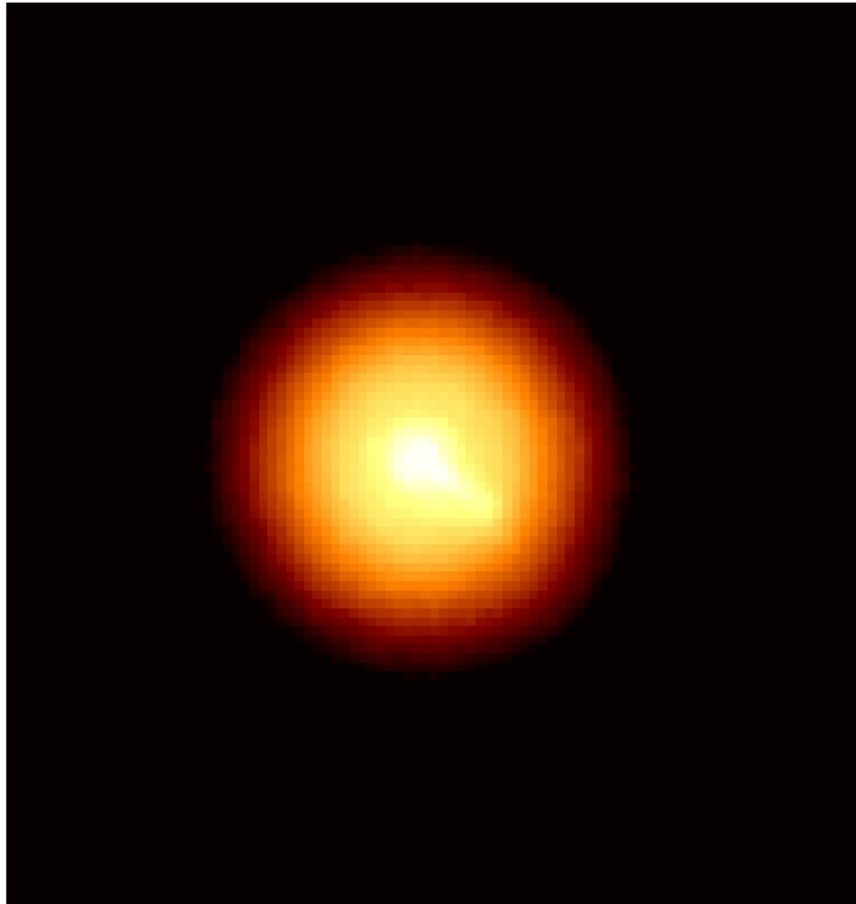


Figure A.28: 3CR 264 HST image.

This galaxy shows the double horn profile, in both transition lines, typical of a molecular gas disk. The velocity width of this galaxy for CO(1-0) and CO(2-1) is about 200 km/s, so its rotational velocity is about 100 km/s without taking into account the inclination. We can see the disk profile in the optical image where a jet is visible as well ([Crane et al. 1993](#)) and studied by [Baum et al. \(1997\)](#) who suggested that the optical synchrotron emission, clearly visible in the optical image from the HST is associated with the jet. According to [Martel et al. \(1999\)](#) the nucleus is unresolved, and the host galaxy is very circular and smooth.

Table A.25: General Data for 3CR 264

RA:	11h45m05.0s
Dec:	+19d36m23s
FR:	I
z_{CO} :	0.02
Distance:	90.90 [Mpc]
Line Width [km/s]:	200
$I_{CO(1-0)}$ [K km/s]:	0.70 ± 0.15
$I_{CO(2-1)}$ [K km/s]:	1.48 ± 0.16
$M_{H_2} M_{\odot}$:	$3.37 \pm 0.74 \times 10^8$
Line Ratio:	2.1 ± 0.2

Table A.26: Fluxes of 3CR 264

Wavelength	flux measurement mJy
S_{3mm}	174.64 ± 0.5
S_{1mm}	87.35 ± 1.13
$f_{12\mu m}$	<36
$f_{25\mu m}$	<42
$f_{60\mu m}$	210 ± 52
$f_{100\mu m}$	<181

Table A.27: Luminosities for 3CR 264

Parameter	Luminosity
L_{CO} [K km/s pc^2]	6.46×10^7
L_{FIR} [L_{\odot}]	$<2.88 \times 10^9$
L_{178MHz} [W Hz $^{-1}$ sr $^{-1}$]	2.20×10^{24} (Evans et al. 2006)

A.9.1 HI data

This is the only galaxy we detected using Effelsbert to study the emission of HI at 1.4 GHz. We found a $M_{HI} = 15.6 \times 10^8 M_{\odot}$.

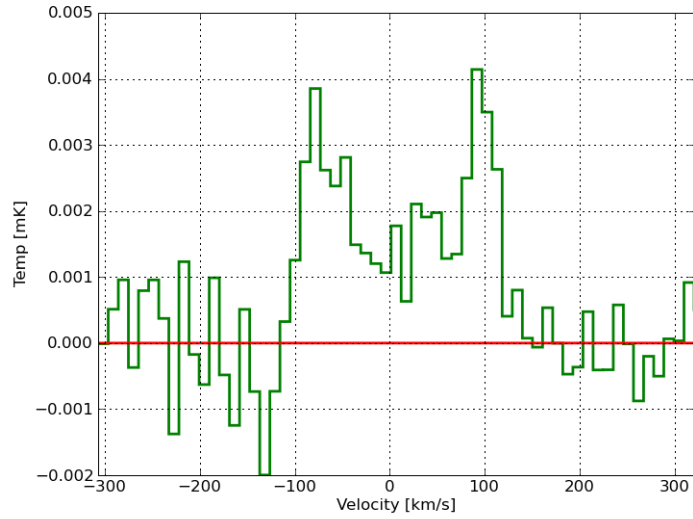


Figure A.29: 3CR 264 CO(1-0)

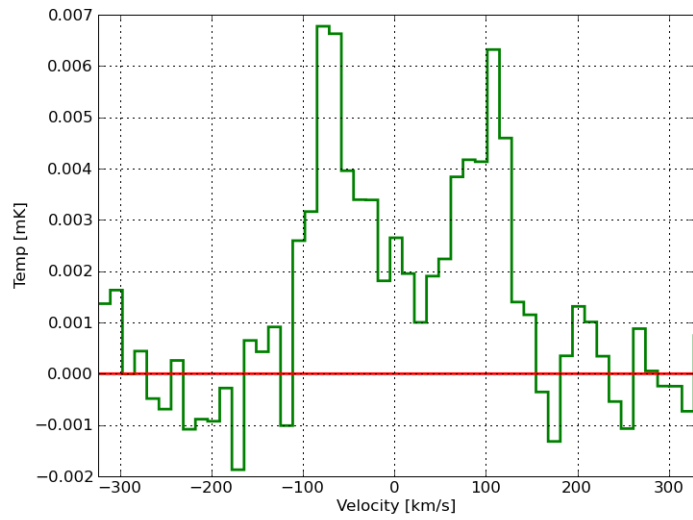


Figure A.30: 3CR 264 CO(1-0)

153; 3 3C264 NONE FRONTTEST-2 O: 28-JUN-2008 R: 29-JUN-2008
 RA: 11:44:30.002 DEC: 19:50:00.00 (2000.0) Offs: +3.533 +2.279 Eq
 Unknown Tau: 0.000 Tsys: 25.94 Time: 58.98 El: 20.40
 N: 127 l0: 64.00 v0: 0.000 Dv: -34.21 LSR
 F0: 1369.66200 Df: 0.1563 Fi: 1219.66200
 B ef: 0.000 F ef: 0.000 G im: 0.000
 H2O : 0.000 Pamb: 0.000 Tamb: 0.0 Tchop: 0.0 Tcold: 0.0
 Tatm: 0.0 Tau: 0.000 Tatm i: 0.0 Tau i: 0.000
 3078- 3090,

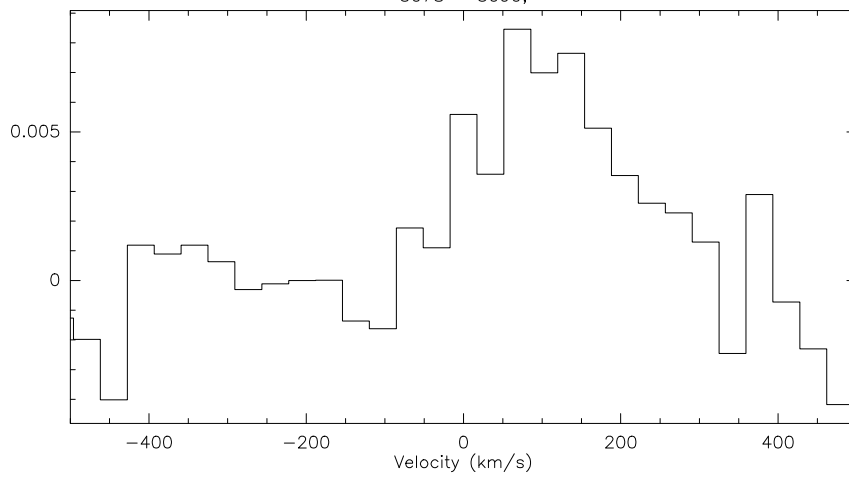


Figure A.31: HI emission for 3CR 264

A.10 3C 270

Other Names: NGC 4261, UGC 07360

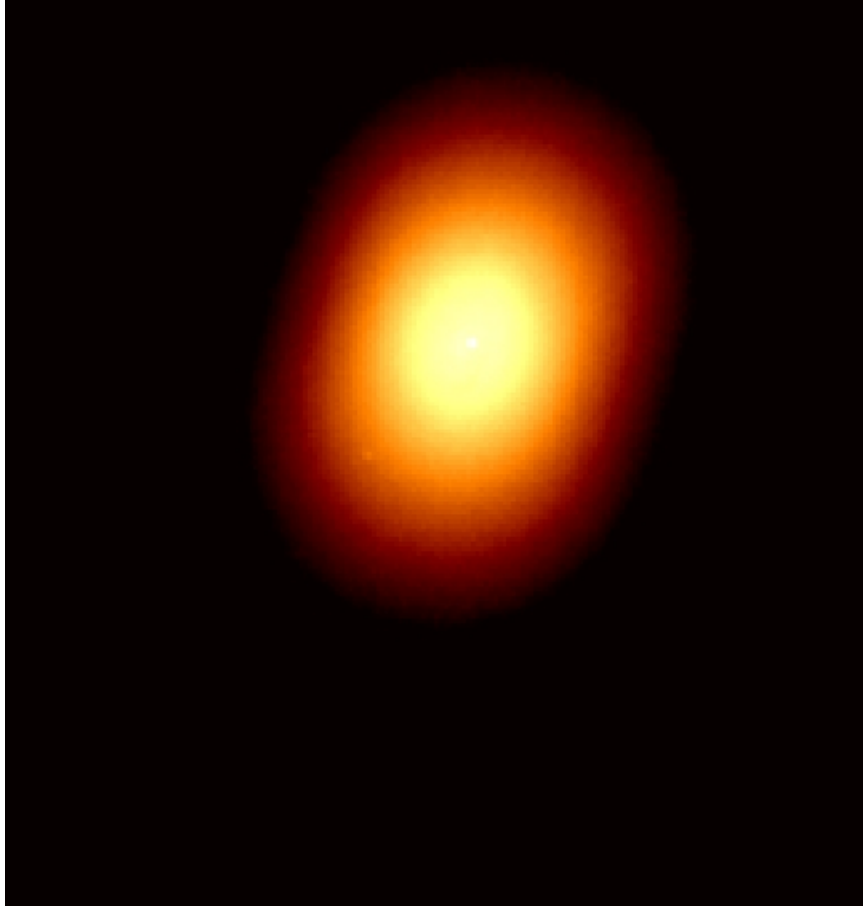


Figure A.32: 3CR 270 HST image.

We found no detection of CO, but [Jaffe et al. \(1993\)](#) have discovered a beautiful disk of dust and gas surrounding a bright unresolved nucleus in this large boxy elliptical galaxy. [Martel et al. \(1999\)](#) found on their HST snapshot images a numerous globular cluster in the halo of the galaxy.

The ~ 120 pc dusty disk originally studied by [Jaffe et al. \(1993\)](#) is notably absent of emission in both $H_{\alpha} + [N II]$ and $[O III]$, though there remains some $H_{\alpha} + [N II]$ emission along the inner regions of the disk. The disk is largely edge-on with respect to the line of sight though is inclined such that the western side of the disk "faces" the observer slightly. Note that the western half of the galaxy is noticeably brighter than the eastern half. Cones of high surface brightness $H_{\alpha} + [N II]$ emission are seen extending from the unresolved nucleus from

both sides of the disk, and are elongated along the direction of the jet (east-west on the sky, and nearly perpendicular to the major axis of the dusty disk). Nuclear [O III] emission is also seen extending from both sides of the disk, though seems to be largely absent on the disk itself Tremblay et al. (2009). Mahabal et al. (1996) studied this galaxy and concluded that it contains a dust lane with dimensions $\sim 21 \times 6$ arcsec², oriented close to the apparent major axis of the galaxy. They interpreted the dust lane as a projection of a dust disk with inclination angle $\sim 75^\circ$ to the plane of the sky.

Table A.28: General Data for 3CR 270

RA:	12h19m23.2s
Dec:	+05d49m31s
FR:	I
z_{CO} :	0.0075
Distance [Mpc]:	30
Line Width [km/s]:	-
$I_{CO(1-0)}$ [K km/s]:	<1.16
$I_{CO(2-1)}$ [K km/s]:	-
$M_{H_2} M_\odot$:	$<0.69 \times 10^8$

Table A.29: Fluxes of 3CR 270

Wavelength	flux measurement mJy
S_{3mm}	326.34 ± 0.82
S_{1mm}	204.71 ± 1.57
$f_{12\mu m}$	180 ± 47
$f_{25\mu m}$	90 ± 65
$f_{60\mu m}$	<155
$f_{100\mu m}$	<385

Table A.30: Luminosities for 3CR 270

Parameter	Luminosity - L_\odot
L_{CO} [K km/s pc ²]	1.35×10^7
L_{FIR} [L_\odot]	$<3.24 \times 10^8$

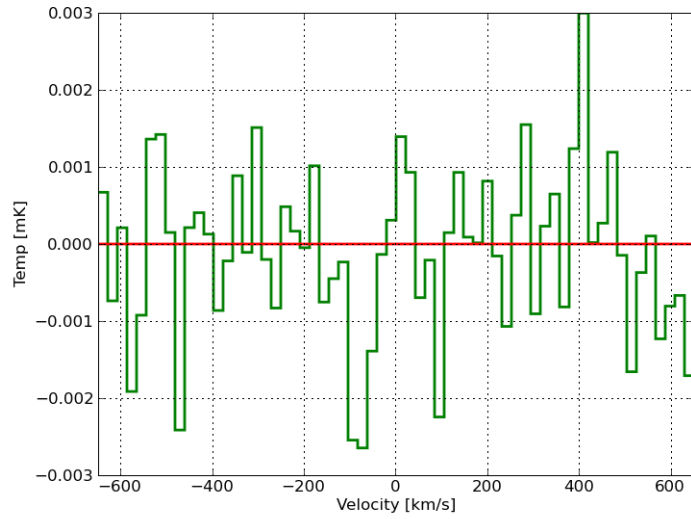


Figure A.33: 3CR 270 CO(1-0)

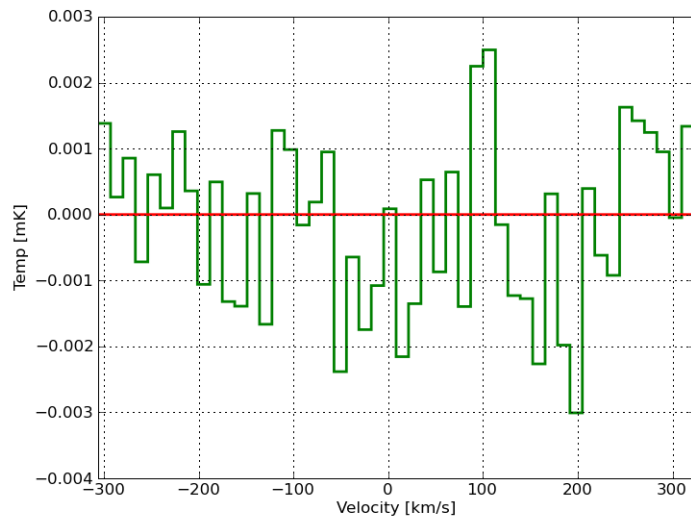


Figure A.34: 3CR 270 CO(2-1)

49; 3 3C270 NONE FRONTTEST-2 O: 07-JUN-2008 R: 12-JUL-2008
 RA: 12:19:23.200 DEC: 05:49:31.00 (2000.0) Offs: -2.002 -0.578 Eq
 Unknown Tau: 0.000 Tsys: 32.23 Time: 112.5 El: 43.50
 N: 127 l0: 64.01 V0: 0.000 Dv: -33.72 LSR
 F0: 1389.54200 Df: 0.1563 Fi: 1239.54200

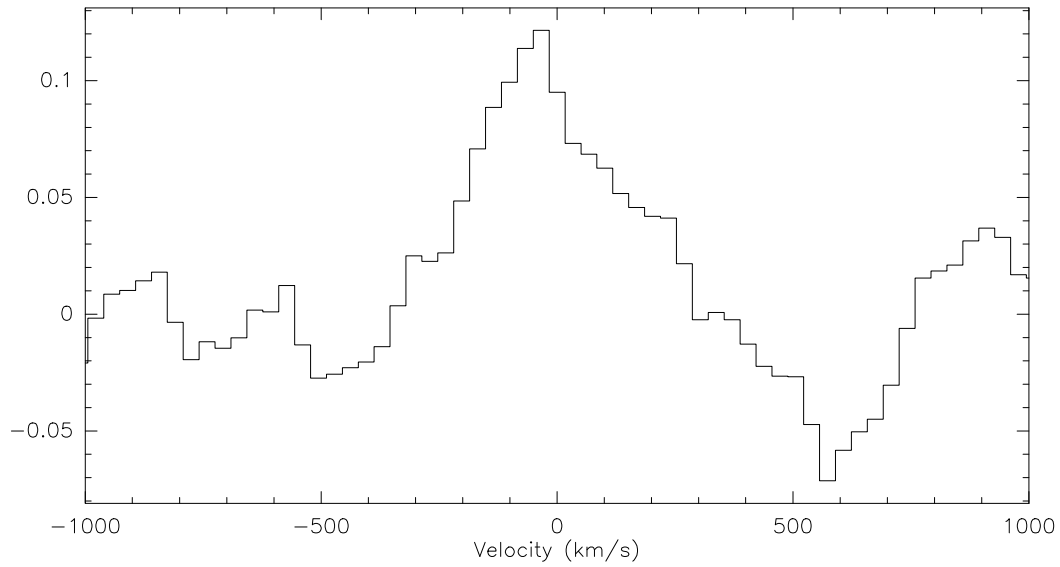


Figure A.35: HI emission for 3CR 270

A.10.1 HI data

We detected this galaxy when observing HI using Effelsberg-100m Telescope. This galaxy has a molecular gas mass of $34 \pm 0.17 \times 10^8 M_{\odot}$.

A.11 3CR 272.1

Other Names: MESSIER 84, NGC 4374, UGC 07494

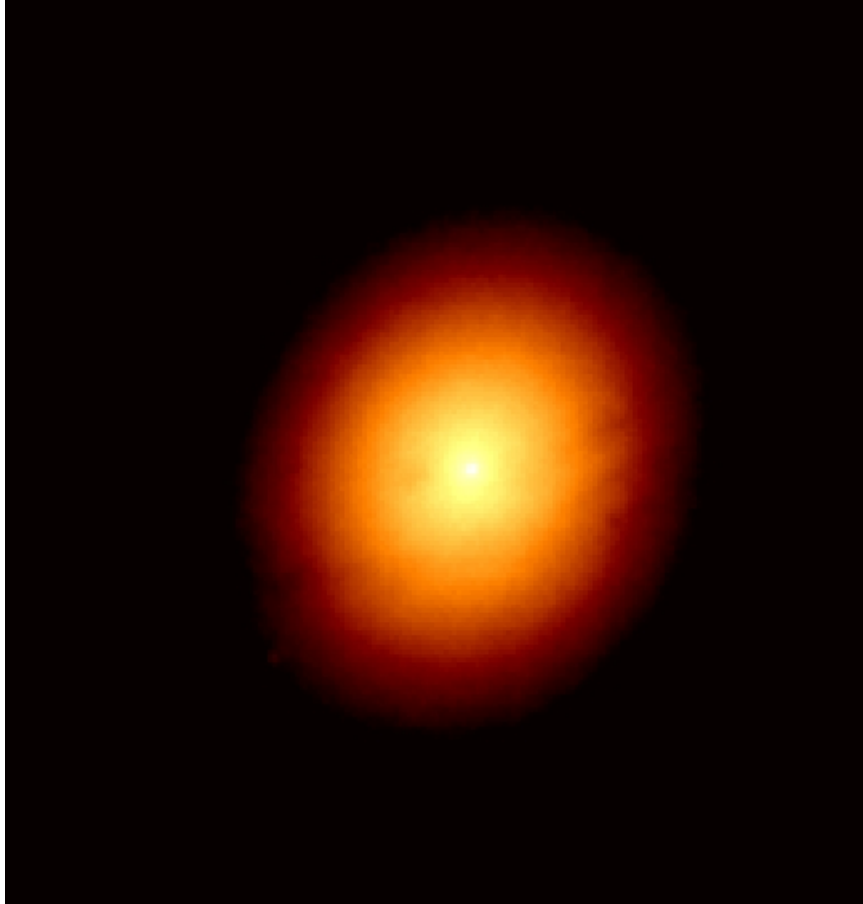


Figure A.36: 3CR 272.1 HST image.

It has a very clear detection in CO(2-1), in CO(1-0) it is more of a tentative detection, but the hint of the line is at the same velocity that the CO(2-1) detection and hence was considered as a detection. This galaxy has then the highest line ratio – 3.03 –.

In the Hubble image presented by [Martel et al. \(1999\)](#) it is possible to see the dust absorption as 2 filaments along the east west directions.

Table A.31: General Data for 3CR 272.1

RA:	12h25m03.7s
Dec:	+12d53m13s
FR:	I
z_{CO} :	0.0028
Distance [Mpc] :	12
Line Width [km/s]:	200
$I_{CO(1-0)}$ [K km/s]:	0.36 ± 0.12
$I_{CO(2-1)}$ [K km/s]:	0.90 ± 0.16
$M_{H_2} M_{\odot}$:	$0.03 \pm 0.01 \times 10^8$
$M_{Dust} M_{\odot}$:	3.63×10^4
T_{Dust} [K]:	36.39
Line Ratio:	2.5 ± 0.4

Table A.32: Fluxes of 3CR 272.1

Wavelength	flux measurement mJy
S_{3mm}	138.29 ± 1.2
S_{1mm}	73.86 ± 6.79
$f_{12\mu m}$	220 ± 38
$f_{25\mu m}$	190 ± 42
$f_{60\mu m}$	556 ± 83.4
$f_{100\mu m}$	1024 ± 154

Table A.33: Luminosities for 3CR 272.1

Parameter	Luminosity
L_{CO} [K km/s pc^2]	5.89×10^5
L_{FIR} [L_{\odot}]	$<1.70 \times 10^8$
L_{178MHz} [W Hz $^{-1}$ sr $^{-1}$]	3.1×10^{22} (Evans et al. 2006)

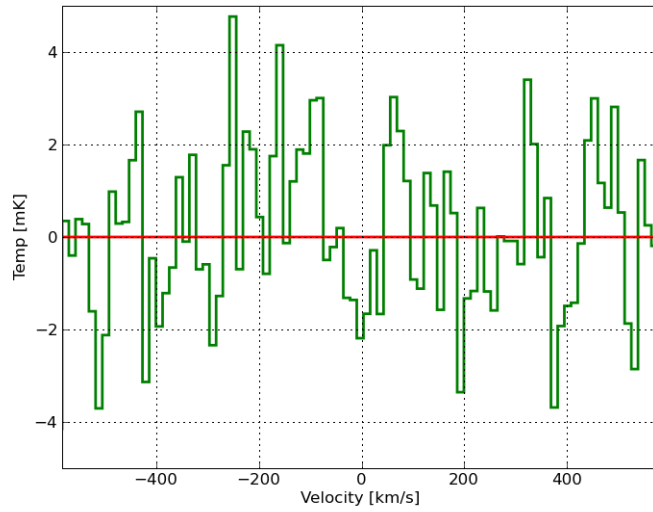


Figure A.37: 3CR 272.1 CO(1-0)

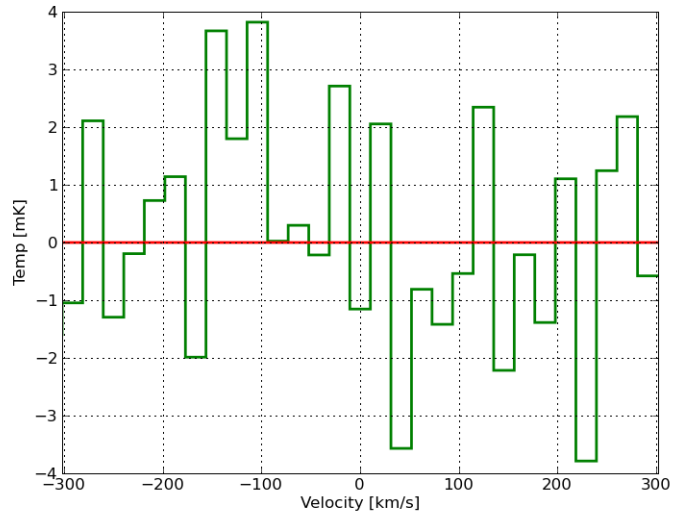
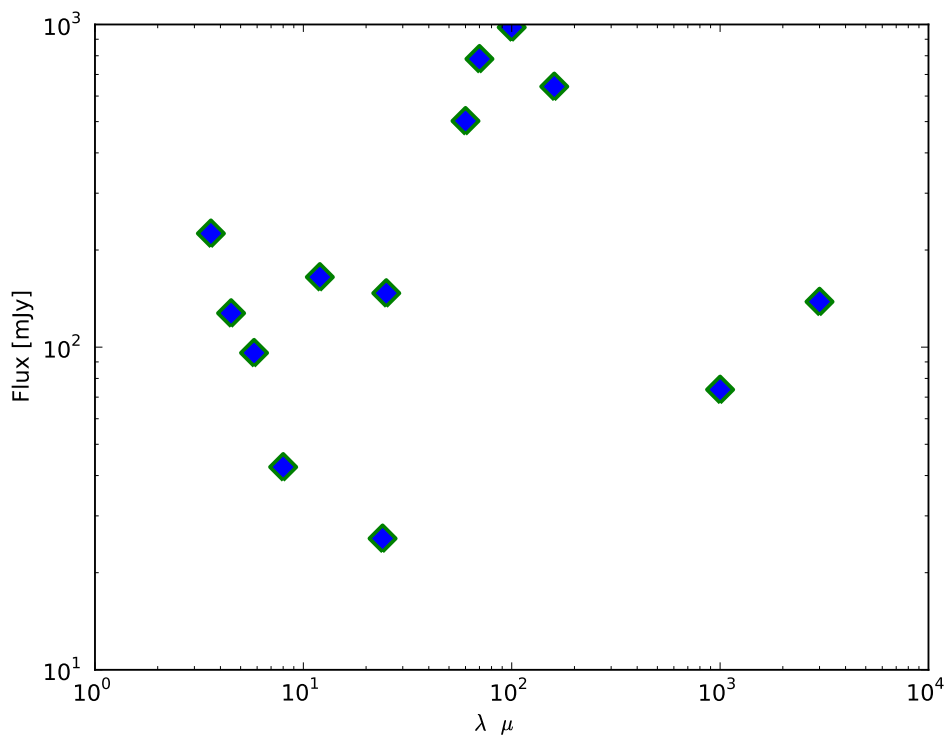


Figure A.38: 3CR 272.1 CO(2-1)

Figure A.39: The Spectral Energy diagram for 3CR 272.1



A.12 3C 274

Other Names: MESSIER 087, NGC 4486, UGC 07654

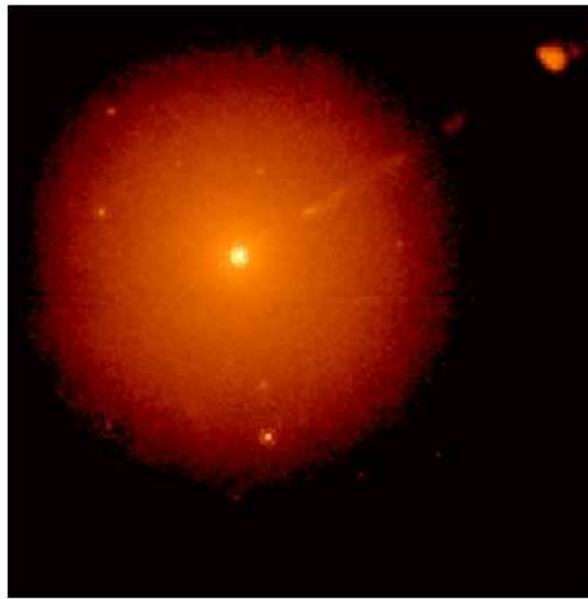


Figure A.40: 3CR 274 HST image.

It is also known as M87. It has been clearly detected in CO(1-0). Looking at the optical image from the HST we can see a clear jet that has been very well studied and that according to [Martel et al. \(1999\)](#) its P.A. is $\sim 65^\circ$. Its velocity width for CO(1-0) is ~ 800 km/s with one of the highest integrated velocity of the sample.

[Capetti et al. \(1997\)](#) obtained polarization measurements of this galaxy with the HST and the nucleus was found to be only marginally polarized ($P=1.6\pm 0.7\%$) in the optical. Which could be interpreted as that this source is not dominated by synchrotron radiation, since according to [Capetti et al. \(2007\)](#) if the nuclear emission is dominated by synchrotron radiation significant polarization is expected to be detected.

3CR 274 lies at a distance of 54 million light-years and is the largest galaxy in the Virgo cluster of galaxies. Bright jets moving at close to the speed of light are seen at all wavelengths coming from the massive black hole at the center of the galaxy. It has also been identified with the strong radio source, Virgo A, and is a powerful source of X-rays as it resides near the center of a hot, X-ray-emitting cloud that extends over much of the Virgo cluster. The extended radio emission consists of plumes of relativistic (extremely hot) gas from the jets rising into the X-ray-emitting cluster medium¹.

Table A.34: General Data for 3CR 274

RA:	12h30m49.4s
Dec:	+12d23m28s
FR:	I
z_{CO} :	0.0035
Distance [Mpc]:	14.90
Line Width [km/s] :	200
$I_{CO(1-0)}$ [K km/s]:	4.02 ± 0.39
$I_{CO(2-1)}$ [K km/s]:	...
$M_{H_2} M_{\odot}$:	$0.52 \pm 0.05 \times 10^8$
$M_{Dust} M_{\odot}$:	1.20×10^4
T_{Dust} [K]:	47.39

Table A.35: Fluxes of 3CR 274

Wavelength	flux measurement mJy
S_{3mm}	2347.13 ± 1.83
S_{1mm}	1312.31 ± 2.78
$f_{12\mu m}$	440 ± 34
$f_{25\mu m}$	187 ± 28.1
$f_{60\mu m}$	546 ± 81.9
$f_{100\mu m}$	559 ± 83.9

Table A.36: Luminosities for 3CR 274

Parameter	Luminosity
L_{CO} [K km/s pc^2]	1.02×10^7
L_{FIR} [L_{\odot}]	$<1.78 \times 10^8$
L_{178MHz} [W Hz ⁻¹ sr ⁻¹]	3.4×10^{24} (Evans et al. 2006)

¹<http://hubblesite.org/newscenter/archive/releases/2008/30/image/k/>

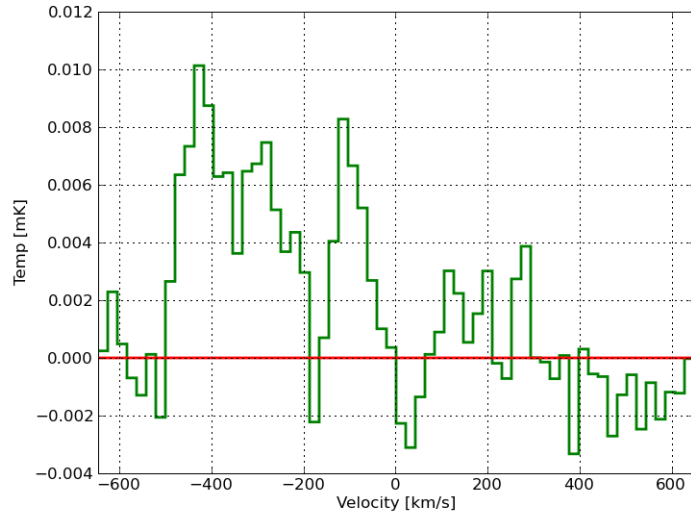
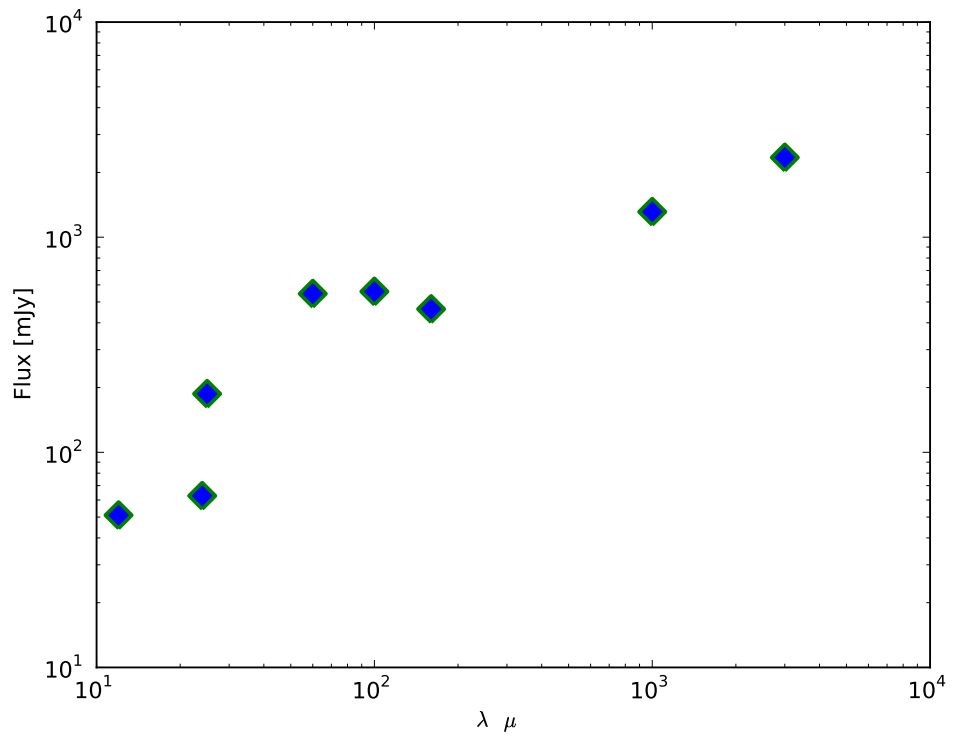


Figure A.41: 3CR 274 CO(1-0)

Figure A.42: The Spectral Energy diagram for 3CR 274



A.13 3CR 296

Other Names: NGC 5532, UGC 09137

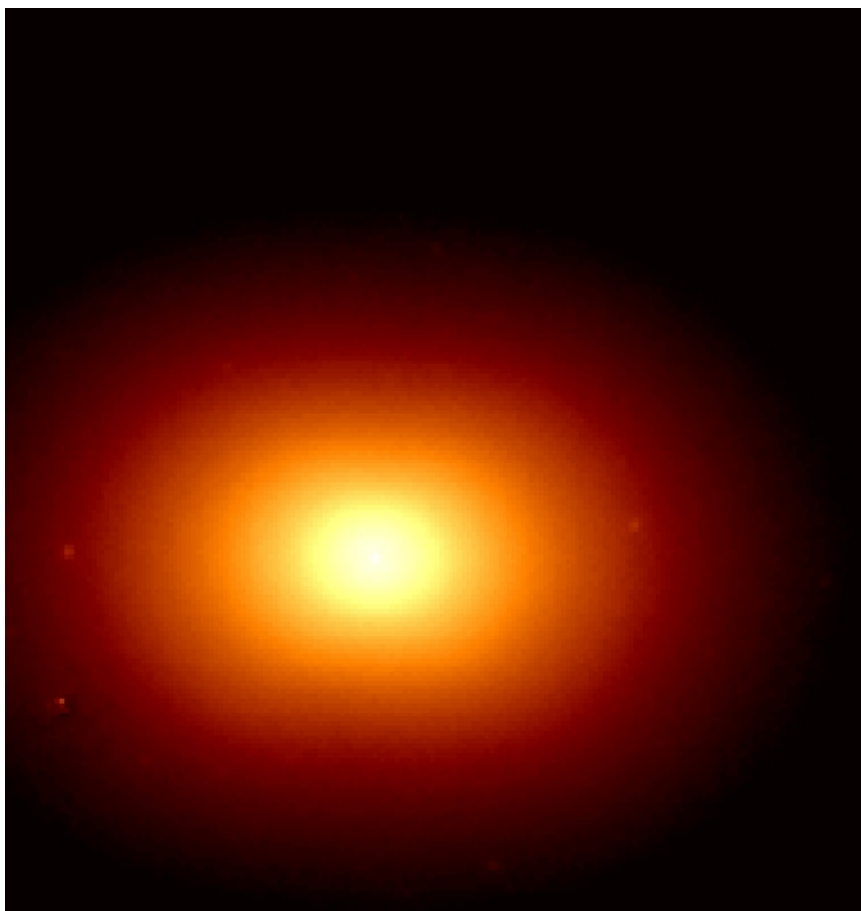


Figure A.43: 3CR 296 HST image.

Table A.37: General Data for 3CR 296

RA:	14h16m52.9s
Dec:	+10d48m27s
FR:	I
z_{CO} :	0.02
Distance [Mpc]:	101
Line Width:	-
$I_{CO(1-0)}$ [K km/s]:	<0.85
$I_{CO(2-1)}$ [K km/s]:	...
$M_{H_2} M_{\odot}$:	$<5.05 \times 10^8$

Table A.38: Fluxes of 3CR 296

Wavelength	flux measurement mJy
S_{3mm}	99.23 ± 0.6
S_{1mm}	54.55 ± 1.22
$f_{12\mu m}$	70 ± 29
$f_{25\mu m}$	<37
$f_{60\mu m}$	<150
$f_{100\mu m}$	<395

Table A.39: Luminosities for 3CR 296

Parameter	Luminosity
L_{CO}	$<9.77 \times 10^7$ [K km/s pc^2]
L_{FIR}	$<3.39 \times 10^9$ [L_{\odot}]
L_{178MHz} [W Hz ⁻¹ sr ⁻¹]	1.43×10^{24} (Evans et al. 2006)

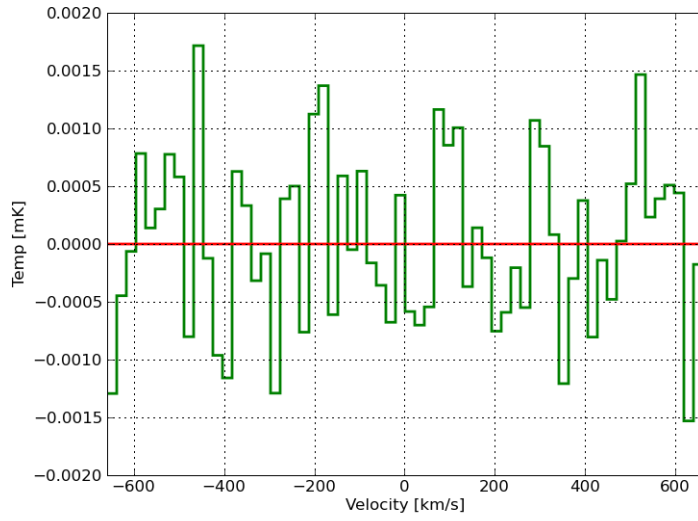


Figure A.44: 3CR 296 CO(1-0)

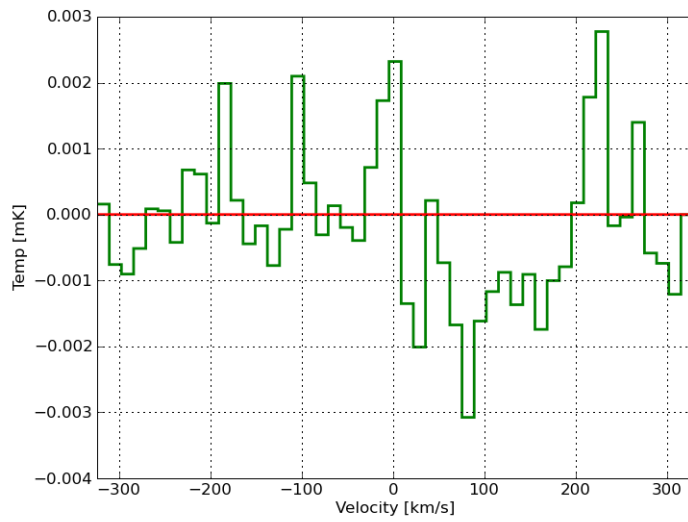


Figure A.45: 3CR 274 CO(2-1)

A.14 3C 305

Other Name: UGC 09553



Figure A.46: 3CR 305 HST image.

In the CO(1-0) spectra, the detection is very clear and the velocity width is ~ 600 km/s. We only have data for the CO(1-0) emission line of this galaxy. The HST image presented by [Martel et al. \(1999\)](#) shows filamentary and disturbed swath of dust stretching across the western side of the galaxy and a twisting "arm" of emission in the eastern side. [Jackson et al. \(1995\)](#) noticed a $1''$ scale cone-line extension of the continuum emission north of the core, in a direction almost 90° removed from the radio axis and proposed that might be an effect of obscuration of near-nuclear emission in all other directions rather than an example of scattering of anisotropic directed radiation from a hidden active nucleus.

According to [Draper et al. \(1993\)](#), in 3CR 305 the nucleus is intrinsically polar-

ized, with vector pattern suggesting that light from the nucleus is collimated into a wide-angled bicone and it is scattered by dust grains within it. Their scattering model implies that significant radiation is escaping at large angle to the radio axis. Thus, in the context of the unify scheme, at least a component of the radiation from AGNs in a cone with a wide opening angle ($>90^\circ$).

Table A.40: General Data for 3CR 305

RA:	14h49m21.6s
Dec:	+63d16m14s
FR:	I
z_{CO} :	0.042
Distance [Mpc]:	171.70
Line Width [km/s]:	600
$I_{CO(1-0)}$ [K km/s]:	1.19 ± 0.14
$I_{CO(2-1)}$ [K km/s]:	Not Observed
$M_{H_2} M_\odot$:	$20.52 \pm 2.49 \times 10^8$
$M_{Dust} M_\odot$:	2.63×10^6
T_{Dust} [K]:	39.45

Table A.41: Fluxes of 3CR 305

Wavelength	flux measurement mJy
S_{3mm}	21.23 ± 4.28
S_{1mm}	Not Observed
$f_{12\mu m}$	<50.1
$f_{25\mu m}$	<95.8
$f_{60\mu m}$	298 ± 44.7
$f_{100\mu m}$	450 ± 67.5

Table A.42: Luminosities for 3CR 305

Parameter	Luminosity - L_\odot
L_{CO} [K km/s pc^2]	3.98×10^8
L_{FIR} [L_\odot]	1.62×10^{10}

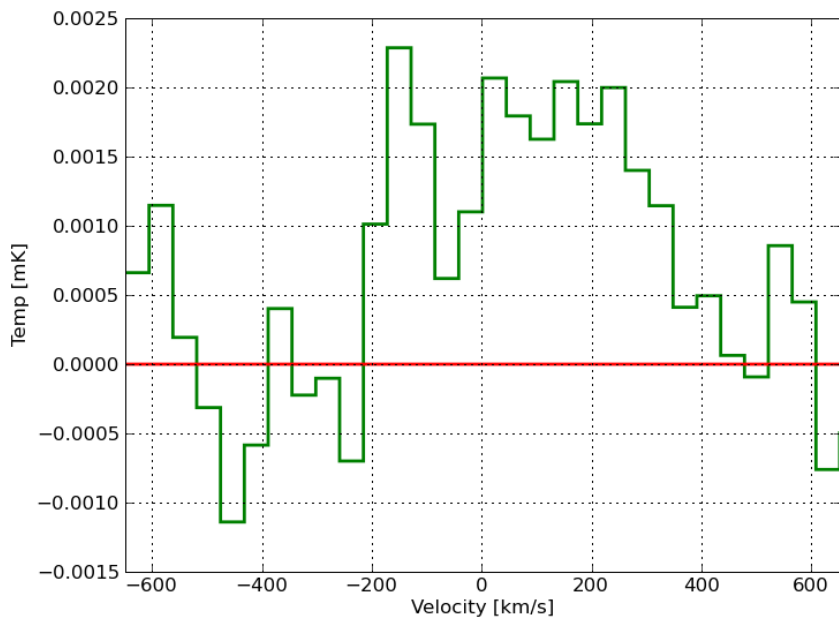
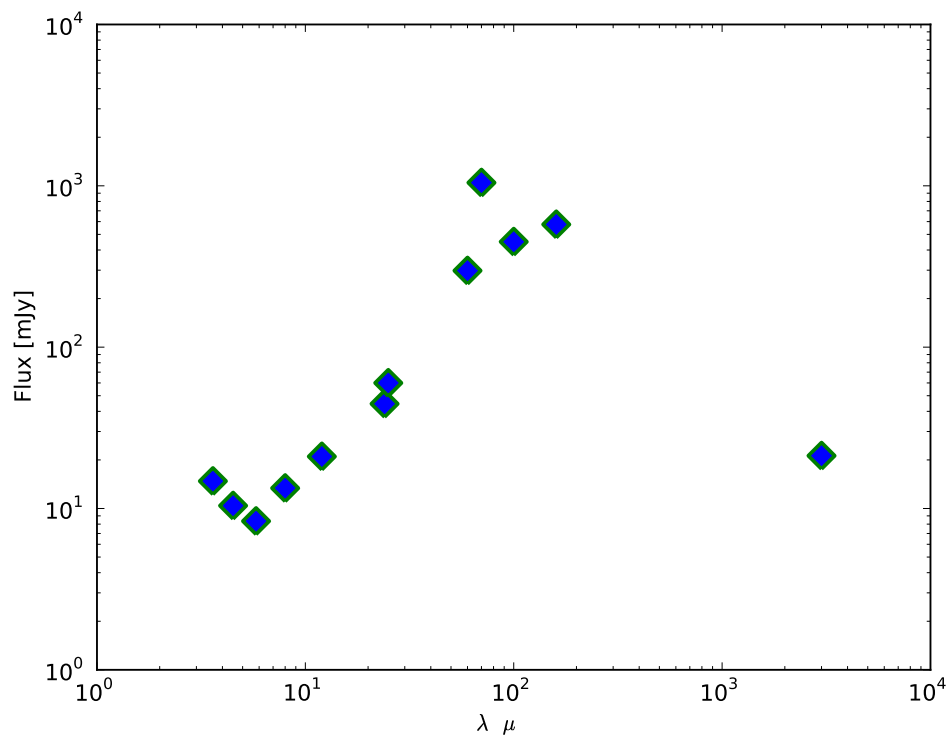


Figure A.47: 3CR 305 CO(1-0)

Figure A.48: The Spectral Energy diagram for 3CR 305



A.15 3C 321

Other Name: B2 1529+24

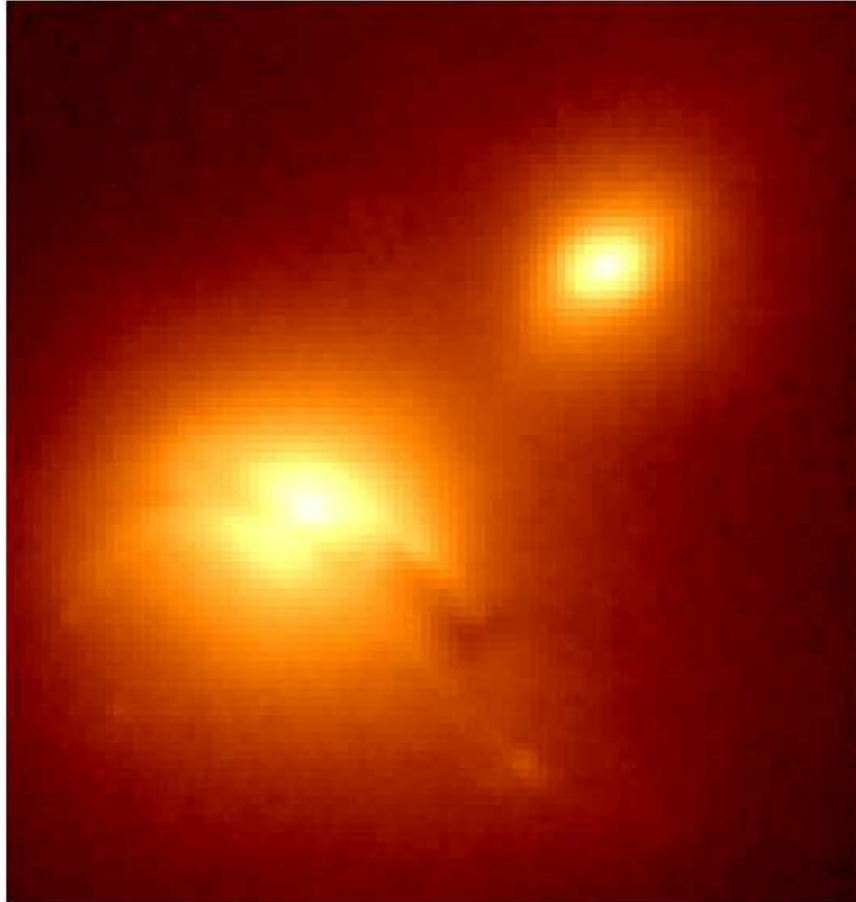


Figure A.49: 3CR 321 HST image.

In the HST optical image we can appreciate the extension of the dust absorption in the galaxy. This galaxy was a clear detection in the CO(1-0) transition with a velocity width of ~ 500 km/s. For the CO(2-1) emission we have no data. In the Hubble image we can see that there is a nearby galaxy that might be interacting with this galaxy.

According to [Draper et al. \(1993\)](#), in 3CR 321 the nucleus is intrinsically polarized, with vector pattern suggesting that light from the nucleus is collimated into a wide-angled bicone and it is scattered by dust grains within it. Their scattering model implies that significant radiation is escaping at large angle to the radio axis. Thus, in the context of the unify schemes, at least a component of the radiation from AGNs in a cone with a wide opening angle ($>90^\circ$).

Table A.43: General Data for 3CR 321

RA:	15h31m43.4s
Dec:	+24d04m19s
FR:	II
z_{CO} :	0.10
Distance [Mpc]:	379.97
Line Width [km/s]:	500
$I_{CO(1-0)}$ [K km/s]:	0.83 ± 0.09
$I_{CO(2-1)}$ [K km/s]:	Not Observed
$M_{H_2} M_\odot$:	$70.58 \pm 7.93 \times 10^8$
$M_{Dust} M_\odot$:	1.32×10^7
T_{Dust} [K]:	50.84

Table A.44: Fluxes of 3CR 321

Wavelength	flux measurement mJy
S_{3mm}	67.33 ± 0.52
S_{1mm}	Not Observed
$f_{12\mu m}$	<120.3
$f_{25\mu m}$	332.6 ± 132
$f_{60\mu m}$	1067 ± 160
$f_{100\mu m}$	961 ± 144

Table A.45: Luminosities for 3CR 321

Parameter	Luminosity
L_{CO}	1.32×10^9 [K km/s pc^2]
L_{FIR}	2.96×10^{11} [L_\odot]
L_{178MHz} [W Hz ⁻¹ sr ⁻¹]	2.96×10^{25} (Evans et al. 2006)

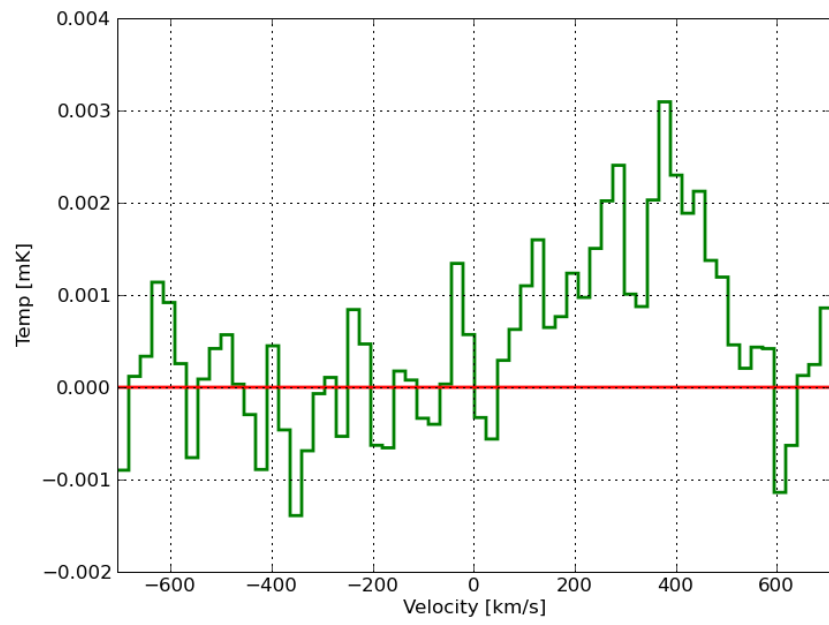
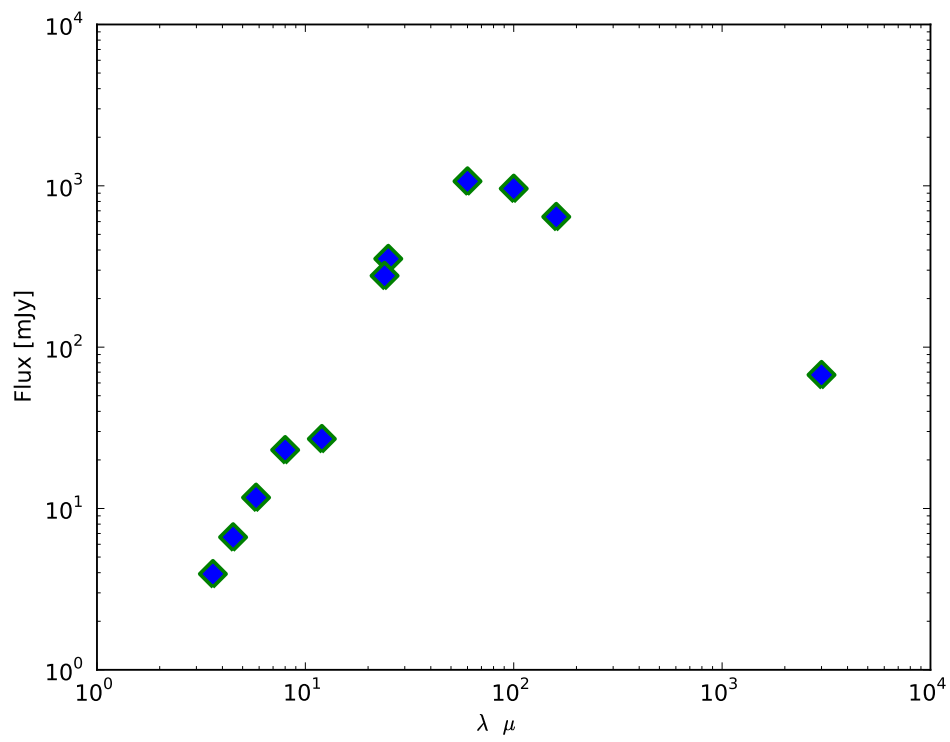


Figure A.50: 3CR 321 CO(1-0)

Figure A.51: The Spectral Energy diagram for 3CR 321



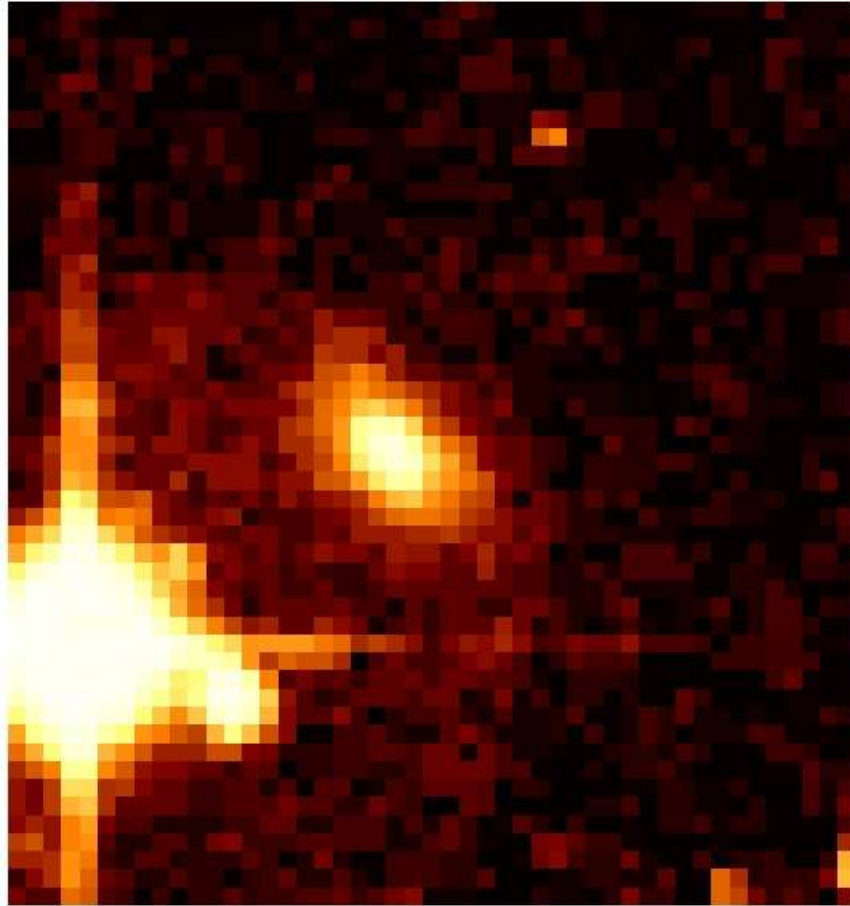
A.16 3C 327

Figure A.52: 3CR 327 optical image.

It is clearly detected in the CO(1-0) transition line, with a velocity width in CO(1-0) of ~ 200 km/s and with one of the highest dust temperature from this sample (64K).

According to [Mack et al. \(2009\)](#), who studied the hotspots in this narrow-line radio galaxies ([Simpson et al. 1996](#)), the eastern hotspot complex consist of a primary knot and a one more diffuse secondary north of it. Both features are embedded in a region of diffuse extended emission. The dominant feature in the western hot spot is the slightly curved structure at the very end of the hotspot complex. [Leahy et al. \(1997\)](#) mention the possibility that the brighter structure in the south is part of the radio jet.

After the observation of [Mack et al. \(2009\)](#) they concluded that the western hotspot does not show any significant NIR counterparts and was removed from their sample because it was impossible for them to whether the hotspot

emission reaches up to the NIR band.

Table A.46: General Data for 3CR 327

RA:	16h02m27.3s
Dec:	+01d57m56s
FR:	II
z_{CO} :	0.1035
Distance [Mpc]:	401.87
Line Width [km/s]:	200
$I_{CO(1-0)}$ [K km/s]:	0.28 ± 0.20
$I_{CO(2-1)}$ [K km/s]:	Not Observed
$M_{H_2} M_{\odot}$:	$26.48 \pm 9.59 \times 10^8$
$M_{Dust} M_{\odot}$:	2.39×10^6
T_{Dust} [K]:	71.33

Table A.47: Fluxes of 3CR 327

Wavelength	flux measurement mJy
S_{3mm}	105.81 ± 0.69
S_{1mm}	Not Observed
$f_{12\mu m}$	91.8 ± 23.0
$f_{25\mu m}$	319 ± 9.18
$f_{60\mu m}$	670 ± 101
$f_{100\mu m}$	371 ± 55.7

Table A.48: Luminosities for 3CR 327

Parameter	Luminosity
L_{CO} [K km/s pc^2]	4.90×10^8
L_{FIR} [L_{\odot}]	1.74×10^{11}

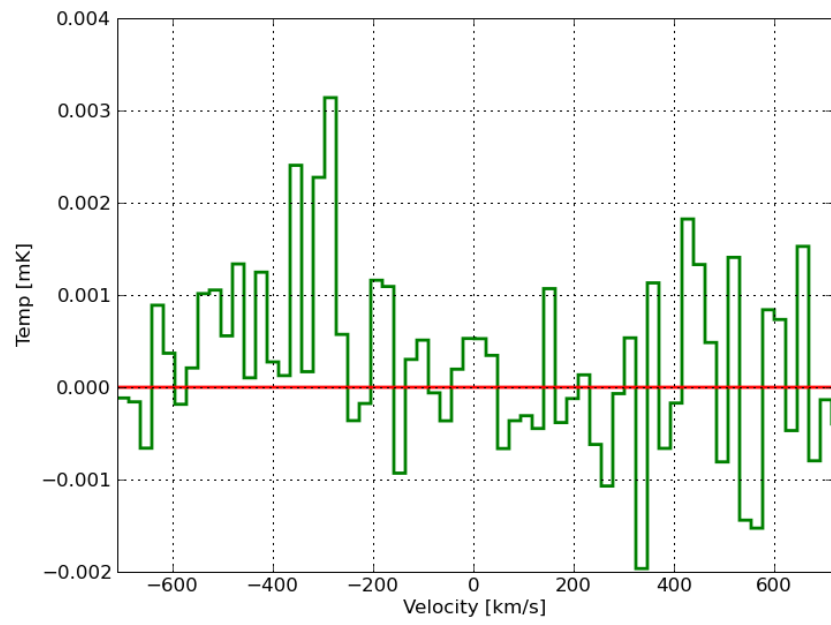
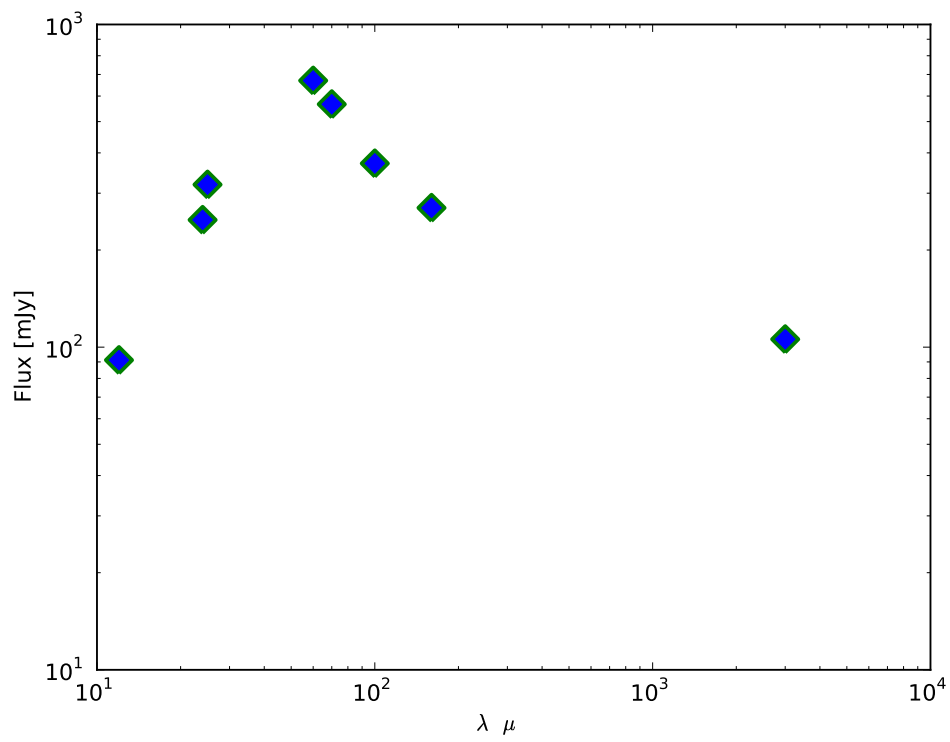


Figure A.53: 3CR 327 CO(1-0)

Figure A.54: The Spectral Energy diagram for 3CR 327



A.17 3CR 353

Figure A.55: 3CR 353 HST image.

It is clearly detected in the CO(1-0) transition line, although we might be missing some emission (see figure [A.56](#)), with a $\text{FWZI}_{\text{CO}(1-0)}$ of ~ 200 km/s. [Martel et al. \(1999\)](#) propose that the outer isophotes of 3C 353 are very circular while the inner isophotes are elongated in a southeast to northeast direction and are roughly peanut-shaped. [Martel et al. \(1999\)](#) also stated that this may result from a small-scale dust lane bifurcating the nucleus in a rough north-south direction or from a true double nucleus.

Table A.49: General Data for 3CR 353

RA:	17h20m28.1s
Dec:	-00d58m47s
FR:	II
z_{CO} :	0.0327
Distance [Mpc] :	153.73
Line Width [km/s]:	200
$I_{CO(1-0)}$ [K km/s]:	0.31 ± 0.05
$I_{CO(2-1)}$ [K km/s]:	...
$M_{H_2} M_{\odot}$:	$4.27 \pm 0.68 \times 10^8$

Table A.50: Fluxes of 3CR 353

Wavelength	flux measurement mJy
S_{3mm}	...
S_{1mm}	3.46 ± 1.35
$f_{12\mu m}$...
$f_{25\mu m}$...
$f_{60\mu m}$...
$f_{100\mu m}$...

Table A.51: Luminosities for 3CR 353

Parameter	Luminosity - L_{\odot}
L_{CO} [K km/s pc^2]	6.31×10^9
L_{FIR} [L_{\odot}]	...

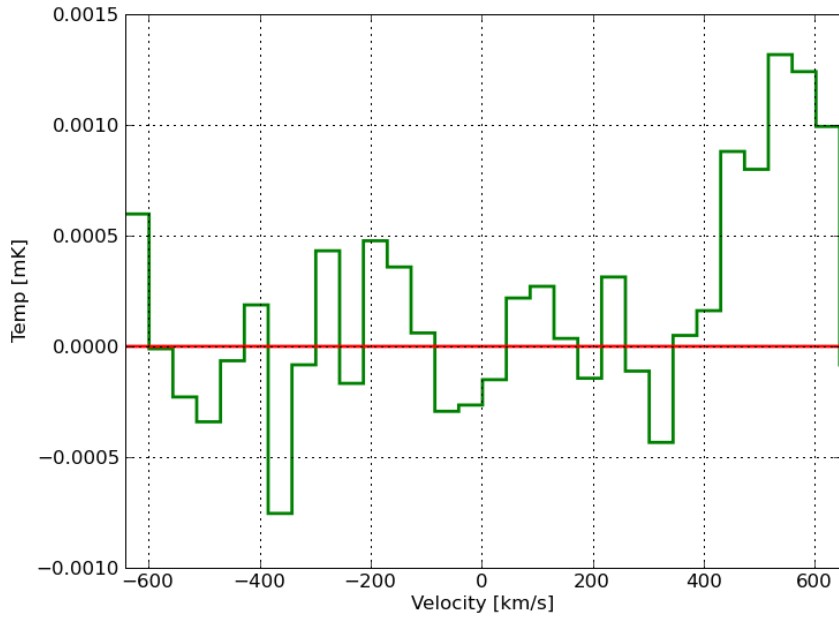


Figure A.56: 3CR 353 CO(1-0)

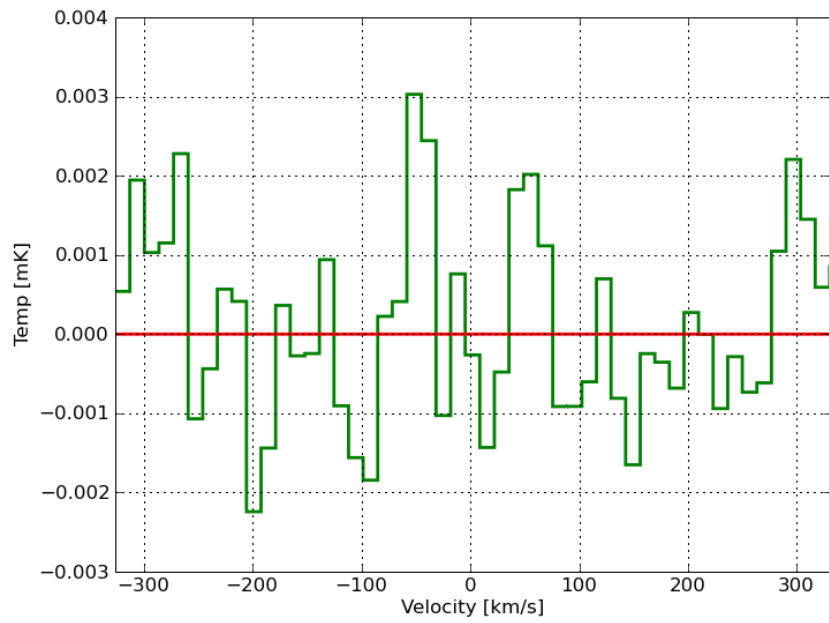


Figure A.57: 3CR 353 CO(2-1)

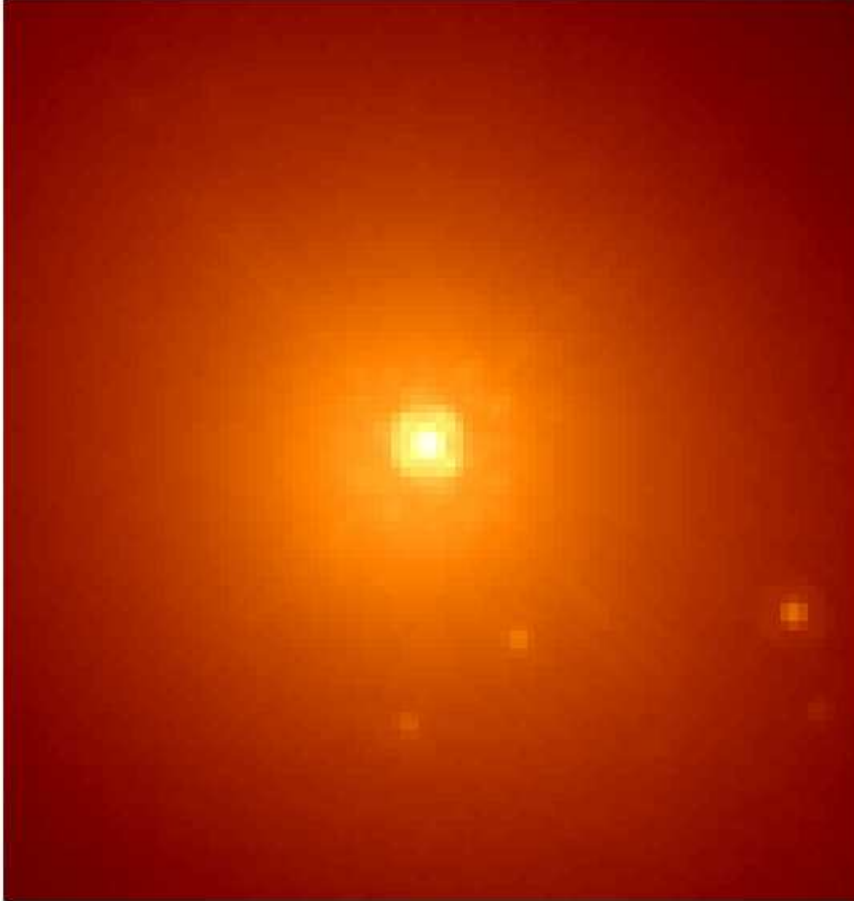
A.18 3C 386**Other Name:**3C 386C

Figure A.58: 3CR 386 HST image.

It is clearly detected in CO(2-1) with a $\text{FWZI}_{\text{CO}(2-1)}$ of ~ 175 km/s, but it was not detected in CO(1-0). We calculated the CO(1-0) intensity using the 2.3 average line ratio of the galaxies detected in both lines. In the HST optical image we can see a bright optical nucleus where a strong diffraction spikes dominates the core of the elliptical galaxy as noticed by [Martel et al. \(1999\)](#).

Table A.52: General Data for 3CR 386

RA:	18h38m26.2s
Dec:	+17d11m49s
FR:	I
z_{CO} :	0.17
Distance [Mpc]:	71.7
Line Width [km/s]:	-
$I_{CO(1-0)}$ [K km/s]:	0.58 ± 0.02
$I_{CO(2-1)}$ [K km/s]:	1.23 ± 0.17
$M_{H_2} M_{\odot}$:	$1.78 \pm 0.058 \times 10^8$

Table A.53: Fluxes of 3CR 386

Wavelength	flux measurement mJy
S_{3mm}	50.21 ± 0.88
S_{1mm}	105.01 ± 2.26
$f_{12\mu m}$	5.6 ± 0.3
$f_{25\mu m}$	<30
$f_{60\mu m}$	<35
$f_{100\mu m}$	<175

Table A.54: Luminosities for 3CR 386

Parameter	Luminosity - L_{\odot}
L_{CO} [K km/s pc^2]	3.31×10^7
L_{FIR} [L_{\odot}]	5.62×10^8

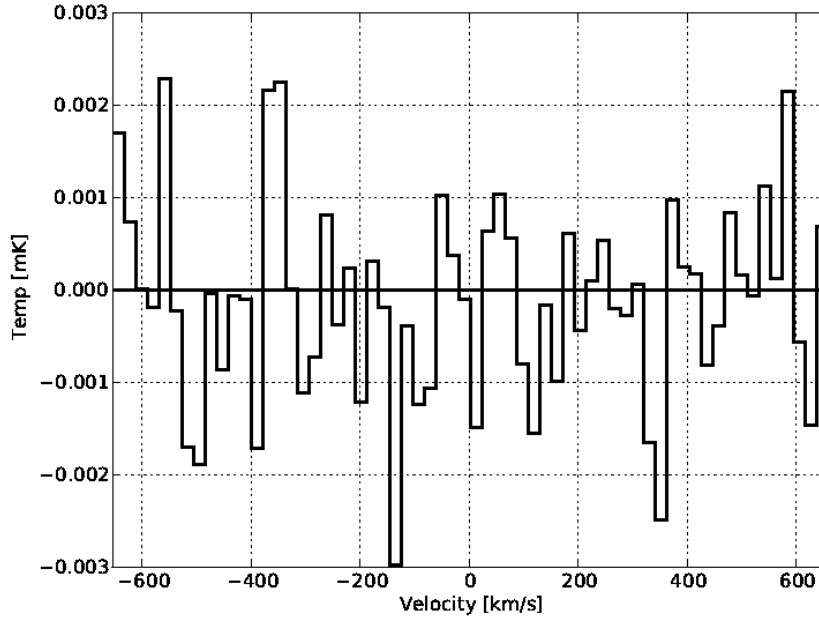


Figure A.59: 3CR 386 CO(1-0)

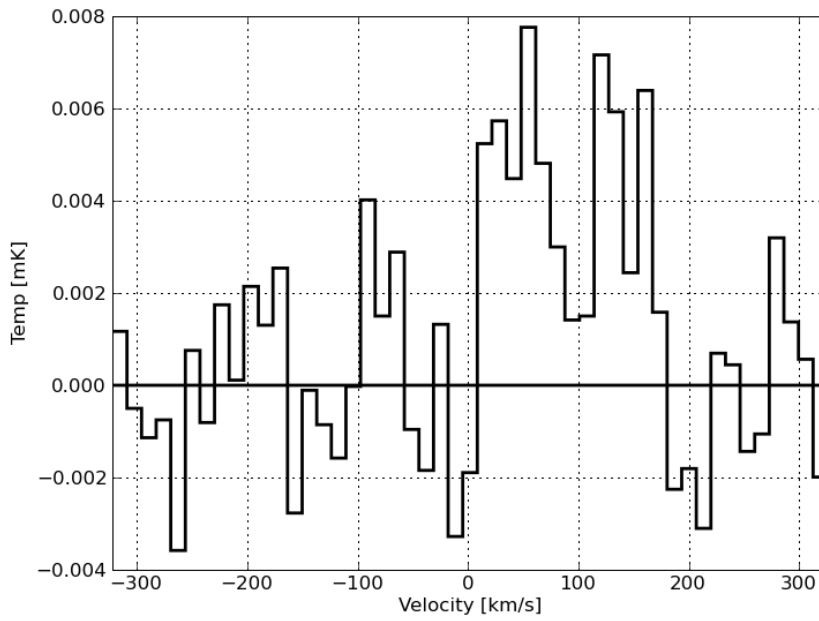


Figure A.60: 3CR 386 CO(2-1)

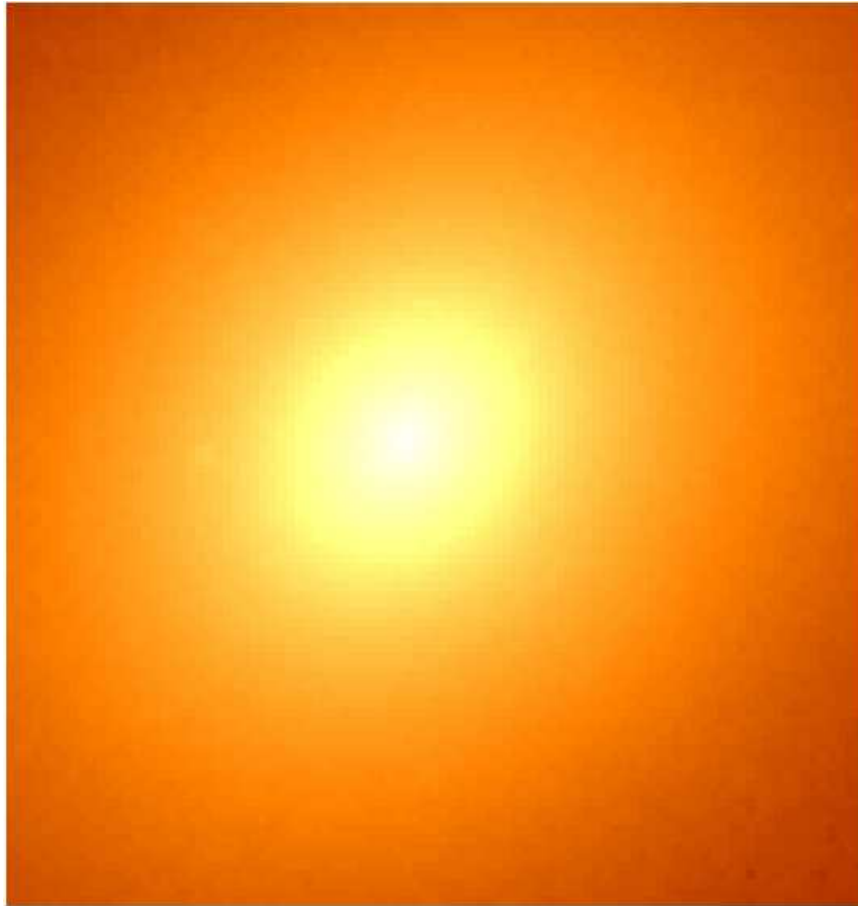
A.19 3CR 402

Figure A.61: 3CR 402 HST image.

This galaxy was observed for CO(1-0) and for CO(2-1) and it was not detected.

Table A.55: General Data for 3CR 402

RA:	19h41m46.0s
Dec:	+50d35m45s
FR:	II
z_{CO} :	0.025
Distance [Mpc]:	107
Line Width:	-
$I_{CO(1-0)}$ [K km/s]:	<0.95
$I_{CO(2-1)}$ [K km/s]:	...
$M_{H_2} M_{\odot}$:	$<6.59 \times 10^8$
$M_{Dust} M_{\odot}$:	1.02×10^7
T_{Dust} [K]:	27.83

Table A.56: Fluxes of 3CR 402

Wavelength	flux measurement mJy
S_{3mm}	332.57 ± 39.27
S_{1mm}	...
$f_{12\mu m}$	<30
$f_{25\mu m}$	30 ± 4.5
$f_{60\mu m}$	257 ± 38.6
$f_{100\mu m}$	1052 ± 158

Table A.57: Luminosities for 3CR 402

Parameter	Luminosity
L_{CO} [K km/s pc^2]	$<1.17 \times 10^8$
L_{FIR} [L_{\odot}]	7.94×10^9

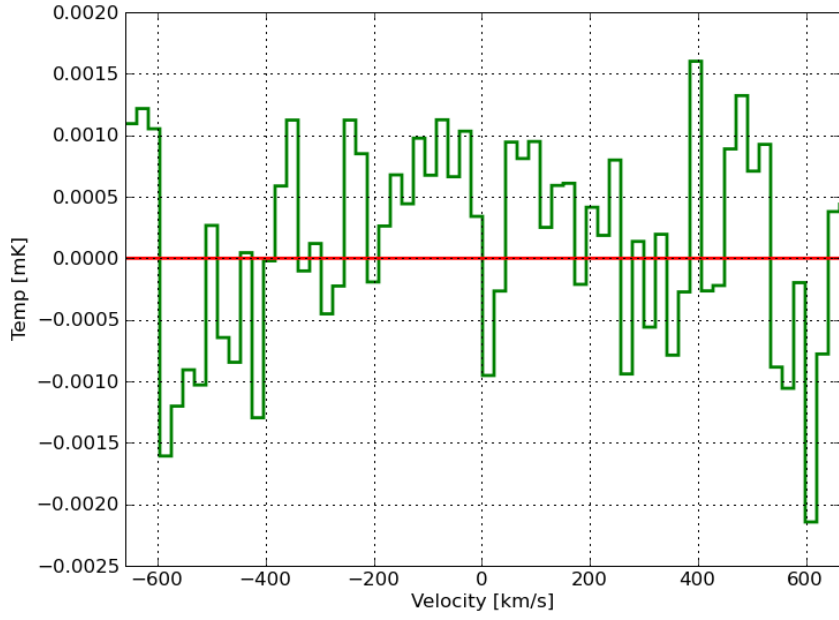


Figure A.62: 3CR 402 CO(1-0)

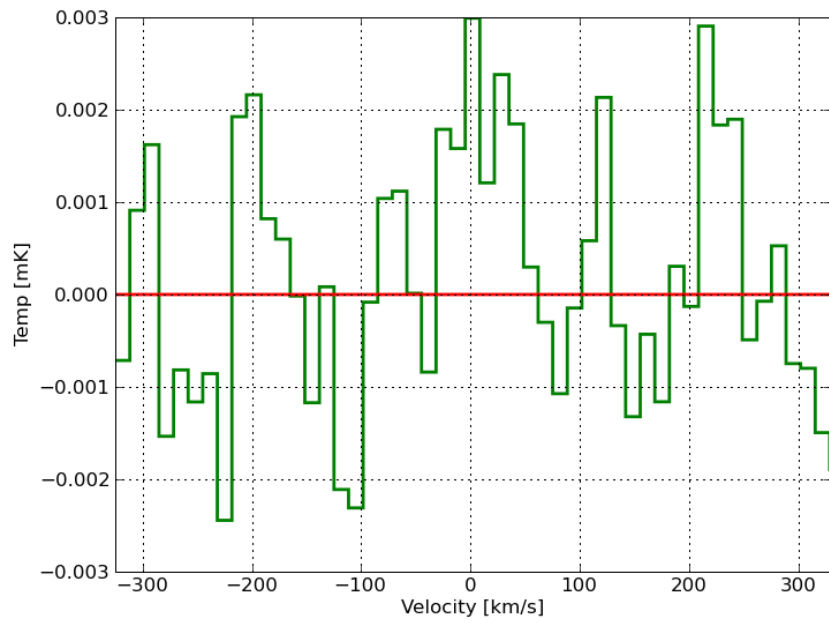
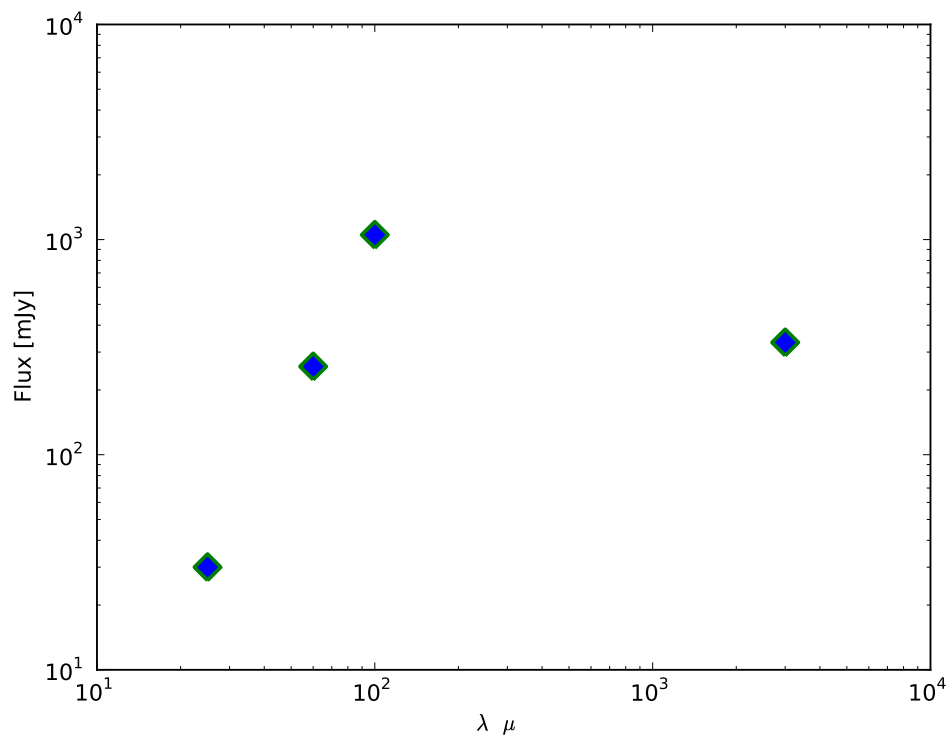


Figure A.63: 3CR 402 CO(2-1)

Figure A.64: The Spectral Energy diagram for 3CR 402



A.20 3C 403

Figure A.65: 3CR 403 HST image.

It is clearly detected in the only transition observed, CO(1-0), with a $\text{FWZI}_{\text{CO}(1-0)}$ of ~ 500 km/s, and a rotational velocity of about 250 km/s. It presents the double horn profile already mentioned on chapter 5. [Martel et al. \(1999\)](#) suggest this galaxy consists of two systems: a central elliptical region surrounded by a low-surface brightness halo with a sharp boundary at a distance of 3 Kpc northwest of the nucleus. In the northwest region of the halo, two or three very weak dust lanes are barely discernible.

According to [Mack et al. \(2009\)](#), this narrow-line radio galaxy belongs to the peculiar class of X-shaped sources which combines two pairs of lobes extending in different directions from the same core. One of these lobe systems is typically more extended and diffuse, while the other one is shorter, brighter and clearly confined. The more extended lobes would be the reminders of an earlier phase of jet activity, while the shorter, brighter systems would mark

the current working direction of the jet. [Black et al. \(1992\)](#) show the overall morphology. [Hardcastle et al. \(1998\)](#) suggest that the knot F6 is the primary hotspot in the western lobe. For [Mack et al. \(2009\)](#)'s detection experiment, they focus on the outermost western hotspot at the edge of the younger lobe system which is describe as an unusually uniform hotspot without apparent substructure by [Black et al. \(1992\)](#).

None of the significant NIR detections made by [Mack et al. \(2009\)](#) seems to be related to the radio hotspots. [Kraft et al. \(2005\)](#) report extended X-ray emission from the western lobe and suggest inverse Compton scattering of beamed IR/optical photons from active nucleus.

Table A.58: General Data for 3CR 403

RA:	19h52m15.8s
Dec:	+02d30m24s
FR:	II
z_{CO} :	0.058
Distance:	134.97 [Mpc]
Line Width:	500
$I_{CO(1-0)}$ [K km/s]:	0.44 ± 0.11
$I_{CO(2-1)}$ [K km/s]:	Not Observed
$M_{H_2} M_{\odot}$:	$4.75 \pm 1.18 \times 10^8$

Table A.59: Fluxes of 3CR 403

Wavelength	flux measurement mJy
S_{3mm}	67.33 ± 0.52
S_{1mm}	Not Observe
$f_{12\mu m}$	117 ± 28.1
$f_{25\mu m}$	231 ± 17.6
$f_{60\mu m}$	441 ± 66.2
$f_{100\mu m}$	<500

Table A.60: Luminosities for 3CR 403

Parameter	Luminosity - L_{\odot}
L_{CO} [K km/s pc^2]	2.69×10^8
L_{FIR} [L_{\odot}]	$<4.17 \times 10^{10}$
L_{178MHz} [W Hz $^{-1}$ sr $^{-1}$]	4.90×10^{27} (Evans et al. 2006)

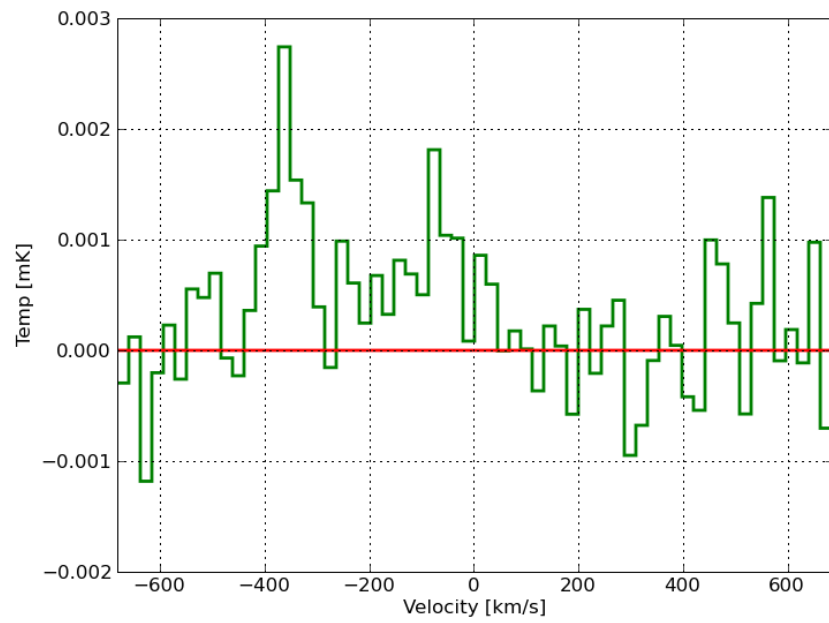


Figure A.66: 3CR 403 CO(1-0)

A.21 3CR 433

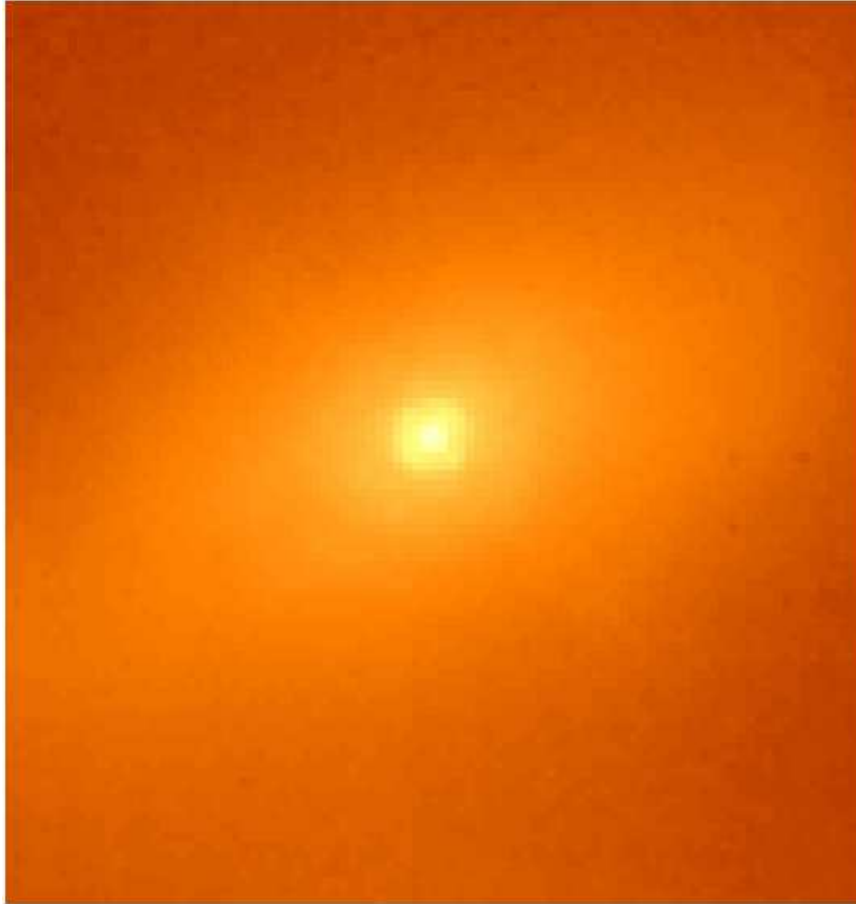


Figure A.67: 3CR 433 HST image.

We observed CO(1-0) for this galaxy and it was not detected. We do not have data for CO(2-1).

Table A.61: General Data for 3CR 433

RA:	21h23m44.5s
Dec:	+25d04m12s
FR:	I
z_{CO} :	0.1
Distance [Mpc]:	420
Line Width:	-
$I_{CO(1-0)}$ [K km/s]:	<0.87
$I_{CO(2-1)}$ [K km/s]:	Not Observe
$M_{H_2} M_{\odot}$:	$<93.13 \times 10^8$

Table A.62: Fluxes of 3CR 433

Wavelength	flux measurement mJy
S_{3mm}	91.20 ± 0.76
S_{1mm}	Not Observe
$f_{12\mu m}$	53 ± 7.95
$f_{25\mu m}$	208 ± 31.2
$f_{60\mu m}$	299 ± 44.9
$f_{100\mu m}$	<1200

Table A.63: Luminosities for 3CR 433

Parameter	Luminosity - L_{\odot}
L_{CO} [K km/s pc^2]	1.48×10^8
L_{FIR} [L_{\odot}]	1.58×10^{11}

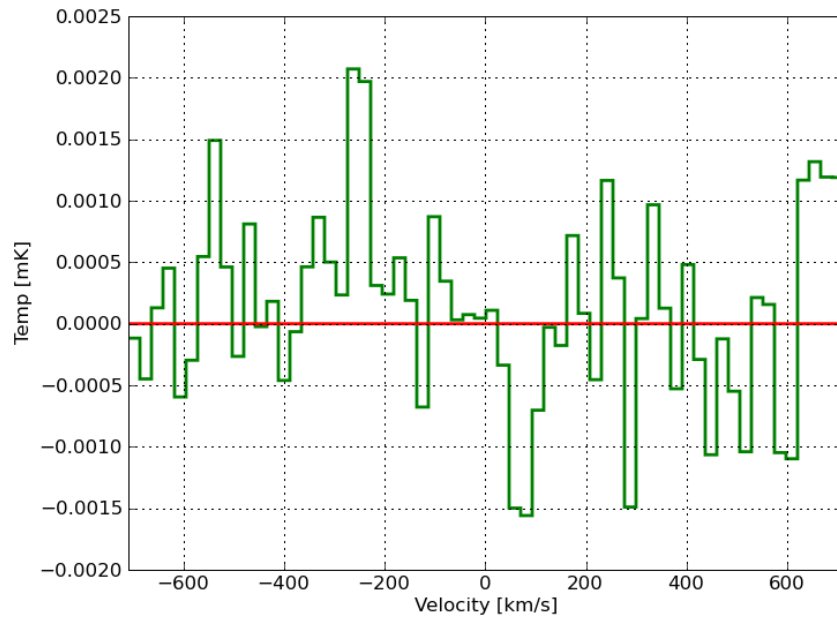


Figure A.68: 3CR 433 CO(1-0)

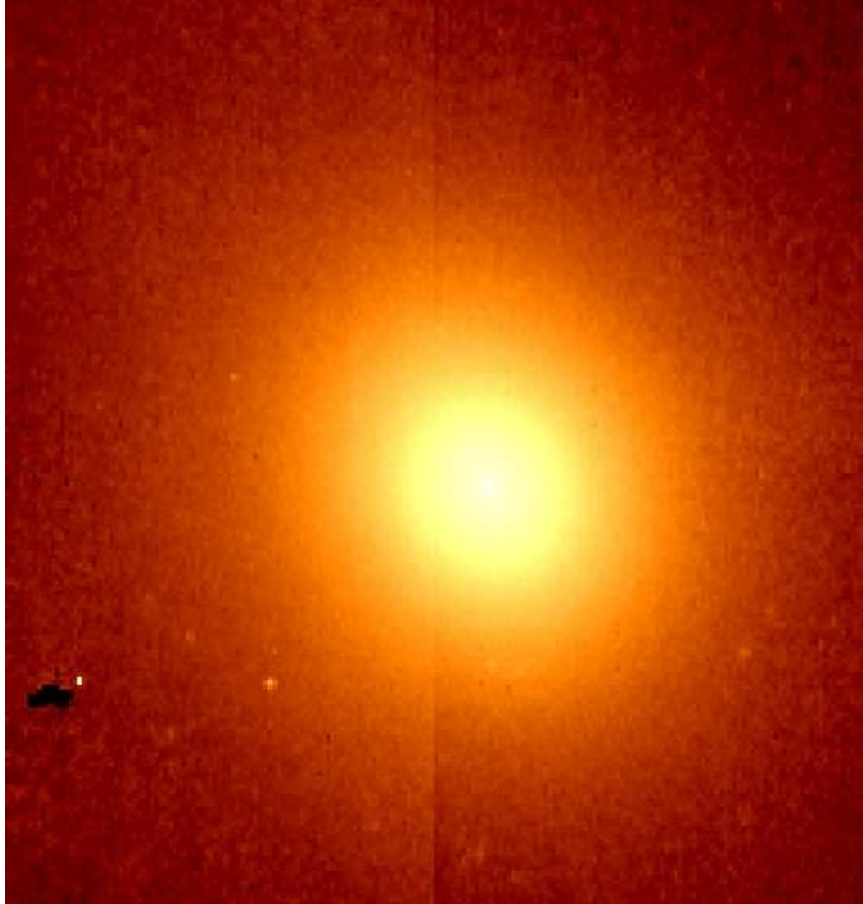
A.22 3C 442**Other Names:** UGC 11958, 3C 442A

Figure A.69: 3CR 442 HST image.

This galaxy was detected in the CO(2-1) emission line, and not detected in the CO(1-0). We calculated the CO(1-0) intensity using the 2.3 average line ratio of the galaxies detected in both lines. In the optical image of the HST we can see the elliptical shape of the galaxy but no trace of the molecular dust. The isophotes of the outer halo of this elliptical galaxy are relatively smooth but within the central 520 pc, they are irregular and the light distribution becomes non-uniform.

Table A.64: General Data for 3CR 442

RA:	22h14m46.9s
Dec:	+13d50m24s
FR:	I
z_{CO} :	0.0263
Distance [Mpc]:	110.5
Line Width:	
$I_{\text{CO}(1-0)}$ [K km/s]:	0.09 ± 0.02
$I_{\text{CO}(2-1)}$ [K km/s]:	0.20 ± 0.07
$M_{\text{H}_2} M_{\odot}$:	$0.67 \pm 0.16 \times 10^8$

Table A.65: Fluxes of 3CR 442

Wavelength	flux measurement mJy
$S_{3\text{mm}}$	9.62 ± 0.43
$S_{1\text{mm}}$	75.51 ± 9.99
$f_{12\mu\text{m}}$...
$f_{25\mu\text{m}}$...
$f_{60\mu\text{m}}$...
$f_{100\mu\text{m}}$...

Table A.66: Luminosities for 3CR 442

Parameter	Luminosity
L_{CO} [K km/s pc^2]	$<1.48 \times 10^9$
L_{FIR} [L_{\odot}]	$<1.58 \times 10^{11}$

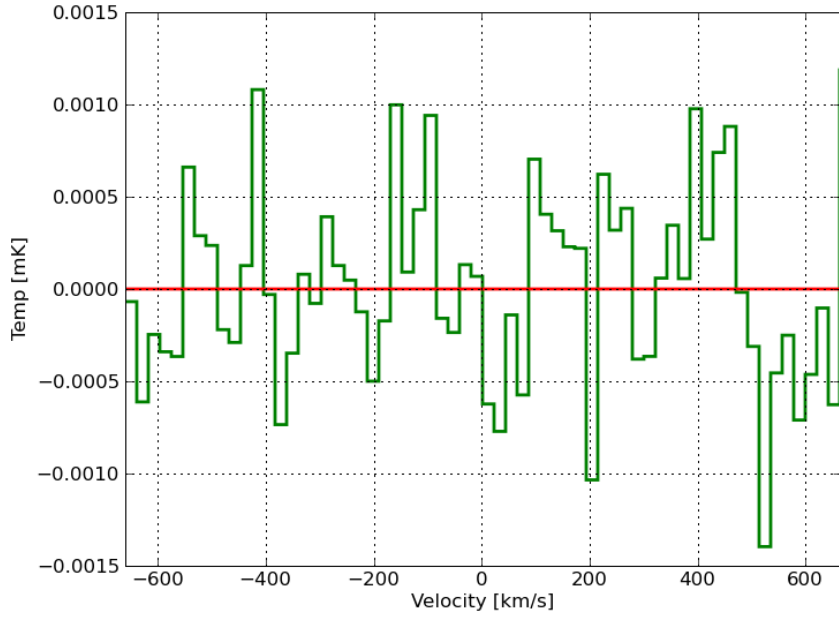


Figure A.70: 3CR 442 CO(1-0)

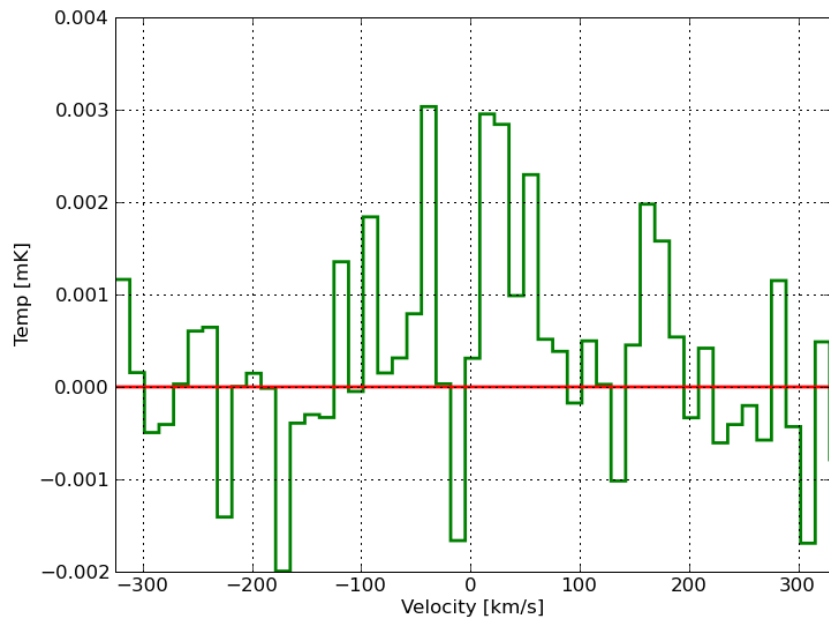


Figure A.71: 3CR 442 CO(2-1)

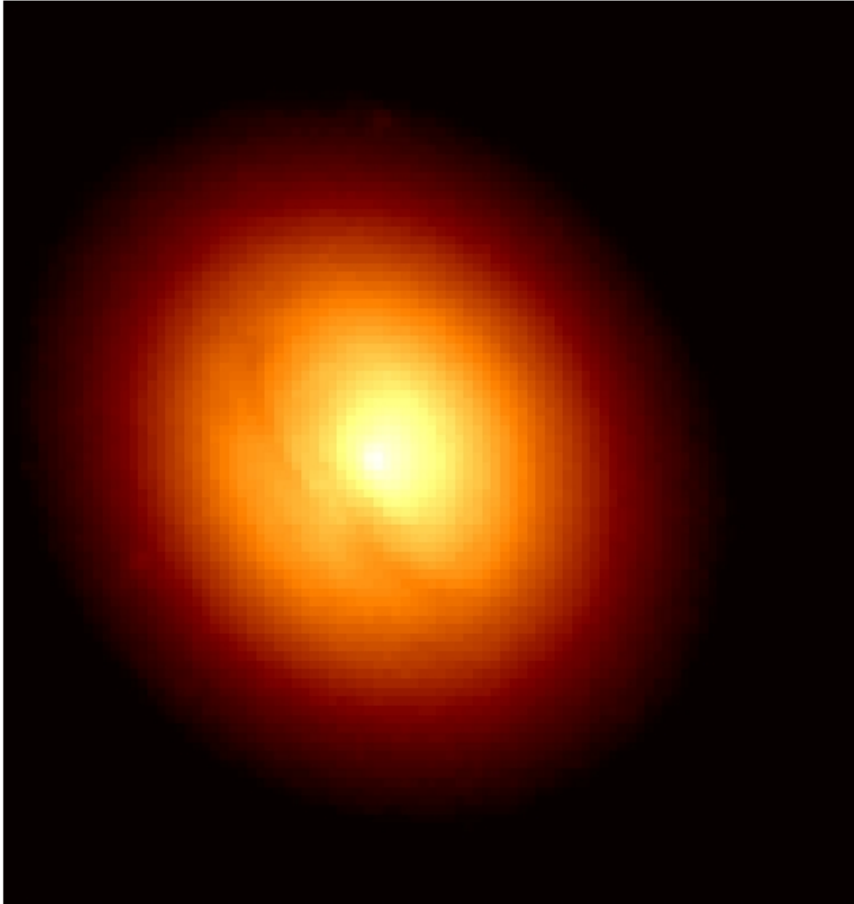
A.23 3C 449**Other Name:** B2 2229+39

Figure A.72: 3CR 449 HST image.

Even though it has a double horn profile that can be noticed from the $CO(1 \rightarrow 0)$ spectra (Figure A.73), one can notice that one side is stronger than the other one. From the HST image of this galaxy it is possible to see the dust absorbing the visible light, but not completely face on. According to [Martel et al. \(1999\)](#) the morphology of this galaxy suggests that we are viewing the near side of an inclined, geometrically thick torus or disk. If we take the detection to be a double horn, we have a $FWZI_{CO(1-0)}$ 500 km/s and a rotational velocity of about 250 km/s.

Table A.67: General Data for 3CR 449

RA:	22h31m20.9s
Dec:	+39d21m48s
FR:	I
z_{CO} :	0.0169
Distance [Mpc]:	71.40
Line Width [km/s]:	500
$I_{CO(1-0)}$ [K km/s]:	1.20 ± 0.24
$I_{CO(2-1)}$ [K km/s]:	...
$M_{H_2} M_{\odot}$:	$3.59 \pm 0.73 \times 10^8$

Table A.68: Fluxes of 3CR 449

Wavelength	flux measurement mJy
S_{3mm}	25.82 ± 0.5
S_{1mm}	15.83 ± 1.65
$f_{12\mu m}$	<35
$f_{25\mu m}$	<40
$f_{60\mu m}$	125 ± 18.8
$f_{100\mu m}$	<720

Table A.69: Luminosities for 3CR 449

Parameter	Luminosity
L_{CO} [K km/s pc^2]	6.92×10^7
L_{FIR} [L_{\odot}]	$<2.19 \times 10^9$
L_{178MHz} [W Hz ⁻¹ sr ⁻¹]	6.51×10^{23} (Evans et al. 2006)

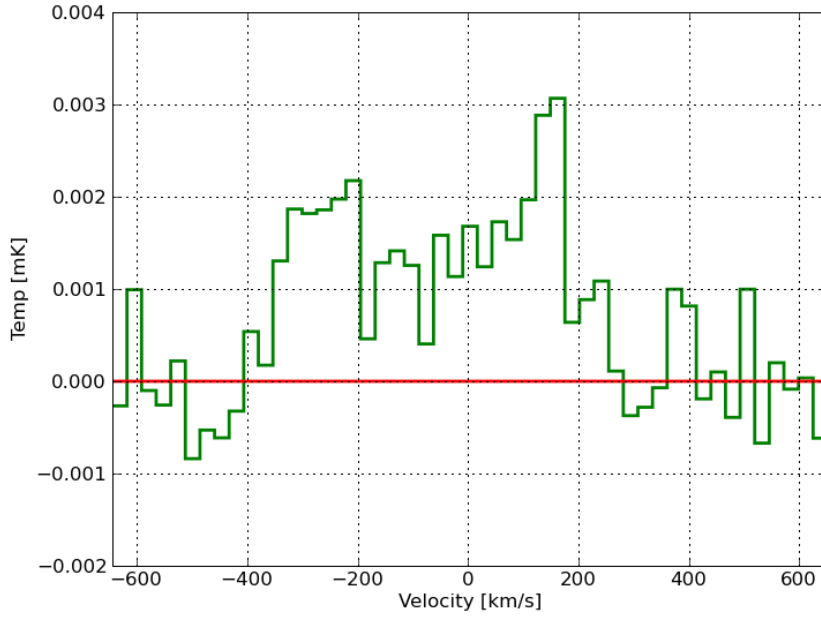


Figure A.73: 3CR 449 CO(1-0)

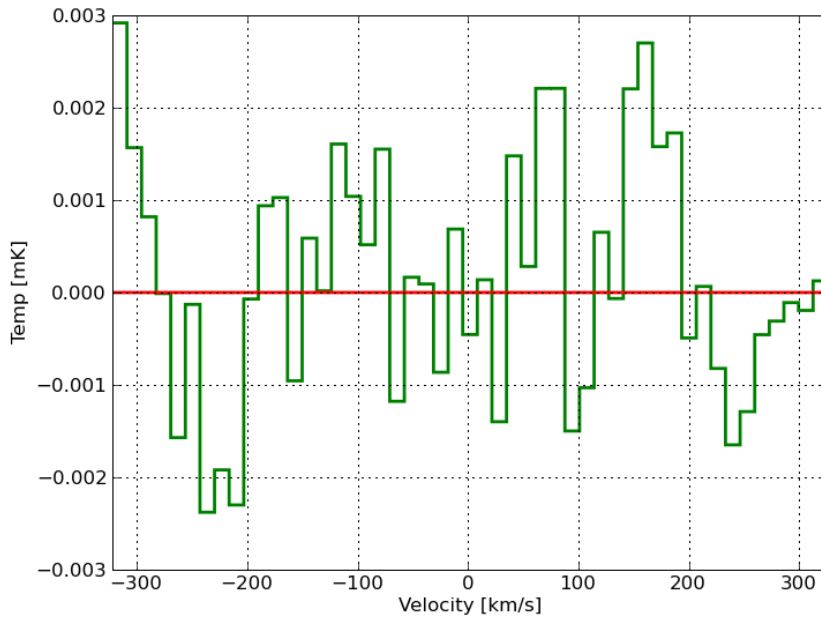


Figure A.74: 3CR 449 CO(2-1)

A.24 3CR 465

Other Names: NGC 7720, B2 2336+26

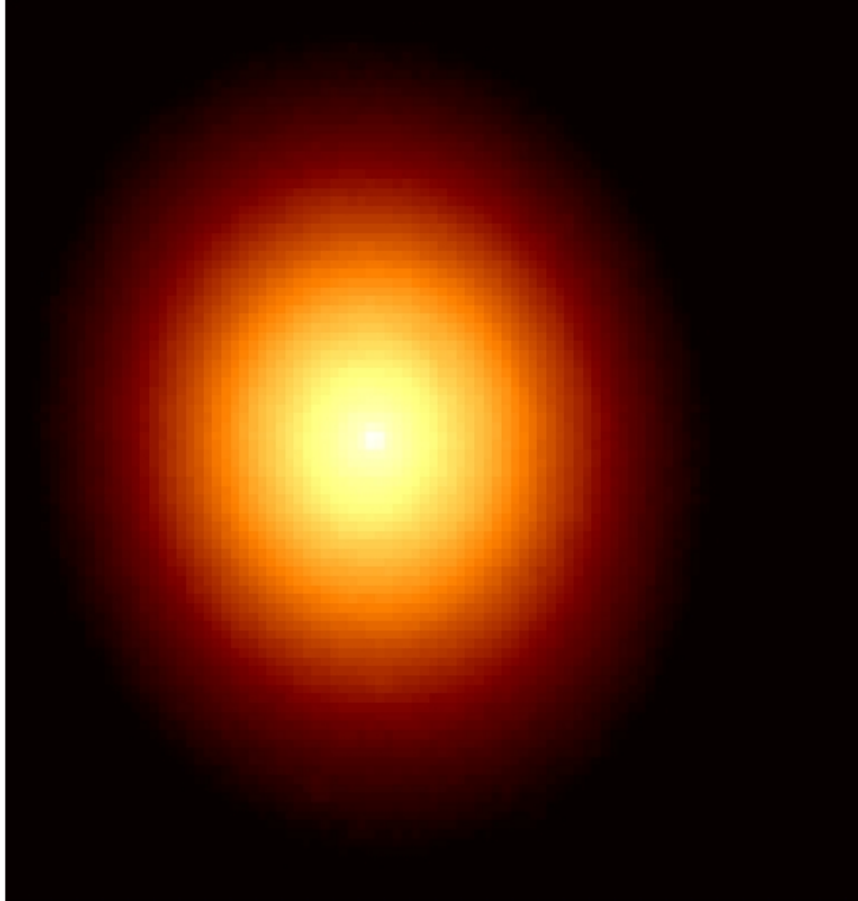


Figure A.75: 3CR 465 HST image.

Table A.70: General Data for 3CR 465

RA:	23h38m29.4s
Dec:	+27d01m53s
FR:	I
z_{CO} :	0.03
Distance [Mpc]:	120
Line Width:	
$I_{CO(1-0)}$ [K km/s]:	<0.78
$I_{CO(2-1)}$ [K km/s]:	...
$M_{H_2} M_{\odot}$:	$<7.69 \times 10^8$

Table A.71: Fluxes of 3CR 465

Wavelength	flux measurement mJy
S_{3mm}	86.06 ± 0.56
S_{1mm}	27.32 ± 1.31
$f_{12\mu m}$	<31
$f_{25\mu m}$	100 ± 27
$f_{60\mu m}$	146 ± 21.9
$f_{100\mu m}$	<300

Table A.72: Luminosities for 3CR 465

Parameter	Luminosity
L_{CO} [K km/s pc^2]	$<1.38 \times 10^8$
L_{FIR} [L_{\odot}]	$<4.57 \times 10^9$
L_{178MHz} [W Hz ⁻¹ sr ⁻¹]	6.41×10^{24} (Evans et al. 2006)

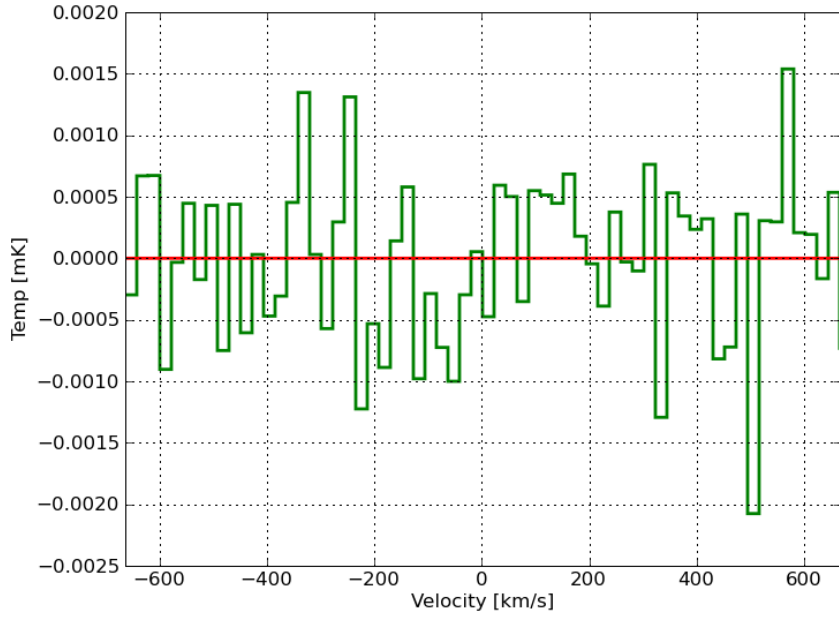


Figure A.76: 3CR 465 CO(1-0)

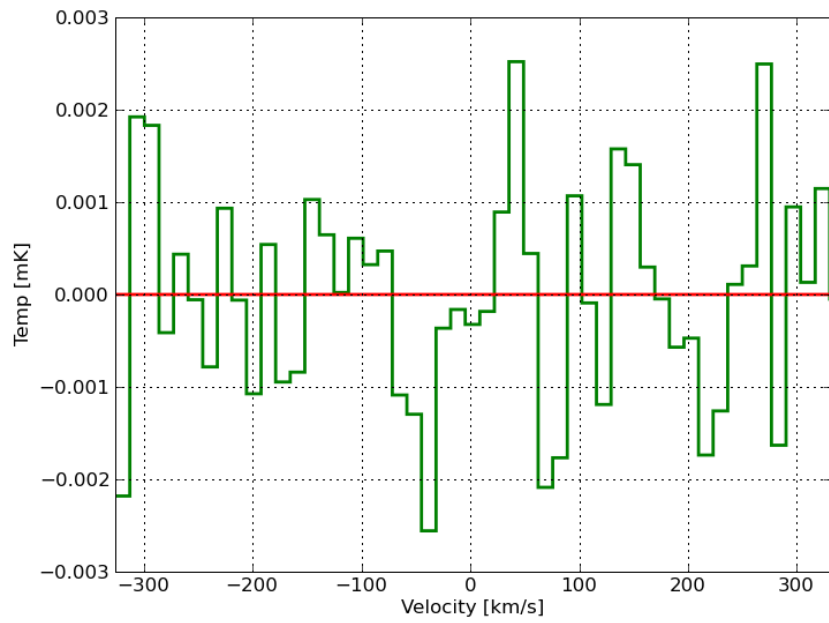


Figure A.77: 3CR 465 CO(2-1)

A.25 NGC 315

Other Name: B2 0055+30

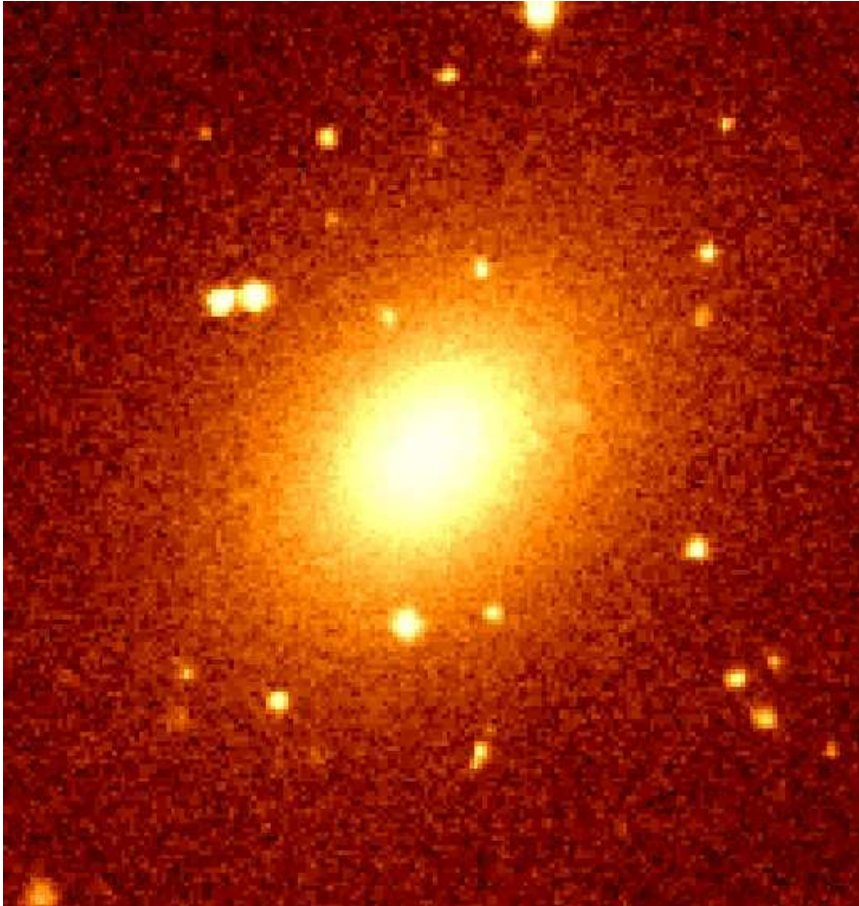


Figure A.78: NGC 315 optical image.

It is detected in $CO(1 \rightarrow 0)$ only, there is no visible feature in the optical image, although it seems that there are dwarf galaxies nearby. [Morganti et al. \(2009\)](#) say that two HI absorbing systems are detected in the central region of this galaxy.

The environment of NGC 315 turns out to be indeed quite gas rich since [Morganti et al. \(2009\)](#) detect five gas-rich companion galaxies in the immediate vicinity of NGC 315.

NGC 315 host a giant radio-source (~ 1 Mpc) ([Bridle et al. 1979](#); [Mack et al. 1998](#); [Laing et al. 2006](#), and references therein)

Table A.73: General Data for NGC 315

RA:	00h57m48.9s
Dec:	+30d21m09s
FR:	I
z_{CO} :	0.0175
Distance [Mpc]:	73.80
Line Width [km/s]:	150
$I_{CO(1-0)}$ [K km/s] :	0.26 ± 0.06
$I_{CO(2-1)}$ [K km/s] :	...
$M_{H_2} M_{\odot}$:	$0.82 \times 10^8 \pm 0.19 \times 10^8$
$M_{Dust} M_{\odot}$:	3.47×10^5
T_{Dust} [K]:	42.93

Table A.74: Fluxes of NGC 315

Wavelength	flux measurement mJy
S_{3mm}	353.56 ± 0.67
S_{1mm}	62.12 ± 1.39
$f_{12\mu m}$	<33
$f_{25\mu m}$	<53
$f_{60\mu m}$	386 ± 55.2
$f_{100\mu m}$	460 ± 69

Table A.75: Luminosities for NGC 315

Parameter	Luminosity
L_{CO} [K km/s pc^2]	1.58×10^7
L_{FIR} [L_{\odot}]	3.31×10^9

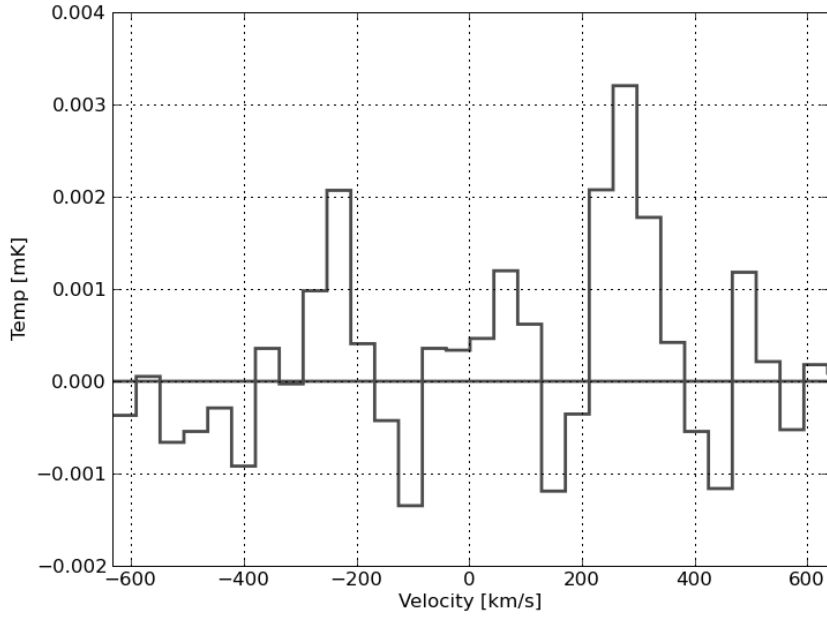


Figure A.79: NGC 315 CO(1-0)

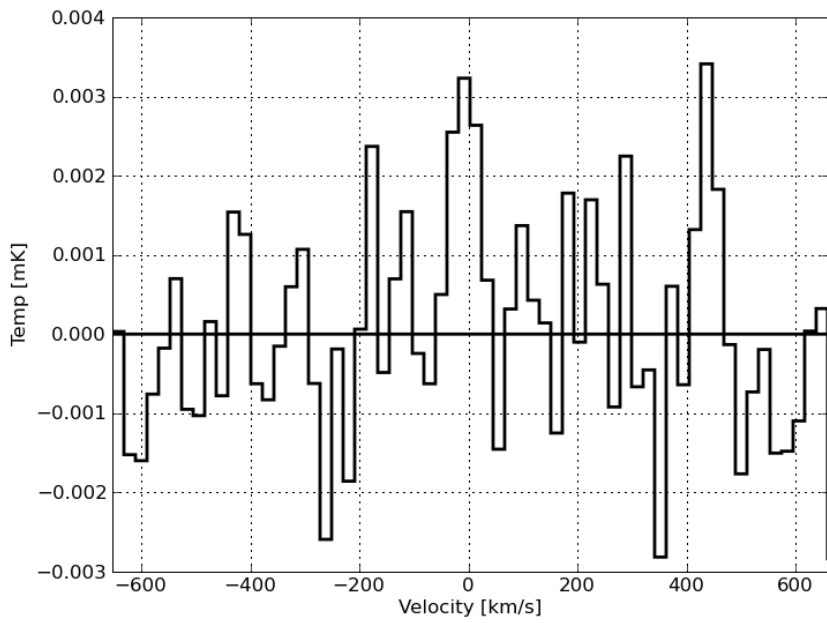
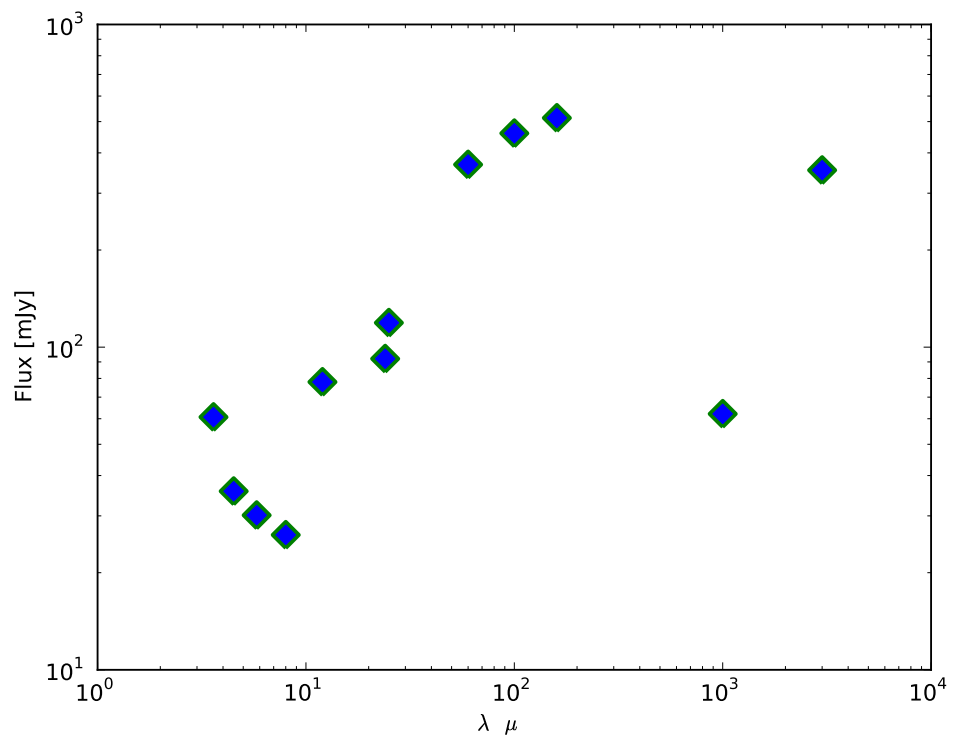


Figure A.80: NGC 315 CO(2-1)

Figure A.81: The Spectral Energy diagram for NGC 315



A.26 NGC 326

Other Names: UGC 00601 , B2 0055+26

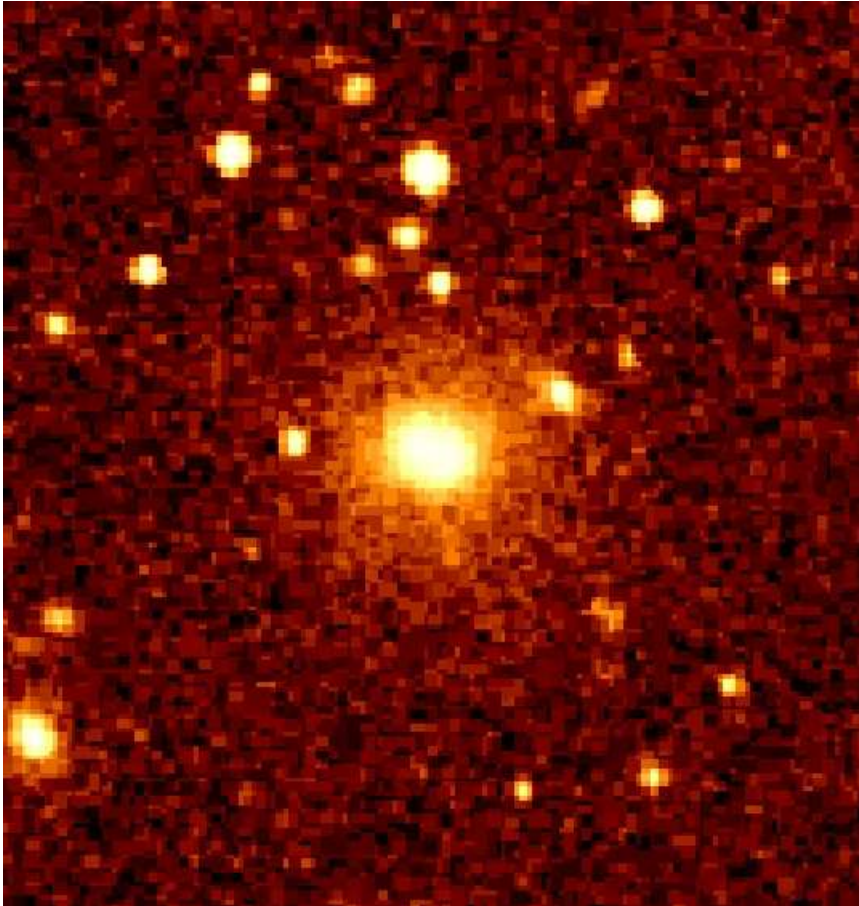


Figure A.82: NGC 326 optical image.

This galaxy has been tentatively detected for CO(1-0) and CO(2-1), observed simultaneously in the IRAM-30m telescope. According to [Murgia et al. \(2001\)](#), NGC 326 is an X-shaped radio source with twin jets ending in two extended radio tails. The curvature of the radio spectrum increases going from the inner parts near the radio core to the ends of the tails. This corresponds to a gradual increase of the age of the electrons as one goes outwards, with the material further out being ejected at an earlier time.

Table A.76: General Data for NGC 326

RA:	00h58m22.7s
Dec:	+26d51m55s
FR:	I
z_{CO} :	0.0474
Distance [Mpc]:	203.18
Line Width:	100
$I_{CO(1-0)}$ [K km/s]:	0.2320 ± 0.05
$I_{CO(2-1)}$ [K km/s]:	0.65 ± 0.2
$M_{H_2} M_{\odot}$:	$5.61 \pm 1.2 \times 10^8$
$M_{Dust} M_{\odot}$:	3.47×10^5
T_{Dust} [K]:	42.93
Line Ratio:	2.8 ± 0.3

Table A.77: Fluxes of NGC 326

Wavelength	flux measurement mJy
S_{3mm}	63.47 ± 0.63
S_{1mm}	...
$f_{12\mu m}$	<40
$f_{25\mu m}$	<50
$f_{60\mu m}$	<80
$f_{100\mu m}$	<250

Table A.78: Luminosities for NGC 326

Parameter	Luminosity
L_{CO} [K km/s pc^2]	9.55×10^7
L_{FIR} [L_{\odot}]	$<7.59 \times 10^9$

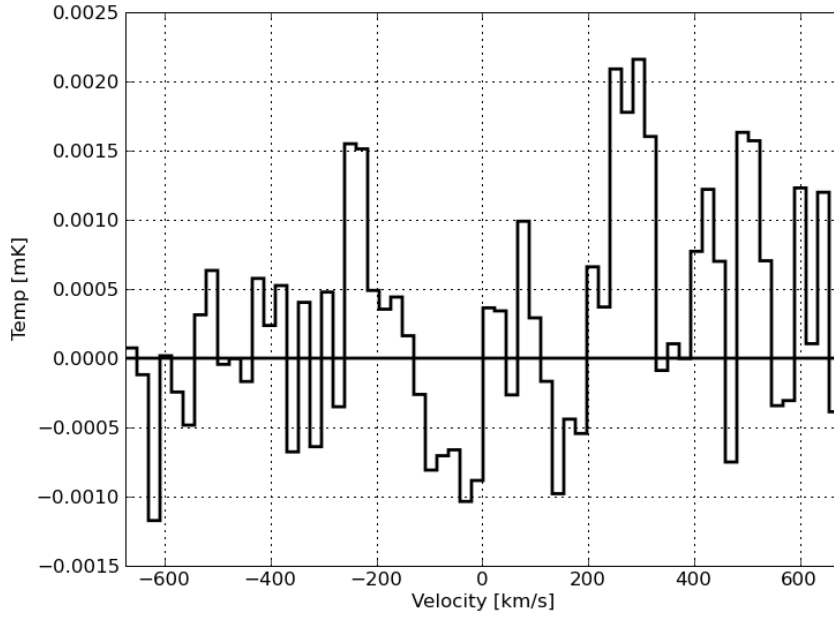


Figure A.83: NGC 326 CO(1-0)

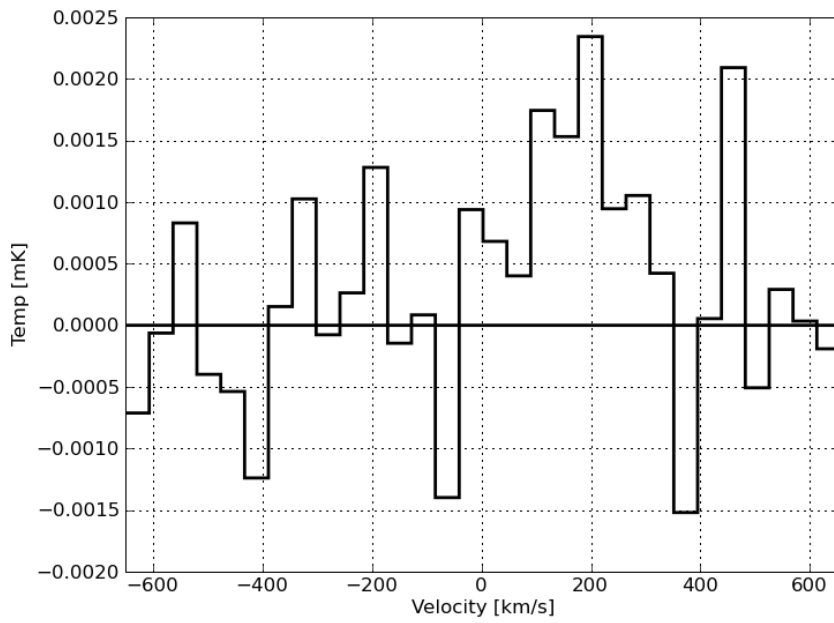


Figure A.84: NGC 326 CO(2-1)

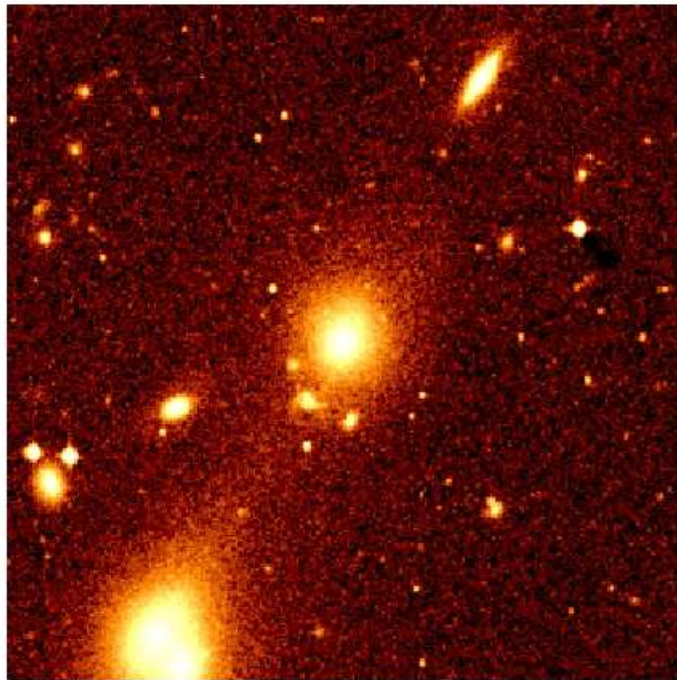
A.27 NGC 541**Other Name:** UGC 01004

Figure A.85: NGC 541 optical image.

This galaxy has been detected in the $CO(2 \rightarrow 1)$ even though no emission can be seen in $CO(1 \rightarrow 0)$. From the optical image there is another galaxy that might be falling into NGC541 and there is another larger galaxy probably having some effects on NGC 541. According to [Noel-Storr et al. \(2003\)](#), this CD SO galaxy has a radio core on VLBA scales and a core-jet morphology on VLA scales. The STIS slits were aligned to a mean of the position angles of the central isophote measured from the WFPC/2 images, which vary considerably. The gas does not exhibit regular rotation profile.

Table A.79: General Data for NGC 541

RA:	01h25m44.3s
Dec:	-01d22m46s
FR:	I
z_{CO} :	0.018
Distance [Mpc]:	75
Line Width:	-
$I_{CO(1-0)}$ [K km/s]:	0.72 ± 0.08
$I_{CO(2-1)}$ [K km/s]:	1.43 ± 0.32
$M_{H_2} M_{\odot}$:	$2.5 \pm 0.27 \times 10^8$

Table A.80: Fluxes of NGC 541

Wavelength	flux measurement mJy
S_{3mm}	4.73 ± 2.02
S_{1mm}	27.23 ± 2.60
$f_{12\mu m}$	<23
$f_{25\mu m}$	<64
$f_{60\mu m}$	<48
$f_{100\mu m}$	<131

Table A.81: Luminosities for NGC 541

Parameter	Luminosity
L_{CO} [K km/s pc^2]	4.37×10^7
L_{FIR} [L_{\odot}]	$<6.17 \times 10^8$

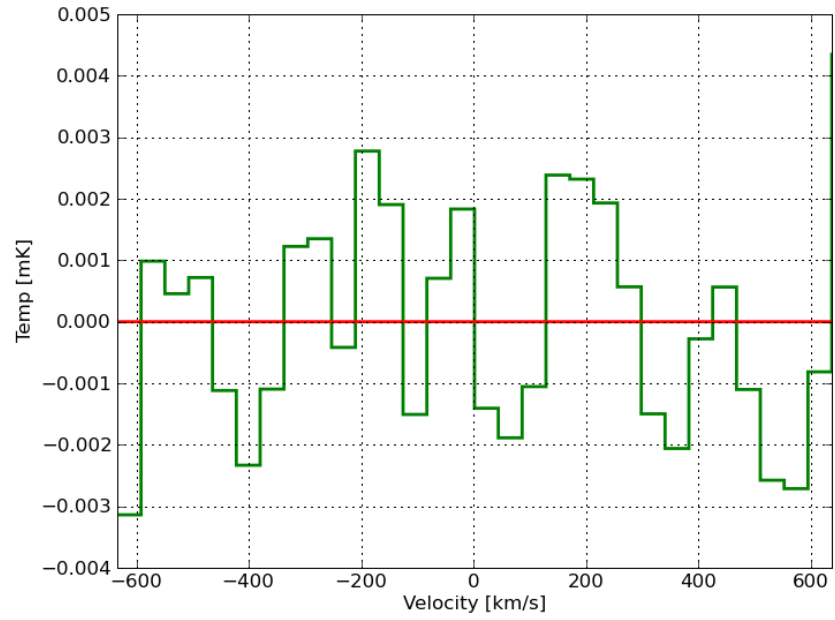


Figure A.86: NGC 541 CO(1-0)

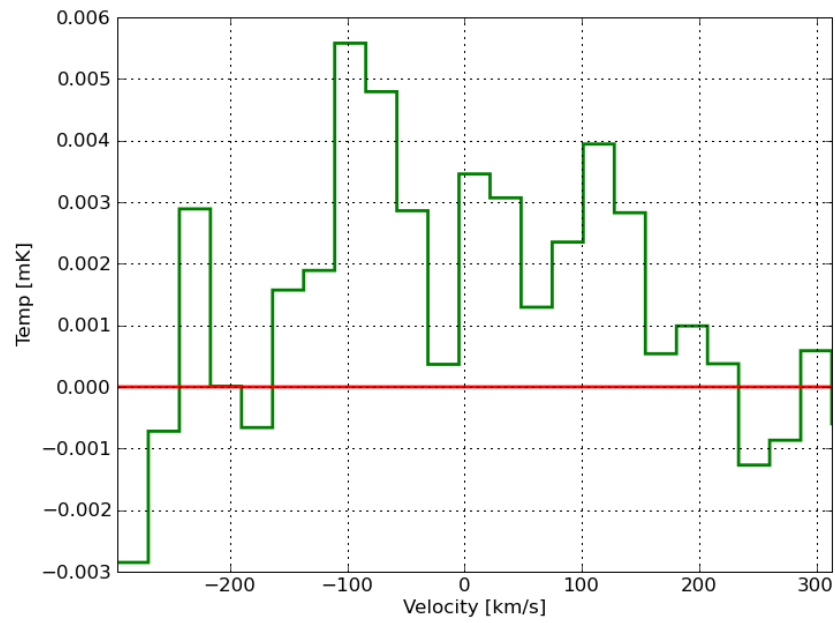


Figure A.87: NGC 541 CO(2-1)

A.28 NGC 708

Other Names: UGC 01348, B2 0149+35

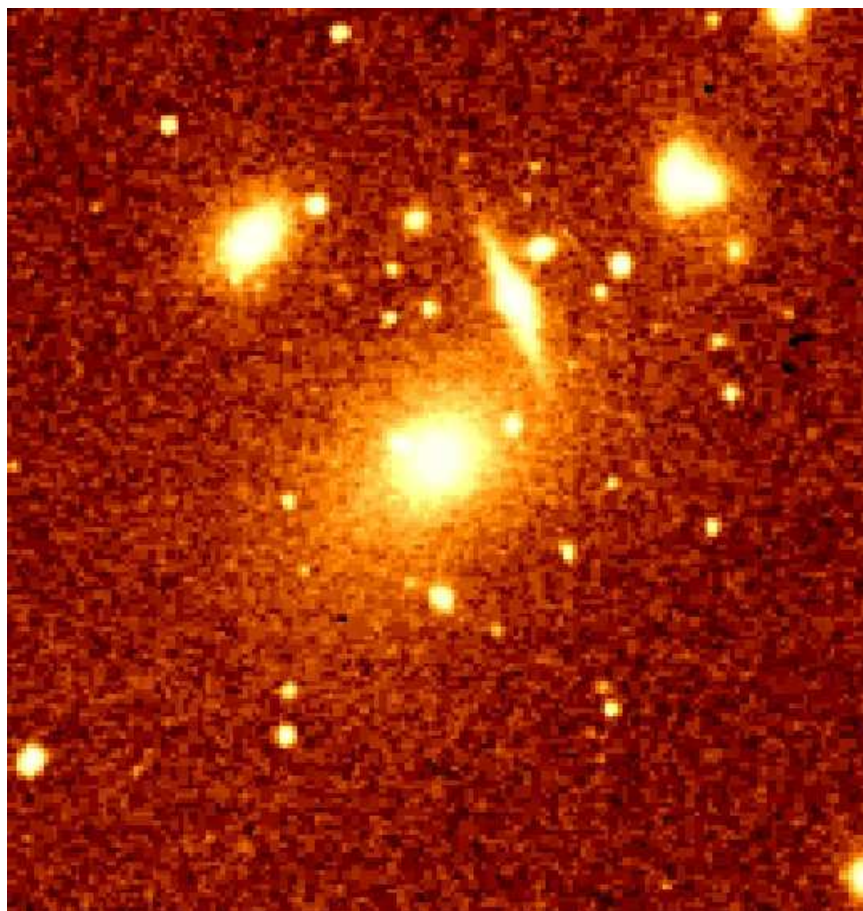


Figure A.88: NGC 708 optical image.

This galaxy has been clearly detected in CO(1-0). This galaxy is located in the Abell 262 galaxy cluster.

Table A.82: General Data for NGC 708

RA:	01h52m46.5s
Dec:	+36d09m07s
FR:	I
z_{CO} :	0.0166
Distance [Mpc]:	69.86
Line Width [km/s]:	600
$I_{\text{CO}(1-0)}$ [K km/s]:	1.84 ± 0.31
$I_{\text{CO}(2-1)}$ [K km/s]:	...
$M_{\text{H}_2} M_{\odot}$:	$5.25 \pm 0.88 \times 10^8$
$M_{\text{Dust}} M_{\odot}$:	2.04×10^6
T_{Dust} :	29.70 [K]

Table A.83: Fluxes of NGC 708

Wavelength	flux measurement mJy
$S_{3\text{mm}}$	8.11 ± 0.98
$S_{1\text{mm}}$	148.94 ± 3.83
$f_{12\mu\text{m}}$	150 ± 55
$f_{25\mu\text{m}}$	<44
$f_{60\mu\text{m}}$	200 ± 34
$f_{100\mu\text{m}}$	660 ± 157

Table A.84: Luminosities for NGC 708

Parameter	Luminosity
L_{CO} [K km/s pc^2]	1.02×10^8
L_{FIR} [L_{\odot}]	2.40×10^9

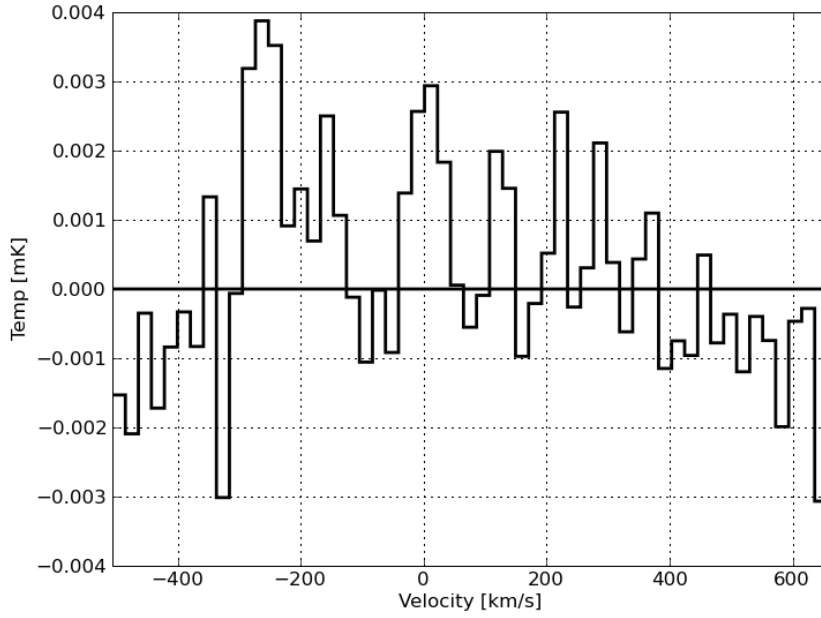


Figure A.89: NGC 708 CO(1-0)

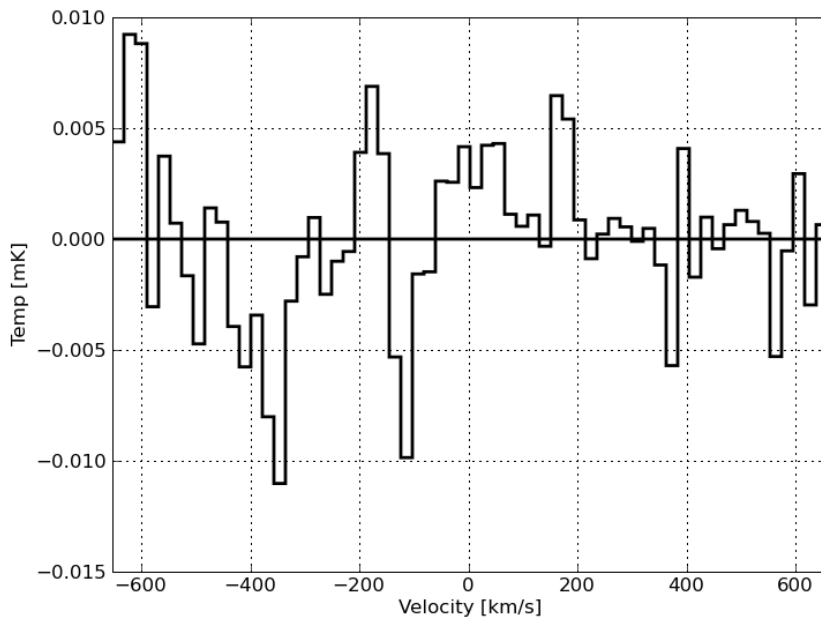
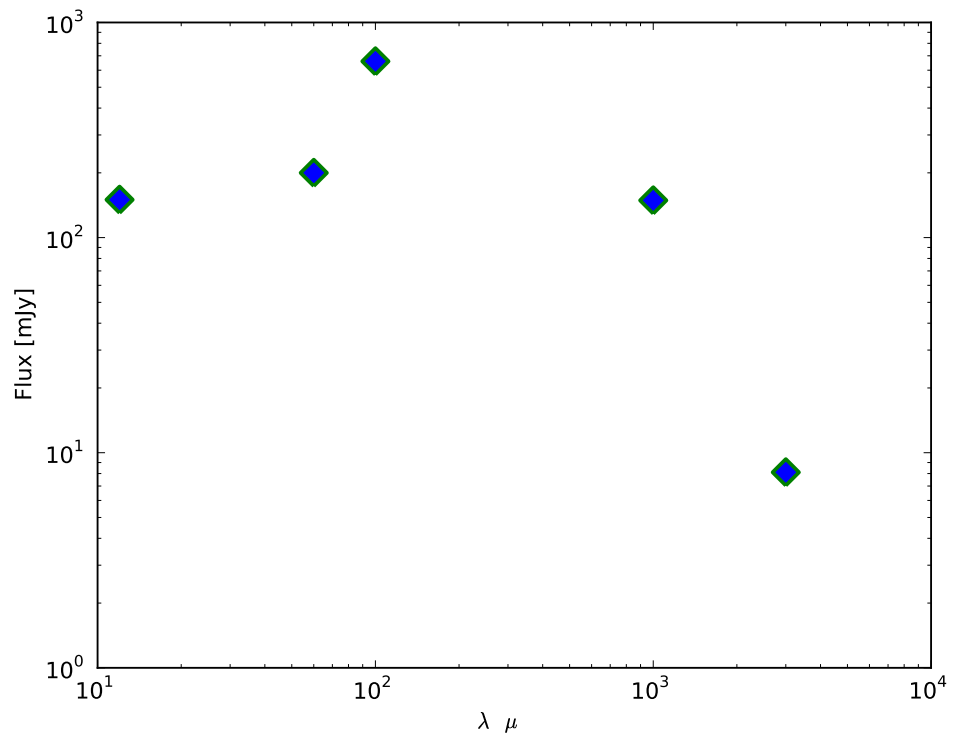


Figure A.90: NGC 708 CO(2-1)

Figure A.91: The Spectral Energy Distribution diagram for NGC 708



A.29 NGC 2484

Other Names: UGC 04125, B2 0755+37, 3C 189

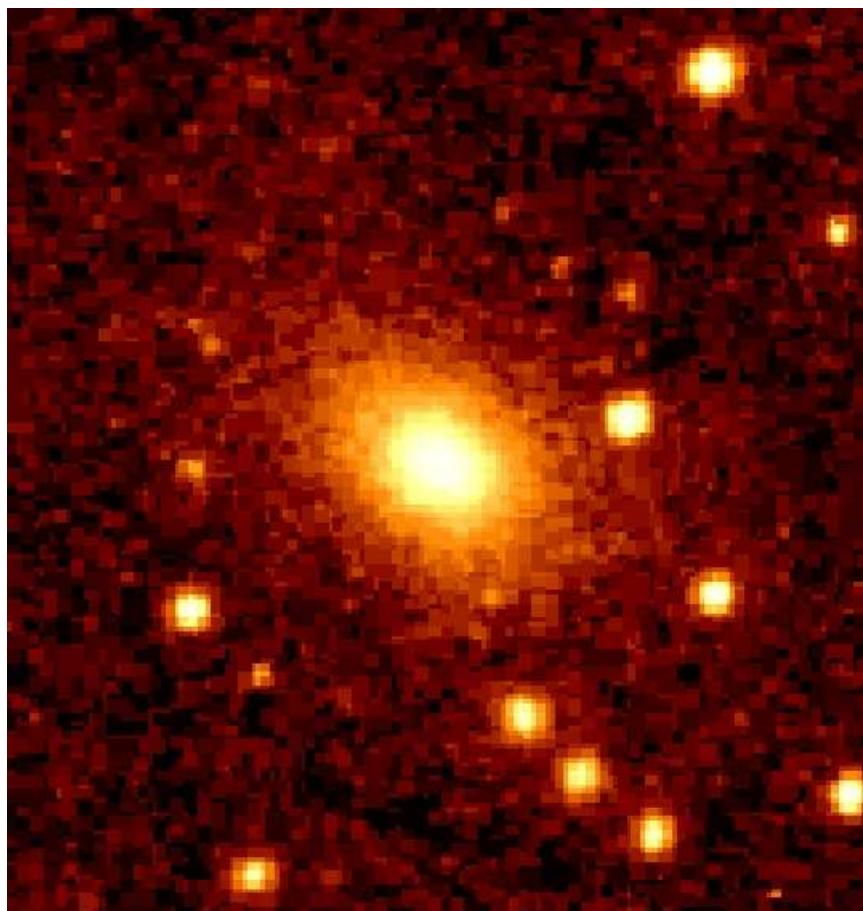


Figure A.92: NGC 2484 optical image.

This galaxy was observed for CO(1-0) and CO(2-1) and it was not detected.

Table A.85: General Data for NGC 2484

RA:	07h58m28.1s
Dec:	+37d47m12s
FR:	I
z_{CO} :	0.043
Distance [Mpc]:	178
Line Width [km/s]:	-
$I_{CO(1-0)}$ [K km/s]:	< 1.00
$I_{CO(2-1)}$ [K km/s]:	...
$M_{H_2} M_{\odot}$:	< 19.17×10^8

Table A.86: Fluxes of NGC 2484

Wavelength	flux measurement mJy
S_{3mm}	110.63 ± 0.69
S_{1mm}	11.92 ± 1.65
$f_{12\mu m}$...
$f_{25\mu m}$...
$f_{60\mu m}$...
$f_{100\mu m}$...

Table A.87: Luminosities for NGC 2484

Parameter	Luminosity - L_{\odot}
L_{CO} [K km/s pc^2]	$< 3.47 \times 10^8$
L_{FIR} [L_{\odot}]	...

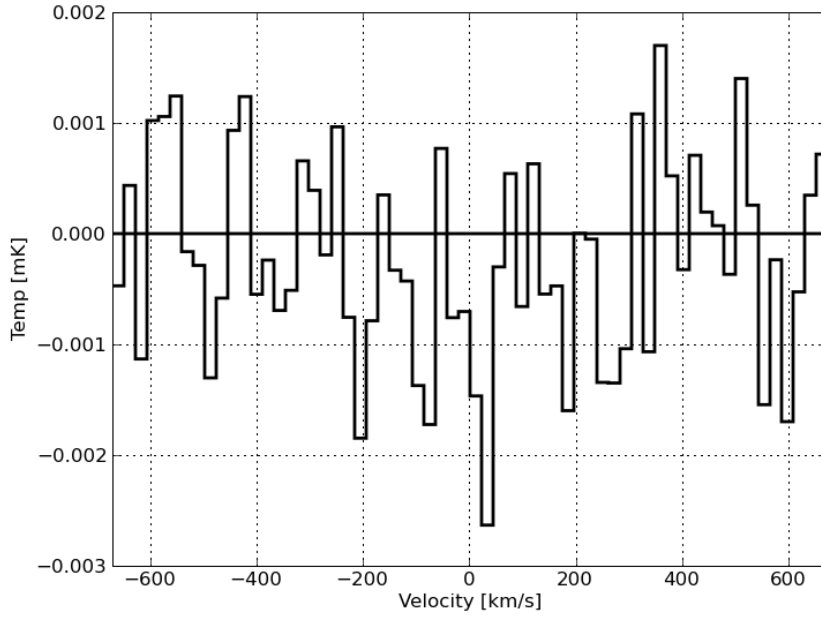


Figure A.93: NGC 2484 CO(1-0)

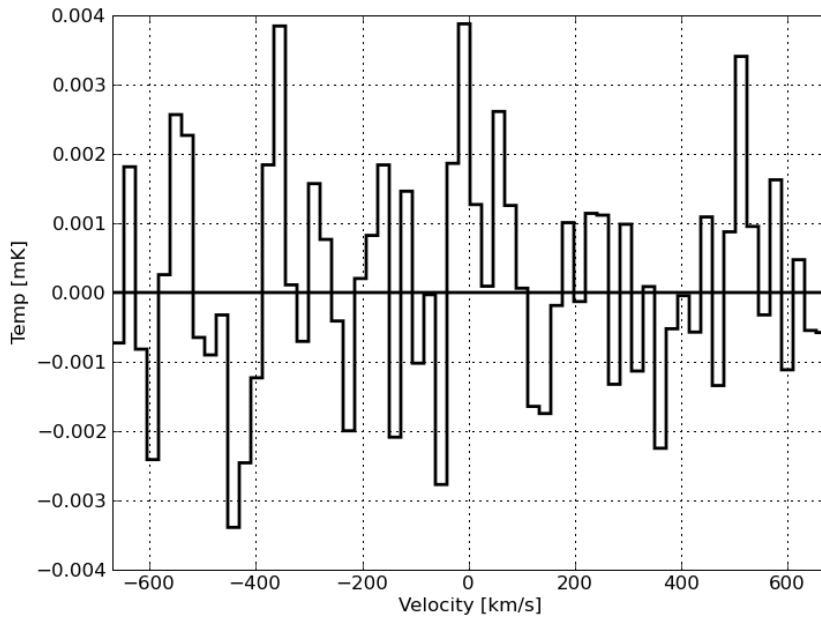


Figure A.94: NGC 2484 CO(2-1)

A.30 NGC 2892

Other Name: UGC 05073

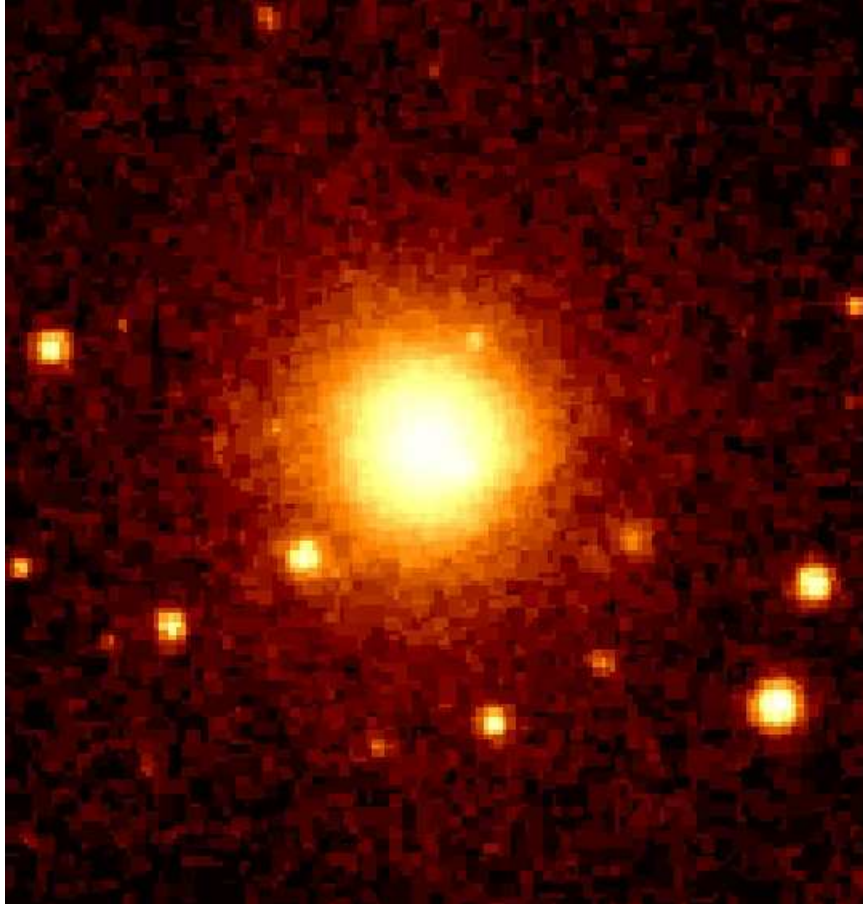


Figure A.95: NGC 2892 optical image.

This galaxy was observed for CO(1-0) and CO(2-1) but it was not detected.

A.30.1 HI data

This galaxy was observed with Effelsberg-100m Telescope for a total of 93 minutes, resulting on a tentative detection.

Table A.88: General Data for NGC 2892

RA:	09h32m52.9s
Dec:	+67d37m03
FR:	I
z_{CO} :	0.022
Distance [Mpc]:	96
Line Width [km/s]:	-
$I_{CO(1-0)}$ [K km/s]:	<1.22
$I_{CO(2-1)}$ [K km/s] :	...
$M_{H_2} M_{\odot}$:	$<6.85 \times 10^8$

Table A.89: Fluxes of NGC 2892

Wavelength	flux measurement mJy
S_{3mm}	190.05 ± 0.87
S_{1mm}	272.39 ± 2.23
$f_{12\mu m}$...
$f_{25\mu m}$...
$f_{60\mu m}$...
$f_{100\mu m}$...

Table A.90: Luminosities for NGC 2892

Parameter	Luminosity
L_{CO} [K km/s pc^2]	$< 1.26 \times 10^8$
L_{FIR} [L_{\odot}]	...

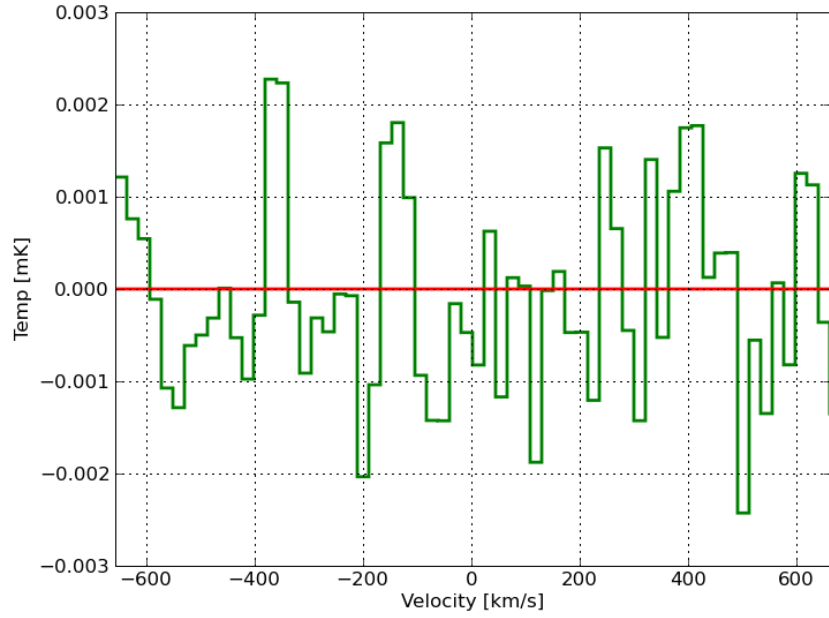


Figure A.96: NGC 2892 CO(1-0)

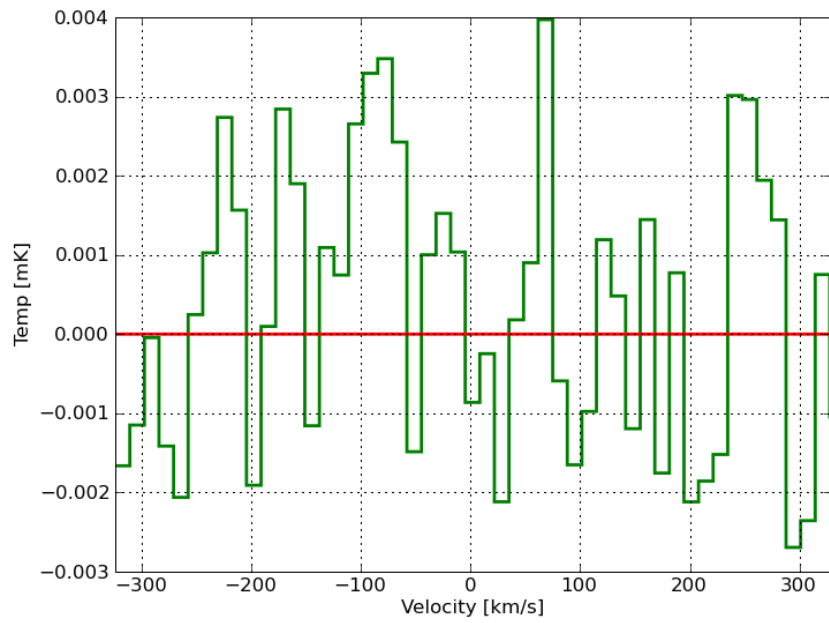


Figure A.97: NGC 2892 CO(2-1)

243; 3 NGC2892 NONE FRONTTEST-2 O: 28-JUN-2008 R: 29-JUN-2008
RA: 09:32:52.901 DEC: 67:37:03.00 (2000.0) Offs: +3.852 -2.706 Eq
Unknown Tau: 0.000 Tsys: 21.23 Time: 93.88 El: 70.57
N: 255 lO: 128.0 vO: 0.000 Dv: 17.11 LSR
FO: 1368.05200 Df: -7.8144E-02 Fi: 1218.05200
B ef: 0.000 F ef: 0.000 G im: 0.000
H2O : 0.000 Pamb: 0.000 Tamb: 0.0 Tchop: 0.0 Tcold: 0.0
Tatm: 0.0 Tau: 0.000 Tatm i: 0.0 Tau i: 0.000
2995- 3014,

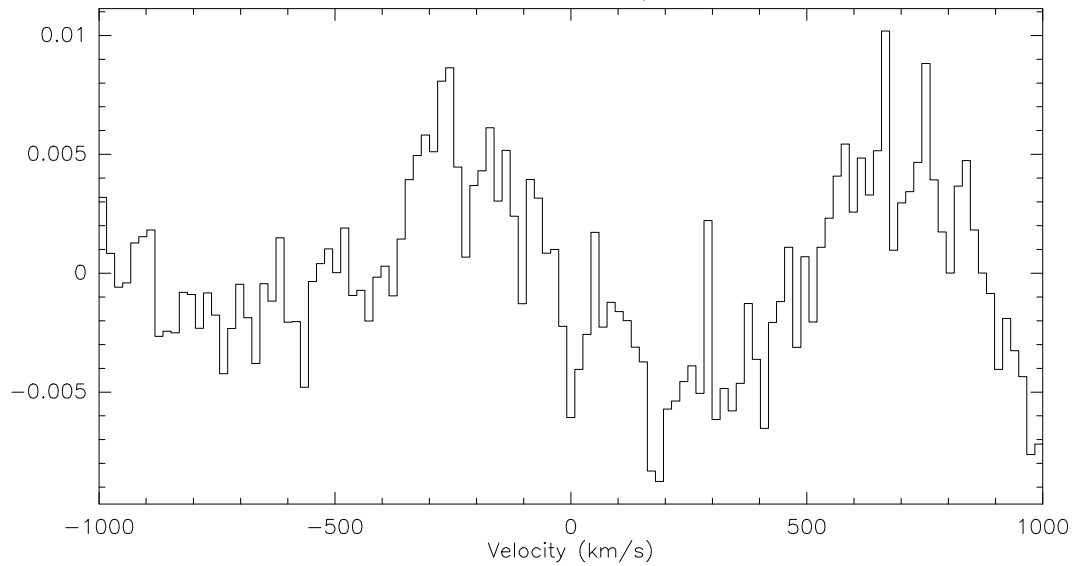


Figure A.98: HI emission for NGC 2892

A.31 NGC 3801

Other Name: UGC 06635

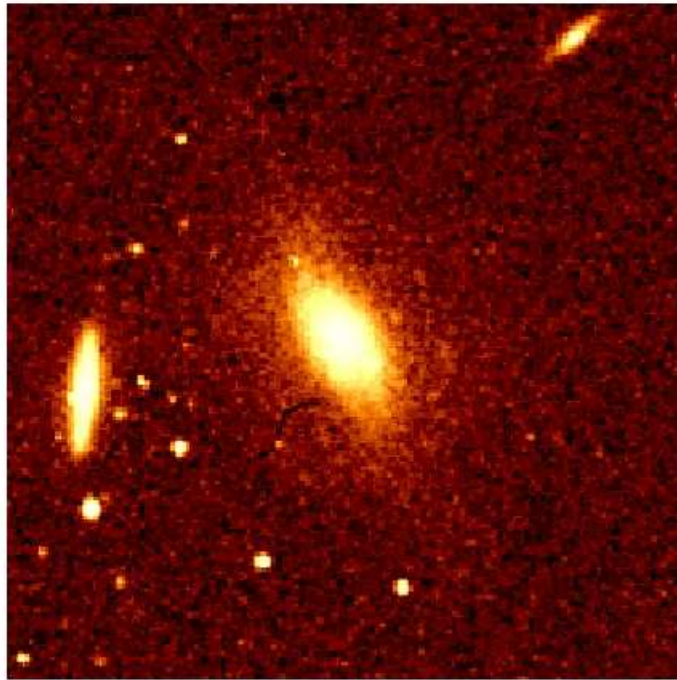


Figure A.99: NGC 3801 optical image.

It shows a double horn profile, detected in the CO(1-0) spectral line, with a velocity width of ~ 600 km/s, and therefore, a rotational velocity of about 300 km/s.

[Croston et al. \(2007\)](#) reported a Chandra detection of shock-heated shells of hot gas surrounding the radio lobes of NGC 3801. They infer Mach numbers of 3-6 for the shock advance speeds, so that their results correspond to the second detection of strong shocks associated with a low-power radio galaxy. The total energy stored in the shock-heated shells represents a large fraction of the total thermal energy of the host galaxy, so that the long-term effects of the NGC 3801 outburst are likely to be dramatic. This is the first case where the total energetic impact of a radio galaxy on its environment can be directly

measured, and suggests that the energetic contribution of an early supersonic phase is likely to be important in low-power radio galaxies. The energy stored in the shocked gas is 25 times the $P dV$ work required to inflate the radio-lobe cavities, so that during this phase of its evolution, shock heating is the dominant mechanism of energy transfer from NGC 3801 to its environment.

Table A.91: General Data for NGC 3801

RA:	11h40m16.9s
Dec:	+17d43m41s
FR:	I
z_{CO} :	0.0117
Distance [Mpc]:	49.50
Line Width [km/s]:	600
$I_{CO(1-0)}$ [K km/s]:	3.82 ± 1.14
$I_{CO(2-1)}$ [K km/s]:	...
$M_{H_2} M_{\odot}$:	$5.49 \pm 1.63 \times 10^8$

Table A.92: Fluxes of NGC 3801

Wavelength	flux measurement mJy
S_{3mm}	1181.72 ± 210
S_{1mm}	...
$f_{12\mu m}$	80 ± 30
$f_{25\mu m}$	150 ± 49
$f_{60\mu m}$	<1150
$f_{100\mu m}$	<1000

Table A.93: Luminosities for NGC 3801

Parameter	Luminosity
L_{CO} [K km/s pc^2]	1.07×10^8
L_{FIR} [L_{\odot}]	$< 3.98 \times 10^9$

A.31.1 HI data

This galaxy was observed with Effelsberg-100m Telescope, but it was not detected.

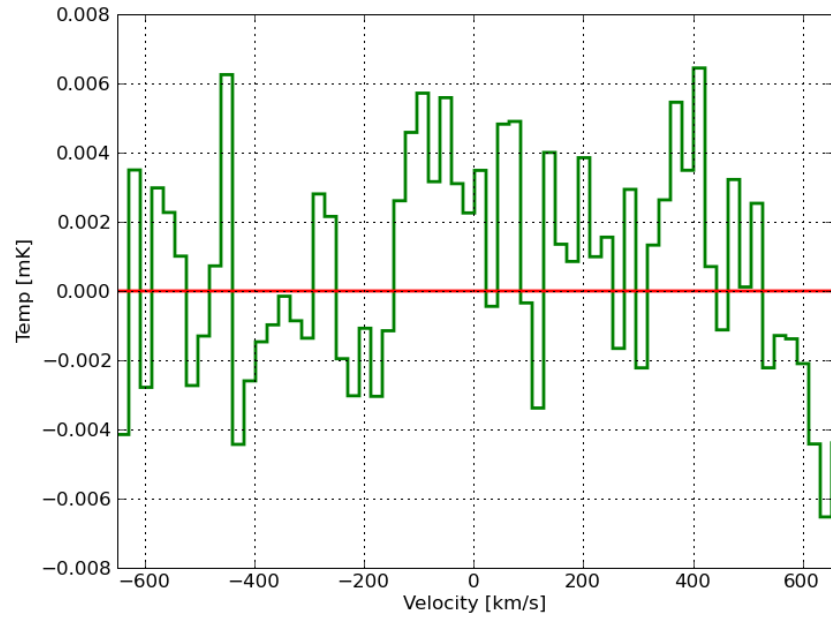


Figure A.100: NGC 3801 CO(1-0)

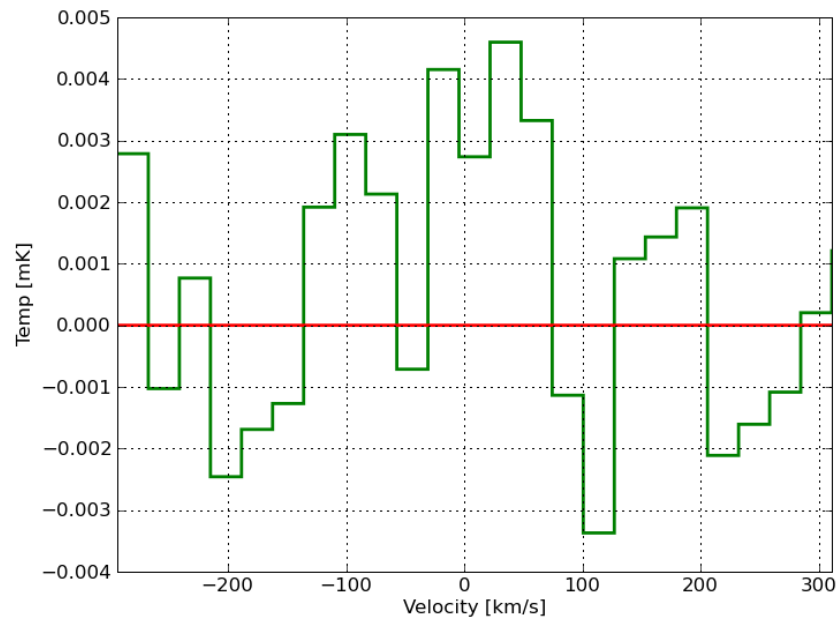


Figure A.101: NGC 3801 CO(2-1)

1; 1 NGC3801 NONE FRONTTEST-2 O: 07-JUN-2008 R: 08-JUN-2008
RA: 11:40:16.899 DEC: 17:43:41.00 (2000.0) Offs: -0.028 -0.012 Eq
Unknown Tau: 0.00 Tsys: 23.79 Time: 225.0 El: 56.37
N: 511 I0: 256.0 V0: 0.00 Dv: 8.468 LSR
F0: 1383.63400 Df: -3.9072E-02 Fi: 1233.63400

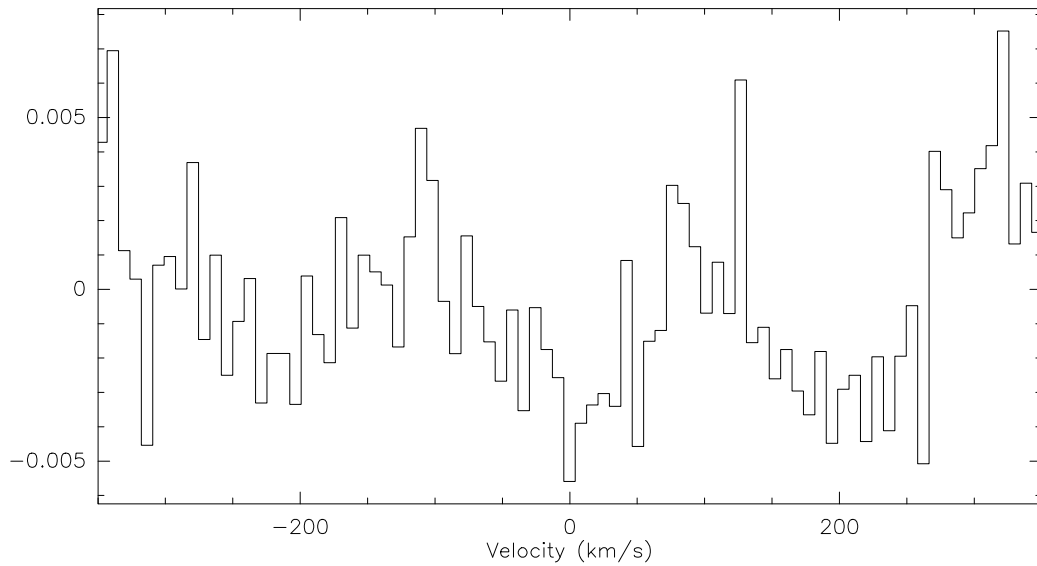


Figure A.102: HI emission for NGC 3801

A.32 NGC 4278

Other Names: B2 1217+29, UGC 07386

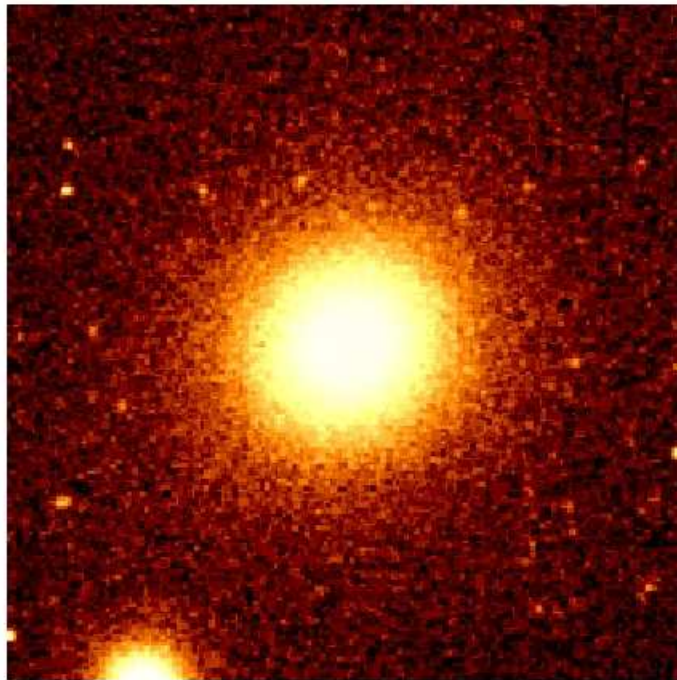


Figure A.103: NGC 4278 optical image.

The line emission is stronger in the CO(2-1) line rather than in CO(1-0) line. Like for 3C272.1, this galaxy has been clearly detected in the CO(2 \rightarrow 1) and we could see a hint of detection in CO(1 \rightarrow 0), and since this tentative detection is at about the same place velocity for both transitions, it has been considered as a detection with stronger emission in the CO(2 \rightarrow 1) line. Note that this is the closest radio galaxy of all (9 Mpc). According to [Combes et al. \(2007\)](#) the dust morphology across the disk is of large scale of irregular patches or lanes; this suggests that this galaxy has recently accreted its gas ([Sarzi et al. 2006](#)).

Table A.94: General Data for NGC 4278

RA:	12h20m06.8s
Dec:	+29d16m51s
FR:	c
z_{CO} :	0.0022
Distance [Mpc]:	49.50
Line Width [km/s]:	600
$I_{CO(1-0)}$ [K km/s]:	1.00 ± 0.22
$I_{CO(2-1)}$ [K km/s]:	3.13 ± 0.31
$M_{H_2} M_{\odot}$:	$0.05 \pm 0.01 \times 10^8$
$M_{Dust} M_{\odot}$:	9.55×10^4
T_{Dust} [K]:	29.97

Table A.95: Fluxes of NGC 4278

Wavelength	flux measurement mJy
S_{3mm}	215.9 ± 1.08
S_{1mm}	194.34 ± 1.28
$f_{12\mu m}$	150 ± 43
$f_{25\mu m}$	<32
$f_{60\mu m}$	580 ± 53
$f_{100\mu m}$	1860 ± 60

Table A.96: Luminosities for NGC 4278

Parameter	Luminosity
L_{CO} [K km/s pc^2]	1.00×10^6
L_{FIR} [L_{\odot}]	1.20×10^8

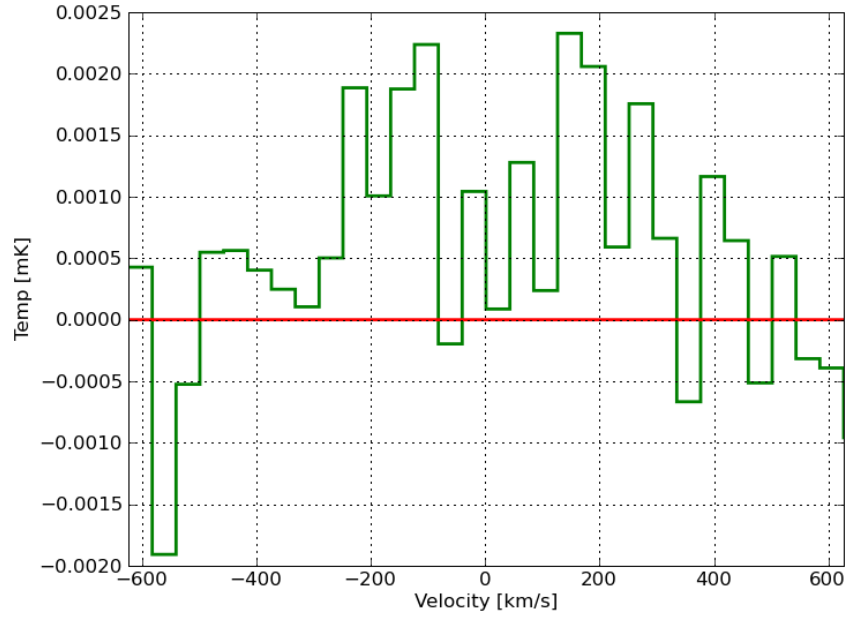


Figure A.104: NGC 4278 CO(1-0)

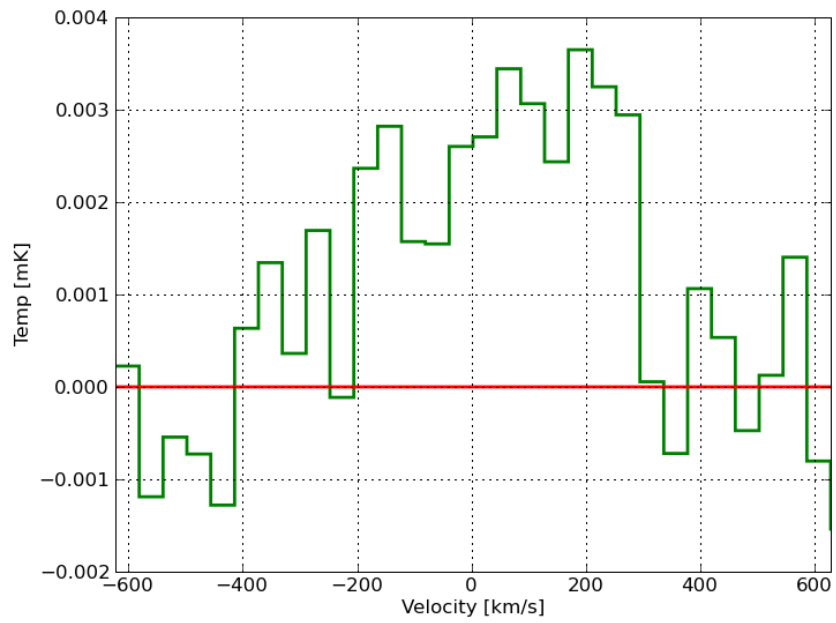
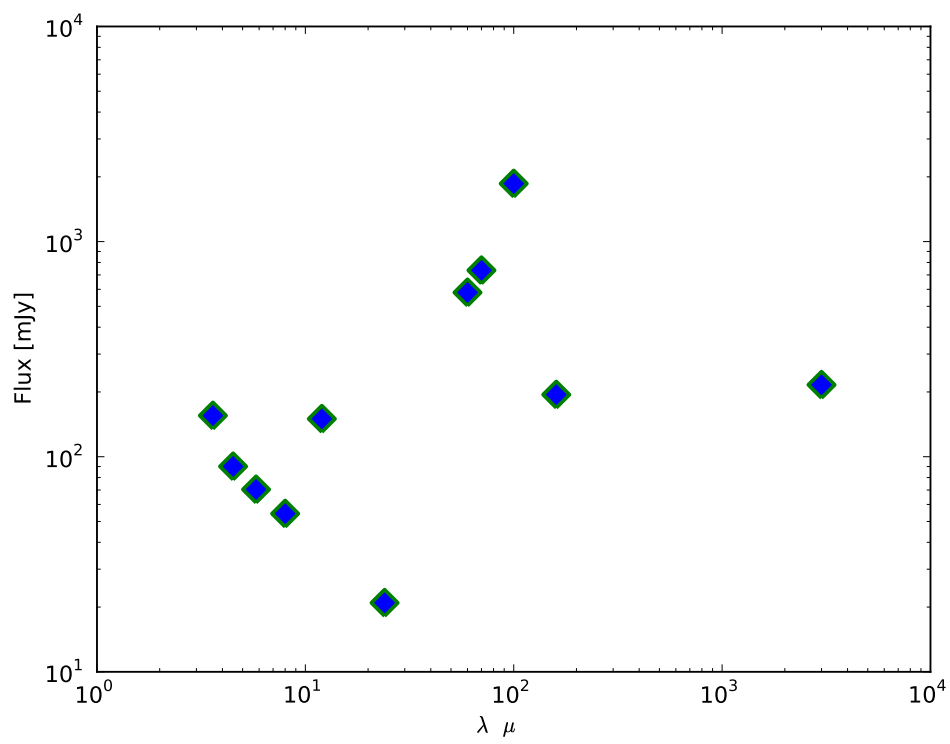


Figure A.105: NGC 4278 CO(2-1)

Figure A.106: The Spectral Energy Distribution diagram for NGC 4278



A.33 NGC 5127

Other Names: UGC 08419, B2 1321+31

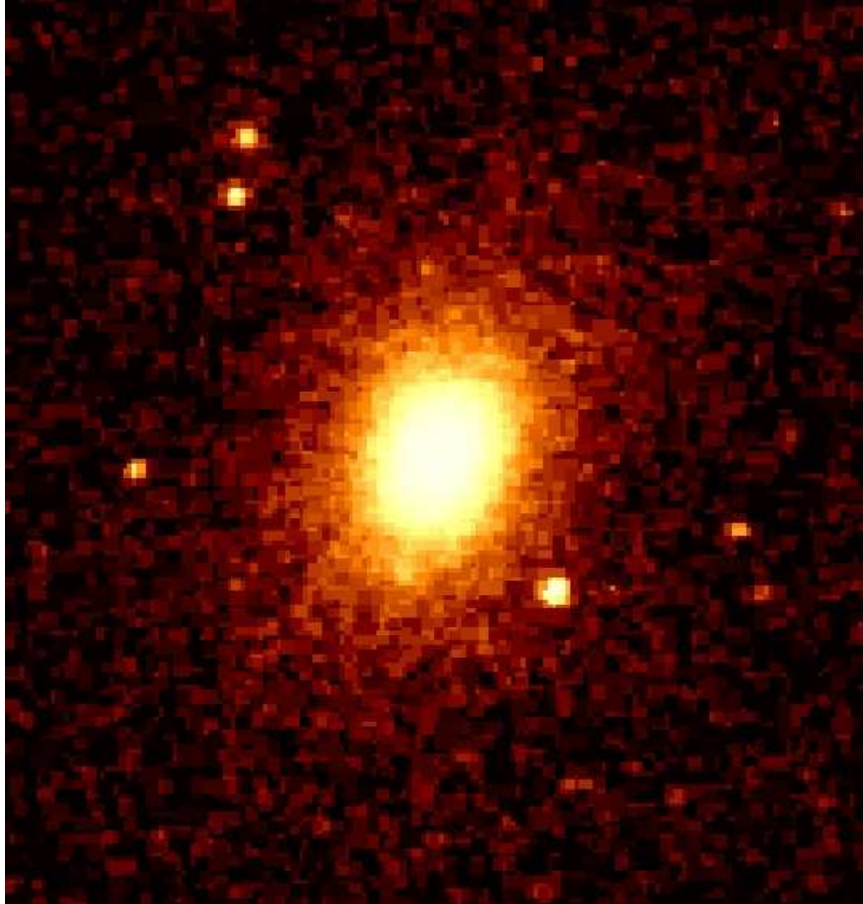


Figure A.107: NGC 5127 optical image.

There is a clear detection in the CO(2-1) line. The dust absorption is not clearly visible from the optical even though the galaxy is in the local universe ($z=0.016$). The $I_{\text{CO}(1-0)}$ was calculated using the CO(2-1)-to-CO(1-0) ratio (2.3) calculated from the galaxies detected at both frequencies.

Table A.97: General Data for NGC 5127

RA:	13h23m45.0s
Dec:	+31d33m57s
FR:	I
z_{CO} :	0.016
Distance [Mpc]:	67.1
Line Width:	-
$I_{CO(1-0)}$ [K km/s]:	0.28 ± 0.02
$I_{CO(2-1)}$ [K km/s]:	0.59 ± 0.10
$M_{H_2} M_{\odot}$:	$0.79 \times 10^8 \pm 0.053 \times 10^8$

Table A.98: Fluxes of NGC 5127

Wavelength	flux measurement mJy
S_{3mm}	25.62 ± 1.13
S_{1mm}	...
$f_{12\mu m}$	<21
$f_{25\mu m}$	<21
$f_{60\mu m}$	<32
$f_{100\mu m}$	<62

Table A.99: Luminosities for NGC 5127

Parameter	Luminosity
L_{CO} [K km/s pc^2]	1.38×10^7
L_{FIR} [L_{\odot}]	$< 2.82 \times 10^8$

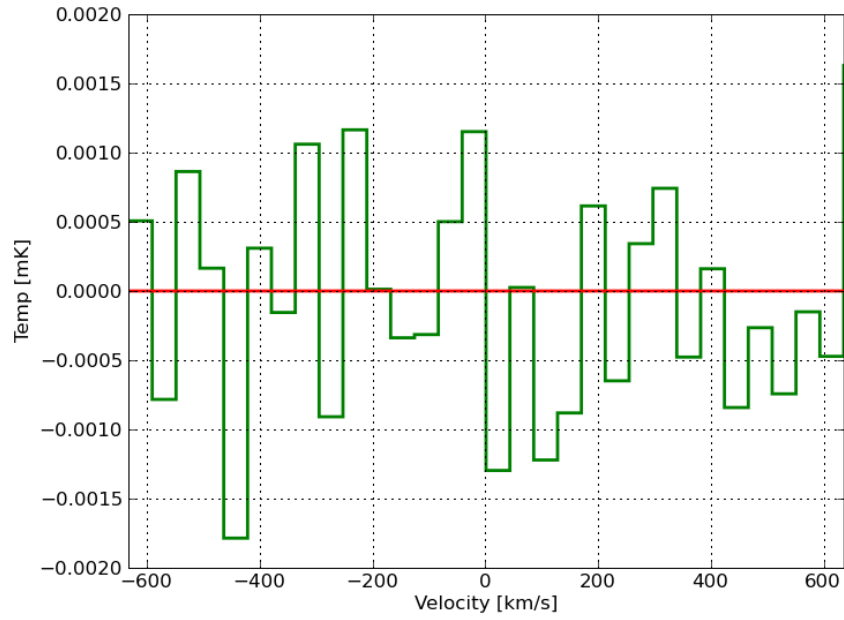


Figure A.108: NGC 5127 CO(1-0)

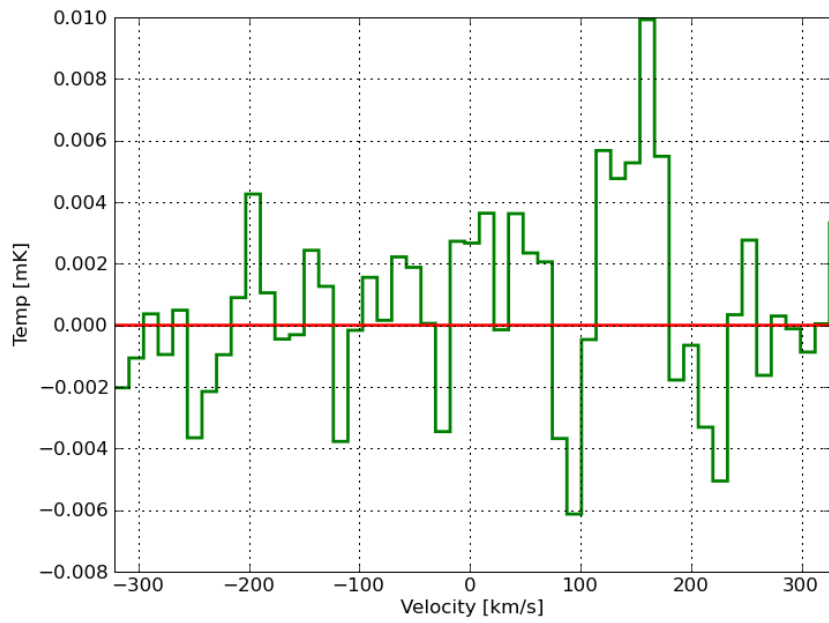


Figure A.109: NGC 5127 CO(2-1)

A.34 NGC 5141

Other Names: B2 1322+36B, UGC 08433

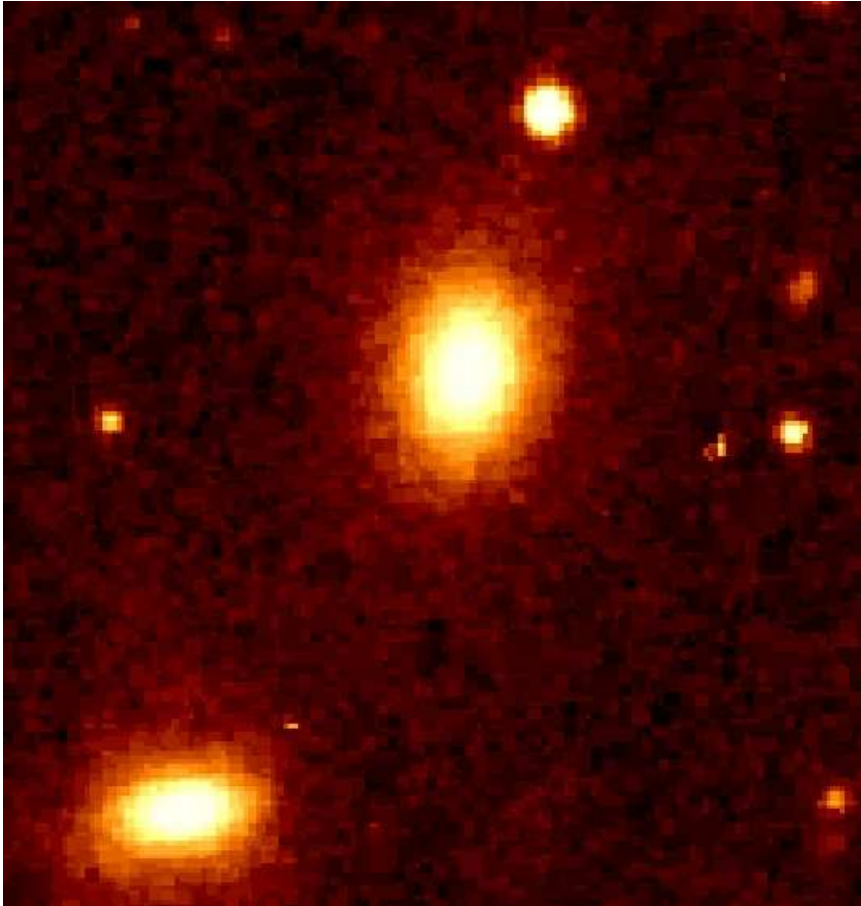


Figure A.110: NGC 5141 optical image.

NGC 5141 shows what [Emonts et al. \(2007\)](#) call "Blobs" of HI emission, as well as slightly extended HI absorption, in the direction of nearby companion, possibly tracing a bridge or tail-like structure.

Table A.100: General Data for NGC 5141

RA:	13h24m51.4s
Dec:	+36d22m42s
FR:	I
z_{CO} :	0.017
Distance [Mpc]:	75
Line Width [km/s]:	-
$I_{CO(1-0)}$ [K km/s]:	<1.55
$I_{CO(2-1)}$ [K km/s]:	...
$M_{H_2} M_{\odot}$:	$<5.04 \times 10^8$

Table A.101: Fluxes of NGC 5141

Wavelength	flux measurement mJy
S_{3mm}	63.50 ± 1.01
S_{1mm}	...
$f_{12\mu m}$	<26
$f_{25\mu m}$	<30
$f_{60\mu m}$	<38
$f_{100\mu m}$	<138

Table A.102: Luminosities for NGC 5141

Parameter	Luminosity
L_{CO} [K km/s pc^2]	$<9.33 \times 10^7$
L_{FIR} [L_{\odot}]	$<5.25 \times 10^8$

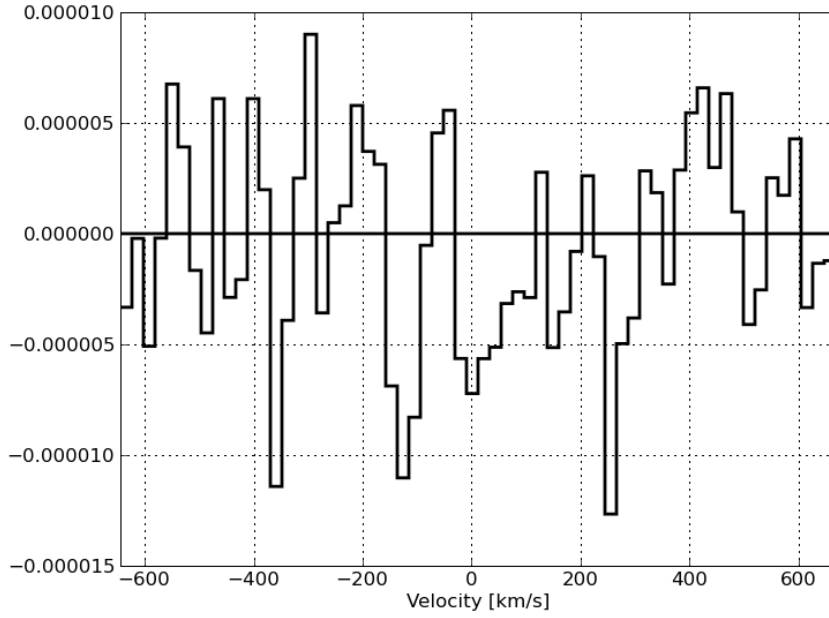


Figure A.111: NGC 5141 CO(1-0)

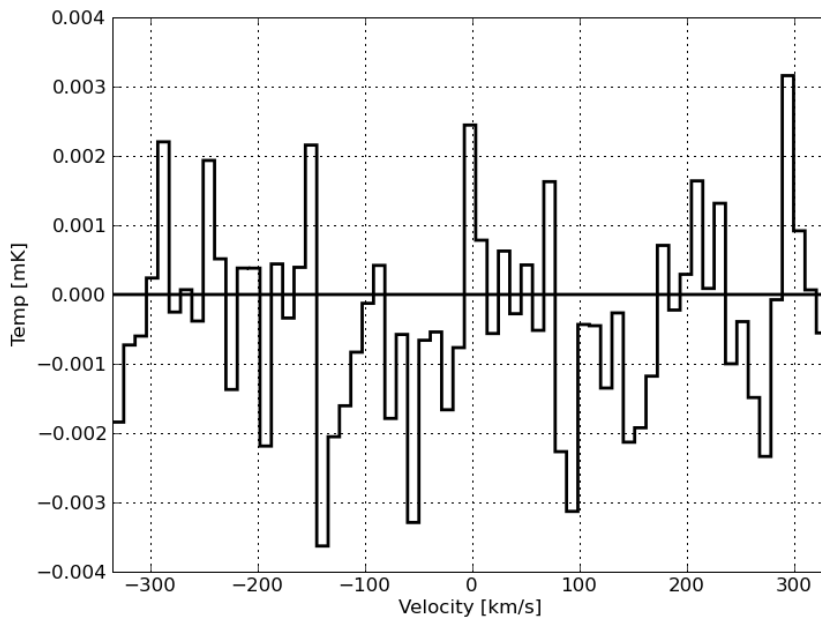


Figure A.112: NGC 5141 CO(2-1)

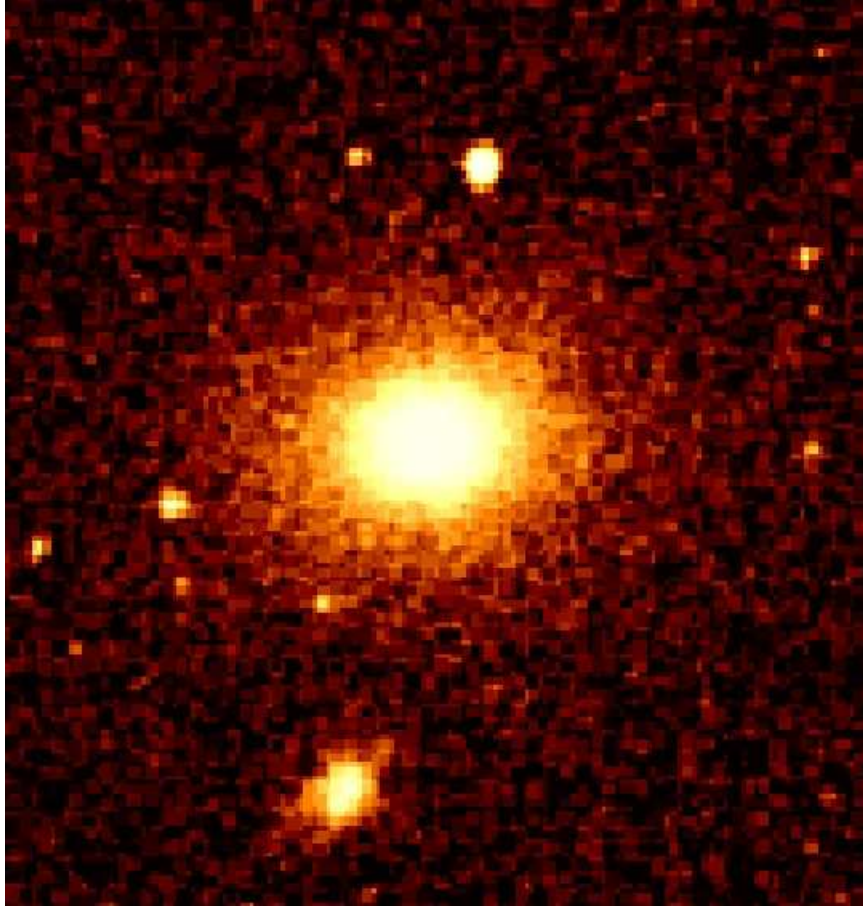
A.35 NGC 5490**Other Name:** UGC 09058

Figure A.113: NGC 5490 optical image.

This galaxy has been observed for CO(1-0) and CO(2-1) but it has not been detected.

Table A.103: General Data for NGC 5490

RA:	14h09m57.3s
Dec:	+17d32m44s
FR:	I
z_{CO} :	0.016
Distance [Mpc]:	66
Line Width [km/s]:	-
$I_{CO(1-0)}$ [K km/s]:	<1.55
$I_{CO(2-1)}$ [K km/s]:	...
$M_{H_2} M_{\odot}$:	$<5.41 \times 10^8$

Table A.104: Fluxes of NGC 5490

Wavelength	flux measurement mJy
S_{3mm}	27.72 ± 1.44
S_{1mm}	88.61 ± 5.46
$f_{12\mu m}$	<35
$f_{25\mu m}$	<44
$f_{60\mu m}$	<34
$f_{100\mu m}$	<194

Table A.105: Luminosities for NGC 5490

Parameter	Luminosity
L_{CO} [K km/s pc^2]	$<1.23 \times 10^8$
L_{FIR} [L_{\odot}]	$<5.50 \times 10^8$

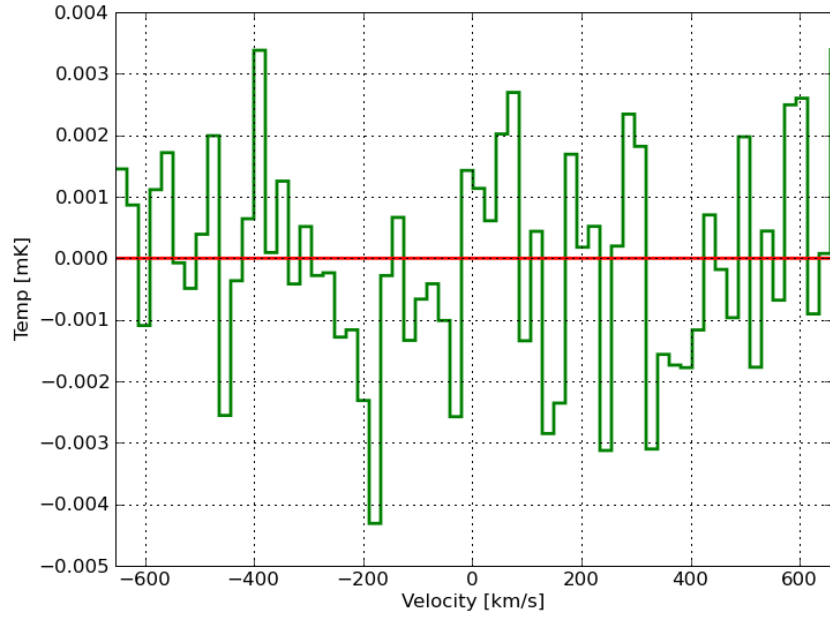


Figure A.114: NGC 5490 CO(1-0)

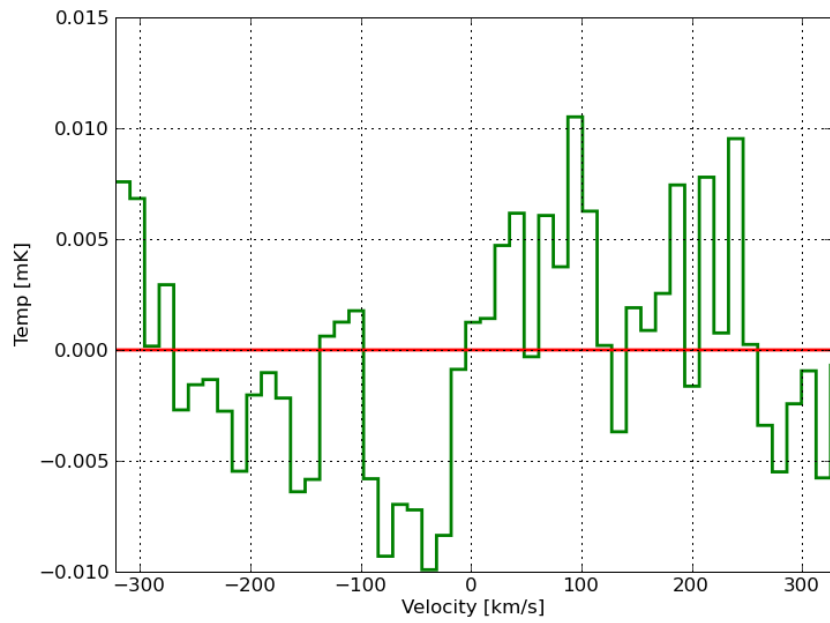


Figure A.115: NGC 5490 CO(2-1)

A.36 NGC 6251

Other Name: UGC 10501

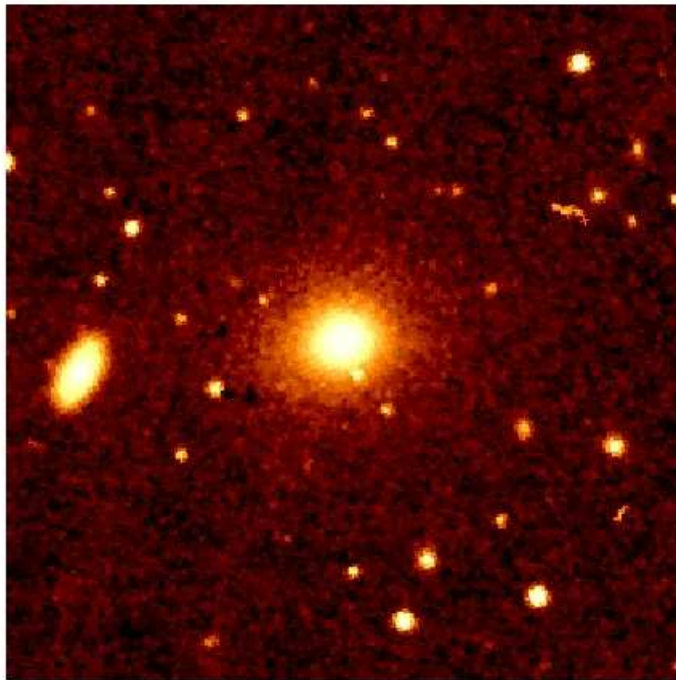


Figure A.116: NGC 6251 optical image.

We observed this galaxy in CO(1-0) and it was not detected. We have not observed for CO(2-1).

Table A.106: General Data for NGC 6251

RA:	16h32m32.0s
Dec:	+82d32m16s
FR:	I
z_{CO} :	0.025
Distance [Mpc]:	26
Line Width [km/s]:	-
$I_{CO(1-0)}$ [K km/s]:	<1.03
$I_{CO(2-1)}$ [K km/s]:	Not Observed
$M_{H_2} M_{\odot}$:	$<6.78 \times 10^8$
$M_{Dust} M_{\odot}$:	3.89×10^6
T_{Dust} [K] :	30.01

Table A.107: Fluxes of NGC 6251

Wavelength	flux measurement mJy
S_{3mm}	367.88 ± 0.71
S_{1mm}	Not Observed
$f_{12\mu m}$	<11
$f_{25\mu m}$	100 ± 22
$f_{60\mu m}$	188 ± 28.2
$f_{100\mu m}$	600 ± 90

Table A.108: Luminosities for NGC 6251

Parameter	Luminosity
L_{CO} [K km/s pc^2]	$<1.23 \times 10^8$
L_{FIR} [L_{\odot}]	4.90×10^9
L_{178MHz} [W Hz ⁻¹ sr ⁻¹]	1.2×10^{24} (Evans et al. 2006)

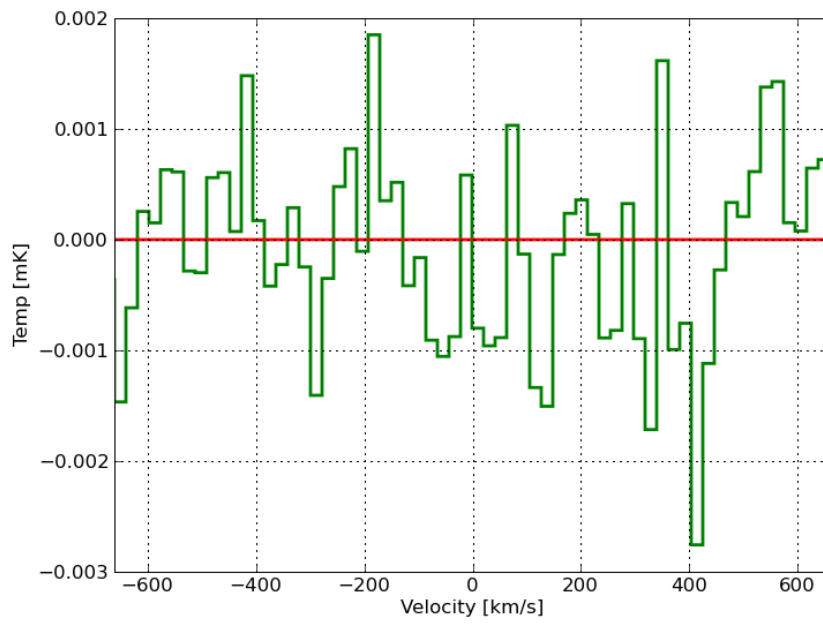
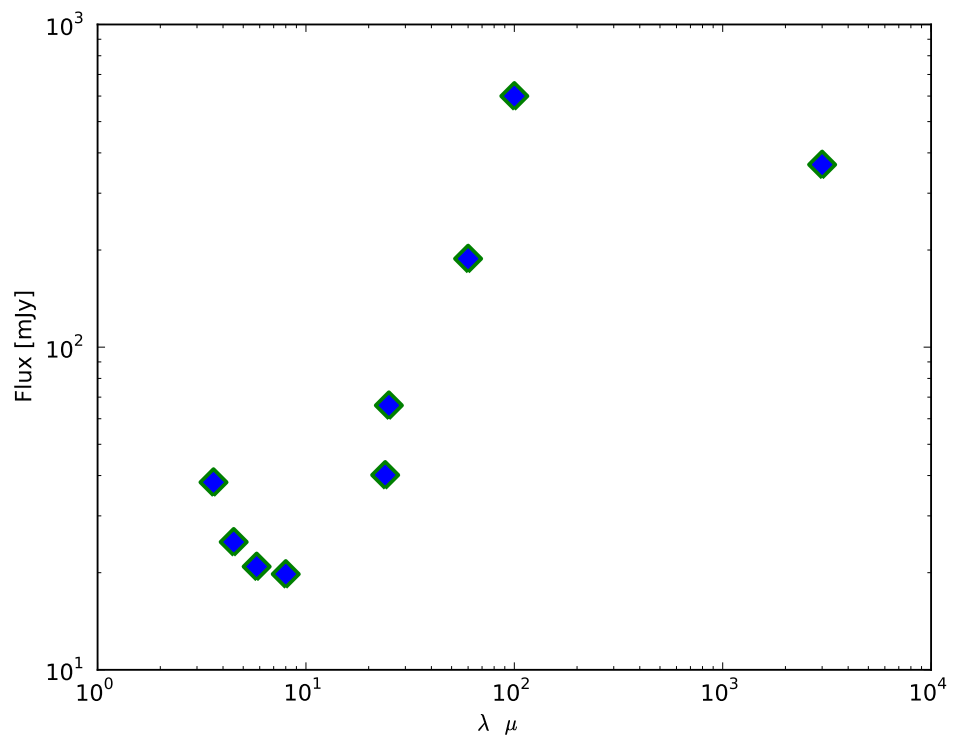


Figure A.117: NGC 6251 CO(1-0)

Figure A.118: The Spectral Energy Distribution diagram for NGC 6251



A.37 NGC 7052

Other Names: UGC 11718, B2 2116+26

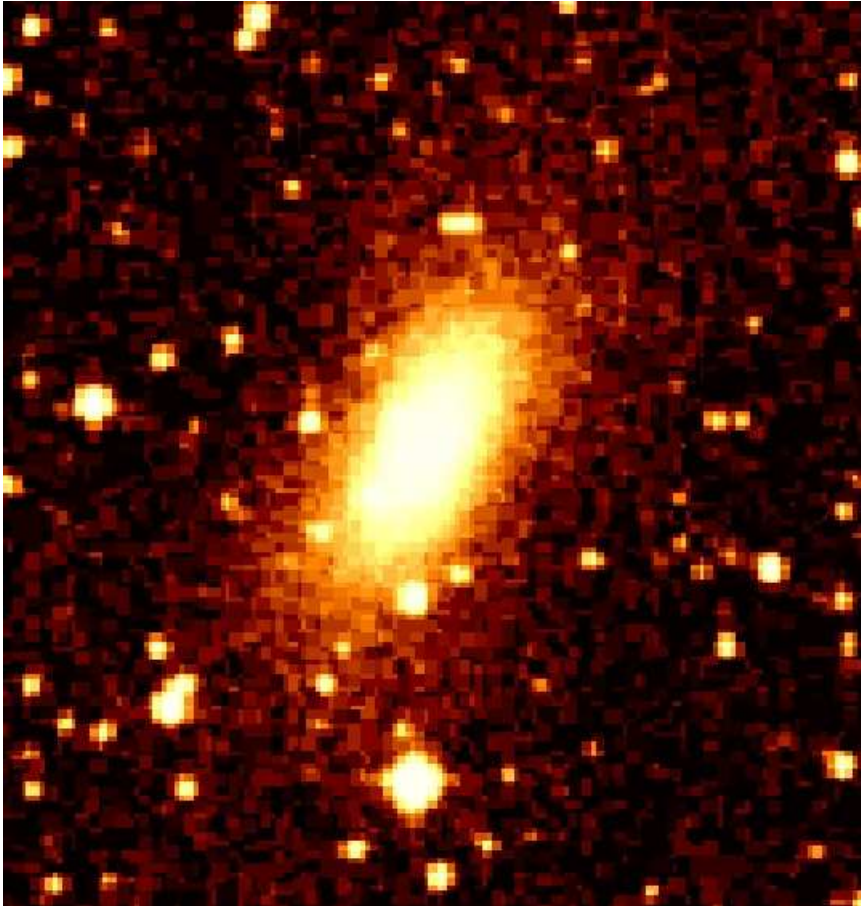


Figure A.119: NGC 7052 optical image.

It exhibits a double horn profile very clear in the CO(1-0) emission, but probably also in the CO(2-1) emission, although it is not so clear that there is a detection. According to [Nieto et al. \(1990\)](#) the size of the dust disk is about 4'' and from the Fig. 5.8 we know that the conversion factor for that dimension is about 0.25, which would change the line ratio of this galaxy from 0.77 to 0.2. According to [Braine & Combes \(1992\)](#) this line ratio means an optically thin gas with an excitation temperature 5K.

Table A.109: General Data for NGC 7052

RA:	21h18m33.0s
Dec:	+26d26m49s
FR:	I
z_{CO} :	0.016
Distance [Mpc]:	66.36
Line Width [km/s]:	700
$I_{CO(1-0)}$ [K km/s]:	0.76 ± 0.16
$I_{CO(2-1)}$ [K km/s]:	0.58 ± 0.16
$M_{H_2} M_{\odot}$:	$1.96 \times 10^8 \pm 0.41 \times 10^8$
$M_{Dust} M_{\odot}$:	1.79×10^6
T_{Dust} [K]:	34.07
Line Ratio:	2.8 ± 0.3

Table A.110: Fluxes of NGC 7052

Wavelength	flux measurement mJy
S_{3mm}	85.51 ± 12.13
S_{1mm}	18.77 ± 1.49
$f_{12\mu m}$	50 ± 20
$f_{25\mu m}$	47 ± 7
$f_{60\mu m}$	524 ± 78.6
$f_{100\mu m}$	1150 ± 173

Table A.111: Luminosities for NGC 7052

Parameter	Luminosity
L_{CO} [K km/s pc^2]	3.80×10^7
L_{FIR} [L_{\odot}]	4.47×10^9

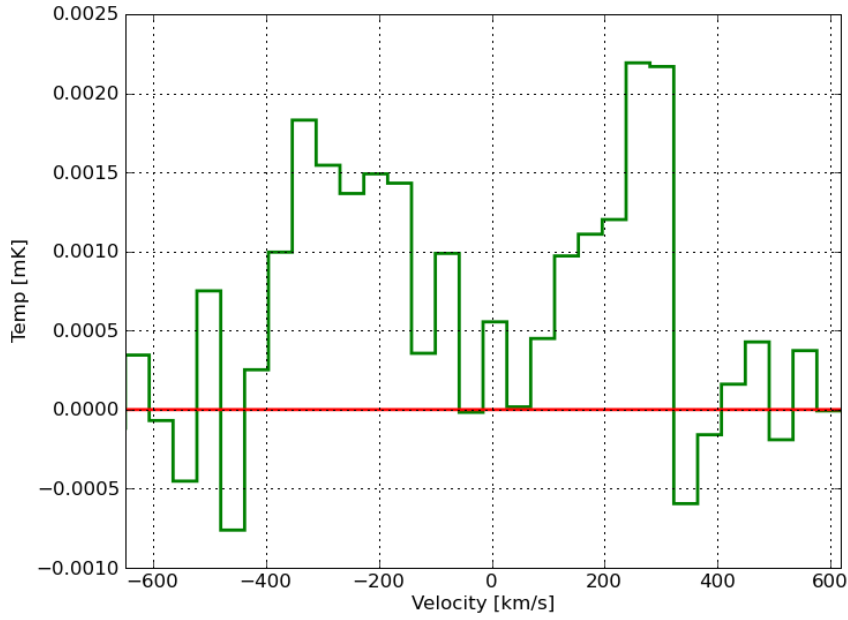


Figure A.120: NGC 7052 CO(1-0)

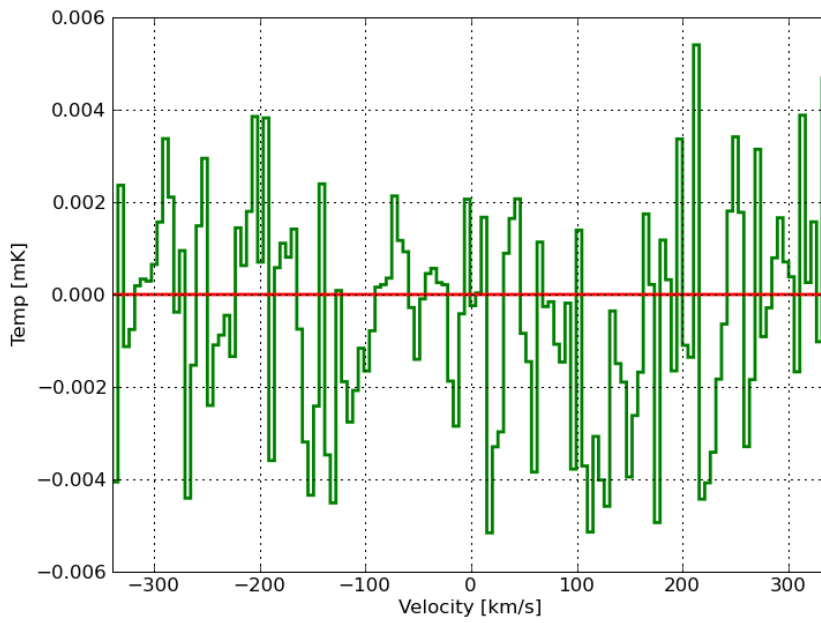
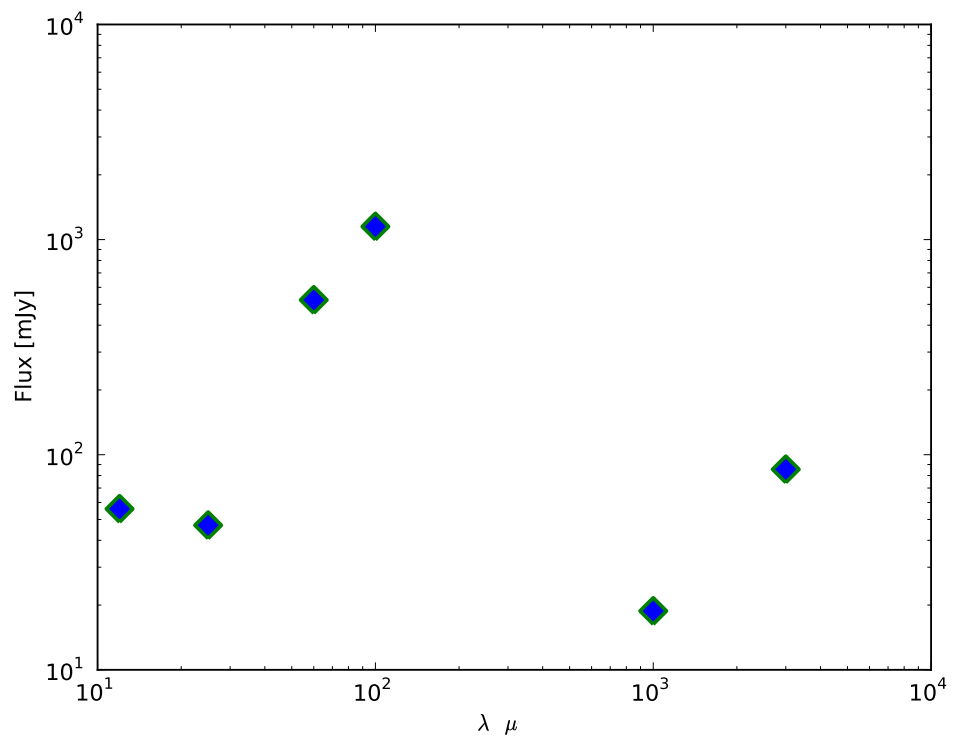


Figure A.121: NGC 7052 CO(2-1)

Figure A.122: The Spectral Energy Distribution diagram for NGC 7052



A.38 B2 0034+25

Other Name: UGC 00367

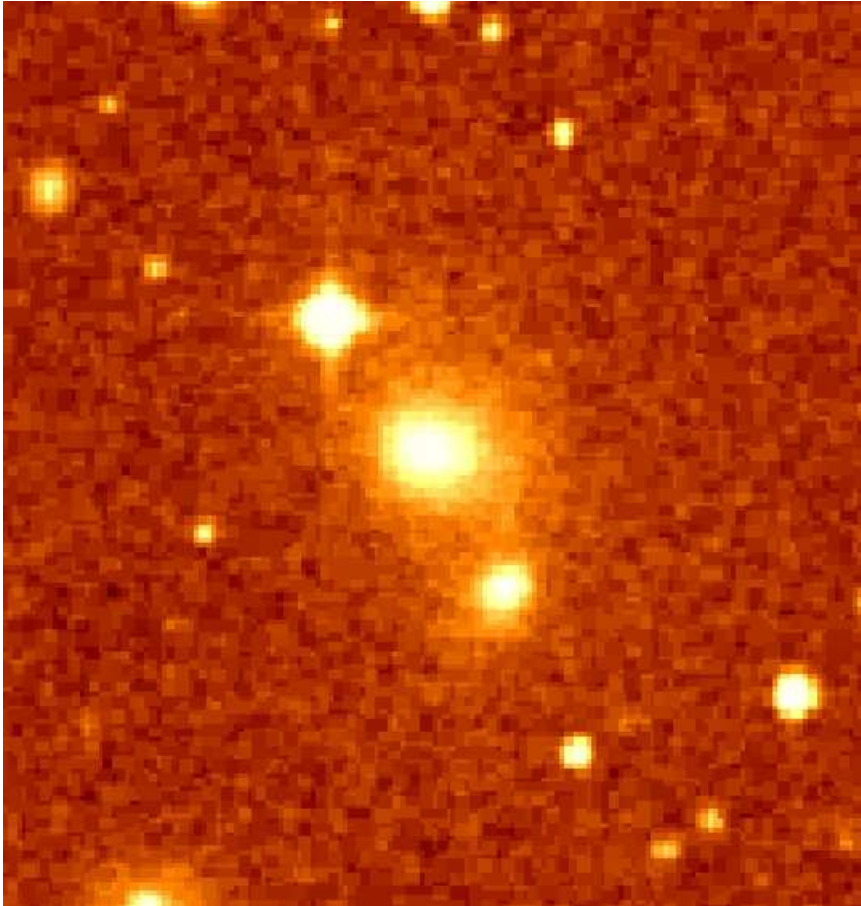


Figure A.123: B2 0034+25 optical image

This galaxy has been observed for CO(1-0) and CO(2-1) but it has not been detected.

Table A.112: General Data for B2 0034+25

RA:	00h37m05.5s
Dec:	+25d41m56s G
FR:	I
z_{CO} :	0.032
Distance [Mpc]:	27
Line Width:	-
$I_{CO(1-0)}$ [K km/s]:	<0.96
$I_{CO(2-1)}$ [K km/s]:	...
$M_{H_2} M_{\odot}$:	<10.41 $\times 10^8$

Table A.113: Fluxes of B2 0034+25

Wavelength	flux measurement mJy
S_{3mm}	72.97 \pm 0.68
S_{1mm}	190.81 \pm 1.82
$f_{12\mu m}$...
$f_{25\mu m}$...
$f_{60\mu m}$...
$f_{100\mu m}$...

Table A.114: Luminosities for B2 0034+25

Parameter	Luminosity
L_{CO} [K km/s pc^2]	<1.86 $\times 10^8$
L_{FIR} [M_{\odot}]	...

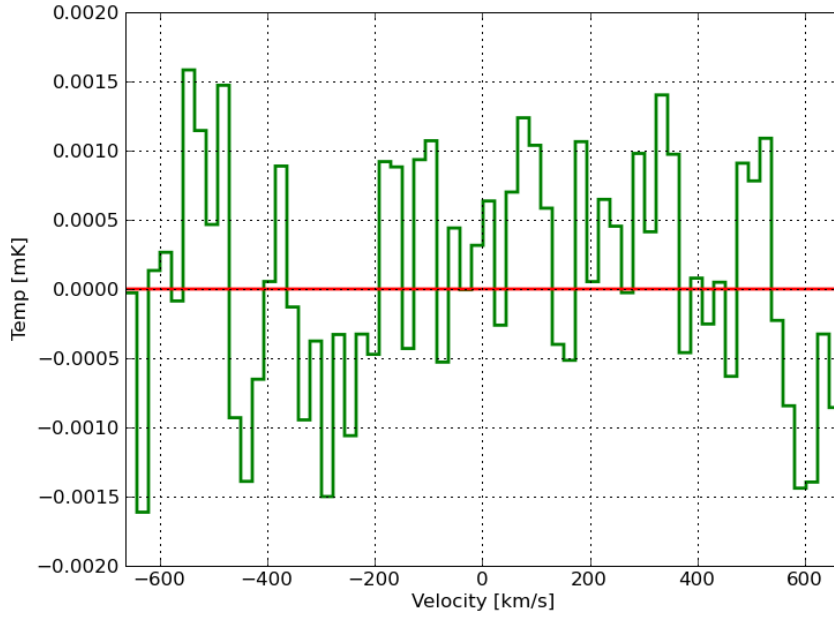


Figure A.124: B2 0034+25 CO(1-0)

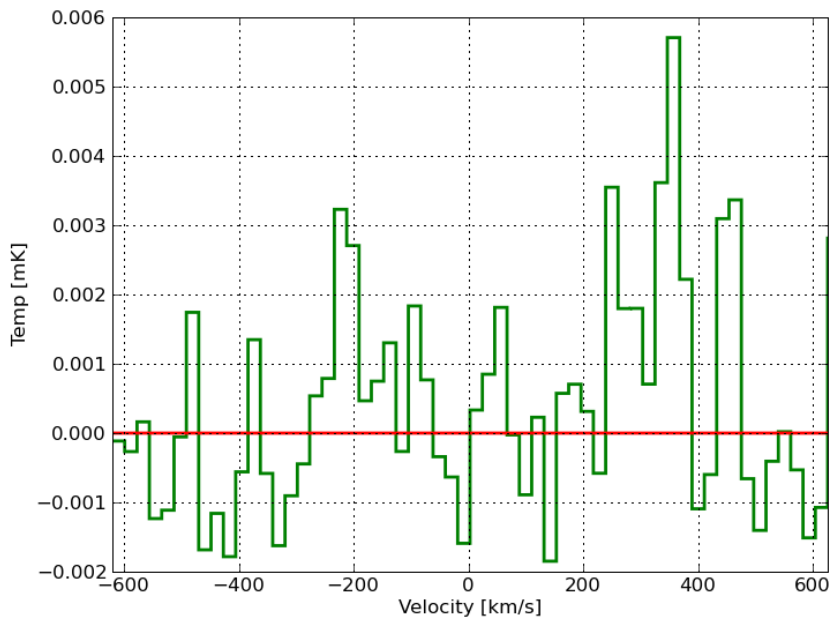


Figure A.125: B2 0034+25 CO(2-1)

A.39 B2 0116+31

Other Name: 4C +31.04

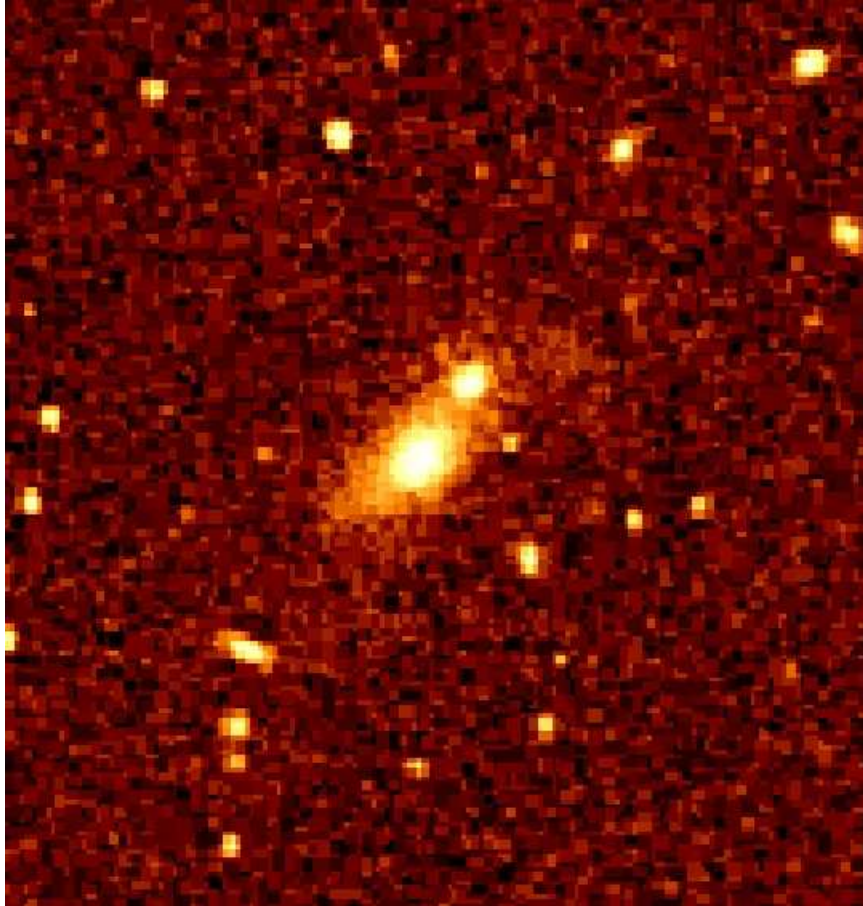


Figure A.126: B2 0116+31 optical image

According to [García-Burillo et al. \(2007\)](#), this galaxy is a nearby compact symmetric object (CSO) located at the nucleus of the giant elliptical MGC 5-8-18. Its massive molecular/dusty disk has been mapped fueling the central engine revealing the existence of significant amounts of molecular gas in the central 1.4 Kpc disk. The kinematics and distribution of molecular gas probed by the HCO^+ observations presented in [García-Burillo et al. \(2007\)](#) illustrate that the detected rotating disk is not in a fully relaxed state and that the relieved distortion may reflect that the disk is still settling after a merger or an event of gas accretion. Alternatively, the disk and the cone-like feature may be interacting with the disk, thus producing the reported distortion. In our sample, this is a peculiar galaxy since it is the only one showing a

clear absorption line in CO(1-0). At each sides of the absorption line we can still see the emission part of the CO(1-0) line. Because of the absorption line we cannot discard a possible double horn profile. The CO(2-1) emission is also interpreted as a double horn profile since there is no continuum at this frequency.

Table A.115: General Data for B2 0116+31

RA:	01h19m35.0s
Dec:	+32d10m50s
FR:	c
z_{CO} :	0.06
Distance [Mpc]:	242.1
Line Width [km/s]:	700
$I_{CO(1-0)}$ [K km/s]:	1.77 ± 0.49
$I_{CO(2-1)}$ [K km/s]:	4.29 ± 0.69
$M_{H_2} M_{\odot}$:	$60.63 \pm 16.92 \times 10^8$
$M_{Dust} M_{\odot}$:	2.3×10^7
T_{Dust} [K]:	29.18
Line Ratio:	2.4 ± 0.3

Table A.116: Fluxes of B2 0116+31

Wavelength	flux measurement mJy
S_{3mm}	164.53 ± 1.22
S_{1mm}	...
$f_{12\mu m}$	<30
$f_{25\mu m}$	<45
$f_{60\mu m}$	150 ± 22.5
$f_{100\mu m}$	524 ± 78.6

Table A.117: Luminosities for B2 0116+31

Parameter	Luminosity
L_{CO} [K km/s pc^2]	1.15×10^9
L_{FIR} [L_{\odot}]	2.1×10^{10}

A.39.1 HI data

This galaxy was observed in Effelsberg-100m telescope and it was not detected.

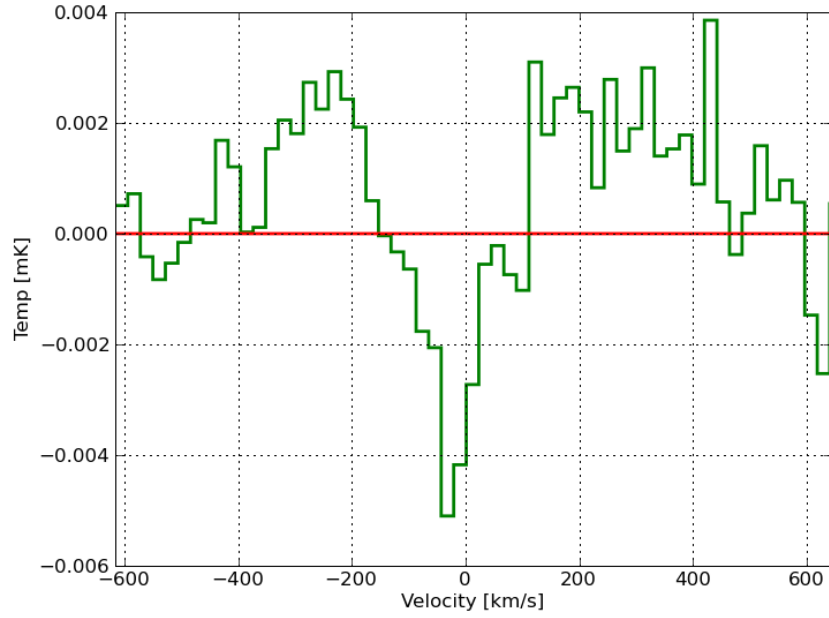


Figure A.127: B2 0116+31 CO(1-0)

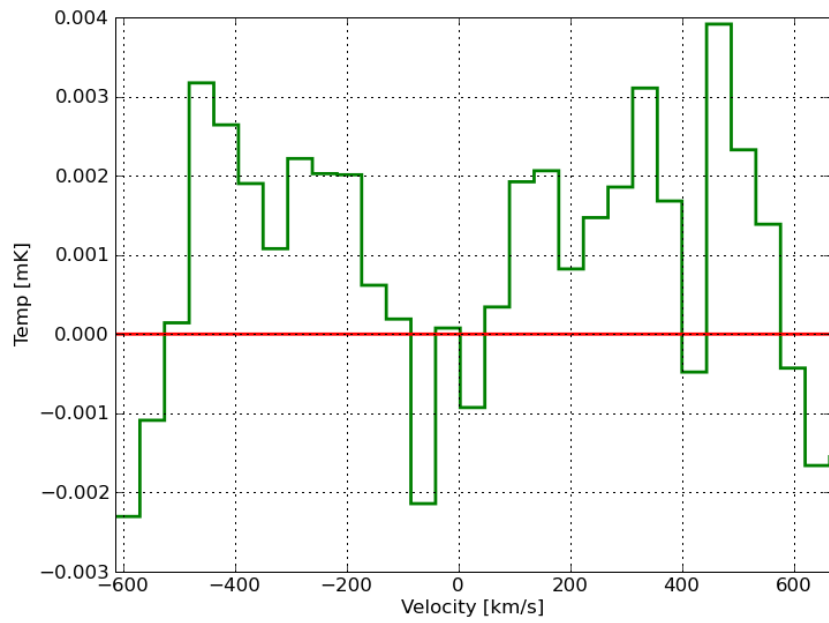


Figure A.128: B2 0116+31 CO(2-1)

291; 3 B2 0116+31 NONE FRONTTEST-2 O: 29-JUN-2008 R: 02-JUL-2008
RA: 01:19:35.000 DEC: 32:10:50.00 (2000.0) Offs: -1.282 -0.470 Eq
Unknown Tau: 0.000 Tsys: 27.23 Time: 37.57 El: 71.04
N: 255 l0: 128.0 v0: 0.000 Dv: -17.80 LSR
F0: 1316.18200 Df: 7.8144E-02 Fi: 1166.18200
B ef: 0.000 F ef: 0.000 G im: 0.000
H2O : 0.000 Pamb: 0.000 Tamb: 0.0 Tchop: 0.0 Tcold: 0.0
Tatm: 0.0 Tau: 0.000 Tatm i: 0.0 Tau i: 0.000
3147- 3154,

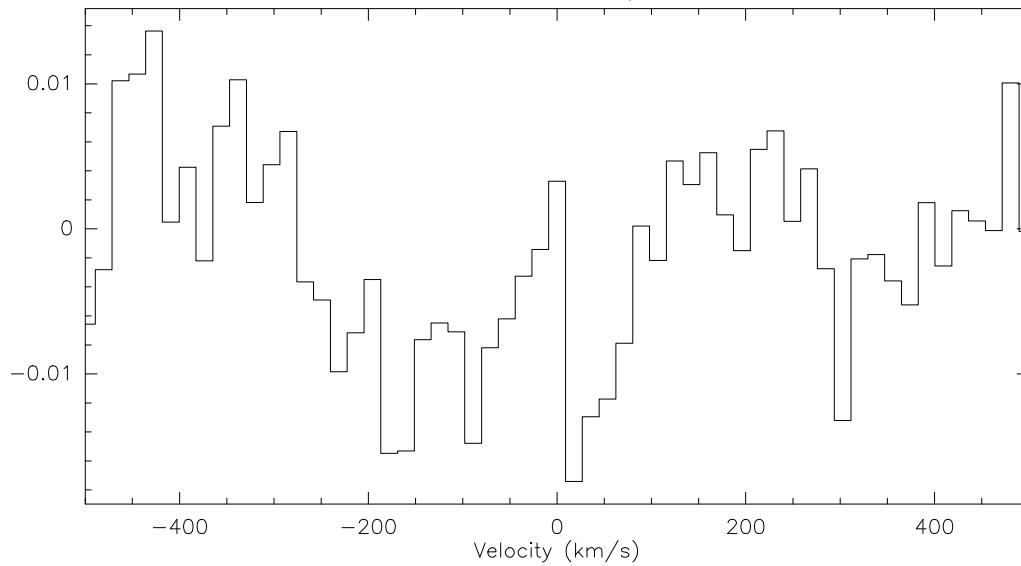
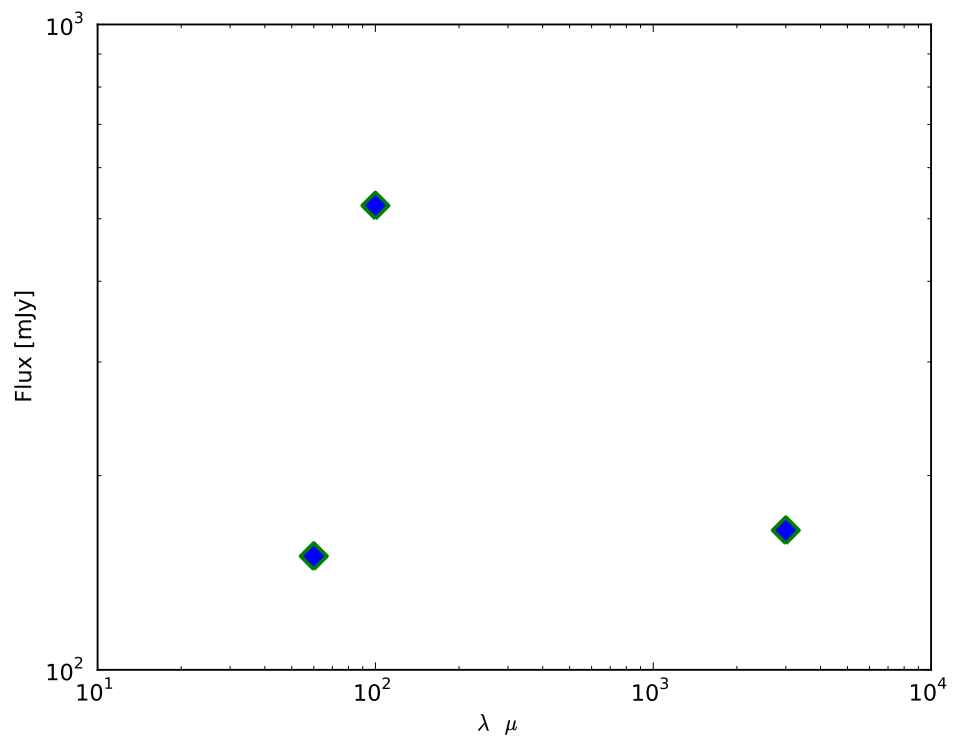


Figure A.129: HI emission for B2 0116+31

Figure A.130: The Spectral Energy Distribution diagram for B2 0116+31



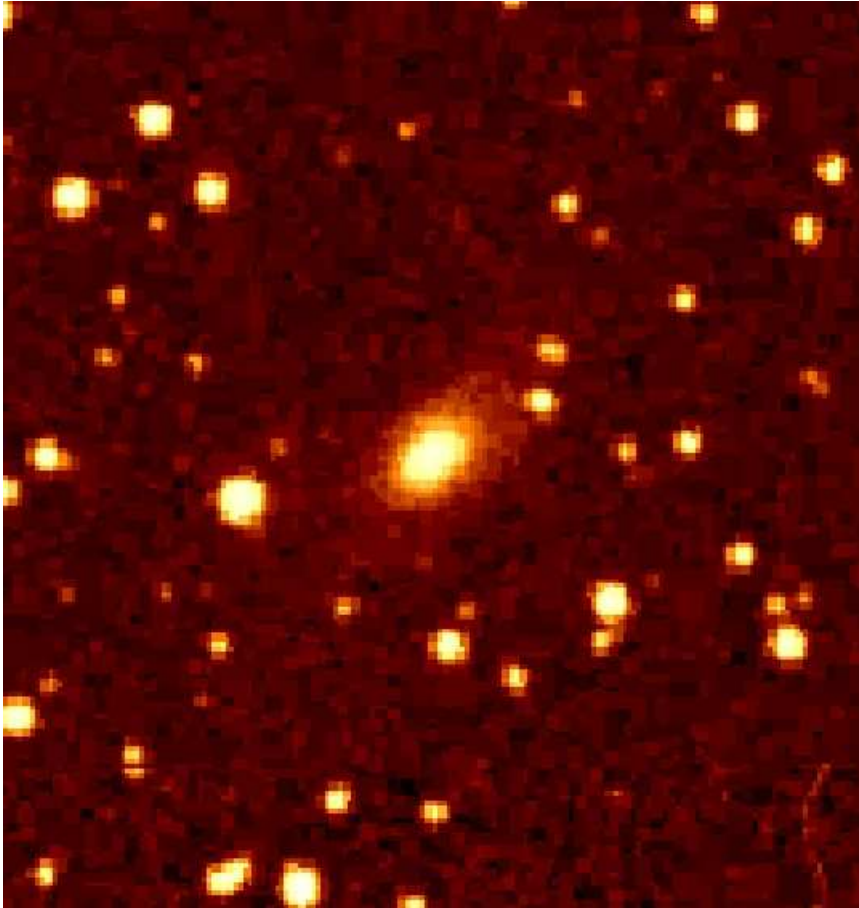
A.40 B2 0648+27

Figure A.131: B2 0116+31 optical image

The spectra of this galaxy for the CO(1 – 0) shows a very clear absorption line, this galaxy has been observed in HI emission and absorption being clearly detected in both (some of the references for this galaxy are (Emonts et al. 2006; Emonts 2006; Morganti et al. 2003b,a; Emonts et al. 2008)).

This galaxy consist of an emission-line AGN plus a compact radio source (Emonts 2006; Giroletti et al. 2005a). It also has a large scale ring of neutral Hydrogen (HI) gas ($M_{HI} \approx 8.5 \times 10^9 M_{\odot}$) around this galaxy, initially discovered by Morganti et al. (2003b). Emonts et al. (2008) argues that the HI ring formed from a major event between two galaxies of comparable masses ≥ 1.5 Gyrs ago, when gas that was tidally expelled during the merger fell back into the host galaxy and settled in regular rotation. This merger scenario was supported by the detection of 0.3-0.4 Gyr young post-starburst stellar population that dominates the starlight throughout the host galaxy and which could have

given B2 0648+27 the appearance of an (Ultra-) Luminous Infra-Red Galaxy at the time of the starburst event. The offset in time between the initial merger event and the starburst activity indicates that the starburst was triggered in an advance stage of the merger. the spectral age of the radio source in B2 0648+27 has been estimated by [Giroletti et al. \(2005a\)](#) to be about 1 Myr, which suggest that there is also a significant time-delay between the starburst event and the triggering of the current episode of radio-AGN activity. Its dust temperature is the highest for this sample (71K).

Table A.118: General Data for B2 0648+27

RA:	06h52m02.5s
Dec:	+27d27m39s
Fanaroff and Riley Classification:	c
z_{CO} :	0.04
Distance [Mpc] :	169.83
Line Width [km/s]:	300
$I_{CO(1-0)}$ [K km/s]:	0.72 ± 0.07
$I_{CO(2-1)}$ [K km/s]:	1.44 ± 0.34
$M_{H_2} M_{\odot}$:	$12.25 \pm 1.18 \times 10^8$
$M_{Dust} M_{\odot}$:	1.66×10^6
T_{Dust} [K]:	68.52
Line Ratio:	2.0 ± 0.3

Table A.119: Fluxes of B2 0648+27

Wavelength	flux measurement mJy
S_{3mm}	152.99 ± 0.37
S_{1mm}	172.99 ± 2.09
$f_{12\mu m}$	130 ± 19.5
$f_{25\mu m}$	880 ± 132
$f_{60\mu m}$	2633 ± 395
$f_{100\mu m}$	1529 ± 229

Table A.120: Luminosities for B2 0648+27

Parameter	Luminosity
L_{CO} [K km/s pc^2]	2.34×10^8
L_{FIR} [L_{\odot}]	1.07×10^{11}

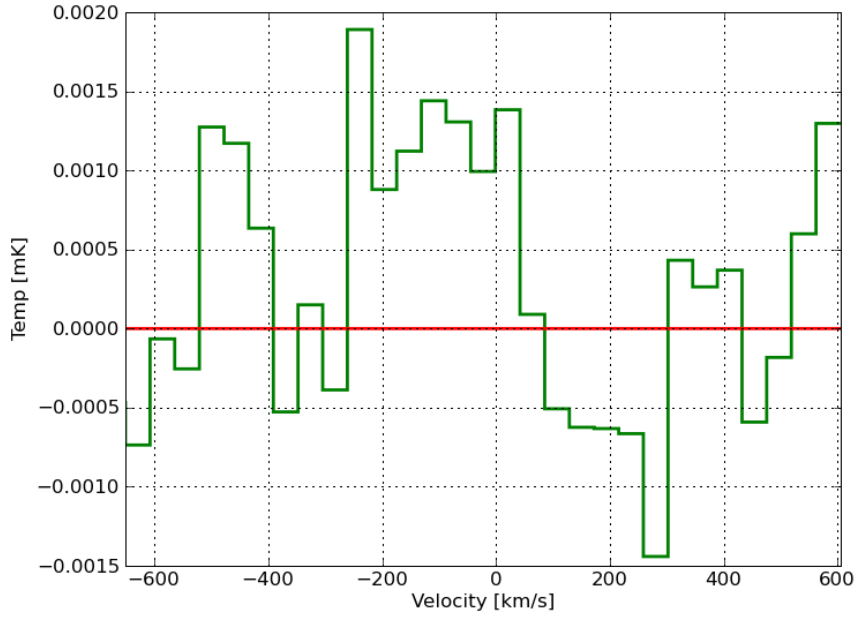


Figure A.132: B2 0648+27 CO(1-0)

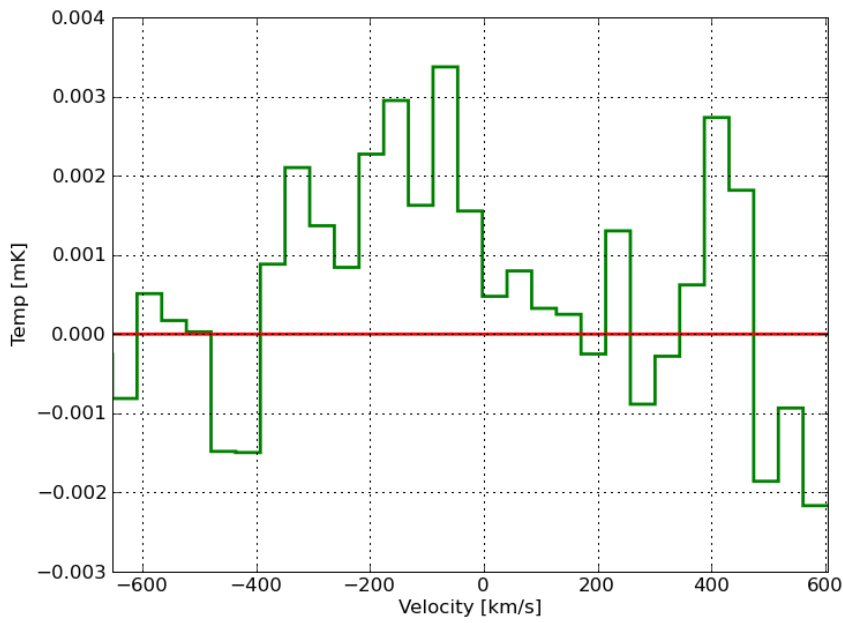
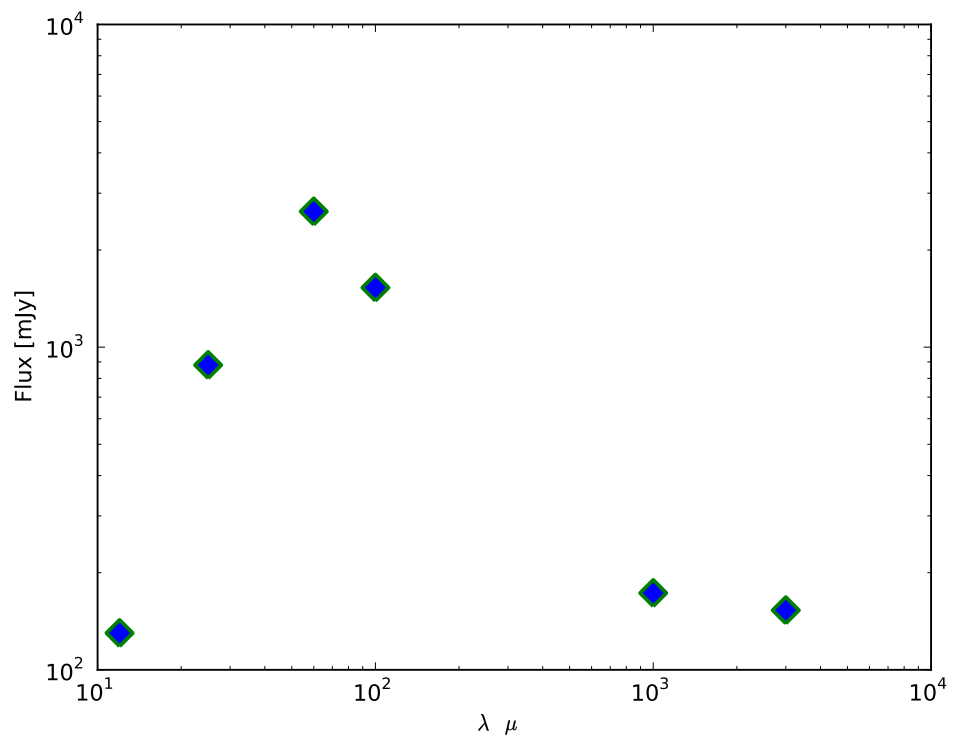


Figure A.133: B2 0648+27 CO(2-1)

Figure A.134: The Spectral Energy Distribution diagram for B2 0648+27



A.41 B2 0836+29B

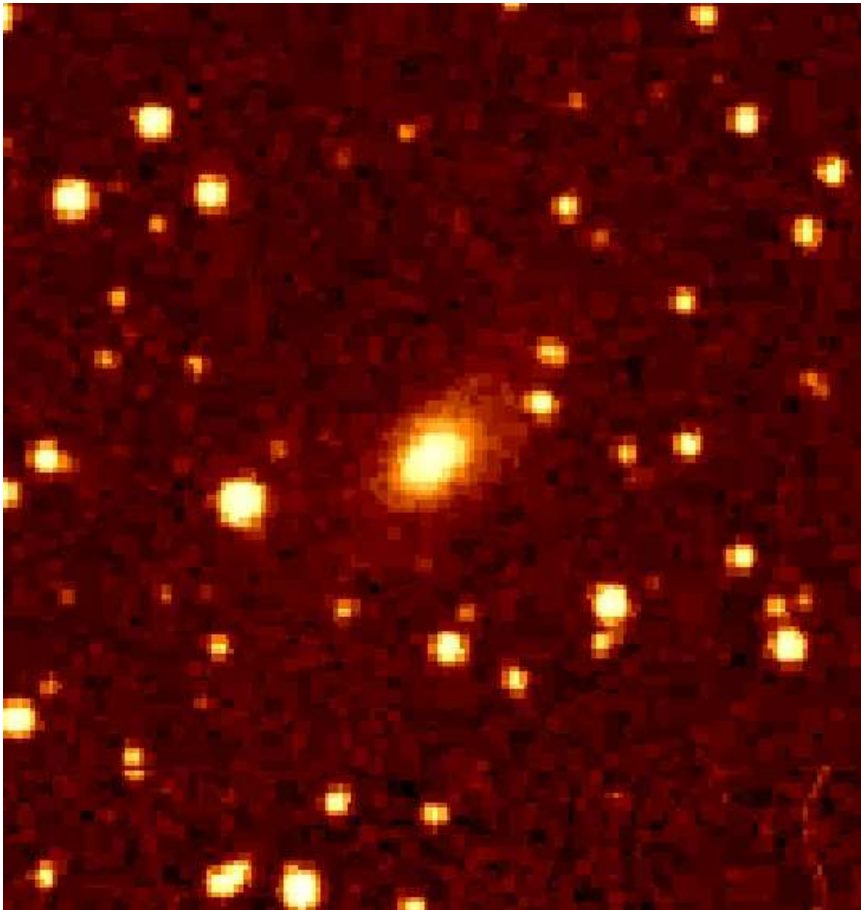


Figure A.135: B2 0116+31 optical image

It is clearly detected in the CO(1-0) emission line, but nothing peculiar in the optical image and no emission was detected in the CO(2-1) emission line.

Table A.121: General Data for B2 0836+29B

RA:	08h40m02.3s
Dec:	+29d49m03s
FR:	I
z_{CO} :	0.065
Distance [Mpc]:	261.70
Line Width [km/s]:	500
$I_{CO(1-0)}$ [K km/s]:	1.20 ± 0.30
$I_{CO(2-1)}$ [K km/s]:	Not Observed
$M_{H_2} M_{\odot}$:	$48.18 \pm 11.95 \times 10^8$
$M_{Dust} M_{\odot}$:	6.31×10^6
T_{Dust} [K]:	34.76

Table A.122: Fluxes of B2 0836+29B

Wavelength	flux measurement mJy
S_{3mm}	... \pm ...
S_{1mm}	Not Observed
$f_{12\mu m}$	<113.8
$f_{25\mu m}$	<242.2
$f_{60\mu m}$	472 ± 70.8
$f_{100\mu m}$	595 ± 89.2

Table A.123: Luminosities for B2 0836+29B

Parameter	Luminosity
L_{CO} [K km/s pc^2]	9.12×10^8
L_{FIR} [L_{\odot}]	5.75×10^{10}

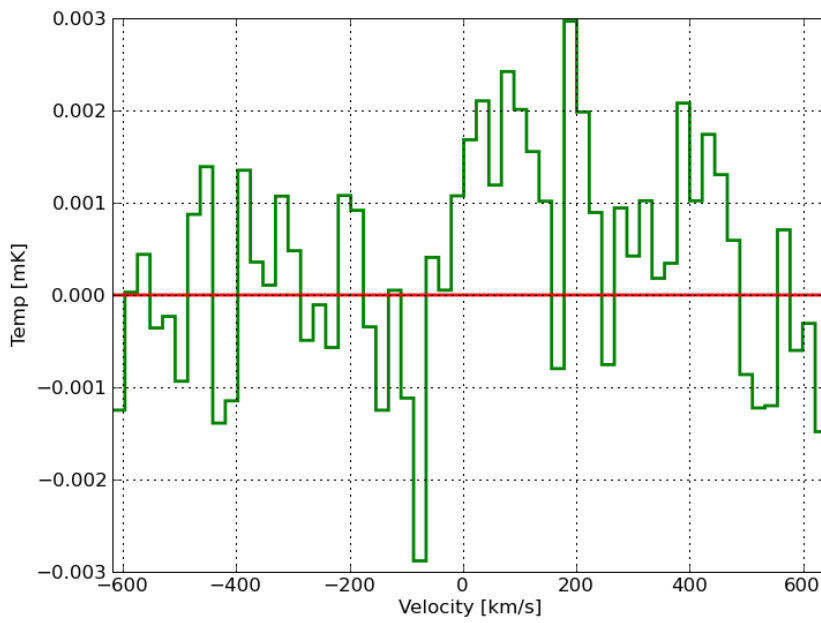


Figure A.136: B2 0836+29B CO(1-0)

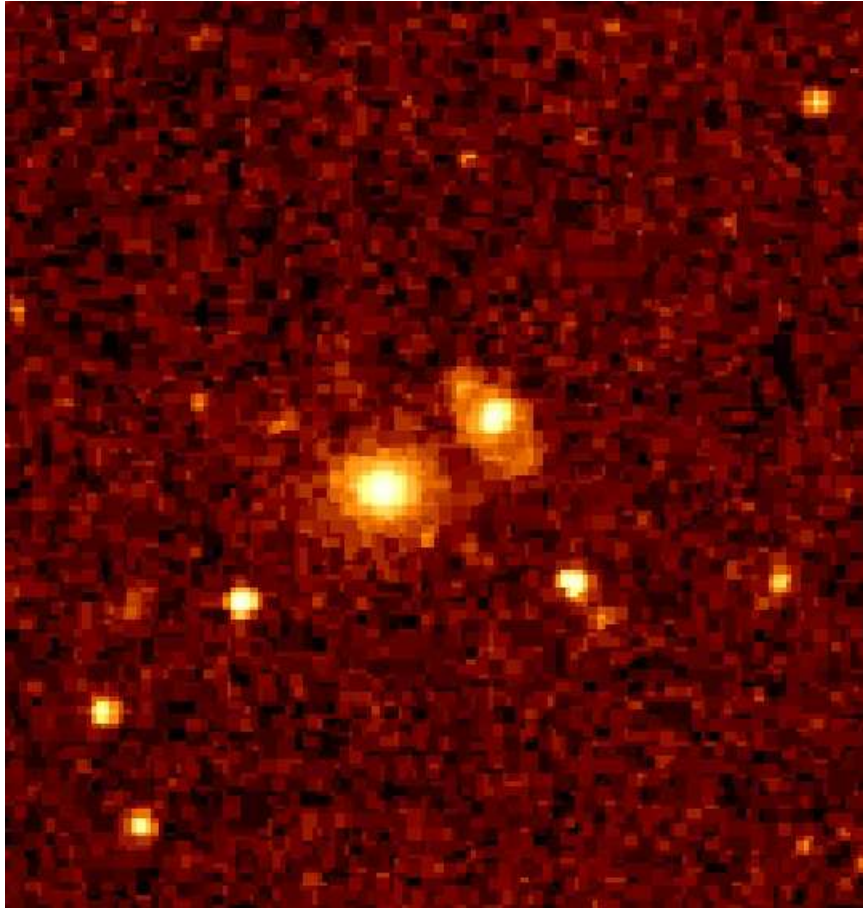
A.42 B2 0915+32B

Figure A.137: B2 0915+32B optical image

It is clearly detected in the CO(1-0) emission line, but nothing peculiar in the optical image and no emission was detected in the CO(2-1) emission line.

Table A.124: General Data for B2 0915+32B

RA:	09h18m58.7s
Dec:	+31d51m26s
Fanaroff and Riley Classification:	I
z_{CO} :	0.062
Distance [Mpc]:	258
Line Width [km/s]:	-
$I_{CO(1-0)}$ [K km/s]:	< 1.83
$I_{CO(2-1)}$ [K km/s]:	...
$M_{H_2} M_{\odot}$:	< 70.52×10^8

Table A.125: Fluxes of B2 0915+32B

Wavelength	flux measurement mJy
S_{3mm}	11.39 ± 1.29
S_{1mm}	24.41 ± 2.17
$f_{12\mu m}$	<50
$f_{25\mu m}$	<95
$f_{60\mu m}$	<55
$f_{100\mu m}$	<150

Table A.126: Luminosities for B2 0915+32B

Parameter	Luminosity
L_{CO} [K km/s pc^2]	< 1.26×10^9
L_{FIR} [L_{\odot}]	< 8.51×10^9

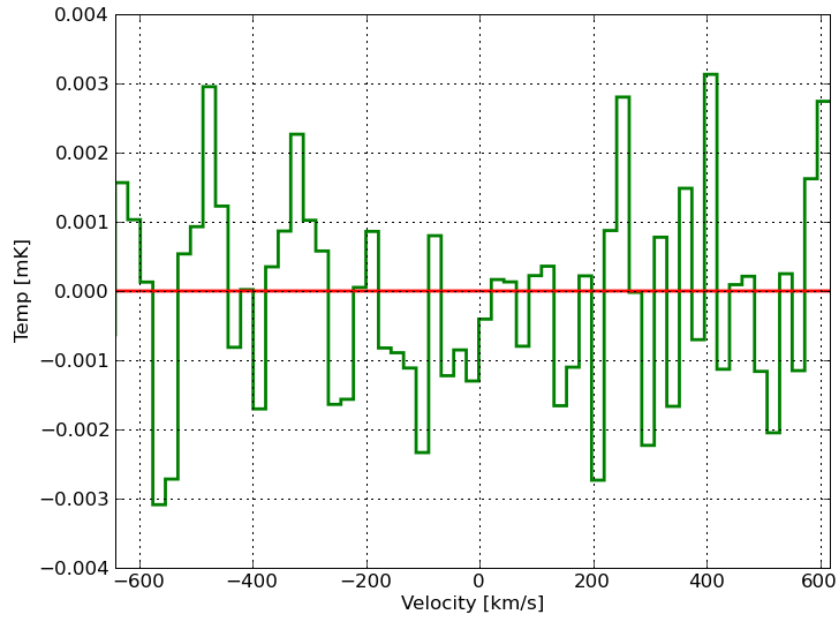


Figure A.138: B2 0915+32B CO(1-0)

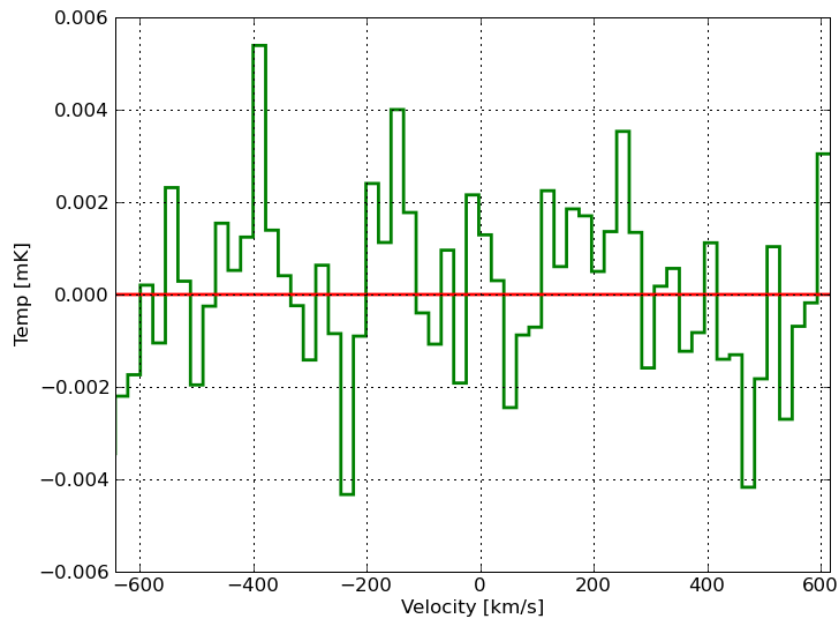


Figure A.139: B2 0615+32B CO(2-1)

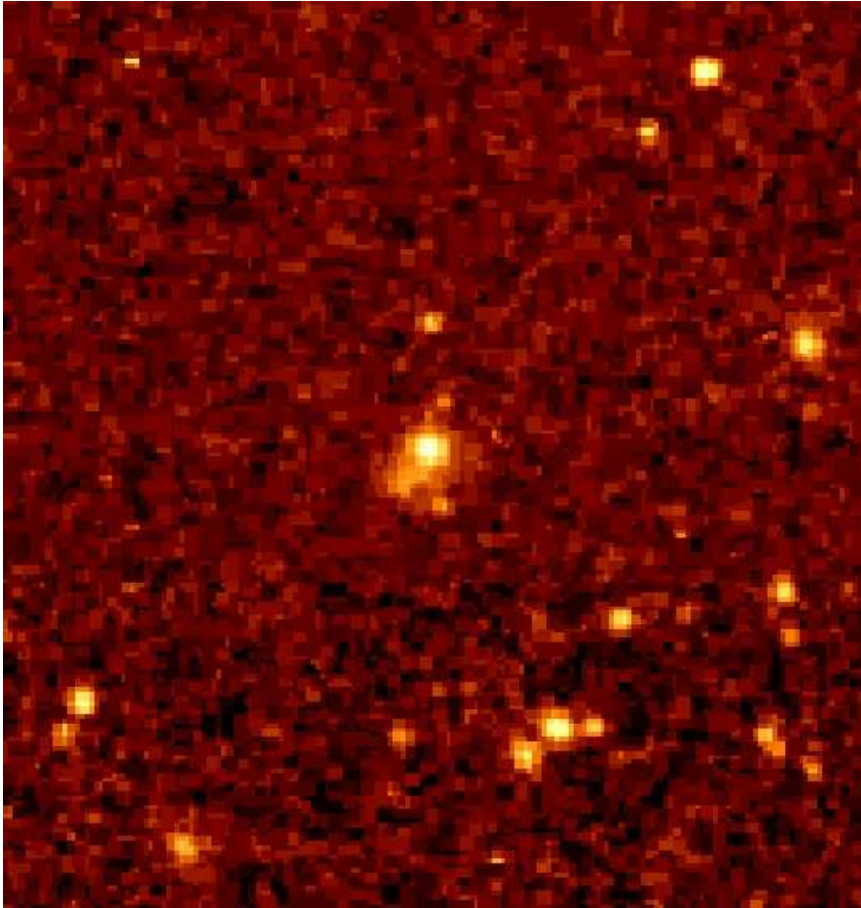
A.43 B2 0924+30

Figure A.140: B2 0924+30 optical image

It shows a peculiar behavior of the dust in the optical image which could possibly be due to interactions. It has not been detected in CO(2-1), although there is a clear detection of the CO(1-0) line. In the HST image there might be another smaller galaxy that has fallen into B2 0924+30.

The average particle age, according to [Jamrozy et al. \(2004\)](#), is 54_{11}^{12} Myrs, and the low-frequency spectral index is determined as $\alpha_i = -0.87 \pm 0.09$, probably reflecting the spectrum of an initially injected electron population which has undergone synchrotron losses. They hypothesize that this source is a relic of a still older period of activity.

Table A.127: General Data for B2 0924+30

RA:	09h27m23.5s
Dec:	+29d55m30s
FR:	I
z_{CO} :	0.025
Distance [Mpc]:	104.24
Line Width [km/s]:	
$I_{\text{CO}(1-0)}$ [K km/s]:	0.32 ± 0.11
$I_{\text{CO}(2-1)}$ [K km/s]:	...
$M_{\text{H}_2} M_{\odot}$:	$2.01 \pm 0.68 \times 10^8$

Table A.128: Fluxes of B2 0924+30

Wavelength	flux measurement mJy
$S_{3\text{mm}}$	0.91 ± 10.29
$S_{1\text{mm}}$...
$f_{12\mu\text{m}}$...
$f_{25\mu\text{m}}$...
$f_{60\mu\text{m}}$...
$f_{100\mu\text{m}}$...

Table A.129: Luminosities for B2 0924+30

Parameter	Luminosity
L_{CO} [K km/s pc^2]	3.90×10^7
$L_{\text{FIR}} L_{\odot}$...

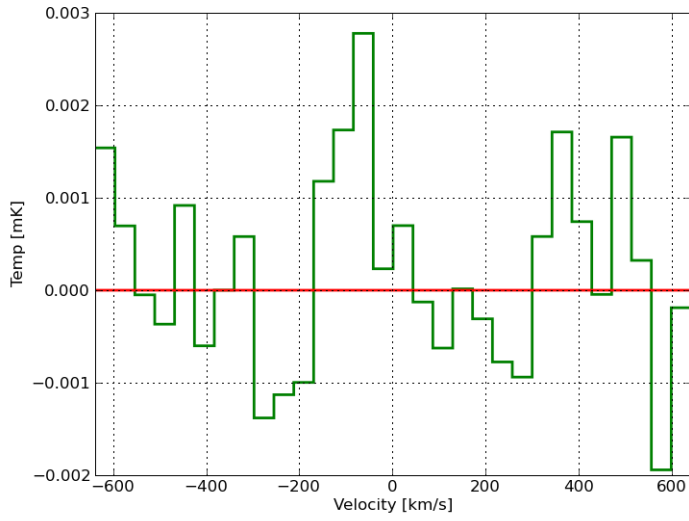


Figure A.141: B2 0924+30 CO(1-0)

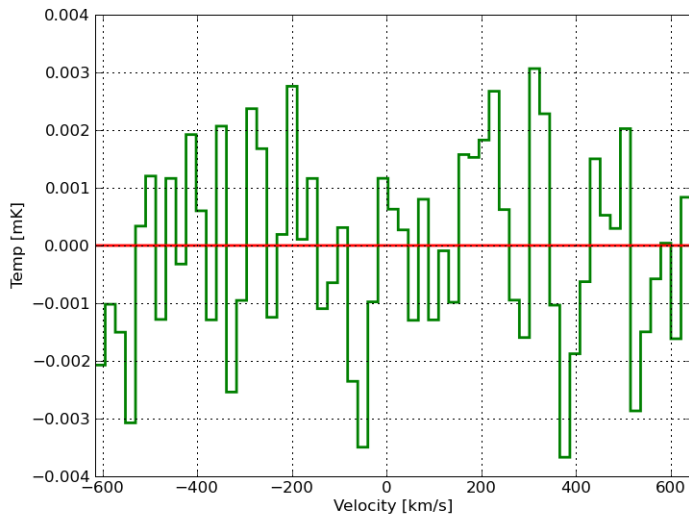


Figure A.142: B2 0924+30 CO(2-1)

A.44 B2 1101+38

Other Names: MRK 421, UGC 06132

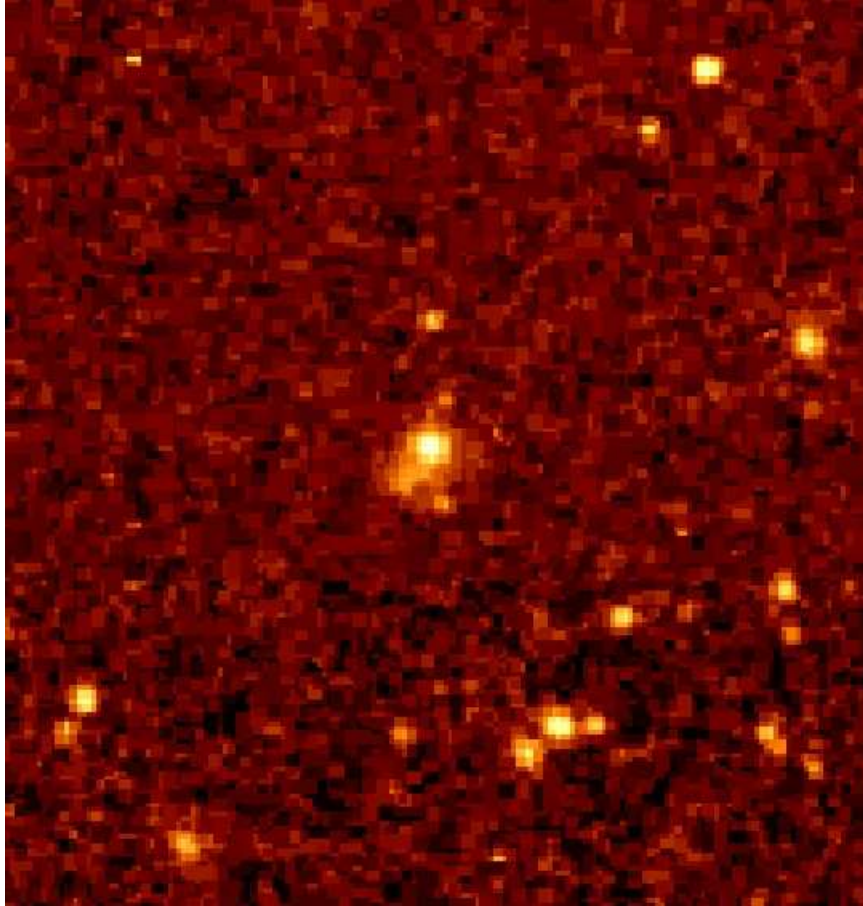


Figure A.143: B2 0924+30 optical image

From the optical image we can possibly see an interaction. Even though this galaxy has not been detected in CO in our sample.

Table A.130: General Data for B2 1101+38

RA:	11h04m27.3s
Dec:	+38d12m32s
FR:	c
z_{CO} :	0.03
Distance [Mpc]:	126
Line Width [km/s]:	-
$I_{CO(1-0)}$ [K km/s]:	<1.35
$I_{CO(2-1)}$ [K km/s]:	...
$M_{H_2} M_{\odot}$:	$<13.09 \times 10^8$

Table A.131: Fluxes of B2 1101+38

Wavelength	flux measurement mJy
S_{3mm}	359 ± 0.97
S_{1mm}	0.165 ± 0.002
$f_{12\mu m}$	90 ± 15
$f_{25\mu m}$	95 ± 19
$f_{60\mu m}$	181 ± 22
$f_{100\mu m}$	361 ± 68

Table A.132: Luminosities for B2 1101+38

Parameter	Luminosity
L_{CO} [K km/s pc^2]	$<2.34 \times 10^8$
L_{FIR} [L_{\odot}]	5.62×10^9

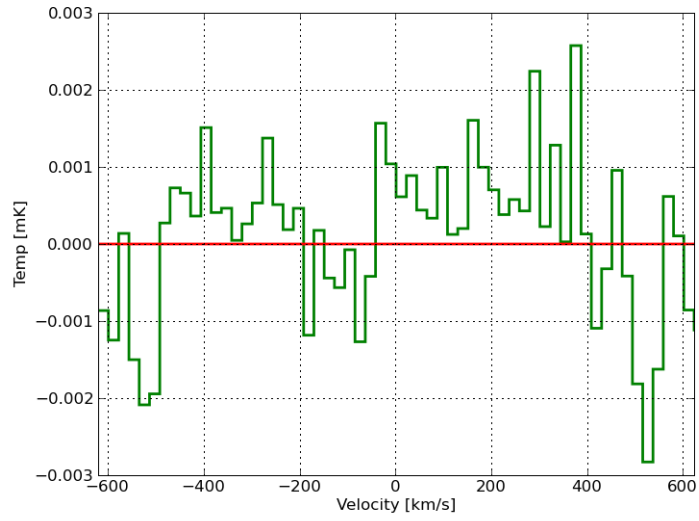


Figure A.144: B2 1101+38 CO(1-0)

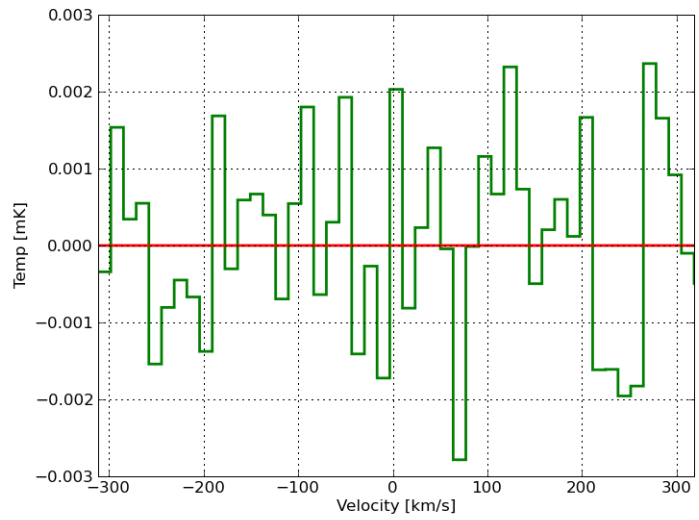


Figure A.145: B2 1101+38 CO(2-1)

A.45 B2 1347+28

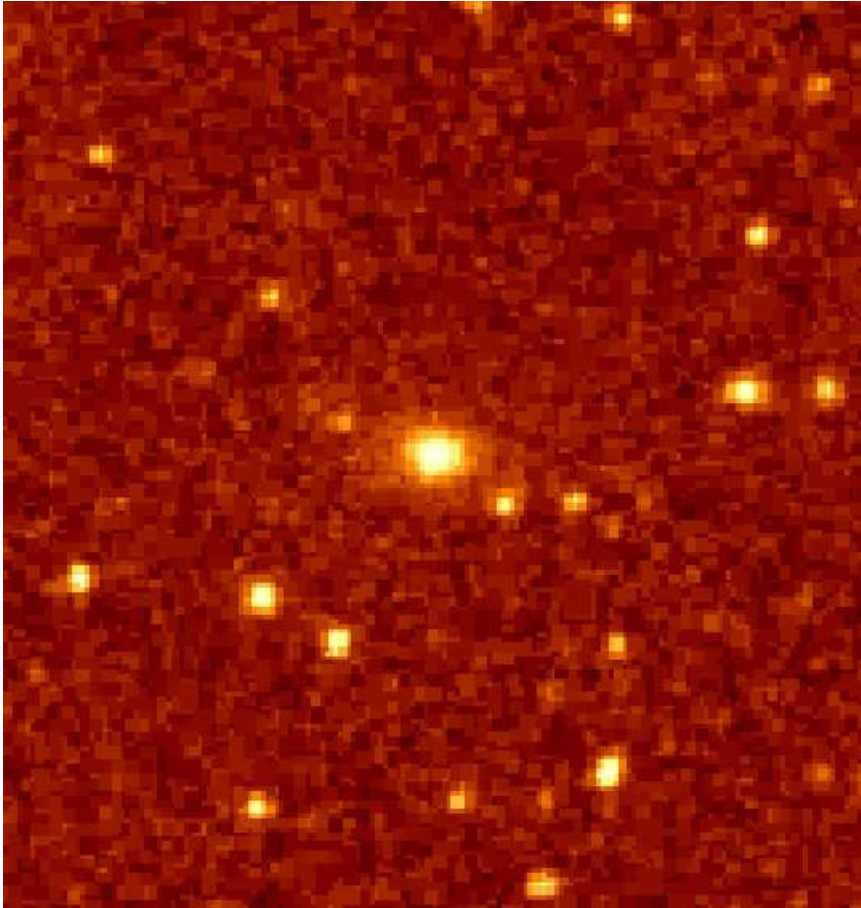


Figure A.146: B2 1347+28 optical image

It has not been detected in the CO(1-0) line but instead it has been detected in the CO(2-1) emission line. We calculated the CO(1-0) intensity using the 2.3 average line ratio of the galaxies detected in both lines.

Table A.133: General Data for B2 1347+28

RA:	13h50m13.6s
Dec:	+28d16m45s
FR:	II
z_{CO} :	0.072
Distance [Mpc]:	297.9
Line Width [km/s]:	
$I_{CO(1-0)}$ [K km/s]:	0.35 ± 0.08
$I_{CO(2-1)}$ [K km/s]:	0.75 ± 0.25
$M_{H_2} M_{\odot}$:	$17.04 \pm 13 \times 10^8$

Table A.134: Fluxes of B2 1347+28

Wavelength	flux measurement mJy
S_{3mm}	8.96 ± 0.51
S_{1mm}	...
$f_{12\mu m}$...
$f_{25\mu m}$...
$f_{60\mu m}$...
$f_{100\mu m}$...

Table A.135: Luminosities for B2 1347+28

Parameter	Luminosity
L_{CO} [K km/s pc^2]	3.16×10^8
L_{FIR} [L_{\odot}]	...

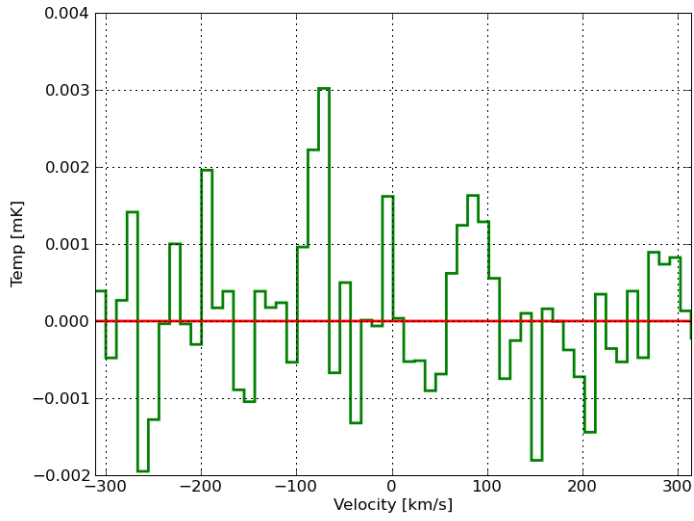


Figure A.147: B2 1347+28 CO(1-0)

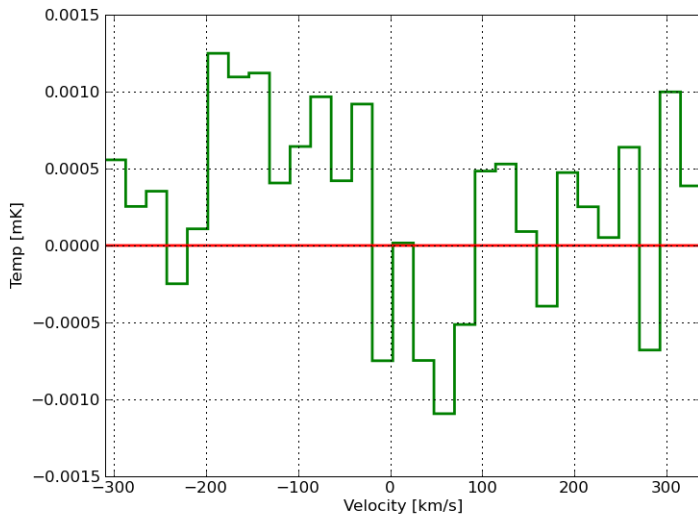


Figure A.148: B2 1347+28 CO(2-1)

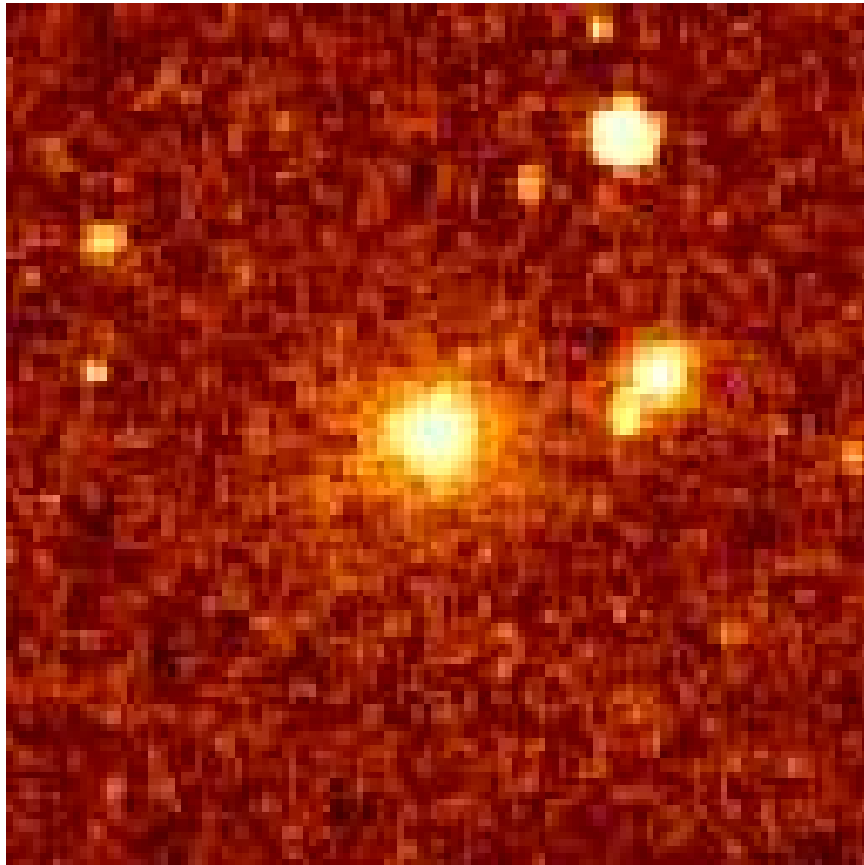
A.46 B2 1357+28

Figure A.149: B2 1357+28 optical image

It is clearly detected in the CO(1-0) emission line, but nothing peculiar in the optical image and no emission was detected in the CO(2-1) emission line.

Table A.136: General Data for B2 1357+28

RA:	14h00m00.8s
Dec:	+28d30m00s
FR:	I
z_{CO} :	0.063
Distance [Mpc]:	260
Line Width [km/s]:	-
$I_{CO(1-0)}$ [K km/s]:	<1.13
$I_{CO(2-1)}$ [K km/s]:	...
$M_{H_2} M_{\odot}$:	$<48.09 \times 10^8$

Table A.137: Fluxes of B2 1357+28

Wavelength	flux measurement mJy
S_{3mm}	...
S_{1mm}	...
$f_{12\mu m}$...
$f_{25\mu m}$...
$f_{60\mu m}$...
$f_{100\mu m}$...

Table A.138: Luminosities for B2 1357+28

Parameter	Luminosity
L_{CO} [K km/s pc^2]	$<7.94 \times 10^9$
$L_{FIR} L_{\odot}$...

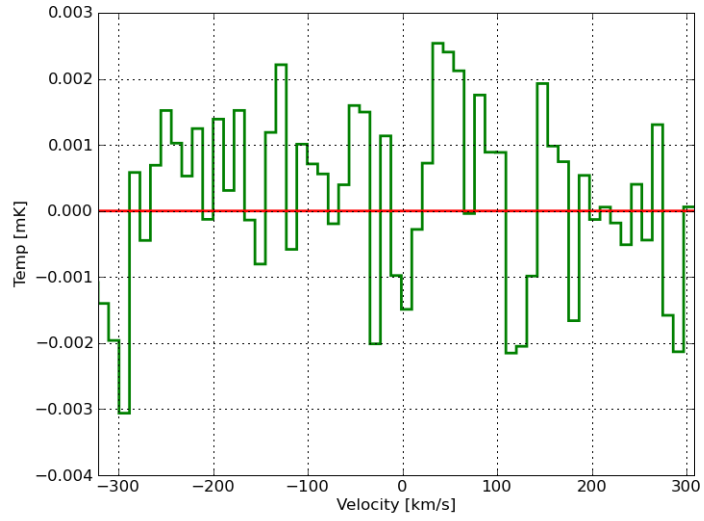


Figure A.150: B2 1357+28 CO(1-0)

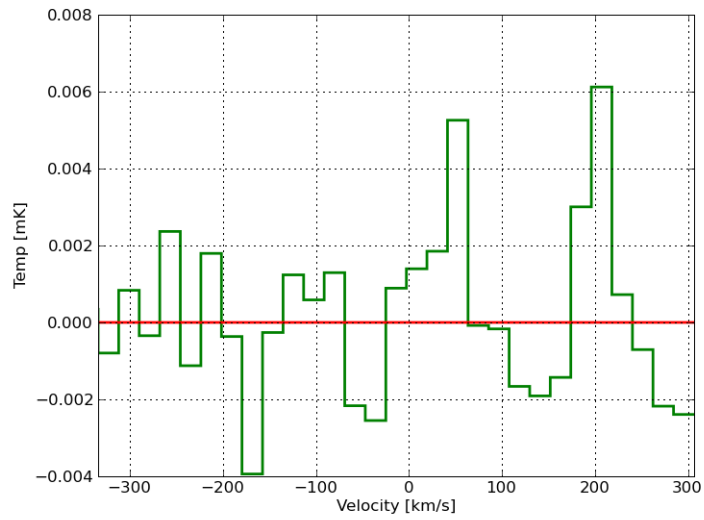


Figure A.151: B2 1357+28 CO(2-1)

A.47 B2 1447+27

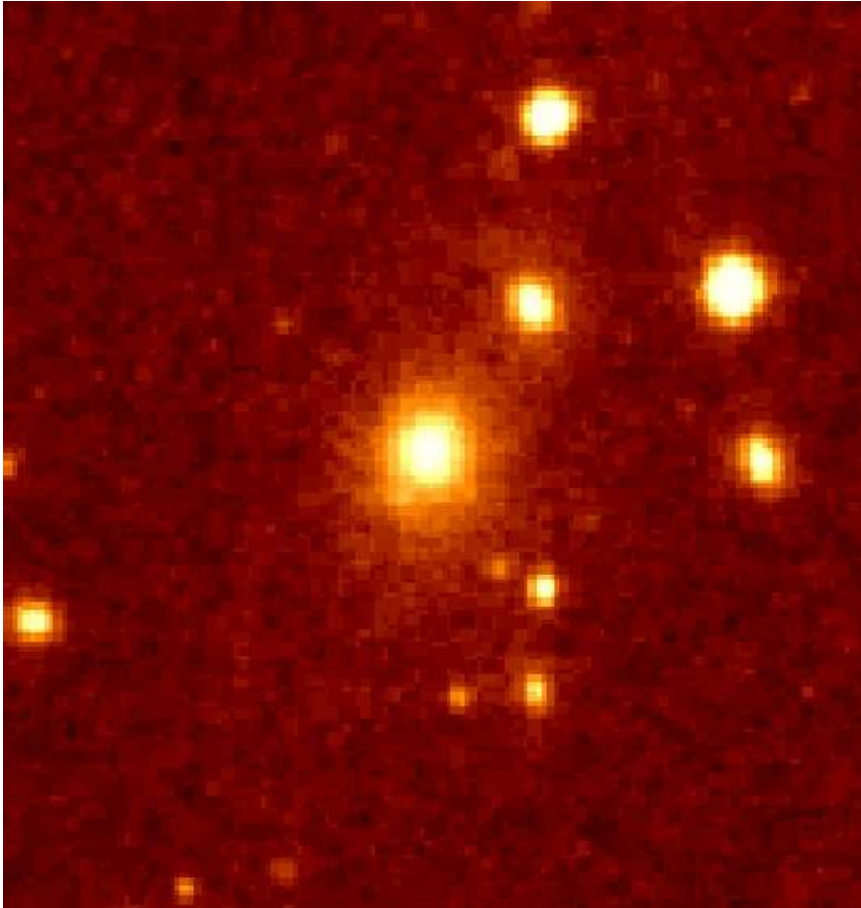


Figure A.152: B2 1447+27 optical image

This galaxy has been observed for CO(1-0) and CO(2-1) emission lines using the IRAM-30m telescope, but it has not been detected.

Table A.139: General Data for B2 1447+27

RA:	14h49m27.9s
Dec:	+27d46m50s
FR:	c
z_{CO} :	0.03
Distance [Mpc]:	127
Line Width [km/s]:	-
$I_{CO(1-0)}$ [K km/s]:	<0.79
$I_{CO(2-1)}$ [K km/s]:	...
$M_{H_2} M_{\odot}$:	<7.96 $\times 10^8$

Table A.140: Fluxes of B2 1447+27

Wavelength	flux measurement mJy
S_{3mm}	13.94 \pm 0.53
S_{1mm}	52.41 \pm 0.81
$f_{12\mu m}$...
$f_{25\mu m}$...
$f_{60\mu m}$...
$f_{100\mu m}$...

Table A.141: Luminosities for B2 1447+27

Parameter	Luminosity
L_{CO} [K km/s pc^2]	<1.45 $\times 10^8$
$L_{FIR} L_{\odot}$...

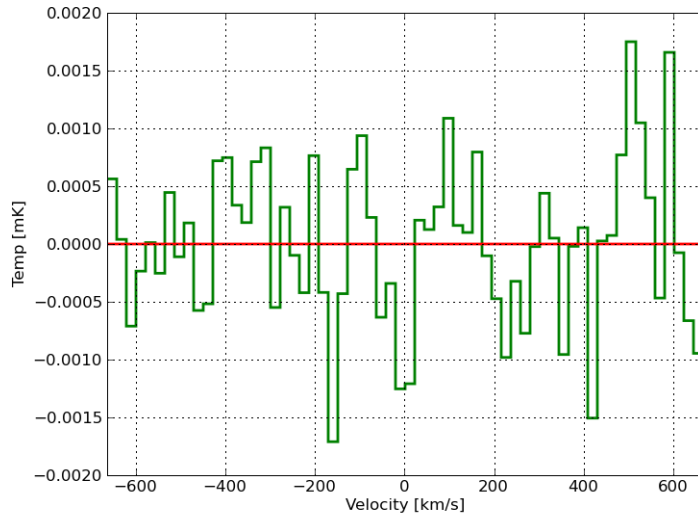


Figure A.153: B2 1447+27 CO(1-0)

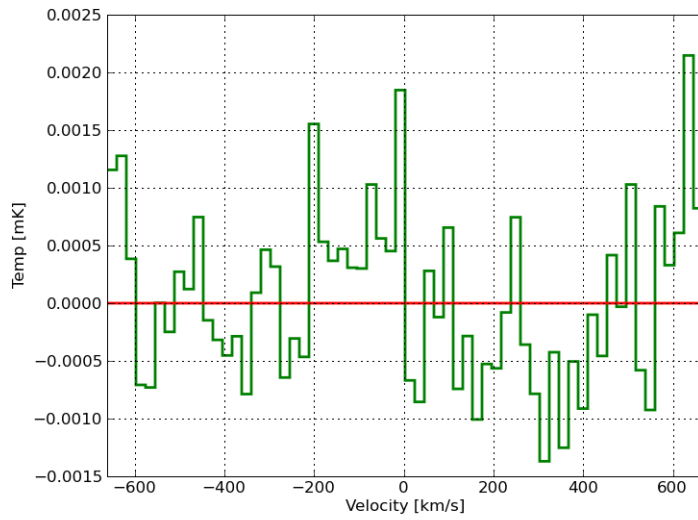


Figure A.154: B2 1447+27 CO(2-1)

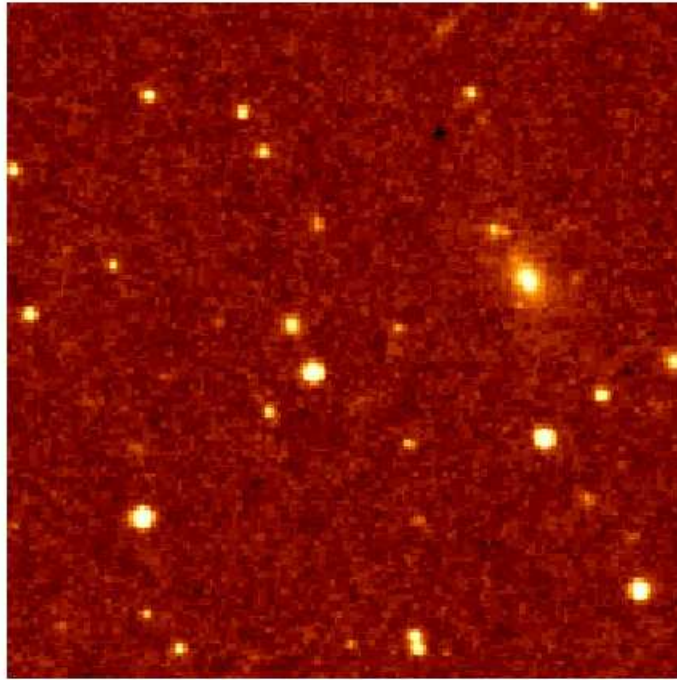
A.48 B2 1512+30

Figure A.155: B2 1512+30 optical image

This galaxy has been observed for CO(1-0) and CO(2-1) emission lines using the IRAM-30m telescope, but it has not been detected.

Table A.142: General Data for B2 1512+30

RA:	15h14m06.6s
Dec:	+30d10m25s
FR:	II
z_{CO} :	0.0931
Distance [Mpc]:	384
Line Width [km/s]:	-
$I_{CO(1-0)}$ [K km/s]:	<1.19
$I_{CO(2-1)}$ [K km/s]:	...
$M_{H_2} M_{\odot}$:	$<110.54 \times 10^8$

Table A.143: Fluxes of B2 1512+30

Wavelength	flux measurement mJy
S_{3mm}	...
S_{1mm}	...
$f_{12\mu m}$...
$f_{25\mu m}$...
$f_{60\mu m}$...
$f_{100\mu m}$...

Table A.144: Luminosities for B2 1512+30

Parameter	Luminosity
L_{CO} [K km/s pc^2]	$<1.70 \times 10^9$
$L_{FIR} L_{\odot}$...

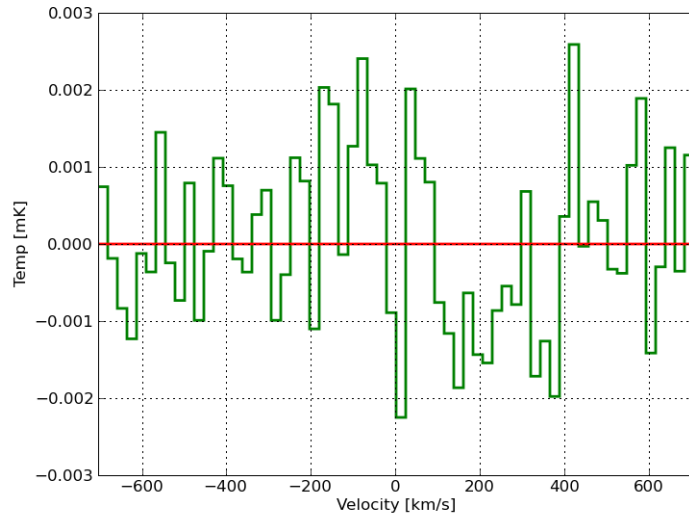


Figure A.156: B2 1512+30 CO(1-0)

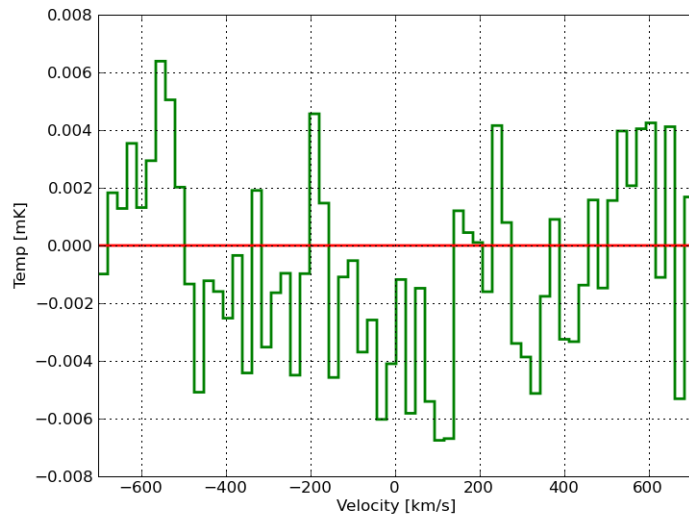


Figure A.157: B2 1512+30 CO(2-1)

A.49 B2 1525+29

Other Name: UGC 09861

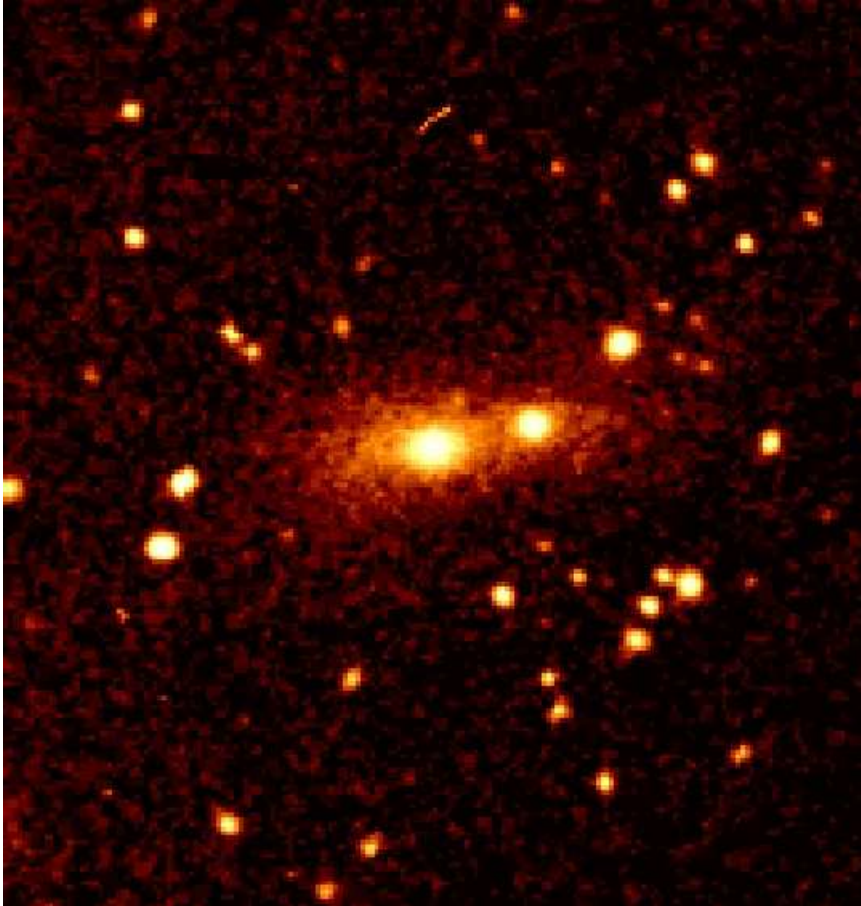


Figure A.158: B2 1525+29 optical image

This galaxy has been observed for CO(1-0) and CO(2-1) emission line using the IRAM-30m telescope, but it has not been detected.

Table A.145: General Data for B2 1525+29

RA:	15h27m44.4s
Dec:	+28d55m07s
FR:	I
z_{CO} :	0.065
Distance [Mpc]:	270
Line Width [km/s]:	-
$I_{CO(1-0)}$ [K km/s]:	<1.52
$I_{CO(2-1)}$ [K km/s]:	...
$M_{H_2} M_{\odot}$:	$<69.55 \times 10^8$

Table A.146: Fluxes of B2 1525+29

Wavelength	flux measurement mJy
S_{3mm}	14.48 ± 1.07
S_{1mm}	0.13 ± 0.003
$f_{12\mu m}$...
$f_{25\mu m}$...
$f_{60\mu m}$...
$f_{100\mu m}$...

Table A.147: Luminosities for B2 1525+29

Parameter	Luminosity
L_{CO} [K km/s pc^2]	$<1.15 \times 10^9$
$L_{FIR} L_{\odot}$...

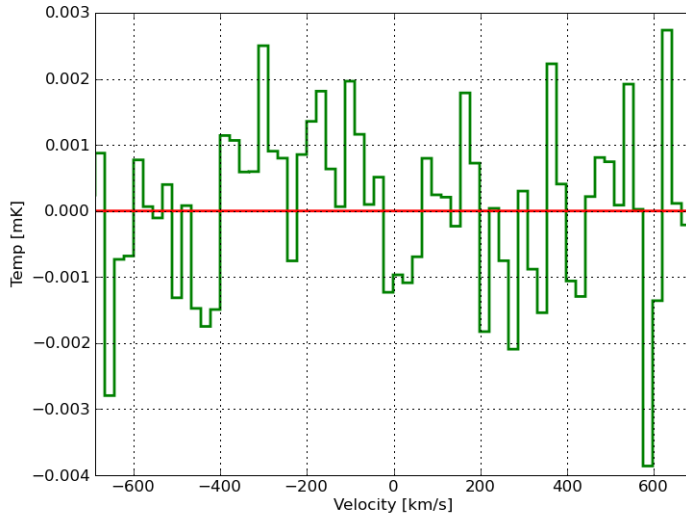


Figure A.159: B2 1525+29 CO(1-0)

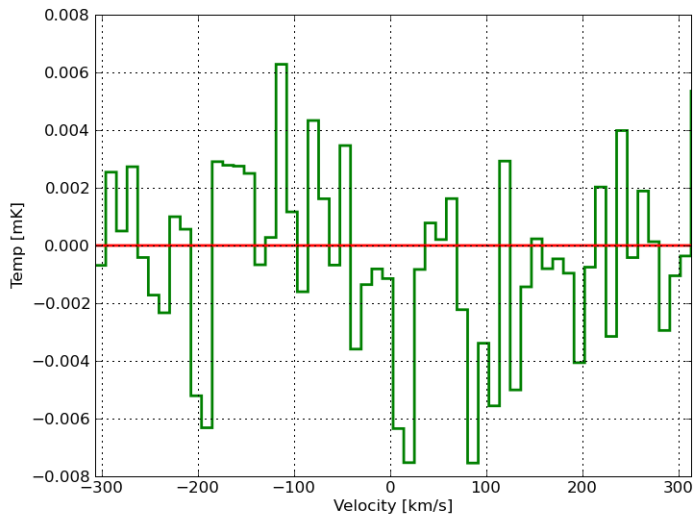


Figure A.160: B2 1525+29 CO(2-1)

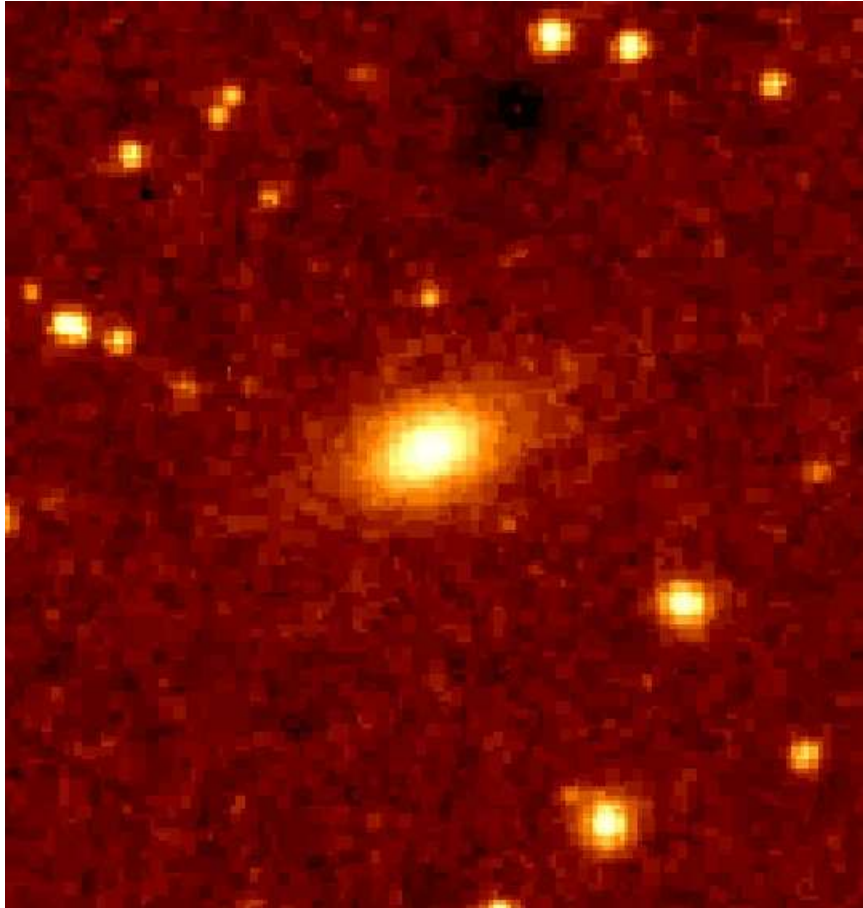
A.50 B2 1553+24

Figure A.161: B2 1553+24 optical image

This galaxy has been observed for CO(1-0) and CO(2-1) emission line using the IRAM-30m telescope, but it has not been detected.

A.50.1 HI data

This galaxy has also been observed in HI, but it is not detected.

Table A.148: General Data for B2 1553+24

RA:	15h56m03.9s
Dec:	+24d26m53s
FR:	I
z_{CO} :	0.043
Distance [Mpc]:	176
Line Width [km/s]:	-
$I_{CO(1-0)}$ [K km/s]:	<1.52
$I_{CO(2-1)}$ [K km/s]:	...
$M_{H_2} M_{\odot}$:	$<26.68 \times 10^8$

Table A.149: Fluxes of B2 1553+24

Wavelength	flux measurement mJy
S_{3mm}	35.28 ± 1
S_{1mm}	...
$f_{12\mu m}$...
$f_{25\mu m}$...
$f_{60\mu m}$...
$f_{100\mu m}$...

Table A.150: Luminosities for B2 1553+24

Parameter	Luminosity
L_{CO} [K km/s pc^2]	$<5.25 \times 10^8$
$L_{FIR} L_{\odot}$...

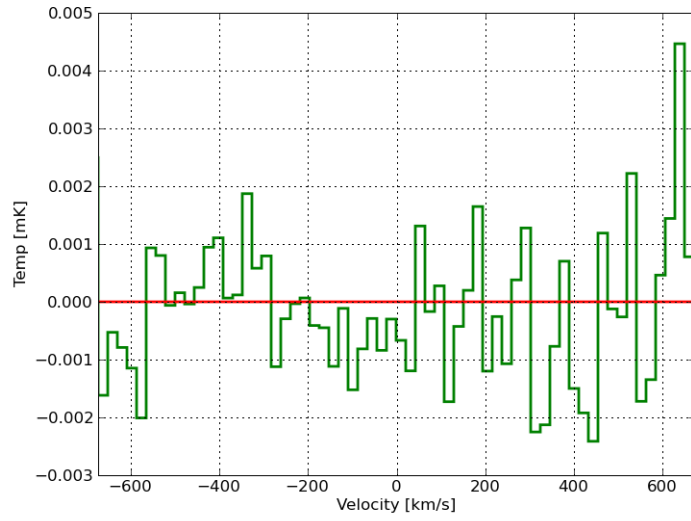


Figure A.162: B2 1553+24 CO(1-0)

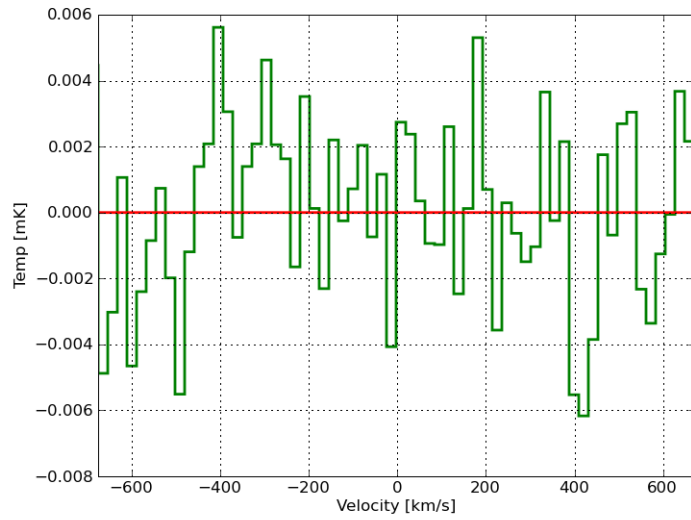


Figure A.163: B2 1553+24 CO(2-1)

265; 4 B2 1553+24 NONE FRONTTEST-2 O: 29-JUN-2008 R: 02-JUL-2008
 RA: 15:56:03.898 DEC: 24:26:53.00 (2000.0) Offs: -5.359 -8.038 Eq
 Unknown Tau: 0.000 Tsys: 46.34 Time: 23.48 El: 9.66
 N: 255 l0: 128.0 v0: 0.000 Dv: 17.47 LSR
 F0: 1339.80000 Df: -7.8080E-02 Fi: 1189.80000
 B ef: 0.000 F ef: 0.000 G im: 0.000
 H2O : 0.000 Pamb: 0.000 Tamb: 0.0 Tchop: 0.0 Tcold: 0.0
 Tatm: 0.0 Tau: 0.000 Tatm i: 0.0 Tau i: 0.000
 3134- 3138,

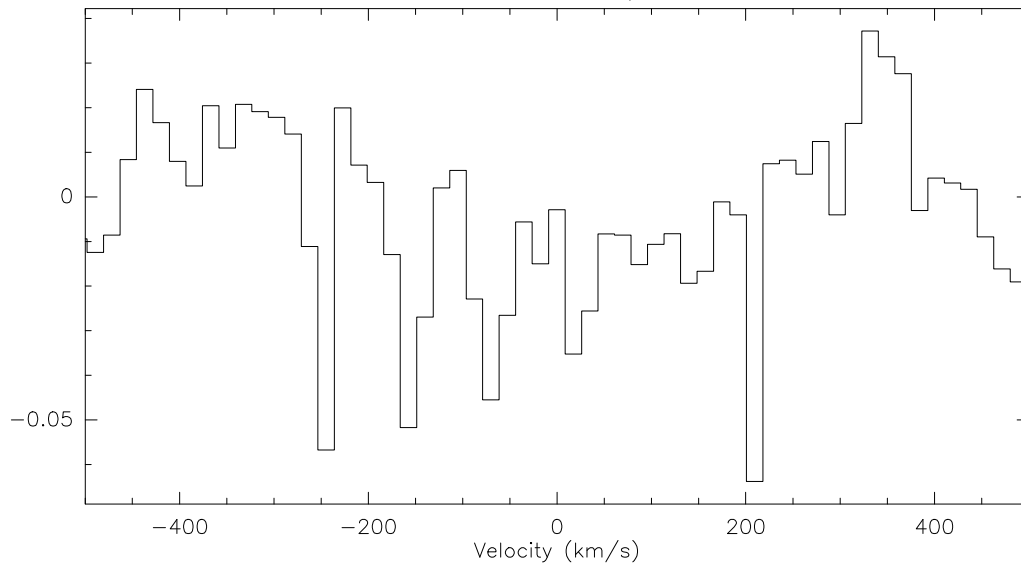


Figure A.164: HI emission for B2 1553+24

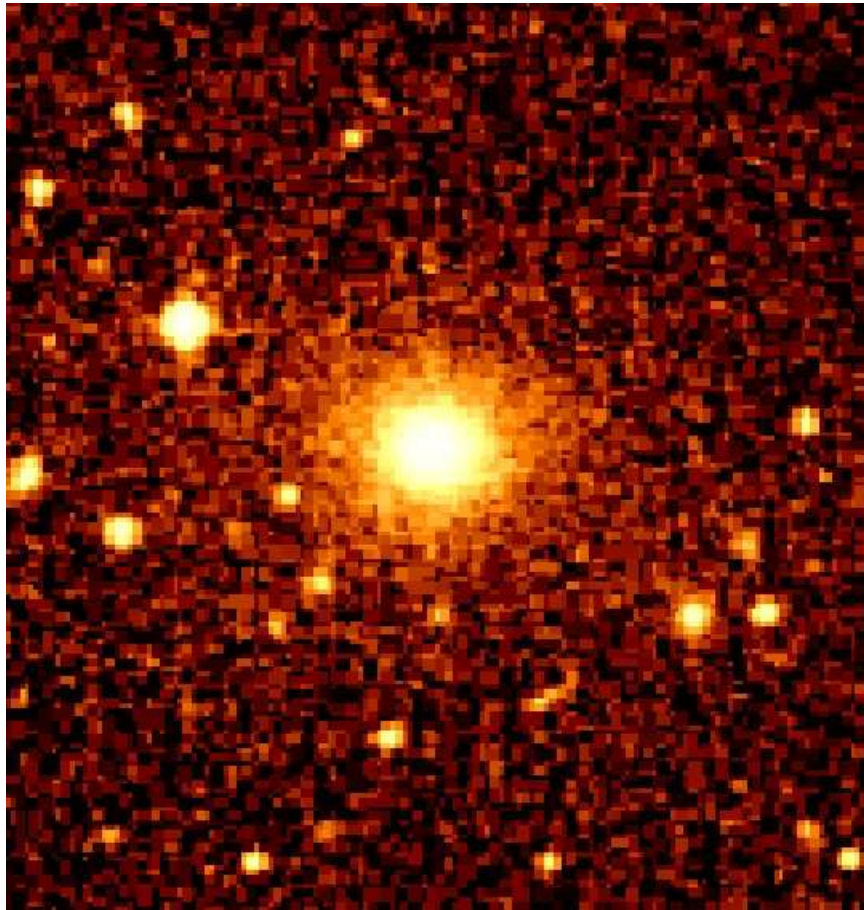
A.51 UGC 7115

Figure A.165: UGC 7115 optical image

This galaxy has been observed for CO(1-0) and CO(2-1) emission line using the IRAM-30m telescope, but it has not been detected.

Table A.151: General Data for UGC 7115

RA:	12h08m05.5s
Dec:	+25d14m14s
FR:	I
z_{CO} :	0.023
Distance [Mpc]:	97
Line Width [km/s]:	-
$I_{CO(1-0)}$ [K km/s]:	< 1.53
$I_{CO(2-1)}$ [K km/s]:	...
$M_{H_2} M_{\odot}$:	$< 7.66 \times 10^8$

Table A.152: Fluxes of UGC 7115

Wavelength	flux measurement mJy
S_{3mm}	30.57 ± 1.03
S_{1mm}	...
$f_{12\mu m}$...
$f_{25\mu m}$...
$f_{60\mu m}$...
$f_{100\mu m}$...

Table A.153: Luminosities for UGC 7115

Parameter	Luminosity
L_{CO} [K km/s pc^2]	$< 1.55 \times 10^8$
$L_{FIR} L_{\odot}$...

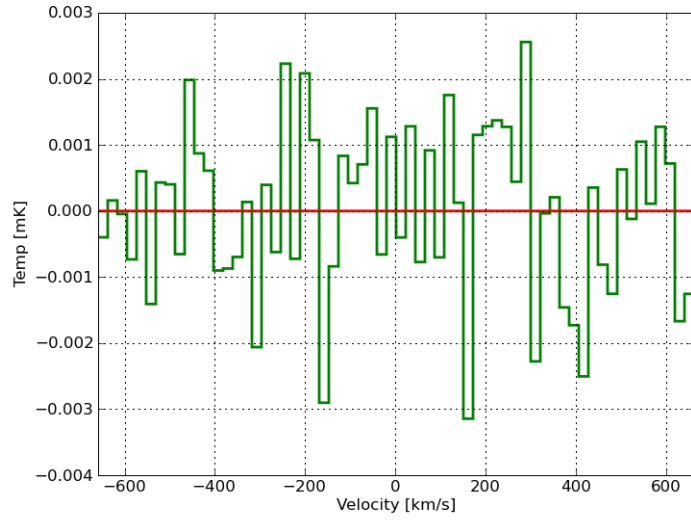


Figure A.166: UGC 7115 CO(1-0)

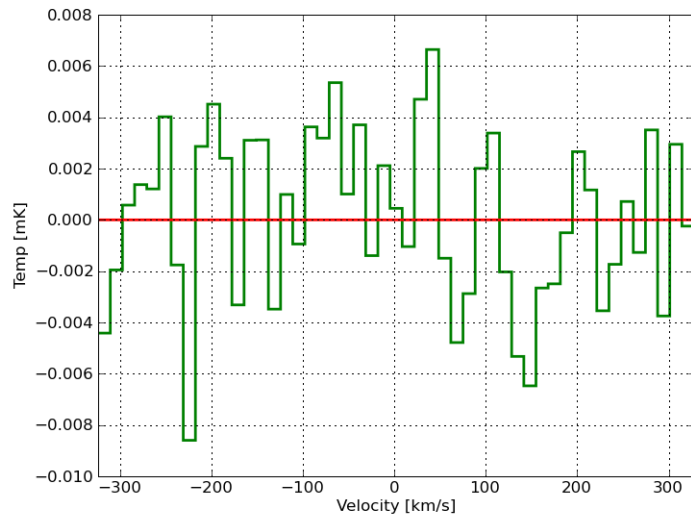


Figure A.167: UGC 7115 CO(2-1)

A.52 OQ 208

Other Name: MRK 0668

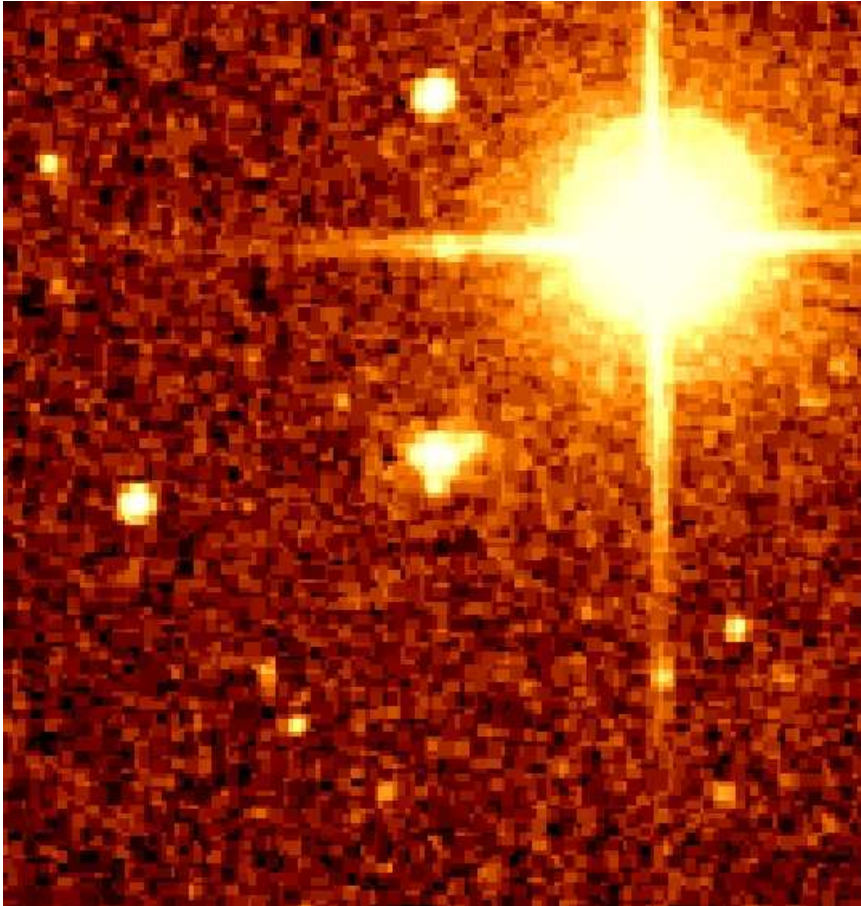


Figure A.168: OQ 208 optical image

It has only been observed in the CO(1-0) line and it presents a clear double horn profile with a velocity width in CO(1-0) of about 400 km/s and a rotational velocity of about 200 km/s.

Table A.154: General Data for OQ 208

RA:	14h07m00.4s
Dec:	+28d27m15s
FR:	c
z_{CO} :	0.0766
Distance [Mpc]:	304.90
Line Width [km/s]:	-
$I_{CO(1-0)}$ [K km/s]:	2.51 ± 0.33
$I_{CO(2-1)}$ [K km/s]:	Not Observed
$M_{H_2} M_{\odot}$:	$136.51 \pm 17.97 \times 10^8$

Table A.155: Fluxes of OQ 208

Wavelength	flux measurement mJy
S_{3mm}	40.43 ± 16.67
S_{1mm}	Not Observed
$f_{12\mu m}$	<185
$f_{25\mu m}$	399 ± 18.5
$f_{60\mu m}$	753 ± 113
$f_{100\mu m}$	1029 ± 154

Table A.156: Luminosities for OQ 208

Parameter	Luminosity
L_{CO} [K km/s pc^2]	2.57×10^9
$L_{FIR} L_{\odot}$	1.32×10^{11}

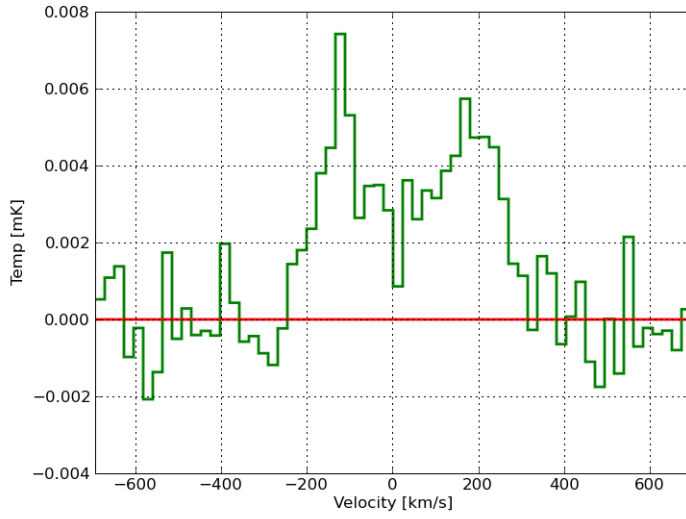
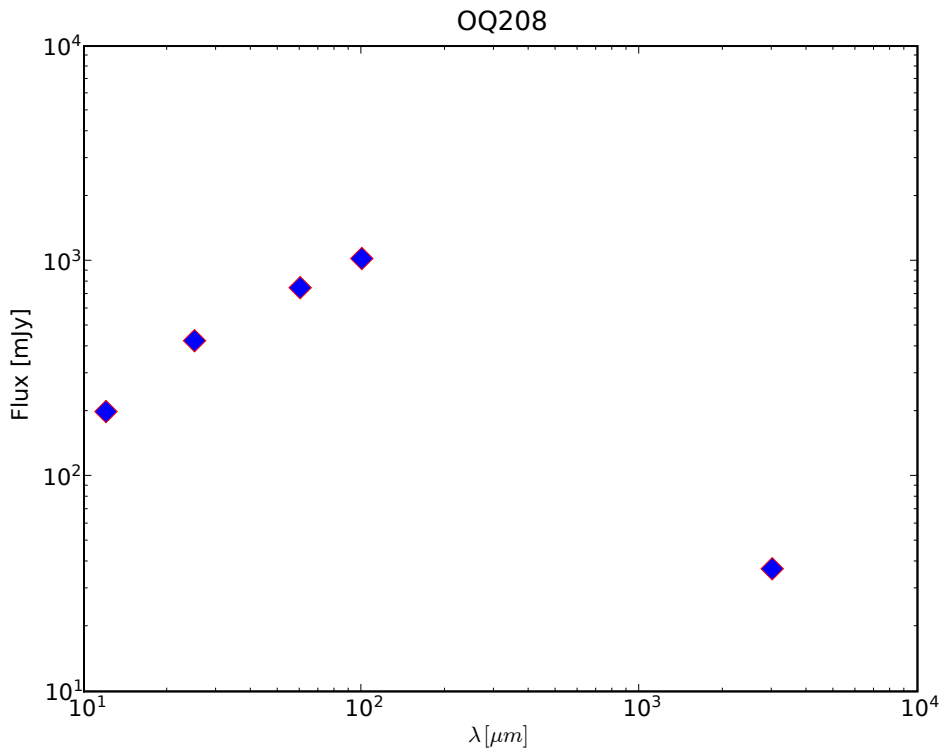


Figure A.169: OQ 208 CO(1-0)

Figure A.170: The Spectral Energy Distribution diagram for OQ 208



Appendix B

Abbreviations

- **ASTRO** A Software To pRepare Observations.
- **AGN** Active Galactic Nuclei.
- **AMIGA** Análisis del Medio Inter-estelar de Galaxias Aisladas.
- **AOR** Astronomical Observation Request.
- **ASURV** Astronomical SURVival Analysis package.
- **BCD** Basic Calibrated Data.
- **BH** Black Hole.
- **CSO** Compact Symmetric Object.
- **CPS** Compact Peaked Spectrum.
- **FIR** Far Infra-Red.
- **FOV** Field of View.
- **FWZI** Full Width Zero Intensity.
- **GB** Green Bank.
- **HST** Hubble Space Telescope.
- **IF** Intermediate Frequency.
- **IR** Infra-Red.
- **IRAC** Infrared Array Camera.
- **IRAM** Institute of Milimetric Radio Astronomy (Instituto de Radio Astronomía Milimétrica).

- **IRAS** Infrared Astronomical Satellite.
- **LIRGs** Luminous Infra-Red Galaxies.
- **LzS** Low redshift sample.
- **MIPS** Multiband Imaging Photometer for Spitzer.
- **MIRA** Multichannel Imaging and Calibration Software for Receiver Arrays.
- **MzS** Medium redshift sample.
- **NIR** Near Infra-Red.
- **PAH** Polycyclic Aromatic Hydrocarbons.
- **POSS** Palomar Observatory Sky Survey.
- **SB** Star Burst.
- **SED** Spectral Energy Distribution.
- **SF** Star Formation.
- **TANGO** Thorough ANalysis of radio-Galaxies Observations.
- **UIB** Unidentified Bands.
- **ULIRGs** Ultra Luminous Infra-Red Galaxies.
- **WILMA** Wideband Line Multiple Autocorrelator.

Bibliography

- 1997, Towards the edge of the universe. A review of modern cosmology [1.3.3.1](#)
- Allen, S. W., Dunn, R. J. H., Fabian, A. C., Taylor, G. B., & Reynolds, C. S. 2006, MNRAS, 372, 21 [1.2](#)
- Antonucci, R. 1993, ARAA, 31, 473 [1.2](#)
- Armus, L., Charmandaris, V., Bernard-Salas, J., et al. 2007, ApJ, 656, 148 [6.4](#)
- Athey, A., Bregman, J., Bregman, J., Temi, P., & Sauvage, M. 2002, ApJ, 571, 272 [5.7](#)
- Baars, J. W. M. 1973, IEEE Trans. Ant. Prop, 461, 21 [5.1](#)
- Baars, J. W. M., Genzel, R., Pauliny-Toth, I. I. K., & Witzel, A. 1977, A&AP, 61, 99 [11.6.1](#)
- Baldi, R. D. & Capetti, A. 2008, ArXiv e-prints [5.7](#)
- Baum, S. A., Heckman, T. M., & van Breugel, W. 1992, ApJ, 389, 208 [7.3](#)
- Baum, S. A., O'Dea, C. P., Giovannini, G., et al. 1997, ApJ, 483, 178 [A.9](#)
- Baum, S. A., O'Dea, C. P., Murphy, D. W., & de Bruyn, A. G. 1990, A&AP, 232, 19 [1.3.3.4](#)
- Bell, E. F. 2003, ApJ, 586, 794 [6.2.1](#), [6.5](#), [11.5.3](#), [8](#), [8](#)
- Bergvall, N., Laurikainen, E., & Aalto, S. 2003, A&AP, 405, 31 [12.1.3](#)
- Bertram, T., Eckart, A., Fischer, S., et al. 2007, A&AP, 470, 571 [10.2](#), [10.3](#), [10.3.1](#), [10.4](#), [10.3](#), [10.5](#), [10.4](#), [13](#), [2](#), [15](#), [2](#)
- Best, P. N., Kaiser, C. R., Heckman, T. M., & Kauffmann, G. 2006, MNRAS, 368, L67 [1.2](#)
- Black, A. R. S., Baum, S. A., Leahy, J. P., et al. 1992, MNRAS, 256, 186 [A.20](#)
- Bordovostsyn, V. A. 1999, Synchrotron Radiation Theory and its Development, ed. V. A. Bordovostsyn (Wold Scientific Publishing Co.Pte. Ltd.) [8.5](#)

- Braine, J. & Combes, F. 1992, *A&AP*, 264, 433 [5.4](#), [10.5](#), [10.4](#), [11.3.1](#), [A.37](#)
- Braude, S. I., Megn, A. V., Rashkovskii, S. L., et al. 1978, *APSS*, 54, 37 [11.6.1](#)
- Bridle, A. H., Davis, M. M., Fomalont, E. B., Willis, A. G., & Strom, R. G. 1979, *ApJL*, 228, L9 [A.25](#)
- Brundage, R. K., Dixon, R. S., Ehman, J. R., & Kraus, J. D. 1971, *AJ*, 76, 777 [2.2.4](#)
- Bushouse, H. A. 1987, *ApJ*, 320, 49 [12.1.3](#)
- Butcher, H. R., van Breugel, W., & Miley, G. K. 1980, *ApJ*, 235, 749 [A.3](#)
- Capetti, A., Axon, D. J., Chiaberge, M., et al. 2007, *A&AP*, 471, 137 [2.3](#), [A.12](#)
- Capetti, A., Macchetto, F. D., Sparks, W. B., & Biretta, J. A. 1997, *A&AP*, 317, 637 [A.12](#)
- Carroll, B. W. & Ostlie, D. A. 1996, *An Introduction to Modern Astrophysics*, ed. Carroll, B. W. & Ostlie, D. A. [1.1](#), [1.1.1](#)
- Chaisson, E. & McMillan, S. 1999, *Astronomy Today*, third edition edn. (Simon & Schuster/A Viacom Company Upper Saddle River, NJ 07458: Prentice Hall) [1.1](#)
- Chiaberge, M., Capetti, A., & Celotti, A. 1999, *A&AP*, 349, 77 [2.3](#)
- Cleary, K., Lawrence, C. R., Marshall, J. A., Hao, L., & Meier, D. 2007, *ApJ*, 660, 117 [6.4](#)
- Colla, G., Fanti, C., Fanti, R., et al. 1973, *AAPS*, 11, 291 [2.2.3](#)
- Colla, G., Fanti, C., Fanti, R., et al. 1972, *AAPS*, 7, 1 [2.2.3](#)
- Colla, G., Fanti, C., Ficarra, A., et al. 1970, *AAPS*, 1, 281 [2.2.3](#)
- Combes, F. 2000, in *Molecular Hydrogen in Space*, ed. F. Combes & G. Pineau Des Forets, 275–+ [1.3.1](#)
- Combes, F. 2002, *ArXiv Astrophysics e-prints* [1.2](#)
- Combes, F., Young, L. M., & Bureau, M. 2007, *MNRAS*, 377, 1795 [A.32](#)
- Condon, J. J., Cotton, W. D., Greisen, E. W., et al. 1998, *AJ*, 115, 1693 [11.6.1](#), [11.2](#)
- Crane, P., Peletier, R., Baxter, D., et al. 1993, *ApJL*, 402, L37 [A.9](#)
- Crawford, C. S., Allen, S. W., Ebeling, H., Edge, A. C., & Fabian, A. C. 1999, *MNRAS*, 306, 857 [5.7](#)

- Croston, J. H., Kraft, R. P., & Hardcastle, M. J. 2007, *ApJ*, 660, 191 [A.31](#)
- Dale, D. A., Helou, G., Contursi, A., Silbermann, N. A., & Kolhatkar, S. 2001, *ApJ*, 549, 215 [8.2](#)
- Dallacasa, D., Bondi, M., Della Ceca, R., & Stanghellini, C. 1997a, *Memorie della Societa Astronomica Italiana*, 68, 55 [1.3.3.5](#)
- Dallacasa, D., Fanti, C., Fanti, R., et al. 1997b, *Memorie della Societa Astronomica Italiana*, 68, 315 [1.3.3.4](#)
- David, L. P., Jones, C., Forman, W., Vargas, I. M., & Nulsen, P. 2006, *ApJ*, 653, 207 [5.7](#)
- de Rijcke, S., Buyle, P., Cannon, J., et al. 2006, *A&AP*, 454, L111 [5.4.1](#)
- de Ruiter, H. R., Parma, P., Capetti, A., Fanti, R., & Morganti, R. 2002, *A&AP*, 396, 857 [1.2](#)
- Dekel, A., Sari, R., & Ceverino, D. 2009, *ApJ*, 703, 785 [5.7](#)
- Depoy, D. L., Becklin, E. E., & Wynn-Williams, C. G. 1986, *ApJ*, 307, 116 [1.3.1](#)
- Desert, F., Boulanger, F., & Puget, J. L. 1990, *A&AP*, 237, 215 [8.2](#)
- Dixon, R. S. 1970, *APJS*, 20, 1 [11.2](#)
- Dixon, R. S. & Kraus, J. D. 1968, *AJ*, 73, 381 [2.2.4](#)
- Douglas, J. N., Bash, F. N., Bozayan, F. A., Torrence, G. W., & Wolfe, C. 1996, *AJ*, 111, 1945 [11.6.1](#), [11.2](#)
- Draper, P. W., Scarrott, S. M., & Tadhunter, C. N. 1993, *MNRAS*, 262, 1029 [A.14](#), [A.15](#)
- Dreyer, J. L. E. 1888, *MmRAS*, 49, 1 [2.2.2](#)
- Edge, D. O., Shakeshaft, J. R., McAdam, W. B., Baldwin, J. E., & Archer, S. 1959, *MmRAS*, 68, 37 [2.2.1](#), [11.2](#)
- Ehman, J. R., Dixon, R. S., & Kraus, J. D. 1970, *AJ*, 75, 351 [2.2.4](#)
- Emonts, B. H. C. 2006, PhD thesis, Groningen University [7.3](#), [7.2](#), [7.3](#), [A.40](#)
- Emonts, B. H. C., Morganti, R., Oosterloo, T. A., et al. 2007, *A&AP*, 464, L1 [7.1](#), [7.1](#), [7.2](#), [A.34](#)
- Emonts, B. H. C., Morganti, R., Tadhunter, C. N., et al. 2006, *A&AP*, 454, 125 [5.7](#), [7.2](#), [A.40](#)

- Emonts, B. H. C., Morganti, R., van Gorkom, J. H., et al. 2008, *A&AP*, 488, 519
A.40
- Engelbracht, C. W., Blaylock, M., Su, K. Y. L., et al. 2007, *PASP*, 119, 994 4.5.1.1
- Evans, A. S., Mazzarella, J. M., Surace, J. A., et al. 2005, *APJS*, 159, 197 1.4,
2.1.1, 5.3, 10.2, 10.3, 10.3.1, 10.4, 10.3, 10.5, 10.4, 10.6, 13, 2, 6, 15, 2, 6
- Evans, A. S., Sanders, D. B., Surace, J. A., & Mazzarella, J. M. 1999, *ApJ*, 511,
730 10.3.1
- Evans, D. A., Worrall, D. M., Hardcastle, M. J., Kraft, R. P., & Birkinshaw, M.
2006, *ApJ*, 642, 96 A.3, A.9, A.12, A.18, A.27, A.33, A.36, A.39, A.45, A.60,
A.69, A.72, A.108
- Fabbiano, G., Miller, L., Trinchieri, G., Longair, M., & Elvis, M. 1984, *ApJ*, 283,
469 A.4
- Fanaroff, B. L. & Riley, J. M. 1974, *MNRAS*, 167, 31P 1.3.3.5
- Fanti, C. & Fanti, R. 1994, in *Astronomical Society of the Pacific Conference Series*, Vol. 54, *The Physics of Active Galaxies*, ed. G. V. Bicknell, M. A. Dopita,
& P. J. Quinn, 341–+ 1.3.3.5
- Fanti, C., Fanti, R., Dallacasa, D., et al. 1995, *A&AP*, 302, 317 1.3.3.4
- Fanti, C., Fanti, R., Ficarra, A., & Padrielli, L. 1974, *AAPS*, 18, 147 2.2.3
- Fanti, R., Fanti, C., Schilizzi, R. T., et al. 1990, *A&AP*, 231, 333 1.3.3.5
- Feigelson, E. D. & Nelson, P. I. 1985, *ApJ*, 293, 192 5.2
- Fitch, L. T., Dixon, R. S., & Kraus, J. D. 1969, *AJ*, 74, 612 2.2.4
- Franco, J. & Cox, D. P. 1986, *PASP*, 98, 1076 6.2.2
- Gao, Y. 1996, PhD thesis, AA(STATE UNIVERSITY OF NEW YORK AT
STONY BROOK) 12.3.1
- Gao, Y. 1997, *PASP*, 109, 1189 12.3.1
- Gao, Y. & Solomon, P. M. 2004a, *APJS*, 152, 63 (document), 12.1.2, 12.1.4, 12.2,
12.3, 12.2, 12.3, 12.3.1, 12.1, 12.4, 13, 1, 3
- Gao, Y. & Solomon, P. M. 2004b, *ApJ*, 606, 271 1.3.1.2, 4.6.2, 9.3, 10.5, 12.1.2,
12.2, 12.3.1, 13
- García-Burillo, S., Combes, F., Neri, R., et al. 2007, *A&AP*, 468, L71 1.3.3.3, 5.7,
A.39

- Genzel, R. & Cesarsky, C. J. 2000, *ARAA*, 38, 761 [1.3.2](#), [6.1](#), [9.3](#)
- Giroletti, M., Giovannini, G., & Taylor, G. B. 2005a, *A&AP*, 441, 89 [A.40](#)
- Giroletti, M., Taylor, G. B., & Giovannini, G. 2005b, *ApJ*, 622, 178 [5.7](#)
- Gordon, K. D., Engelbracht, C. W., Fadda, D., et al. 2007, *PASP*, 119, 1019 [4.5.1.1](#)
- Gordon, M. A., Baars, J. W. M., & Cocke, W. J. 1992, *A&AP*, 264, 337 [4.3](#), [5.1](#)
- Govoni, F. & Feretti, L. 2004, *International Journal of Modern Physics D*, 13, 1549 [8.5.1](#), [8.5.1](#), [11.6.2](#)
- Graciá-Carpio, J., García-Burillo, S., Planesas, P., & Colina, L. 2006, *ApJL*, 640, L135 [12.1.2](#), [12.1.4](#)
- Gregory, P. C. & Condon, J. J. 1991, *APJS*, 75, 1011 [11.6.1](#), [11.2](#)
- Gregory, P. C., Scott, W. K., Douglas, K., & Condon, J. J. 1996, *APJS*, 103, 427 [11.6.1](#), [11.2](#)
- Hardcastle, M. J., Alexander, P., Pooley, G. G., & Riley, J. M. 1998, *MNRAS*, 296, 445 [A.20](#)
- Hardcastle, M. J., Kraft, R. P., Worrall, D. M., et al. 2007, *ApJ*, 662, 166 [1.2](#)
- Haynes, R. F., Huchtmeier, W. K. G., & Siegman, B. C. 1975, *A compendium of radio measurements of bright galaxies*, ed. Haynes, R. F., Huchtmeier, W. K. G., & Siegman, B. C. [11.6.1](#), [11.2](#)
- Heckman, T. M., Smith, E. P., Baum, S. A., et al. 1986, *ApJ*, 311, 526 [7.3](#)
- Helou, G., Roussel, H., Appleton, P., et al. 2004, *APJS*, 154, 253 [8.2](#)
- Hernquist, L. 1989, *Nature*, 340, 687 [12.1.3](#)
- Huchtmeier, W. K. 1994, *A&AP*, 286, 389 [7.1](#)
- Huchtmeier, W. K., Sage, L. J., & Henkel, C. 1995, *A&AP*, 300, 675 [7.1](#)
- Isobe, T., Feigelson, E. D., & Nelson, P. I. 1986, *ApJ*, 306, 490 [5.2](#)
- Jackson, N., Sparks, W. B., Miley, G. K., & Macchetto, F. 1995, *A&AP*, 296, 339 [A.14](#)
- Jaffe, W., Ford, H. C., Ferrarese, L., van den Bosch, F., & O'Connell, R. W. 1993, *Nature*, 364, 213 [A.10](#)
- Jamrozy, M., Klein, U., Mack, K., Gregorini, L., & Parma, P. 2004, *A&AP*, 427, 79 [A.43](#)

- Kellermann, K. I. & Pauliny-Toth, I. I. K. 1973, *AJ*, 78, 828 [11.2](#)
- Kellermann, K. I. & Verschuur, G. L. 1988, *Galactic and extragalactic radio astronomy* (2nd edition) (*Galactic and Extragalactic Radio Astronomy*) [1.2](#)
- Kennicutt, Jr., R. C. 1998, *ARAA*, 36, 189 [1.2](#)
- Kleinmann, S. G., Cutri, R. M., Young, E. T., Low, F. J., & Gillett, F. C. 1986, in Tucson, Univ. of Arizona (1986), 0–+ [11.2](#)
- Knapp, G. R., Guhathakurta, P., Kim, D., & Jura, M. A. 1989, *APJS*, 70, 329 [1.2](#), [1.3.2](#), [6.1](#)
- Knapp, G. R., Gunn, J. E., & Wynn-Williams, C. G. 1992, *ApJ*, 399, 76 [1.3.2](#), [6.1](#)
- Kohno, K. 2003, in *Astronomical Society of the Pacific Conference Series*, Vol. 289, *The Proceedings of the IAU 8th Asian-Pacific Regional Meeting*, Volume I, ed. S. Ikeuchi, J. Hearnshaw, & T. Hanawa, 349–352 [1.3.1](#)
- Kohno, K. 2005, in *American Institute of Physics Conference Series*, Vol. 783, *The Evolution of Starbursts*, ed. S. Hüttmeister, E. Manthey, D. Bomans, & K. Weis, 203–208 [1.3.1](#)
- Kohno, K., Kawabe, R., & Vila-Vilaró, B. 1999a, *ApJ*, 511, 157 [1.3.1](#), [12.1.2](#)
- Kohno, K., Kawabe, R., & Vila-Vilaró, B. 1999b, in *The Physics and Chemistry of the Interstellar Medium*, *Proceedings of the 3rd Cologne-Zermatt Symposium*, held in Zermatt, September 22–25, 1998, Eds.: V. Ossenkopf, J. Stutzki, and G. Winnewisser, GCA-Verlag Herdecke, ISBN 3-928973-95-9, ed. V. Ossenkopf, J. Stutzki, & G. Winnewisser, 34–+ [12.1.2](#)
- Kohno, K., Matsushita, S., Vila-Vilaró, B., et al. 2001, in *Astronomical Society of the Pacific Conference Series*, Vol. 249, *The Central Kiloparsec of Starbursts and AGN: The La Palma Connection*, ed. J. H. Knapen, J. E. Beckman, I. Shlosman, & T. J. Mahoney, 672–+ [1.3.1](#)
- Kraft, R. P., Hardcastle, M. J., Worrall, D. M., & Murray, S. S. 2005, *ApJ*, 622, 149 [A.20](#)
- Kramer, C. 1997, in *Calibration procedures and efficiencies (IRAM)* [4.3](#), [4.4.2](#)
- Kraus, J. D. & Andrew, B. H. 1971, *AJ*, 76, 103 [2.2.4](#)
- Krips, M., Neri, R., García-Burillo, S., et al. 2008, *ApJ*, 677, 262 [1.3.1.3](#), [4.6.3](#)
- Kühr, H., Nauber, U., & Pauliny-Toth, I. I. K. 1979 [11.6.1](#)
- Kühr, H., Witzel, A., Pauliny-Toth, I. I. K., & Nauber, U. 1981, *AAPS*, 45, 367 [11.6.1](#), [11.2](#)

- Lagos, C. D. P., Padilla, N. D., & Cora, S. A. 2009, MNRAS, 397, L31 [5.7](#)
- Laing, R. A., Canvin, J. R., Cotton, W. D., & Bridle, A. H. 2006, MNRAS, 368, 48 [A.25](#)
- Laing, R. A. & Peacock, J. A. 1980, MNRAS, 190, 903 [11.6.1](#), [11.2](#), [11.6.2](#)
- Lavalley, M., Isobe, T., & Feigelson, E. 1992, in Astronomical Society of the Pacific Conference Series, Vol. 25, Astronomical Data Analysis Software and Systems I, ed. D. M. Worrall, C. Biemesderfer, & J. Barnes, 245–+ [5.2](#)
- Leahy, J. P., Black, A. R. S., Dennett-Thorpe, J., et al. 1997, MNRAS, 291, 20 [A.16](#)
- Lee, H., Skillman, E. D., Cannon, J. M., et al. 2006, ApJ, 647, 970 [8.2](#)
- Leon, S., Eckart, A., Laine, S., et al. 2007, A&AP, 473, 747 [12.1.4](#)
- Leon, S. & Verdes-Montenegro, L. 2003, A&AP, 411, 391 [12.1.2](#)
- Leon, S., Verdes-Montenegro, L., Sabater, J., et al. 2008, A&AP, 485, 475 [12.1.1](#)
- Lightman, A. P. & Brawer, R. 1990, Origins : the lives and worlds of modern cosmologists Lightman and Roberta Brawer., ed. Lightman, A. P. & Brawer, R. [1.3.3.2](#)
- Lim, J., Leon, S., Combes, F., & Dinh-V-Trung. 2000, ApJL, 545, L93 [4.4](#), [5.4](#), [5.7](#)
- Lisenfeld, U., Verdes-Montenegro, L., Sulentic, J., et al. 2007, A&AP, 462, 507 [12.1.1](#), [12.1.3](#), [12.1.4](#)
- Mack, K., Klein, U., O’Dea, C. P., Willis, A. G., & Saripalli, L. 1998, A&AP, 329, 431 [A.25](#)
- Mack, K., Prieto, M. A., Brunetti, G., & Orienti, M. 2009, MNRAS, 392, 705 [A.16](#), [A.20](#)
- Madden, S. C., Vigroux, L., & Sauvage, M. 1999, in ESA Special Publication, Vol. 427, The Universe as Seen by ISO, ed. P. Cox & M. Kessler, 933–+ [1.3.2](#), [6.1](#)
- Mahabal, A., Kembhavi, A., Singh, K. P., Bhat, P. N., & Prabhu, T. P. 1996, ApJ, 457, 598 [A.10](#)
- Maraston, C., Daddi, E., Renzini, A., et al. 2006, ApJ, 652, 85 [8.2](#)
- Martel, A. R., Baum, S. A., Sparks, W. B., et al. 1999, APJS, 122, 81 ([document](#)), [2.3](#), [5.7](#), [11.1](#), [A.4](#), [A.9](#), [A.10](#), [A.11](#), [A.12](#), [A.14](#), [A.17](#), [A.18](#), [A.20](#), [A.23](#)

- Mazzarella, J. M., Graham, J. R., Sanders, D. B., & Djorgovski, S. 1993, *ApJ*, 409, 170 [10.2](#), [10.3](#), [10.3.1](#), [10.4](#), [10.3](#), [10.5](#), [10.4](#), [13](#), [2](#), [15](#), [2](#)
- Meng, D.-M. & Zhou, H.-Y. 2006, *Chinese Journal of Astronomy and Astrophysics*, 6, 25 [A.3](#)
- Mihos, J. C. & Hernquist, L. 1994, *ApJ*, 437, 611 [1.2](#)
- Mihos, J. C. & Hernquist, L. 1996, *ApJ*, 464, 641 [1.2](#)
- Miley, G. 1980, *ARAA*, 18, 165 [8.5.1](#), [11.6.2](#)
- Moffet, A. T. 1975, *Strong Nonthermal Radio Emission from Galaxies*, ed. Sandage, A., Sandage, M., & Kristian, J. (the University of Chicago Press), 211–+ [8.5.1](#)
- Morganti, R., de Zeeuw, P. T., Oosterloo, T. A., et al. 2006, *MNRAS*, 371, 157 [7.1](#), [7.2](#)
- Morganti, R., Oosterloo, T., Tadhunter, C., & Emonts, B. 2003a, *New Astronomy Review*, 47, 273 [A.40](#)
- Morganti, R., Oosterloo, T. A., Capetti, A., et al. 2003b, *A&AP*, 399, 511 [A.40](#)
- Morganti, R., Peck, A. B., Oosterloo, T. A., et al. 2009, *A&AP*, 505, 559 [7.2](#), [A.25](#)
- Moshir, M. & et al. 1990, in *IRAS Faint Source Catalogue*, version 2.0 (1990), 0–+ [11.2](#)
- Murgia, M., Fanti, C., Fanti, R., et al. 1999, *A&AP*, 345, 769 [8.5.1](#), [8.5.1](#), [11.6.2](#)
- Murgia, M., Parma, P., de Ruiter, H. R., et al. 2001, *A&AP*, 380, 102 [A.26](#)
- Nguyen, Q.-R., Jackson, J. M., Henkel, C., Truong, B., & Mauersberger, R. 1992, *ApJ*, 399, 521 [1.3.1.3](#), [4.6.3](#), [12.1.2](#)
- Niell, A. E. 1971, PhD thesis, CORNELL UNIVERSITY. [11.2](#)
- Nieto, J.-L., McClure, R., Fletcher, J. M., et al. 1990, *A&AP*, 235, L17 [A.37](#)
- Nilson, P. 1973, *Nova Acta Regiae Soc. Sci. Upsaliensis Ser. V*, 0 [2.2.5](#)
- Noel-Storr, J., Baum, S. A., Verdoes Kleijn, G., et al. 2003, *APJS*, 148, 419 [A.27](#)
- Northover, K. J. E. 1973, *MNRAS*, 165, 369 [A.3](#)
- Ocaña Flaquer, B., Leon, S., & Combes, F. 2010 ([document](#)), [10.3](#), [10.3.1](#), [10.3](#), [10.5](#), [10.4](#), [11.6.1](#), [11.2](#), [13](#), [15](#)
- O’Dea, C. P., Baum, S. A., & Stanghellini, C. 1991, *ApJ*, 380, 66 [1.3.3.5](#)

- Okuda, T., Kohno, K., Iguchi, S., & Nakanishi, K. 2005, *ApJ*, 620, 673 [10.3.1](#), [11.3.1](#)
- Pacholczyk, A. G. 1970, *Radio astrophysics. Nonthermal processes in galactic and extragalactic sources*, ed. Pacholczyk, A. G. [8.5.1](#)
- Pahre, M. A., Ashby, M. L. N., Fazio, G. G., & Willner, S. P. 2004, *APJS*, 154, 229 [8.2](#)
- Papadopoulos, P. P. 2007, *ApJ*, 656, 792 [1.3.1](#)
- Parma, P., Murgia, M., de Ruiter, H. R., et al. 2007, *A&AP*, 470, 875 [8.5.1](#), [11.6.2.1](#)
- Phillips, R. B. & Mutel, R. L. 1982, *A&AP*, 106, 21 [1.3.3.3](#), [1.3.3.4](#)
- Polatidis, A. G., Wilkinson, P. N., Xu, W., et al. 1995, *APJS*, 98, 1 [11.6.1](#), [11.2](#)
- Readhead, A. C. S., Taylor, G. B., Pearson, T. J., & Wilkinson, P. N. 1996, *ApJ*, 460, 634 [1.3.3.4](#)
- Rees, N. 1990, *MNRAS*, 243, 637 [11.6.1](#)
- Rengelink, R. B., Tang, Y., de Bruyn, A. G., et al. 1997, *AAPS*, 124, 259 [11.2](#)
- Reynaud, D. & Downes, D. 1997, *A&AP*, 319, 737 [12.1.2](#)
- Rieke, G. H., Young, E. T., Engelbracht, C. W., et al. 2004, *APJS*, 154, 25 [3.4.4](#)
- Rinsland, C. P., Dixon, R. S., Gearhart, M. R., & Kraus, J. D. 1974, *AJ*, 79, 1129 [2.2.4](#)
- Rinsland, C. P., Dixon, R. S., & Kraus, J. D. 1975, *AJ*, 80, 759 [2.2.4](#)
- Riquelme, D., B. L. M. R. M. J. W. T. 2010, *A&A* [1.3.1.3](#), [4.6.3](#)
- Roger, R. S., Costain, C. H., & Stewart, D. I. 1986, *AAPS*, 65, 485 [11.6.1](#), [11.2](#)
- Rohlfs, K. & Wilson, T. L. 2004, *Tools of radio astronomy (Tools of radio astronomy, 4th rev. and enl. ed., by K. Rohlfs and T.L. Wilson. Berlin: Springer, 2004)* [4.4.2](#), [5.6](#)
- Sabater, J., Leon, S., Verdes-Montenegro, L., et al. 2008, *A&AP*, 486, 73 [12.1.1](#), [12.1.3](#), [12.1.4](#)
- Sage, L. J. & Solomon, P. M. 1989, *ApJL*, 342, L15 [9.5](#)
- Salomé, P., Combes, F., Revaz, Y., et al. 2008, *A&AP*, 484, 317 [5.7](#)
- Sanders, D. B. & Mirabel, I. F. 1996, *ARAA*, 34, 749 [9.2](#)

- Sanders, D. B., Scoville, N. Z., & Soifer, B. T. 1991, *ApJ*, 370, 158 [10.2](#)
- Sanders, D. B., Soifer, B. T., Elias, J. H., et al. 1988, *ApJ*, 325, 74 [10.2](#)
- Sarzi, M., Falcón-Barroso, J., Davies, R. L., et al. 2006, *MNRAS*, 366, 1151 [A.32](#)
- Scheer, D. J. & Kraus, J. D. 1967, *AJ*, 72, 536 [2.2.4](#)
- Schmitt, J. H. M. M. 1985, *ApJ*, 293, 178 [5.2](#)
- Schoenmakers, A. P., de Bruyn, A. G., Röttgering, H. J. A., van der Laan, H., & Kaiser, C. R. 2000, *MNRAS*, 315, 371 [11.6.2](#), [11.6.4](#)
- Scoville, N. Z., Sargent, A. I., Sanders, D. B., & Soifer, B. T. 1991, *ApJL*, 366, L5 [1.3.1](#)
- Seaquist, E. R. & Frayer, D. T. 2000, *ApJ*, 540, 765 [1.3.1.3](#), [4.6.3](#)
- Serra, P. & Oosterloo, T. A. 2010, *MNRAS*, 401, L29 [7.1](#)
- Shlosman, I., Begelman, M. C., & Frank, J. 1990, *Nature*, 345, 679 [1.2](#)
- Simpson, C., Ward, M., Clements, D. L., & Rawlings, S. 1996, *MNRAS*, 281, 509 [A.16](#)
- Smith, J. D. T., Draine, B. T., Dale, D. A., et al. 2007, *ApJ*, 656, 770 [8.2](#)
- Soifer, B. T., Helou, G., & Werner, M. 2008, *ARAA*, 46, 201 [8.2](#)
- Solomon, P. M., Downes, D., & Radford, S. J. E. 1992, *ApJL*, 387, L55 [1.3.1.2](#), [4.6.2](#), [12.1.2](#)
- Solomon, P. M., Downes, D., Radford, S. J. E., & Barrett, J. W. 1997, *ApJ*, 478, 144 [9.1](#), [10.2](#), [10.3](#), [10.5](#), [10.3](#), [10.4](#), [12.3.1](#), [13](#), [15](#)
- Solomon, P. M. & Sage, L. J. 1988, *ApJ*, 334, 613 [10.5](#)
- Stansberry, J. A., Gordon, K. D., Bhattacharya, B., et al. 2007, *PASP*, 119, 1038 [4.5.1.1](#)
- Sternberg, A., Genzel, R., & Tacconi, L. 1994, *ApJL*, 436, L131 [1.3.1](#)
- Sternberg, R., Aflalaye, A., & Raulin, F. 1996, *Origins of Life and Evolution of the Biosphere*, 26, 507 [1.3.1](#)
- Strauss, M. A., Huchra, J. P., Davis, M., et al. 1992, *APJS*, 83, 29 [10.2](#)
- Strong, A. W., Bloemen, J. B. G. M., Dame, T. M., et al. 1988, *A&AP*, 207, 1 [5.1](#)
- Sturm, E., Lutz, D., Genzel, R., et al. 1996, *A&AP*, 315, L133 [1.3.1](#)

- Sugai, H., Malkan, M. A., Ward, M. J., Davies, R. I., & McLean, I. S. 1997, *ApJ*, 481, 186 [1.3.1](#)
- Sulentic, J. W. 1976, *APJS*, 32, 171 [12.1.3](#)
- Sulentic, J. W. & Tifft, W. G. 1973, *The revised new catalogue of nonstellar astronomical objects*, ed. W. G. Sulentic, J. W. & Tifft [2.2.2](#)
- Sulentic, J. W., Verdes-Montenegro, L., Bergond, G., et al. 2006, *A&AP*, 449, 937 [12.1.1](#), [12.1.2](#), [12.1.3](#)
- Thakkar, D. D., Xu, W., Readhead, A. C. S., et al. 1995, *APJS*, 98, 33 [11.2](#)
- Thi, W.-F., van Zadelhoff, G.-J., & van Dishoeck, E. F. 2004, *A&AP*, 425, 955 [5.4.1](#)
- Tremblay, G. R., Chiaberge, M., Sparks, W. B., et al. 2009, *APJS*, 183, 278 [A.2](#), [A.7](#), [A.10](#)
- Valentijn, E. A., van der Werf, P. P., de Graauw, T., & de Jong, T. 1996, *A&AP*, 315, L145 [1.3.1](#)
- van Breugel, W., Miley, G., & Heckman, T. 1984, *AJ*, 89, 5 [1.3.3.3](#), [1.3.3.4](#)
- van der Werf, P. P., Genzel, R., Krabbe, A., et al. 1993, *ApJ*, 405, 522 [1.3.1](#)
- van Driel, W. & van Woerden, H. 1991, *A&AP*, 243, 71 [7.1](#)
- Verdes-Montenegro, L., Sulentic, J., Lisenfeld, U., et al. 2005, *A&AP*, 436, 443 [4.6.2](#), [12.1.1](#), [12.1.2](#), [12.1.3](#)
- Verdes-Montenegro, L., Yun, M. S., Perea, J., del Olmo, A., & Ho, P. T. P. 1998, *ApJ*, 497, 89 [12.1.3](#)
- Verkhodanov, O. V., Andernach, H., & Verkhodanova, N. V. 2000, *Bull. Special Astrophys. Obs.*, 49, 53 [11.6.1](#), [11.2](#)
- Verley, S., Leon, S., Verdes-Montenegro, L., et al. 2007a, *A&AP*, 472, 121 [12.1.1](#), [12.1.3](#)
- Verley, S., Odewahn, S. C., Verdes-Montenegro, L., et al. 2007b, *A&AP*, 470, 505 [12.1.1](#)
- White, R. L. & Becker, R. H. 1992, *APJS*, 79, 331 [11.2](#)
- Wiklind, T., Combes, F., & Henkel, C. 1995, *A&AP*, 297, 643 [10.2](#), [10.3](#), [10.3.1](#), [10.4](#), [10.1](#), [10.3](#), [10.5](#), [10.4](#), [13](#), [2](#), [15](#), [2](#)
- Wiklind, T. & Henkel, C. 1995, *A&AP*, 297, L71+ [1.2](#), [10.5](#)

- Wiklind, T. & Rydbeck, G. 1986, *A&AP*, 164, L22 [1.2](#)
- Wilkinson, P. N., Polatidis, A. G., Readhead, A. C. S., Xu, W., & Pearson, T. J. 1994, *ApJL*, 432, L87 [1.3.3.4](#)
- Wills, B. J. 1973, *ApJ*, 180, 335 [11.6.1](#)
- Wilson, R. W., Jefferts, K. B., & Penzias, A. A. 1970, *ApJL*, 161, L43+ [1.3.1.1](#), [4.6.1](#)
- Wilson, T. L., Rohlfs, K., & Hüttemeister, S. 2009, *Tools of Radio Astronomy*, ed. Wilson, T. L., Rohlfs, K., Hüttemeister, S. (Springer-Verlag) [1.3.1.3](#)
- Wu, J., Evans, II, N. J., Gao, Y., et al. 2005, *ApJL*, 635, L173 [12.1.2](#)
- Xu, C. & Sulentic, J. W. 1991, *ApJ*, 374, 407 [12.1.3](#)
- Xu, W., Readhead, A. C. S., Pearson, T. J., Polatidis, A. G., & Wilkinson, P. N. 1995, *APJS*, 99, 297 [11.2](#)
- Yamada, M., Wada, K., & Tomisaka, K. 2009, in *Astronomical Society of the Pacific Conference Series*, Vol. 408, *Astronomical Society of the Pacific Conference Series*, ed. W. Wang, Z. Yang, Z. Luo, & Z. Chen, 254–+ [14](#)
- Young, J. S., Allen, L., Kenney, J. D. P., Lesser, A., & Rownd, B. 1996, *AJ*, 112, 1903 [10.5](#), [10.4](#)
- Young, J. S. & Devereux, N. A. 1991, *ApJ*, 373, 414 [12.1.2](#)
- Young, J. S. & Scoville, N. 1982, *ApJ*, 258, 467 [12.1.2](#)
- Young, J. S., Xie, S., Tacconi, L., et al. 1995, *APJS*, 98, 219 [10.5](#), [10.4](#)
- Young, L. M. 2002, *AJ*, 124, 788 [5.1](#)
- Young, L. M., Bureau, M., & Cappellari, M. 2008, *ApJ*, 676, 317 [5.4](#)
- Zhang, X., Zheng, Y., Chen, H., et al. 1997, *AAPS*, 121, 59 [11.6.1](#), [11.2](#)
- Zwicky, F., Herzog, E., & Wild, P. 1961, *Catalogue of galaxies and of clusters of galaxies*, Vol. I [2.2.5](#)
- Zwicky, F., Herzog, E., & Wild, P. 1963, *Catalogue of galaxies and of clusters of galaxies*, Vol. II [2.2.5](#)
- Zwicky, F., Karpowicz, M., & Kowal, C. T. 1965, *Catalogue of Galaxies and of Clusters of Galaxies*, Vol. V [2.2.5](#)